Author:
Kettley, Tom

Title:
Microseismic and geomechanical investigation of injection-induced fault reactivation

Microseismic and geomechanical investigation of injection-induced fault reactivation

By

THOMAS KETTLETY

School of Earth Sciences
UNIVERSITY OF BRISTOL

A dissertation submitted to the University of Bristol in accordance with the requirements of the degree of DOCTOR OF PHILOSOPHY in the Faculty of Science.

JUNE 2020

Word count: 34,786

Abstract

Earthquakes caused by human activities are of increasing concern around the world. Injection of fluid into the subsurface is a vital part of many industries, but it is known that it can trigger felt and sometimes damaging events. Geothermal energy, waste water disposal, carbon dioxide sequestration, and hydraulic fracturing, or fracking, have all been associated with seismicity of varying severity, and over the past decade the number of cases has noticeably increased. Large parts of central North America experience weekly $M \sim 3$ events, seismicity has now put a halt to all hydraulic fracturing in the UK, and an induced earthquake has lead to many dozens of people being injured in South Korea. Understanding the controls underlying the propensity for an area to exhibit induced seismicity is now an integral component of one of the biggest challenges facing the world today: meeting the demand for energy whilst simultaneously reducing greenhouse gas emissions.

In this thesis I use measurements of microseismic events (broadly $M < 2$) to examine the physical processes controlling the activation of faults, and test statistical methods to forecast the onset of larger earthquakes. I examine multiple case studies of hydraulic fracturing-induced seismicity, using microseismic data from operations in the Horn River Basin, British Columbia, Canada, and at the Preston New Road site near Blackpool, Lancashire, UK. These large catalogues, each containing tens of thousands of events, provide a uniquely detailed perspective on the seismic activity that occurs during stimulation. As these datasets are acquired using borehole sensors placed near the reservoirs, they have low detection thresholds and enhanced location accuracy, which allows for the interplay between injection and fault activation to be clearly resolved. Whilst the seismicity recorded had little impact in the case of the Horn River Basin data, large events triggered by the Preston New Road operations have lead to a de facto moratorium of fracking in the UK.

Using these data, I show that one of the mechanisms that strongly controls the likelihood and behaviour of fault activation by injection is the in situ stress state. Well oriented faults are naturally more prone to failure, however the relative magnitudes of the principle stresses are a substantial factor in a fault's tendency to slip. Regions with high stress anisotropy – where there is a bigger difference between the smallest and largest principle stress – will host well oriented faults that require only a small perturbation to the stress in order to reach failure, giving them a higher slip tendency. In chapters 2 and 5, microseismic data and geomechanical modelling are used to show that the slip tendency of activated faults can affect not only the mechanisms controlling fault activation, but also the magnitudes of induced events for a given pressure perturbation.

One of these mechanisms controlling fault activation is elastic stress transfer. This mechanism, which results from deformation of prior seismic events stimulating further seismicity, has been shown to contribute to the continuation of induced seismicity in a number of recent cases. However, in chapter 2, using the microseismic data from the Horn River Basin, I show that these

smaller magnitude stress changes are not a significant driver in activating faults in areas of low stress anisotropy, where slip tendency is low. In contrast, the sequences for which elastic stress transfer is a contributing mechanism are predominantly in fields where there is high stress anisotropy, where only a small magnitude perturbation to the stress state is required to stimulate failure. In chapter 5, using data from the Preston New Road operations in 2019, I show that smaller faults with a higher slip tendency can produce larger magnitude events for a smaller perturbation when compared to larger, less well oriented faults. Thus, these well oriented faults in areas of high stress anisotropy should be much more of a concern when assessing seismic hazard.

In chapter 3, I investigate another physical mechanism controlling the activation of faults during injection – elastic stress transfer from the opening of hydraulic fractures. During the Preston New Road operations in 2018, the spatiotemporal distribution of events is not easily explained by the mechanisms most frequently ascribed to fault activation: increased pore pressure or poroelastic stress changes. Clusters of events were offset from injection, large numbers of events were occurring for very small volumes injected, and the seismicity on the activated fault was more compartmentalised than expected. A stochastic model of hydraulic fracture opening was developed, and showed that these unexpected locations could be explained by the stressing effect of tensile opening fractures. This mechanism appeared to be controlling which parts of a fault were most active once it was stimulated by injection. This again has direct impact on seismic hazard assessment, with faults that are well oriented with respect to the opening fractures more of a risk of stress interaction. This effect could also influence operational decision making, with the order of injection stages affecting the amount of stress nearby faults receive as a result of fracture opening.

In chapter 4, I examine the ability of statistics-based maximum magnitude forecasting to aid real-time operational decision-making. Traffic Light Systems are a commonly used framework for regulating seismicity during hydraulic fracturing, but are fundamentally retroactive in nature – mitigating actions are taken after the large events occur. Through live monitoring of the magnitude-frequency distribution of events, and the rate of seismicity as a function of the amount of fluid injected, the expected magnitude of the largest event can be forecast. When I applied this technique during the Preston New Road operations in 2018, it was able to successfully forecast the largest events observed and was an aid to the operator during decision-making. Careful application of the forecasting method was required, with successive stages of injection having to be treated cumulatively. In contrast, it's application to a second case study in chapter 5, the 2019 Preston New Road operations, slightly underestimated the largest events. This underprediction was produced by the failure of a key assumption – that all events follow a single Gutenberg-Richter b-value. A clear shift was observed as seismicity progressed from a hydraulic fracturing regime, with high b-values, to a fault activation regime with low b-values. Robust characterisation of the magnitude-frequency distribution for the largest events is thus a crucial aspect of this statistical forecasting method.

I have shown that a number factors control whether or not a fault will be reactivated by injection. The relative significance of these controlling factors is situational and will change between reservoirs. Assessing the likelihood of injection-induced seismicity requires knowledge of the in situ stress field, the presence and orientation of faults, and the geomechanical, hydrological, and frictional properties of the rocks. Steps to mitigate induced seismicity are important for social acceptance and safety, but are also important for ensuring efficient operations. I have shown how statistical methods can be used to forecast event magnitudes, though care must be taken in their application.

Dedication and acknowledgements

I never thought I would do a PhD. Growing up, I had known very few people who had even gone to university, let alone considered postgraduate research an option. I'm therefore as surprised as most of my family that there is a thesis with my name on the front. That would not have been possible without the very subtle nudge in this direction from Mike Kendall, who in a meeting about geophysics grad schemes four years ago said: "You should do a PhD. I've got a couple of cool projects coming up. . . " Providing scientific advice, securing funding, acquiring datasets, building a relaxed and supportive group, giving me more opportunities to do interesting work, and making a great Negroni are some of the many reasons I am thankful for having Mike as a supervisor. Mike's supervision and encouragement is a big part of why this experience has been a joy. I am very grateful for it.

None of what follows would have been possible without the technical, academic, and moral support of James Verdon. His advice and guidance have been beyond helpful, and gave me the best environment in which to do research. This was combined with the support of Max Werner, who's expertise, statistical skill, and incisive questioning made the work here significantly better. Each paper would not have been possible without their scientific rigor and editing prowess.

I would like to thank NERC and its GW4+ DTP for funding my project, and providing many training courses and workshops. I would also like to thank the operators and regulators of the Bristol University Microseismic Projects (BUMPs) consortium, who provided data for the project.

I am grateful for the advice and guidance of my PhD committee – Max Werner, Katsu Goda, and Heidy Mader – as well as that of my examiners, Juliet Biggs and Zoe Shipton. I would also like to acknowledge the reviewers of the papers which make up part of this thesis, whose helpful and constructive feedback improved those chapters.

I will always be grateful to my fellow PhDs for their friendship, advice, and unforgettable lunchtime conversations: Anna Williams, Gareth Pontgratz-Coleman, Emma Landon, Jacob Wood, Ailsa Naismith, George Rowland, Melissa Garcia, Joseph Asplet, Nick Hayes, Frances Boreham, David Edwards, Ben Heinen, Tim Culwick, Ben Griffin, Tom Smith, and Kathryn Shaw.

The Bristol Geophysics group have been a very supportive bunch, and I am very grateful for their company over the last four years, namely: Bob Myhill, David Schlaphorst, Hannah Susorney, Antony Butcher, Alan Baird, Anna Stork, Neil Wilkins, Nicky Young, Tesfaye Tessema, Cristina Rodriguez, Adam Klinger, Robbie Churchill, Jessica Sanchez, Cindy Lim Shin Yee, Nick Teanby, and James Wookey.

My last thank yous go to my family, who have supported me through *many* more years of education than they expected, and my other half, Ellen MacDonald. Without her love and support, this would've all been a heck of a lot harder.

AUTHOR'S DECLARATION

I declare that the work in this dissertation was carried out in accordance with the requirements of the University's Regulations and Code of Practice for Research Degree Programmes and that it has not been submitted for any other academic award. Except where indicated by specific reference in the text, the work is the candidate's own work. Work done in collaboration with, or with the assistance of, others, is indicated as such. Any views expressed in the dissertation are those of the author.

SIGNED: Tom Kettlety

DATE: June 18th 2020

Table of Contents

Page

List of Figures **xi**

1 Introduction **1**

1.1 A brief history . . . 1

1.1.1 Hydraulic fracturing and induced earthquakes . . . 4

1.2 Geological and Operational Background . . . 5

1.2.1 Horn River Basin, British Columbia, Canada . . . 6

1.2.2 Bowland Basin, Lancashire, UK . . . 9

1.3 Event magnitudes . . . 11

1.4 Traffic Light Systems . . . 14

1.5 Central questions of IIS . . . 14

1.6 Thesis outline . . . 16

2 Interevent elastic stress transfer during hydraulic fracturing-induced fault activation **19**

2.1 Introduction . . . 20

2.2 Data . . . 23

2.2.1 Identifying Fault Reactivation . . . 26

2.2.2 Stress Model for Horn River Basin . . . 29

2.3 Methods & Results . . . 31

2.3.1 Elastic Stress Modelling . . . 31

2.3.2 Resolving Stresses onto Fault Structures . . . 33

2.3.3 Sensitivity Analysis . . . 35

2.3.4 Cluster Stress Budget . . . 38

2.3.5 Fault Slip Potential . . . 39

2.4 Discussion . . . 42

2.4.1 Elastic Stress Modelling . . . 42

2.4.2 Focal Mechanism Sensitivity Analysis . . . 44

2.4.3 Fault Orientations . . . 44

2.5 Conclusions . . . 45

3 Fracture opening stress transfer controlling the spatial distribution of fault activation **47**
3.1 Introduction . . . 48
3.2 Hydraulic fracturing at Preston New Road, UK . . . 50
3.2.1 Microseismic observations in detail . . . 54
3.2.2 Spatiotemporal evolution of microseismicity . . . 56
3.3 Elastostatic stress modelling . . . 58
3.3.1 Stochastic hydraulic fracture model . . . 58
3.3.2 Modelling Stress Change . . . 61
3.3.3 Model Scenarios . . . 62
3.4 Results . . . 63
3.5 Discussion . . . 69
3.5.1 Model Uncertainties . . . 69
3.5.2 Possible Impact on Fault Rupture Dimensions . . . 71
3.6 Conclusions . . . 72

4 Real-time maximum magnitude forecasting during hydraulic fracturing **75**
4.1 Introduction . . . 76
4.2 Preston New Road microseismicity . . . 77
4.2.1 Local and moment magnitudes . . . 80
4.3 Maximum magnitude forecasting . . . 83
4.3.1 Seismic efficiency . . . 83
4.3.2 Seismogenic index . . . 84
4.4 Methods and results . . . 85
4.4.1 Stage-by-stage forecasts . . . 85
4.4.2 Combined forecasts . . . 89
4.5 Discussion . . . 89
4.5.1 Effect on operations . . . 89
4.5.2 Stage-by-stage vs. combined forecasts . . . 91
4.5.3 Seismic efficiency and seismogenic index . . . 92
4.6 Conclusion . . . 93

5 Interpretation and analysis of Preston New Road PNR-2 fault activation **95**
5.1 Introduction . . . 96
5.2 Hydraulic fracturing at Preston New Road . . . 99
5.2.1 Local and moment magnitudes . . . 100
5.3 Evolution of seismicity during PNR-2 operations . . . 102
5.3.1 The ML 2.9 earthquake . . . 106
5.3.2 Relationship between PNR-1z and PNR-2 seismicity . . . 108

5.4 Microseismic event magnitude distributions 108
5.5 Maximum magnitude forecasting 110
5.6 In-situ stress acting on faults 114
5.7 Conclusion 116

6 Conclusions **119**
6.1 Summary of results 119
6.2 Overall findings 121
6.3 Applications and recommendations 122
6.3.1 Stress state and fault orientation 122
6.3.2 Maximum magnitude forecasting 122
6.4 Future work 125

Bibliography **127**

List of Figures

Figure **Page**

1.1 The effect on the stress acting on a fault of pore pressure and poroelastic stress changes, demonstrated using Mohr circle diagrams. A point on the Mohr circle represents the shear τ and normal σ_n stress resolved onto a plane (i.e., a fault). Moving around the circle is equivalent to changing the orientation of the plane in the stress field (with principle stresses σ_1 and σ_2), rotating the plane such that τ and σ_n both change. Points on the solid lines show the initial stress state for a fault, and points on the dashed line show the effect to the stress state of a fluid pressure increase. The point where the circle meets the failure envelope corresponds to the orientation which is optimally aligned for failure. Points on a dotted lines, where the pressure change goes beyond the failure envelope, corresponds to the larger range of orientations which are now capable of failure, besides those that are perfectly optimally aligned. (a) shows the effect of increased pore pressure, reducing the effective normal stress and bringing the fault closer to the failure envelope. (b) shows the effect of poroelastic coupling between pore pressure changes and the stress in the rock frame, increasing differential stress. These effects are combined in the case of fluid injection, though the spatial and temporal scale over which each dominates is dependant on the geomechanical and diffusive properties of the rock. 2

1.2 A schematic of elastic stress transfer as a mechanism for triggering seismicity. Elastic deformation around a slipping source fault (shown above as the black line) induces changes to the stress field. These can be resolved onto a plane with a given orientation at any point around the source. Shear stress change $\Delta\tau$ is shown in (a), normal stress change $\Delta\sigma_n$, is shown in (b), and the Coulomb failure stress change ΔCFS is shown in (c). The colour maps above show the value of the stress changes at a slice through the volume at the depth of the fault. In this example, the stress change is resolved onto a receiver orientation of a left lateral strike-slip fault striking at 45°, which is demonstrated by the green line. The above shows the stress changes resulting from a 25 m, left lateral strike-slip fault striking north and slipping uniformly by 1 mm. Here, $\Delta\sigma_n$ is positive extensive, the shear modulus is 25 GPa, and the effective coefficient of friction μ' is 0.42. In (c), areas in which ΔCFS is positive (red) are those where failure on the receiver fault is encouraged. Conversely, failure on the receiver is inhibited by the source slip in areas which receive negative ΔCFS (blue). 4

1.3 Map showing the locations of the two sites of hydraulic fracturing-induced seismicity studied in this thesis. The red square and blue circle show their locations within Europe and North America respectively. 6

1.4 (a) The location of Horn River Basin hydraulic fracturing site in British Columbia, Canada. (b) A map view of the site, with the locations of the well paths shown as black lines, the injection stages as red diamonds, and the stations as blue triangles. (c) The same plot as (b), but in depth view. Inset here is a zoomed-in view of the targeted reservoir units, with formation tops delineated by grey lines. 8

1.5 (a) The location of the site of the Preston New Road (PNR) hydraulic fracturing wells in the northwest of England, UK. (b) Map view of the wells and stages at PNR. Two horizontal wells were drilled, with PNR-1z targeting the deeper Lower Bowland, and PNR-2 targeting the Upper Bowland shale. Injection stages that were actually pumped are shown as red diamonds and blue squares, for operations during PNR-1z and PNR-2 respectively. The locations of the stations used to monitor the two operations are shown as red and blue triangles. (c) A depth view of the site, with the same symbols as in (b). Stratigraphic units are those at the horizontal of the wells, and are delineated by grey lines. 10

1.6 A schematic summary of the triggering mechanisms and controls of induced earthquakes. The triggering mechanisms are shown in red, whilst the geological controls are shown in blue. Structures and other features are labeled in black. Each of the triggering mechanisms acts to change the stress on the fault to induce failure. This can occur through a reduction in normal stress (by an increase in pore pressure or an elastic stress change) or an increase in shear stress (through an elastic or poroelastic stress change). Each of the mineralogical and tectonic controls will affect the likelihood of a fault to produce felt seismicity, through either arresting the rupture process or requiring a very large pressure perturbation to initiate failure. 15

2.1 Hypocentres in plan view (a) and cross section (b) of all events detected and located during hydraulic stimulation of the 10 wells at the study site. Events are coloured by moment magnitude M_W. Wells 1 to 4 are shown as coloured lines, with the other wells being shown in black. The events associated with these wells show the clearest evidence for fault reactivation, and are the subject of this study. The red dashed boxes delineate the approximate positions of these hypothesised fault-related events. Also shown in (b) is the 1D geologic model, showing the depth of the overlying Fort Simpson formation, the three targeted shale layers (Muskwa, Otter Park and Evie), and the underlying Keg River limestone. The wells and corresponding targeted shale layers have matching colours. 25

2.2 Frequency-magnitude distributions for event clusters associated with fracturing stages in Wells 1 to 4. Each line corresponds to one cluster. The resulting b-values are clearly bimodal, with most clusters having $b > 1.5$ (coloured blue/green), and a smaller number of clusters having $b < 1.5$ (coloured yellow/red). The 4 low b-value clusters are those shown in Figure 2.3, which make up the activity in reactivation periods 1 and 2. . . . 27

2.3 **(a)** Hypocentre locations of the studied seismicity, grouped into "reactivation periods" 1 and 2 (RP1 & RP2). Perforation shots are shown as squares, coloured in the same manner as their associated RP. Circles show nearby events considered not to be associated with the fault activation, and are coloured by their associated injection well. The map view of the seismicity is inset. **(b)** Temporal distribution of the seismicity. Injection durations are shown above, with colours denoting the well from which injection was occurring. 28

2.4 **(a)** Edge on view of events hypocentres used to define the visible fault planes. Light blue downward triangles show fault 1 events, whilst dark blue upward triangles show fault 2 events. **(b)** Histograms of lateral distance away from plane for events associated with each fault. Colours are the same as those used in (a). Red lines show fitted normal distributions, where for F1 $\mu = 0 \pm 2$ m and $\sigma = 25 \pm 2$ m, and for F2 $\mu = 0 \pm 3$ and $\sigma = 46 \pm 2$ m. These uncertainties represent the 95% confidence intervals. 30

2.5 Stress gradients produced from Bell (2015) data for the Laird and Horn River Basin. The error bars show the uncertainties used for each of the stress parameters (see Walsh and Zoback, 2016). Estimates for the stresses acting at the depth of the reservoir are shown in grey boxes. 32

2.6 The values of the ΔCFS for the two reactivation periods, using the preferred NP. Events receiving positive Coulomb stress change are shown in red, and negative in blue. Events with $M_W > 0$ are shown as yellow stars. Note that a number of the larger magnitude events have higher magnitude, positive ΔCFS. The CI is estimated across moving windows each containing 50 events, and shown by green diamonds connected with a dotted line. The green lines show the CI for the entire period. Above, bars indicate the duration of injection plotted over the same time periods. 33

2.7 The results of mapping elastic Coulomb stress changes onto the fault planes shown in Figure 2.4. Grey bars show in the number of sources that occurred in each of the 30 minute time-bins. Green lines show the effective CI - the proportion of points across the planes which are experiencing positive ΔCFS at the time bin shown. Red show the sum of ΔCFS across every sample point on the planes. Blue show the average ΔCFS at the sample points. 35

2.8 Coulomb index distributions for the subset of events used to investigate the effect of FM uncertainty. The vertical lines indicate the CIs when the preferred and secondary NPs are chosen from the original FM. The red bars shows the distribution for catalogues when the NP is chosen randomly from the original FM. The green bars show the catalogues where FMs are permuted by Von Mises distributed rotation angles. The blue bars show the catalogues with randomly oriented FMs. The horizontal lines show the standard deviations of the distributions, with squares indicating the mean CI. 37

2.9 The CI change for the first 500 events in the first activation period, with a varying value of Skempton's ratio β. **(a)** The CI-β relationship for all the of events in the sample. **(b)** The temporal change in CI, calculated using moving windows, each containing 50 events. The grey-scale lines show the values of CI for the varying β values, whilst the green triangles show the mean CI for that time. The error bars give the standard deviation. The green dashed line shows the mean CI for the entire sample of events. 37

2.10 **(a)** Locations of the five clusters determined by the DBSCAN algorithm. **(b)** Temporal distribution of the clusters. 38

2.11 **(a)** The relationship between the total ΔCFS from all possible sources, and the stress change due to sources from only within the same cluster. Percentages break down the proportions of events (865 within clusters of a possible 1064) in each octant. For example, the NNE octant indicates 22% of events have a positive cluster ΔCFS equal to or greater than the total ΔCFS experienced from all possible sources. **(b)** The difference in intra-cluster stress change and total ΔCFS. It is clear that for the vast majority of events (97%), intra-cluster ΔCFS makes up the majority of the stress change received. The absolute difference exceeds ± 0.05 MPa for only 27 of 865 events. 39

2.12 Cluster stress change against total stress change for each of the five clusters. Percentages break down the proportions of events in each octant, as in Figure 2.11a. Clusters 1 and 4 receive very little stress change, as they are low magnitude, broadly clustered events associated with the fracturing. 40

2.13 Modelled HRB in situ stresses resolved onto fault planes, assuming a coefficient of friction of 0.7. **(a)** Effective normal stress. **(b)** Shear stress. **(c)** Critical pore pressure required to reach the Mohr failure criterion. The resolved stresses are contoured at the polar projection of the normal to the fault plane, with polar angle representing the fault-normal trend, and radial angle representing the fault-normal plunge. The orientations of the two faults F1 and F2 are shown respectively by the square and the triangle, both close to the minimum P_C values. 41

2.14 Fault slip potential probability curves for the two modelled faults. 41

3.1 Hypocentres of events recorded by the downhole monitoring array during hydraulic fracturing operations at the Preston New Road PNR-1z well with magnitudes greater than -0.5 and a signal-to-noise ratio greater than 5. Events are shown as circles, with marker sizes indicating the magnitude range, whilst colour shows the injection stage with which the event time overlapped. Diamonds denote the centre of the sleeve position on the well, and are also coloured by stage. The grey plane denotes the inferred seismogenic "fault zone", with a strike of 230° and a dip of 70°. This was found from the least squares fit to events with M_W above 0 and the events which continued to occur during the month hiatus in operations (see Clarke et al., 2019a, for a detailed discussion). Lower hemisphere focal mechanisms are shown as black and white beach-balls, derived from the surface station polarity data (Clarke et al., 2019a). 53

3.2 Hypocentres for 172 events located using data from both the surface and downhole arrays, and the same velocity model, allowing for comparison of the two locations. These surface-derived locations were calculated by the British Geological Survey (Baptie, 2019). Naturally, the lateral and depth resolution is far lower than that of the downhole locations. However, these surface locations generally mirror the spatial and temporal trends seen in the downhole locations, with a bias (74%) of events north of the PNR-1z well, and events trending further NE as the heel stages are injected. . . 54

3.3 Event locations for several stages during which unexpected or anomalous seismicity occurred. Events shown here are those with a signal-to-noise ratio of greater than 5. Events and stations are shown in the same manner as Figure 3.1. Pertinent observations are annotated on the figures with red arrows and text boxes. 57

3.4 Spatiotemporal evolution of microseismicity for selected stages. We show the distance of events from the mid-point of the active injection sleeve as a function of time from the start of the main injection phase for each stage. Points are coloured by the event magnitude, showing the magnitude of the TLS, with $M_w < 0$ coloured green, $M_w > 0$ yellow, and $M_w > 0.5$ coloured red. The injection rate for each stage is shown as a red line. Blue lines denote the expected distance of diffusion-controlled microseismicity (Equation 3.3) for three different diffusivities. The black line shows the distance expected for events showing the growth of hydraulic fractures (Equation 3.4). 59

3.5 An example fracture set randomly generated for opening fractures around stage 1 (shown as a yellow diamond), given in three perspectives: **(a)** map view; **(b)** z-x cross-section view; and **(c)** an z-y cross-section. The patches of tensile opening as shown as black squares. The distributions that govern their location, length, and orientation are described in section 3.3. The Monte-Carlo model takes 1000 of these sets for each stage, and calculates the resulting median elastic ΔCFS for a volume around the well and fault zone. 61

3.6 Elastic stress change maps showing the ΔCFS resolved onto the fault zone orientation received during Stage 22. An example of a single fracture set is shown as black patches within the volume. (a) and (b) show the value of the median stress change at two slices within the 3d volume (though the position of the stage location), whilst (c) and (d) show the median absolute deviation in that average value. 63

3.7 An example of the median stress changes calculated for stage 32. Each shows the stage 32 events, with the median elastic ΔCFS resolved onto the inferred orientation of slip on the fault plane and their hypocentre location. The map of ΔCFS is a slice through the 3D volume taken at the depth of the stage, which is shown as a yellow diamond. **(a)** The "current stage" ΔCFS is the stress change from the opening of fractures during stage 30. **(b)** The "prior stage" ΔCFS is the linear sum of the stress changes from all the previous stages resolved onto the stage 30 events. **(c)** The total ΔCFS is the combined prior and current stage stress changes. 64

3.8 The Coulomb Index – the proportion of events in a population receiving positive median ΔCFS – for each of the events separated by stage for the **(a)** current stage, **(b)** prior stage, and **(c)** combined prior and current stage ΔCFS calculations. It can be seen that for stages from 18 (those that encountered the seismogenic fault zone), CI is largely well above 50%, and frequently in excess of 70%. The heel stage (37-41), whilst not appearing to be significantly effected by stress triggering during each of the stages, show strong signals for the prior stages. Stages 3 and 18, both of which showed anomalous seismicity, show significant correlation between positive stress change and event hypocentre location, with CI in excess of 70%. 65

3.9 Changes in Coulomb stress during stages at the toe of the well. In (a) we show a map of ΔCFS produced by Stages 1 to 3 combined, with the microseismic events from Stage 3 overlain. The cluster of events to the NE, further from the injection point, occurs in a region of positive ΔCFS. In (b) we show a cross-section of ΔCFS produced by Stage 3: the lobe of positive ΔCFS below the well extends with a dip of approximately 45°, matching the observed microseismicity. In (c) we show a map of ΔCFS produced by Stage 12, with the microseismicity produced this stage. The region to the west of this stage is now in a lobe of negative ΔCFS, and microseismicity is suppressed here. . . 66

3.10 Map of ΔCFS changes produced by all stages prior to Stage 18, with the Stage 18 microseismicity overlain. Stage 18 saw minimal injection, yet produced significant amounts of microseismicity. In this figure we see that the effect of the prior stages was to create positive ΔCFS in this region. 67

3.11 Maps of ΔCFS in stages towards the heel of the well. In (a) we show the ΔCFS produced by Stage 22, overlain with the microseismicity from this stage: a lobe of positive ΔCFS extends to the north-east, in which microseismicity is observed. In (b) we show the ΔCFS produced by all stages up to 38 (inclusive), and the microseismicity produced by Stage 38: the area to the west, behind the active stage is now in a region of negative ΔCFS, and microseismicity in this region is suppressed. 68

4.1 Hypocentral locations of events recorded by the downhole array during PNR-1z operations. The lines show the well paths, with the black showing PNR-1z, and the grey showing PNR-2. Diamonds show the locations of the sliding sleeves along the well, through which injection takes place. Events are shown are dots, coloured by stage with size indicating the magnitude. 78

4.2 The magnitude evolution of events that occurred during PNR-1z. Events are shown as dots, coloured by stage with sizes indicating the magnitude of events. The coloured background shows the magnitude thresholds imposed by the UK TLS, converted from local magnitude M_L to moment magnitude M_w using Equation 4.2. Events with no colour occurred at least one day after injection of the last stage. These predominantly took place during the hiatus period, during which many small events continued along the NE fault structure. 79

4.3 Moment M_w to local M_L magnitude relation for PNR-1z events. Events with M_L recorded by the surface array are shown as blue triangles, whilst those recorded by the downhole (DH) are shown as light blue dots. The solid lines give two M_w-M_L relationships for comparison, the black showing the Munafò et al. (2016) relation for small tectonic earthquakes ($M < 4$), and the blue showing the relation derived using the surface waveforms recorded during PNR-1z. These surface calculations were performed by another contractor, Q-con. The blue dashed line shows the least squares fit of a line with a gradient of 2/3, the expected gradient from the theoretical derivations of M_w-M_L for small events (Deichmann, 2006, 2017). It is clear that the downhole calculations are systematically underestimating M_w by around 0.6 magnitude units, when compared calculations from surface measurements. 81

4.4 The magnitude-frequency distribution for PNR-1z events, with two corrections applied. (a) shows the distribution when the magnitudes of the larger events have been corrected using their surface M_L and the M_w-M_L relationship (Equation 4.2). There is clearly a discontinuity between the surface-derived M_w and the M_w given in the downhole catalogue. (b) shows the distribution when a correction of +0.6 has been applied to all events that weren't detected on the surface, and thus don't have a reliable M_L. This now gives a consistent b-value from $-1 < M_w < 2$. 81

4.5 Maximum magnitude stage-by-stage forecasts, calculated in 5 minute increments, for Stages 1 through 14 of PNR-1z operations. Each figure shows the forecasts in the upper panel, as black solid or dotted lines, with events shown as circles coloured by magnitude. Background colours show how each event is classified with respect to the TLS thresholds, converted from M_L to M_w using Equation 4.2. The tile shows the total volume V_T used in the calculation of M_max, which corresponds to the fluid injected during that stage. The bottom panel of each figure shows the running GR b-value, S_{eff}, and SI. 86

4.6 Maximum magnitude stage-by-stage forecasts, calculated in 5 minute increments, for Stages 18 through 32 of PNR-1z operations. They are formatted as in Figure 4.5. . . . 87

4.7 Maximum magnitude stage-by-stage forecasts, calculated in 5 minute increments, for Stages 37 through 41 of PNR-1z operations. They are formatted as in Figure 4.5. . . . 88

4.8 Maximum magnitude combined forecasts, calculated in 2 hour increments. These forecasts use data for Stages 37 through 41 of PNR-1z operations, those which occurred prior to the largest event during operations. They are formatted as in Figure 4.5. . . . 90

4.9 Maximum magnitude combined forecasts, calculated in 2 hour increments, for all injection stages of PNR-1z operations. They are formatted as in Figure 4.5. 90

5.1 Map (a) and depth (b) view of the well paths and sliding sleeve locations worked during hydraulic fracturing at Preston New Road in 2018 (PNR-1z) and 2019 (PNR-2). Sleeves (shown as diamonds) are numbered from the toe (the furthest extent of the well) to the heel of the well. Microseismic monitoring stations are shown as triangles. During PNR-2 operations in 2019, only the first 7 sleeves were worked. 99

5.2 Evolution of seismicity for operations at PNR-2. The start of pumping each stage is highlighted by dotted lines and is accompanied by an increased rate of seismicity. After Stage 6 (S06) the magnitude of events markedly increases, indicating the interaction between injection and the fault zone. Events are denoted to be "Post-Stage 7" two days after the stage was injected. The M_L 2.9 occurred more than 48 hours after the injection of Stage 7. The small number of events which took place before Stage 1 were the result of injection tests through Sleeve 1. 100

5.3 Magnitude-frequency distributions for events recorded during PNR-2. Magnitudes shown here are computed in two different ways. Solid lines show the moment (black) and local (red) magnitude calculated by the service company using the downhole array. The red dashed line shows the local magnitude of events as reported by the BGS using the surface array, and black dashed line shows the corresponding moment magnitude derived from the M_w-M_L relationship for PNR (Equation 5.1). A step can be seen between the downhole and surface derived moment magnitudes at around $M = 0.3$, indicative of a processing or instrumental artefact. 101

5.4 Map view of all events recorded up to September 13th 2019 with M_w greater than -1.5. Event hypocentres are shown as circles, coloured by the stage with which they were associated, and sized by magnitude. The well paths of PNR-1z and PNR-2 are shown as black lines, with PNR-1z to the south of and below PNR-2. 103

5.5 Temporal evolution of microseismicity at PNR-2. In (a) we show a map of Stages 1-5, in (b) we show Stage 6, in (c) we show Stage 7 (up to midnight on August 26), and in (d) we show the seismicity that occurred from midnight on August 26th until the end of the monitoring period. 104

5.6 The hypocentres of aftershocks occurring within 1 hour of the M_L 2.9 event, used to delineate the activate SE fault. (a) shows a map view, whilst (b) and (c) show two oblique perspectives of the fault in three dimensions. The lower hemisphere focal mechanism shown in (a) is that of the M_L 2.9 earthquake. The plane shown in (a) and (c) is found by a least square fit to the events in the aftershock cluster. The "halo" annotated in (b) highlights the ring of the events around a region of quiescence, with the inferred location of the M_L 2.9 event at its centre. 107

5.7 Magnitude distributions of event populations for each injection stage, with GR b-values for the populations fitted. It is clear that from Stage 6, the population becomes distinctly bimodal, with a far lower b at the tail-end of the distribution, with values indicative of tectonic earthquakes. 109

5.8 M_{MAX} forecasts on a stage-by-stage basis. Circles show the events, coloured by their magnitude with respect to the TLS thresholds in M_w. The solid black line shows the M_{MAX} produced by the Hallo et al. (2014) S_{eff} method, whilst the dotted line shows the M_{MAX} from the Shapiro et al. (2010) SI method. The lower figure for each stage shows the evolution of the b-value (solid blue line), S_{eff} (solid purple), and SI (dotted purple) during operations. 112

5.9 Maximum magnitude forecast when (a) data from Stages 5 through 7 are combined, and (b) all PNR-2 event and injection data are combined. Figures are formatted in the same manner as Figure 5.8. 113

5.10 Lower-hemisphere stereographic poles-to-plane projections of critical pore pressure P_C for the two fault depths at PNR. (a) shows the P_C for the NE-striking fault of PNR-1z (at a depth of 2300 m), with the green triangle showing the orientation of the plane. (b) shows P_C for the SE fault activated during PNR-2 (at around 2100 m depth), with an inverted green triangle showing its orientation. The titles in each plot show the P_C value at the orientations of the faults. (c) shows the cumulative probability curves for failure for a given P_C. 115

6.1 A flowchart of the processing steps necessary to conduct the maximum magnitude forecasting used in Chapters 4 and 5. This represents the steps that had to be taken during the application of forecasting, some of which (e.g. "Correct M_w magnitudes") could be excluded if monitoring and processing methods are improved. Some processes, like "Correct M_w magnitudes", are only possible after some data has already been collected, and inaccuracies in downhole (DH) measurements have been identified. Update frequencies in purple refer to how frequently calculations or measures were made, and how frequently their products can be fed back into the modelling. While much can be done during operations, many corrections required a significant amount of analysis post-pumping to compute. 124

CHAPTER 1

INTRODUCTION

1.1 A brief history

Earthquakes induced by industrial activities have been recognised since the early 20th century. Increased rates of seismicity accompanied cases related to reservoir impoundment (e.g., Carder, 1945; Gupta, 1985) and extraction from oil and gas reservoirs (e.g., Pratt and Johnson, 1926; Segall, 1989) in the 1920s and 1930s. It became clear in the decades that followed that human activities which induce fluid pressure changes in the subsurface can be a significant driver of the triggering of earthquakes (e.g., Hsieh and Bredehoeft, 1981; Hubbert and Rubey, 1959; Segall, 1989). Two cases of injection-induced seismicity (IIS) in Colorado in the 1960s particularly cemented this understanding: fluid disposal at the Rocky Mountain Arsenal (Bardwell, 1966; Evans, 1966); and experimental injection at the Rangely oil field (Raleigh et al., 1976).

Injection at the Rock Mountain Arsenal stimulated hundreds of events which continued for years after injection ceased, including the formerly largest injection-induced earthquake (M ~ 4.8), which occurred 18 months after injection ceased (Healy et al., 1968; Herrmann et al., 1981). At Rangely, injection intentionally targeted a fault to stimulate earthquakes, and tests were conducted into the effect of varying reservoir pressure on the rate of seismicity (Raleigh et al., 1976). Both cases showed that earthquake rates were correlated directly with injection rates, with a time delay. This delay is controlled by the transmission of fluid pressure and is thus dependant on the hydraulic conductivity of the rocks (see Hsieh and Bredehoeft, 1981; Raleigh et al., 1976).

From the 1970s to the mid 2000s, more cases of IIS were identified, mostly in North America (e.g., Ake et al., 2005; Hamilton and Meehan, 1971; Seeber and Armbruster, 1993). In the past

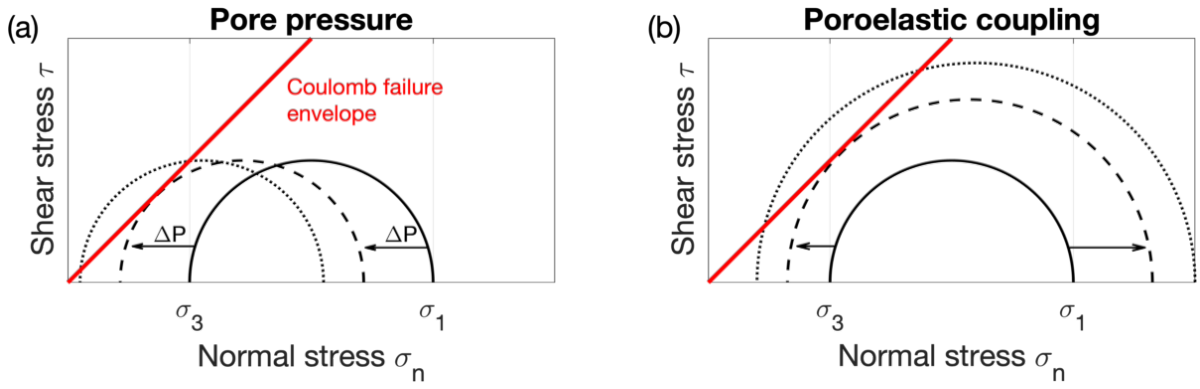

Figure 1.1: The effect on the stress acting on a fault of pore pressure and poroelastic stress changes, demonstrated using Mohr circle diagrams. A point on the Mohr circle represents the shear τ and normal σ_n stress resolved onto a plane (i.e., a fault). Moving around the circle is equivalent to changing the orientation of the plane in the stress field (with principle stresses σ_1 and σ_2), rotating the plane such that τ and σ_n both change. Points on the solid lines show the initial stress state for a fault, and points on the dashed line show the effect to the stress state of a fluid pressure increase. The point where the circle meets the failure envelope corresponds to the orientation which is optimally aligned for failure. Points on a dotted lines, where the pressure change goes beyond the failure envelope, corresponds to the larger range of orientations which are now capable of failure, besides those that are perfectly optimally aligned. (a) shows the effect of increased pore pressure, reducing the effective normal stress and bringing the fault closer to the failure envelope. (b) shows the effect of poroelastic coupling between pore pressure changes and the stress in the rock frame, increasing differential stress. These effects are combined in the case of fluid injection, though the spatial and temporal scale over which each dominates is dependant on the geomechanical and diffusive properties of the rock.

15 years, however, the number of identified cases around the world has massively increased (Davies et al., 2013; Ellsworth, 2013). In the US, fields in California (e.g., Goebel et al., 2016), Texas (e.g., Frohlich et al., 2011), Arkansas (e.g., Horton, 2012), Ohio (e.g., Kim, 2013), Oklahoma (e.g., Keranen et al., 2014), and Kansas (e.g., Weingarten et al., 2015) have all experienced large numbers of earthquakes associated with industrial activities, mostly related to waste-water disposal (see McGarr and Barbour, 2017; Walsh and Zoback, 2015). These include several $M_w > 5$ events which caused damage to nearby homes and infrastructure (Manga et al., 2016), namely the August 2011 M_w 5.3 earthquake in the Raton Basin, Colorado (Barnhart et al., 2014), two M_w 5.0 events and a M_w 5.7 event near Prague, Oklahoma in November 2011 (Keranen et al., 2013), and the September 2016 M_w 5.8 event near Pawnee, Oklahoma (Barbour et al., 2017). Minor damage to vulnerable buildings from induced seismicity has also been reported in Europe. Reservoir compaction at the Groningen natural gas field in the Netherlands has lead to subsidence and up to M 3.6 induced events occurring (e.g., van Thienen-Visser and Breunese, 2015), and geothermal enhancement in Basel, Switzerland, induced several $M_L > 2$ events.

Understanding of the mechanisms behind fluid-induced seismicity developed naturally from

models of slip on tectonic faults (Hubbert and Rubey, 1959). These mechanisms are summarised graphically in Figure 1.1. Figure 1.1a shows the Mohr circle diagram for a fault undergoing an increase in pore pressure P. P acts against the normal stress σ_n acting on the fault plane. This reduces the effective normal stress, encouraging failure by shifting the Mohr circle closer to the failure envelope (Raleigh et al., 1976). This can be understood mathematically using the equation for the Mohr-Coulomb failure criterion (the red line in Figure 1.1):

$$|\tau| = C + \mu\sigma_n \quad , \tag{1.1}$$

with shear stress stress τ, coefficient of friction μ and cohesion C, which needs to be overcome in order for slip to occur. In the example failure criterion in Figure 1.1, $C = 0$, representing faults or fractures with very little inherent strength. This is simulating a scenario where slip on features is more likely, where fault or fracture cementation is assumed to be negligible.

Figure 1.1b shows the effect of poroelastic coupling between pore pressure and the stress field. (Altmann et al., 2010; Segall, 1989; Segall and Lu, 2015). As the pressure of fluid in the pore space increases, the rock frame itself is deformed elastically, analogous to an inflation of the rock mass. The stress change that results from this deformation propagates out from the pressurised zone, with a length and time scale strongly dependant on the mechanical and hydraulic properties of the rock. Figure 1.1b shows that this effect acts to expand the Mohr circle, increasing differential stress, which can clearly lead to optimally oriented faults meeting the failure criterion. As is also shown in Figure 1.1, the stress changes due to fluids can also lead to failure of non-optimally oriented faults, when the perturbation is large enough. This is inferred by the Mohr circle continuing to move beyond the failure criterion, meaning a larger number of potential faults or fractures are now able to failure under the current stress conditions.

Mechanisms first identified in the triggering of tectonic earthquakes have recently been applied to induced sequences. Elastic stress transfer is routinely used to explain and forecast the spatial distribution of earthquakes (Harris, 1998; Steacy et al., 2004; Stein, 1999). Slip of faults alters the surrounding stress field, which propagates elastically through the rock. This can then increase the shear stress, or decrease the normal stress, acting on nearby faults, encouraging failure. This is encompassed in the equation for the change in the Coulomb failure stress ΔCFS:

$$\Delta CFS = \Delta\tau + \mu'\Delta\sigma_n \quad , \tag{1.2}$$

where μ' is now the effective coefficient of friction. This is a form of μ modified to take into account of the resistive effect that materials with inherent pore pressure posses to compressive stress changes. Here $\mu' = \mu(1-\beta)$, where β is the Skempton's ratio (Skempton, 1954). This was first derived for porous materials, such as soils, but can be applied to large scales, where the faults and fractures in a large volume of rock are analogous to the "pores". This Skempton's ratio mathematically accounts for how pore pressure changes act against the compressive stress. Though the exact spatial scale where this assumption breaks down is not strictly quantified, this

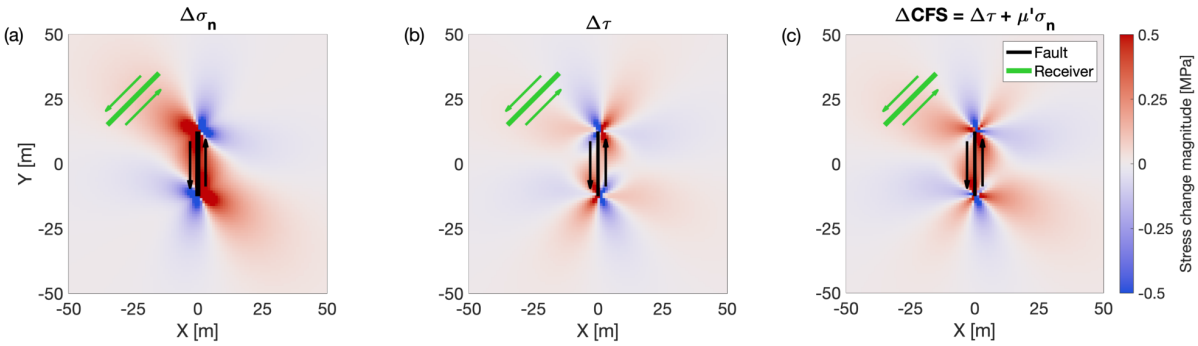

Figure 1.2: A schematic of elastic stress transfer as a mechanism for triggering seismicity. Elastic deformation around a slipping source fault (shown above as the black line) induces changes to the stress field. These can be resolved onto a plane with a given orientation at any point around the source. Shear stress change $\Delta\tau$ is shown in (a), normal stress change $\Delta\sigma_n$, is shown in (b), and the Coulomb failure stress change ΔCFS is shown in (c). The colour maps above show the value of the stress changes at a slice through the volume at the depth of the fault. In this example, the stress change is resolved onto a receiver orientation of a left lateral strike-slip fault striking at 45°, which is demonstrated by the green line. The above shows the stress changes resulting from a 25 m, left lateral strike-slip fault striking north and slipping uniformly by 1 mm. Here, $\Delta\sigma_n$ is positive extensive, the shear modulus is 25 GPa, and the effective coefficient of friction μ' is 0.42. In (c), areas in which ΔCFS is positive (red) are those where failure on the receiver fault is encouraged. Conversely, failure on the receiver is inhibited by the source slip in areas which receive negative ΔCFS (blue).

μ' model is widely applied at a range of scales, from tectonic to induced sequences (e.g. Cocco et al., 2010; Schoenball et al., 2012). These assumptions and their affect on ΔCFS calculations are discussed further in Chapter 2.

Elastic stress changes resulting from strike-slip dislocation are demonstrated graphically in Figure 1.2. This mechanism is the basis of many physics-based earthquake forecasting models (Cattania et al., 2018; Cocco et al., 2010; Parsons et al., 2012; Toda et al., 2005, e.g.,). Elastostatic models have been applied to numerous induced sequences, examining how interevent stress transfer interacts with fluid-triggered seismicity (e.g., Catalli et al., 2013; Schoenball et al., 2012; Sumy et al., 2014). Dynamic triggering, where failure is triggered by transient stress changes that occur during the passage of seismic waves from distant earthquakes, has also been shown to be an indicator of regions particularity susceptible to induced seismicity (van der Elst et al., 2013).

1.1.1 Hydraulic fracturing and induced earthquakes

Hydraulic fracturing-induced seismicity (HF-IS) specifically has been associated with some of the largest induced events in the world. HF in the Changning shale gas reservoir in the Sichuan Basin, China, has been associated with two $M_L > 5$ events: a M_L 5.7 and a M_L 5.3 in December 2018 and January 2019 respectively (Lei et al., 2019). Recent evaluation of the seismicity in

the central USA has also shown that it is frequently associated with HF (Hennings et al., 2019; Holland, 2013; Skoumal et al., 2015, 2018, 2020). The Western Canadian Sedimentary Basin (WCSB; e.g., Atkinson et al., 2016; Bao and Eaton, 2016; Farahbod et al., 2015) has also hosted several $M > 4$ events associated with nearby HF operations.

During hydraulic fracturing, where high pressure fluids are injected into low permeability formations in order to fracture the rocks and increase permeability, all of the above mechanisms described can come into play. Whilst the duration of pumping in HF is a lot shorter for a single operation relative to say waste water disposal, in active shale gas reservoirs large numbers of HF pads are relatively closely spaced, and thus the volumes of fluid injected into the subsurface, and the potential perturbation to the stress field, can be significant. As HF is acting to deform the rock through the creation and opening of fractures, it also can induce significant elastic stress changes in the rock that immediately surrounds injection. This can naturally compound with the interevent triggering effects that occur in areas where many induced events are occurring in close proximity.

Generally in the cases of IIS described here, reactivation on the field scale is attributed to increased pore pressure near wells diffusing through natural fracture networks into the crystalline basement, affecting a broad area that contains pre-existing faults at depth (e.g., Schoenball and Ellsworth, 2017). In some other cases, induced seismicity occurs on a single fault that was well oriented for failure and located close to injection, and there was a more direct hydraulic connection between the two. This was the case for Rangely (Raleigh et al., 1976), the hydraulic-fracturing induced events in the UK (Clarke et al., 2014), and cases of HF-IS in the WCSB, Canada (e.g., Eyre et al., 2019; Igonin et al., 2018). When distant faults reactivate many tens of kilometres from any particular operation, a large scale permeable pathway appears to be required to transmit this increased fluid pressure to critically stressed faults in the basement (Keranen et al., 2014, e.g.,). The transmission of this pressure perturbation along pre-existing fracture networks or faults is however aseismic, or is perhaps stimulating events that were too small to be detectable on regional networks (King et al., 2014; Yeck et al., 2016).

1.2 Geological and Operational Background

As is clear, the exact mechanisms which come into play are affected by the local geology and pre-existing structures. In this work, data from two settings are studied (locations shown globally in Figure 1.3): the Horn River Basin, NE British Columbia, Canada in Chapter 2; and the Bowland Basin, Lancashire, NW England, UK in Chapters 3, 4, and 5. Here, the geological background for these areas is discussed.

Also given here are some introductory details of the hydraulic fracturing operations which produced the microseismic data, with an aim to help frame the scale of the operations, and clarify details of their completion.

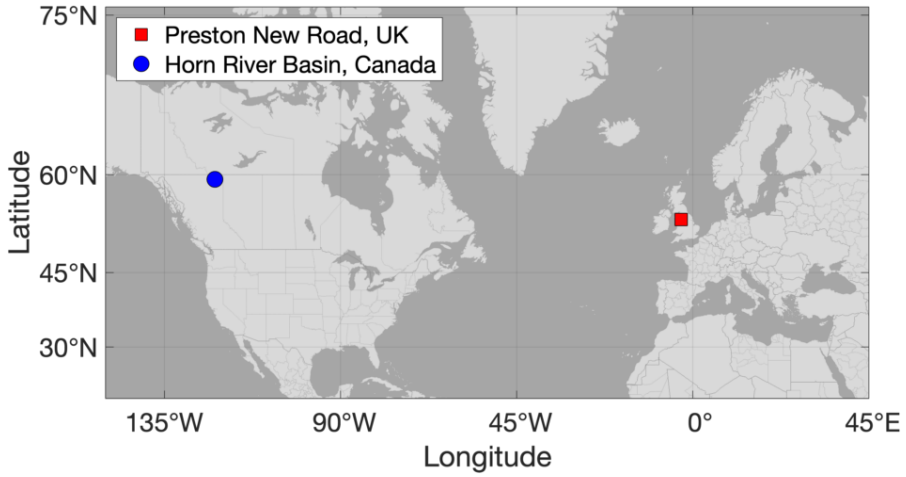

Figure 1.3: Map showing the locations of the two sites of hydraulic fracturing-induced seismicity studied in this thesis. The red square and blue circle show their locations within Europe and North America respectively.

1.2.1 Horn River Basin, British Columbia, Canada

1.2.1.1 Geology

The Horn River Formation is a Devonian shale gas play at the NW edge of the WCSB, in the NE of British Columbia (BC), Canada. It is made up of three over pressured, organic-rich shale formations: the Muskwa, Otter Park, and Evie (Barker, 2014). It is overlain by the Fort Simpson shale, a calcareous shale with little organic content, and underlain by the Keg River carbonate. It extends up to the Bovie Lake thrust fault zone to the west, and it is bounded to the east and south by a reef platform, the Slave Point/Keg River Carbonate Barrier Complex. The basin-fill strata thin to the north, up to the northwest extent of the WCSB (Price, 1994). The Horn River shales are characterised by fine grained sediments and structural homogeneity that are indicative of a deep-water depositional setting (Yoon et al., 2018).

The extensional environment prior to the Jurassic produced the Horn River Basin as well as the adjacent Liard Basin, the two separated by the Bovie Lake fault zone (MacLean and Morrow, 2004; Price, 1994). The HRB area remained in a deep water environment through to the Jurassic, allowing the deposition of the thick, overlying Fort Simpson shale. During in the Jurassic the Cordilleran fold-and-thrust belt was formed along the western edge of North America, bringing BC into a compressional tectonic setting. This developed into a Late Cretaceous to Paleocene right-lateral transpression phase, where strike-slip deformation produced zones of compression, shortening and thickening strata in southern BC and folding structures in the north of the province. The transpressional regime became transtensional in the early Eocene, resulting in uplift in the region (Price, 1994; Wilson and Bustin, 2019; Wright et al., 1994). The Rocky Mountain thrust belt, which runs through the centre of BC, is now characterised by NW-SE to

N-S trending thrust faults. This complex is over 150 km to the west of the HRB, however, the trend of faults and fractures in the basin is largely the same (approximately trending N-S) (Price, 1994; Wilson and Bustin, 2019).

Many at-depth stress measurements have been taken across the region due to the large number of hydrocarbon extraction wells that have been drilled in the last 10 years (Bell, 2015). This allows for a relatively robust characterisation of the present in-situ stress state. The strike-slip stress regime in still present in the basin, with a maximum horizontal stress σ_1 orientation of $\sim 55°$. This means the pre-existing NW-SE faults are near perpendicular to σ_1 and are thus not optimally aligned for failure in the stress state, however the more N-S faults are more well oriented. There is evidence of well oriented faults (NNE-SSW trending) extending from the underlying carbonates into the reservoir, acting as conduits for fluid and pressure transfer (Latimer et al., 2017). This has resulted in varying pore pressure across the reservoir, with parts above hydrostatic pore pressure. This is however not well characterised for the whole region (Bell, 2015).

1.2.1.2 Operations

The microseismic data used in this thesis from the HRB were acquired during a large hydraulic fracturing operation which targeted all three of the gas-bearing shale units. Ten horizontal extraction wells were drilled perpendicular to the maximum horizontal stress direction, to maximise the stimulated reservoir volume from injection. Each well was hydraulically stimulated in 24 "plug-and-perf" stages, equally spaced along each well's horizontal section. For this method of stage completion, a section of the well is isolated from the previous stage (the "plug") and an small explosive charge is detonated (the perforation shot, or "perf") creating holes in the well casing through which fluid can then be injected. This perf shot can also act to generate small fractures from which hydraulic fractures can nucleate. This style of injection means the stages are injected from the toe of the well (its deepest/further extent) to the heel (where the horizontal starts to deviate to vertical). In the operation that produced the HRB data used here, the wells were stimulated in using a "zipper-frac" technique, where stages in adjacent wells are intermittently injected, much like a zip being fastened. Each stage had a volume of approximately 2000 m^3 of slickwater, a fracturing fluid which is composed of mostly water with added chemicals designed to reduce the viscosity and prevent the build up of algae. Stages were around 4 hours long, with injection rates of around 8 m^3 min^{-1}.

In total, this dataset has around 92,000 detected and processed events, that took place during 119 of the fracturing stages. These stages were monitored by three downhole geophone arrays of between 24 and 36 3-component 15 Hz geophones, placed in the build sections (the part of the that well where it deviates from vertical to horizontal) of three adjacent wells, being around 2 km from the furthest events. Whilst no events exceeded magnitude M_w 1.5, there is still evidence for the activation of small faults, with the microseismic events mapping out planar features

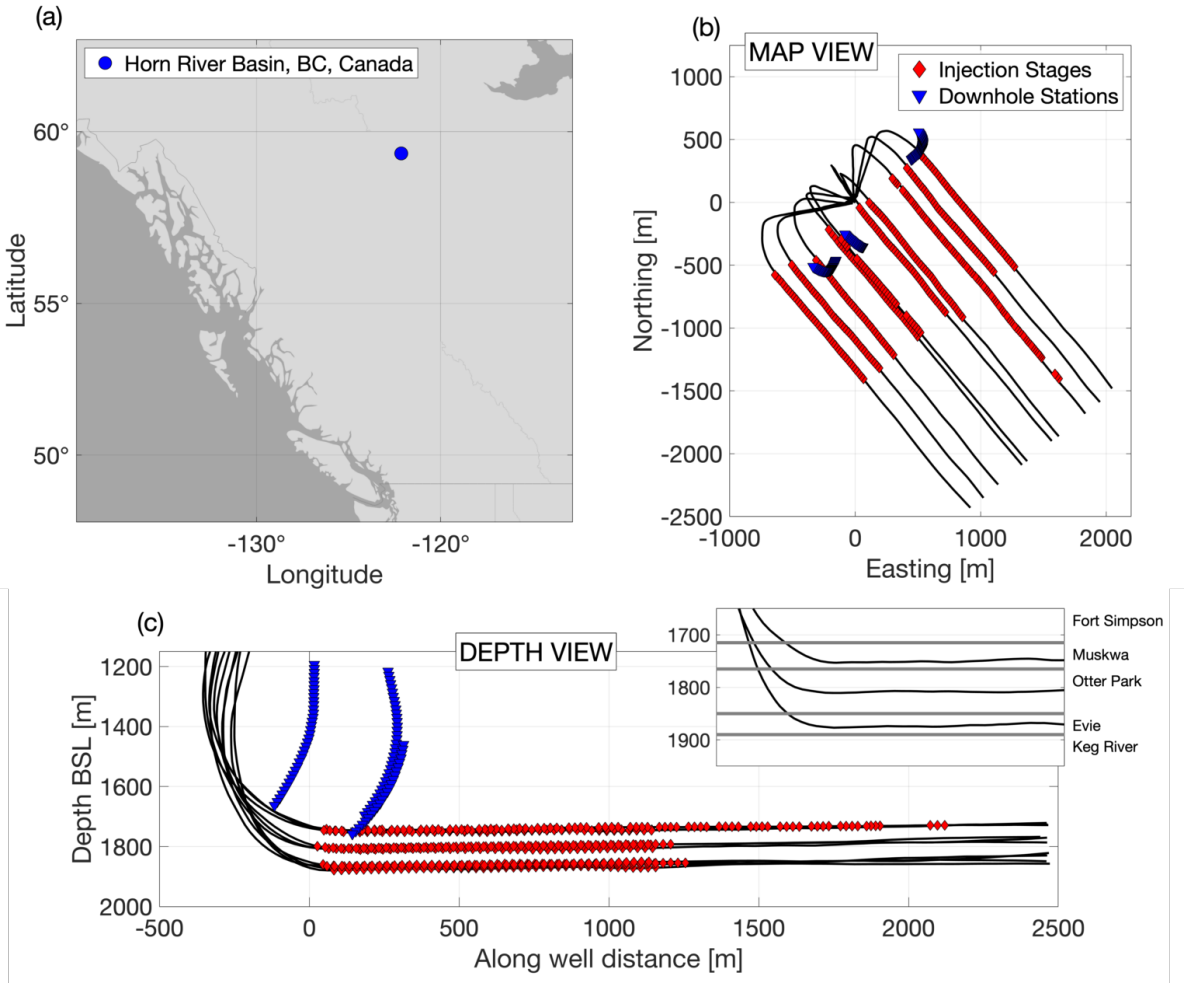

Figure 1.4: (a) The location of Horn River Basin hydraulic fracturing site in British Columbia, Canada. (b) A map view of the site, with the locations of the well paths shown as black lines, the injection stages as red diamonds, and the stations as blue triangles. (c) The same plot as (b), but in depth view. Inset here is a zoomed-in view of the targeted reservoir units, with formation tops delineated by grey lines.

extending into the underlying Keg River carbonate.

1.2.2 Bowland Basin, Lancashire, UK

1.2.2.1 Geology

The Bowland Basin is a Mississippian source of shale gas in NW England, UK, which makes up a part of the larger Carboniferous play which spans the north of England (Andrews, 2013). It is broadly composed of two main reservoir units, the Upper and Lower Bowland, which are similar in composition but stratigraphically distinct (Clarke et al., 2018). Both are shales interbedded with limestones, calcareous mudstones, siltstones, sandstones, and a thin, carbonate marine band separates the two units (Kirby et al., 2000). The bedding dips eastward, by around $5° - 10°$. The Fylde peninsula, around 40 km north of Liverpool and the location of the town of Blackpool, has been identified as a viable locale for shale gas production from the Bowland shale (Andrews, 2013). The location of the Preston New Road (PNR) site, where the microseismic data used in this work was collected, in the SE Fylde is shown in Figure 1.5.

The Bowland is one of many basinal structures formed by N-S extension in the early Carboniferous, with the tectonically active environment leading to thickening and accumulation of shales and carbonates (Guion et al., 2000). The Bowland basin is bounded to the north by the Craven Fault System, and the Pendle Lineament faults to the south. During the Variscan Orogeny, the basin was structurally inverted and folded. This gave rise to the present day basin strata being bounded between NE-SW trending en echelon folds and faults (Corfield et al., 1996). The current stress field is strike-slip, consistent with much of the central UK (Fellgett et al., 2017). The maximum horizontal stress direction in the Fylde (170°) does deviate slightly from that of the majority of northern England (140°; Andrews, 2013; Clarke et al., 2014, 2019a,b).

The operator of the PNR site conducted many 3D reflection seismic surveys in the years prior to operations, identifying the depth of the reservoir units and illuminating nearby pre-existing faults and structures (Clarke et al., 2018). They found 16 structural features in the reflection seismic data, some of which are faults, and some of which are smaller “seismic discontinuities” – either small, low-throw faults, or zone of fractures that produce a small signature on the reflection seismic data (Cuadrilla Resources Ltd, 2019). The large, reverse faults, such as the Anna’s Road, Moor Hey, or Haves Ho, trend NE-SW, parallel to the larger structural trends in the Fylde, and have dips around 70°. Given their orientation with respect to the maximum horizontal stress direction, they are somewhat well oriented for failure. Whilst some of these faults are in excess of 10 kilometres long, their nearest points are each over 1 km away from the well, and are thus unlikely to be directly hydraulically connected to injection. The six smaller seismic discontinuities are nearer the well, with one intersecting the well path at the toe. However, they are mostly trending N-S and dipping at around 45°, and are thus less well oriented for slip. It should be noted here that there was no clear correlation in location between the induced seismicity and the identified faults or seismic discontinuities during operations at PNR.

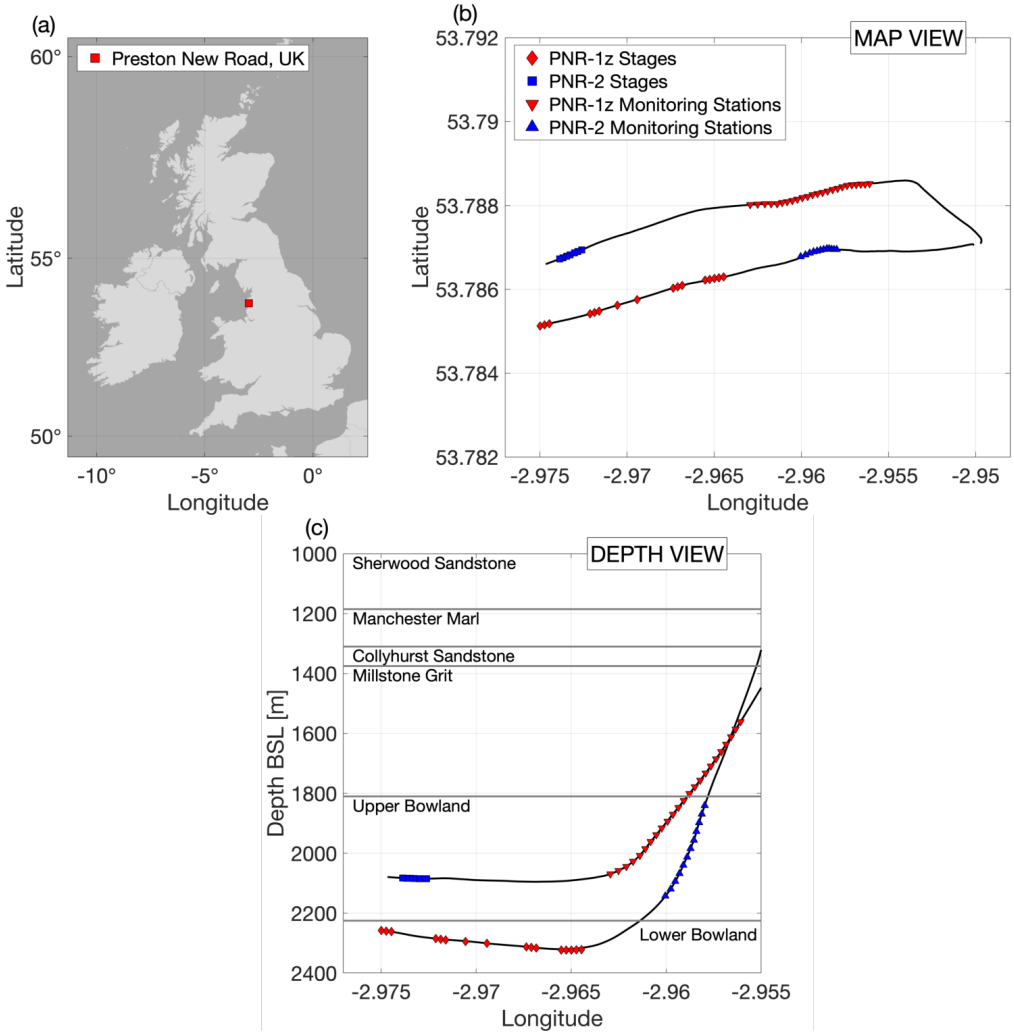

Figure 1.5: (a) The location of the site of the Preston New Road (PNR) hydraulic fracturing wells in the northwest of England, UK. (b) Map view of the wells and stages at PNR. Two horizontal wells were drilled, with PNR-1z targeting the deeper Lower Bowland, and PNR-2 targeting the Upper Bowland shale. Injection stages that were actually pumped are shown as red diamonds and blue squares, for operations during PNR-1z and PNR-2 respectively. The locations of the stations used to monitor the two operations are shown as red and blue triangles. (c) A depth view of the site, with the same symbols as in (b). Stratigraphic units are those at the horizontal of the wells, and are delineated by grey lines.

1.2.2.2 Operations

Hydraulic fracturing operations at PNR took place in two phases: PNR-1z in 2018, targeting the Lower Bowland; and then PNR-2 in 2019, targeting the Upper Bowland. The horizontal of each well is around 800 m long, with 41 “sliding-sleeve” stages equally spaced along their lengths. This method of completion forgoes the use of explosive perforation shots, using a more complex lining to the well casing at each of the stage locations that can be opened and closed. As one

sleeve can be opened at a time to isolate pressure, it can allow for stages to be completed in any order, without the restriction of the obligatory toe-to-heel frac order of plug-and-perf completions. This can be also be used to minimise seismic risk, by allowing for stages to be easily "skipped" up or down the well, in an effort to avoid areas of enhanced seismicity. The planned volume of each stage was 400 m^3 of fluid (slickwater during PNR-1z and a higher viscosity frac fluid during PNR-2) and 50 t of proppant (sand used to hold the hydraulic fractures open once downhole fluid pressures are reduced). This per stage volume of fluid is considerably less than that used in the Horn River Basin case (~ 2000 m^3), and the injection rates at PNR (~ 4 m^3) were far lower: around half that used in the HRB case.

This property of skipping stages was utilised multiple times during the injection of PNR-1z. Only 16 of the possible 41 stages were injected with volumes larger than minifracs (small test volumes, ~ 10 m^3, used to examine the breakdown pressure of the rock in that part of the well). This was in an effort to avoid areas of high seismic activity which were encountered during injection, including a previously unknown NE-SW trending strike-slip fault which was identified from the microseismic data. Over 38,000 events were detected in total during PNR-1z operations, recorded by 24 3-component 15 Hz geophones located in the adjacent PNR-2 well. Operations were also monitored by a dedicated network of 11 surface stations: a mix of 8 broadband and 3-C geophone stations installed by the operator, and 3 broadband stations operated by the British Geological Survey. A single event produced felt seismicity – a M_L 1.6 – and only 15 events had $M_L > 0$.

During PNR-2 operations, only the first 7 stages at the toe of the well were hydraulically fractured with ~ 400 m^3 of fluid before a NW-SE trending fault was activated around 250 m south of the well. This was monitored by the same surface network of seismometers, but with fewer downhole stations than for PNR-1z operations – 12 as opposed to 24. Over 55,000 events were recorded in total, and though again only 15 events had $M_L > 0$, four events had $M_L > 1$, up to M_L 2.9, three of which were felt by the local population.

1.3 Event magnitudes

Both the monitoring and mitigation of induced seismicity require robust and accurate measurement of the size of events (see Kendall et al., 2019). This is valuable not only for understanding seismic risk, but also operationally, as it provides a way to assess the stimulated volume in the rock or efficacy of the hydraulic fracturing. Determining the magnitude M of a population of events can also allow for more accurate estimates of seismic risk. A higher proportion of small events ($M < 0$) can indicate that small fractures are being created or opened around the injection point, while a higher proportion of larger events ($M > 0$) can indicate the activation of a fault. The Gutenberg-Richter law for the magnitude-frequency distribution of earthquakes (Gutenberg and Richter, 1944) can be used in this manner to determine the likely maximum event size, given

the population already observed:

$$\log(N) = a - bM \quad . \tag{1.3}$$

Here, a and b are constants describing a line, relating $log(N)$ and M. When the magnitude-frequency distribution has a high slope ($b > 1.5$), there are relatively few large events. Seismicity with high b has been used as an indicator of hydraulic fracturing, whilst seismicity with lower b ($b \sim 1$) is generally indicative of natural earthquake sequences, and has been used to identify fault activation during injection (e.g. Eaton and Maghsoudi, 2015; Verdon et al., 2013a).

These inferences, however, can only be made robustly when event magnitudes have been calculated accurately. There are many ways in which to estimate event magnitude (see Stork et al., 2014). The first to be developed, local magnitudes M_L, are empirical in nature, using the maximum amplitude A recorded by seismometer and a series of constants to calibrate the magnitude scale for each region of interest. Some of these constants are function of the distance from the earthquake to the receiver. These local scales do reflect the relative amounts of ground shaking for different earthquakes within a region, but do not directly relate to the earthquakes physical properties (e.g., slip amount, rupture size, stress drop). For that, Hanks and Kanamori (1979) developed the moment magnitude M_w, which is derived from the seismic moment M_0:

$$M_w = \frac{2}{3}\log(M_0) - 6.0 \quad , \tag{1.4}$$

where M_0 is given in Nm. Seismic moment is defined by a simple relation between the shear modulus of the rock G, and the average amount of slip $\bar{D}$ across a surface with area S:

$$M_0 = G\bar{D}S \quad . \tag{1.5}$$

More complex analysis is required than the simple measurement of the amplitude A to calculate seismic moment from a waveform of an earthquake. The waveforms are first integrated to displacement, and then windowed around the P- or S-wave arrival. They are then converted into the frequency domain using a Fourier transform. It should be noted that the exact type and application of the transform can significantly affect the resulting magnitude Stork et al. (2014). M_0 can then be estimated from the value of the amplitude spectrum at low frequencies Ω_0 (Aki and Richard, 2002), sometimes called the low-frequency plateau, using the equation:

$$M_0 = \frac{4\pi\rho v^3 r\Omega_0}{\mathbf{R}} \quad , \tag{1.6}$$

where ρ is the rock density at the hypocentre of the earthquake, v is the P- or S-wave velocity, r is the distance from the source to the receiver, and $\mathbf{R}$ is the radiation pattern correction. This last term is required to account for the non-uniform spatial propagation of energy from the earthquake. To calculate $\mathbf{R}$ directly for a given station, the focal mechanism for the event is required, however this is routinely not possible in regions with poor coverage, and is especially difficult for low signal-to-noise microseismic events. When no focal mechanism is available, the

average radiation pattern correction $\bar{R}$ can be used: 0.44 and 0.60 for P- and S-waves respectively (Boore and Boatwright, 1984). As M_L is naturally easier to calculate than M_w, numerous relations have been developed to relate the two magnitude scales (e.g. Deichmann, 2017; Jost et al., 1998; Munafò et al., 2016; Pearson, 1982), but each are generally region specific and only valid over a limited magnitude range.

Numerous problems and inaccuracies occur naturally from the processing methodology to calculate M_0, some of which are especially pertinent for calculating magnitudes for microseismic events. The density, and more importantly, the velocity at the source are generally taken from 1-D velocity models determined for a reservoir, which do not reflect lateral heterogeneity or velocity changes that occur during injection. The source-receiver distance also has inherent uncertainty, though with recent advances is microseismic location techniques, location uncertainties are generally small, on the order of tens of metres (e.g. Drew et al., 2013; Jones et al., 2010; Verdon et al., 2017; Viegas et al., 2012).

Methods to convert waveforms into the frequency domain have to be carefully applied in order for an accurate spectra, and thus an accurate Ω_0, to be produced (see Stork et al., 2014). The sensitivity of the instruments used in downhole monitoring arrays can also limit the accuracy of Ω_0. These instruments are generally 3-component geophones, which have little to no sensitivity to frequencies below their design limits, which is generally around ~ 10 Hz. This can severely affect the ability to estimate the amplitude of the low frequency plateau Ω_0 for larger events ($M > 1$), where a larger proportion of the energy released is in the low frequencies (less than 10 Hz). These spectral errors are exacerbated further by picking inaccuracies, where P- or S-wave arrival time is inaccurate, or the window around the arrival is either too short or long.

The radiation pattern correction is also another source of uncertainty. The use of the average, which is generally necessary with microseismic events, implicitly assumes that the receivers are broadly spaced across a range of azimuths. However, the downhole geophone arrays commonly used to detect and locate the vast majority of microseismic events during injection are housed in a single monitoring well, and thus cover a relative narrow range of azimuths and inclinations, meaning the use of $\bar{R}$ can lead to systematic inaccuracies in M_w estimates.

These effects can generally lead to M_w errors of ~ 0.5 (Stork et al., 2014). Local magnitude estimates can be more precise (~ 0.1) due to their simplicity, however their precision is also limited due to path and site effects (Butcher et al., 2017; Luckett et al., 2019).

For the very large microseismic datasets produced by servicing companies, such as those used in this thesis, processing methods are used which attempt to account for these uncertainties (see Drew et al., 2013; Stork et al., 2014). With many thousands of events detected and processed per stage, the effect of sampling within the random error is also better resolved. Most of the microseismic catalogues used here also have combined surface and downhole microseismic monitoring, which allows for direct comparisons to be made between their respective M_L and M_w estimates. As is described in Chapters 4 and 5, this can allow for further verification of magnitude

estimates, and can overcome some systematic uncertainties with estimates of M_w from downhole instruments.

1.4 Traffic Light Systems

Monitoring of operations is a key component in examining the response of a fault or fracture system to injection. A very broad range of event magnitude needs to be measured accurately such that these developing pressure perturbations can be resolved. Varying levels of regulation exist internationally, with some territories requiring very sensitive microseismic monitoring, requiring a detectability of $M < 0$ or lower (Kendall et al., 2019). The UK is a prime example of a region with strict enforced monitoring practises. Downhole and surface microseismic monitoring is required to track fracture growth and monitor the ground motion resulting from induced events (Oil and Gas Authority, 2018).

A key part of regulation applied in many territories, including the UK, in the mitigation of HF-IS is a Traffic Light System (TLS), whereby operations have to respond to the occurrence of set threshold event magnitudes (e.g., Bommer et al., 2006). Frequently there are two levels of intervention: “amber”, where some proactive measure must be taken by the operator to mitigate seismicity whilst operations continue; and “red”, where injection must be halted in response to induced events. The exact magnitude thresholds vary greatly between different jurisdictions (see Kendall et al., 2019).

The UK system is the most conservative of these TLSs, requiring injection pressures to be reduced and well integrity checked if a $M_L > 0$ event is detected during injection, and pumping stopped if a $M_L > 0.5$ occurs. This is contrasted with some territories in North America, such as Alberta and Illinois, which have amber light thresholds at $M = 2$, and red light thresholds at $M_L = 4$. When thought of in terms of seismic moment M_0, this corresponds to difference in the size of maximum tolerable red light events of around 3000 times. However, the consequences of exceedance of these thresholds are somewhat scaled to the size of the events. A red light event in the UK ($M_L > 0.5$) requires operations to be suspended for at least 18 hours whilst seismicity is monitored. The same in Alberta ($M_L > 4$), for example, requires the well site to be shut down for many months whilst a full inquiry is conducted, which can lead to the well being shut in permanently. Conservative TLS thresholds, such as those in the UK, are also attempting to take into account the potential for growth in event magnitude after injection (Clarke et al., 2014; Deichmann and Giardini, 2009).

1.5 Central questions of IIS

Whilst much progress has been made into the understanding of induced earthquakes, three broad research areas are the subject of ongoing investigations:

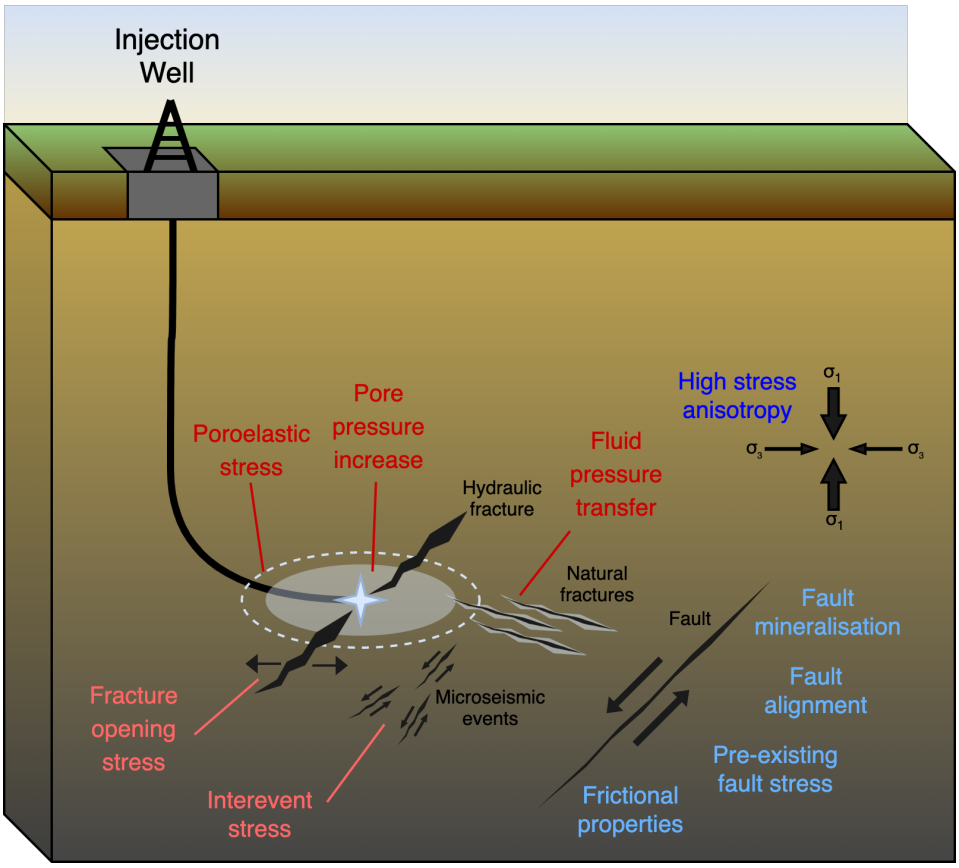

Figure 1.6: A schematic summary of the triggering mechanisms and controls of induced earthquakes. The triggering mechanisms are shown in red, whilst the geological controls are shown in blue. Structures and other features are labeled in black. Each of the triggering mechanisms acts to change the stress on the fault to induce failure. This can occur through a reduction in normal stress (by an increase in pore pressure or an elastic stress change) or an increase in shear stress (through an elastic or poroelastic stress change). Each of the mineralogical and tectonic controls will affect the likelihood of a fault to produce felt seismicity, through either arresting the rupture process or requiring a very large pressure perturbation to initiate failure.

- What are the geologic controls on induced seismicity? What makes different reservoirs more or less susceptible to large induced events?
- What are the controlling physical processes occurring when faults are activated by injection? At what spatial or temporal scales are each of these mechanisms most dominant?
- What operational or regulatory techniques can best mitigate the onset or propagation of seismicity after fault activation has been identified?

Figure 1.6 shows a schematic summary of the factors which control the likelihood of induced seismicity and the triggering of faults by injection. By analysing and applying novel techniques to case studies of HF-IS, this thesis is a study several of these factors, namely: interevent

and fracture opening stress transfer, pore pressure increase and fluid pressure transfer, stress anisotropy, and fault orientation.

The three main hypotheses I explore in this thesis relate directly to these central questions. Firstly, in chapters 2 and 3, I test whether elastic stress transfer is a physical mechanism that can control the behaviour of induced sequences. Secondly, in chapters 2 and 5, I test whether stress anisotropy and fault orientation affects the behaviour of fault activation. Lastly, in chapters 4 and 5, I see if statistical modelling is able to accurately forecast HF-IS in real-time.

1.6 Thesis outline

As this thesis is mostly a series of publications, each includes its own introduction with more specific background. I will here provide a brief overview of the contents of each the chapters.

Chapter 2 of this thesis addresses the question of the underlying physical process occurring during HF-IS, and whether interevent triggering from microseismic events can lead to the continuation of induced seismicity. A large microseismic dataset from the Horn River Basin, British Columbia, Canada, is used to examine a particularly clear case of a pre-existing fault structure being stimulated during injection. As part of this work, a sensitivity analysis into the uncertainties in elastic stress modelling is conducted, elaborating on further recent studies into difficulties that arise in using this method (e.g., Catalli et al., 2013; Meier et al., 2014). The latter part of this study addresses the first central question, looking at the regional stress state and the orientation of the activated faults as a controlling factor of their activation.

Chapter 3 examines a recent and topical case of HF-IS at the Preston New Road HF wells near Blackpool, Lancashire, UK, in 2018. The unexpected spatial distribution of microseismic events raised questions surrounding the physical process encouraging failure during the activation of a fault. This motivated a study on examining how elastic stress transfer from opening fractures affects the location of microseismic events stimulated by injection.

Chapter 4 uses this same case of HF-IS to test methods of real-time statistical forecasting of event size during operations. These techniques relate directly to the third central question posed above. As TLSs are inherently retrospective in nature – mitigating action is taken after large events occur – statistical methods have recently been developed to use the live data collected during HF to forecast the magnitudes of events and alert operators to potential fault activation, prior to the occurrence of larger events. This chapter presents the results as they were applied in real-time, during HF operations, of two of these methods.

Chapter 5 examines one of the most recent cases of IIS, the 2019 Preston New Road earthquakes, which in part lead to the UK government imposing a de facto moratorium on HF in the UK. The development of the microseismicity is interpreted with respect to the previous induced events at the site, with the differences between the seismicity in 2018 and 2019 being compared and contrasted. We apply methods developed in previous chapters of this thesis, and examine

their applicability to a case with higher magnitude seismicity.

CHAPTER 2

INTEREVENT ELASTIC STRESS TRANSFER DURING HYDRAULIC FRACTURING-INDUCED FAULT ACTIVATION

The contents of the following chapter has been published as *Investigating the role of elastostatic stress transfer during hydraulic fracturing-induced fault activation* by Tom Kettlety, James P. Verdon, Maximilian J. Werner, J. Michael Kendall, and Jessica Budge in Geophysical Journal International, issue 217, pages 1200-1216, in 2019 (Kettlety et al., 2019). I conducted all analysis and wrote the manuscript for this paper, which was then edited by James Verdon, Maximilian Werner, and Michael Kendall. All figures were produced by myself, except for Figure 2.2, which was adapted from a figure by James Verdon. Jessica Budge provided background information on the dataset used in this work. Figures have been altered slightly than those published with added annotations.

I begin this thesis with a paper addressing the question of the physical mechanism driving induced seismicity. This work uses a large microseismic dataset, in which fault activation is apparent, and elastostatic modelling to examine the contribution of interevent stress transfer as a mechanism for driving the observed seismicity.

We investigate the physical processes that generate seismicity during hydraulic fracturing. Fluid processes (increases in pore pressure and poroelastic stress) are often considered to be the primary drivers. However, some recent studies have suggested that elastic stress interactions may significantly contribute to further seismicity. In this work we use a microseismic dataset acquired during hydraulic fracturing to calculate elastic stress transfer during a period of fault activation and induced seismicity. We find that elastic stress changes may have weakly promoted initial failure, but at later times stress changes generally acted to inhibit further slip. Sources from within tight clusters are found to be the most significant contributor to the cumulative elastic stress changes. Given the estimated in situ stress field, relatively large increases in pore pressure are required to reach the failure envelope for these faults – on the order of 10 MPa. This threshold is far greater than the reliable cumulative elastic stress changes found in this study, with the vast majority of events receiving no more than 0.1 MPa of positive ΔCFS, further indicating that elastic stress changes were not a significant driver, and that interaction with the pressurised fluid was required to initiate failure. Thus, cumulative stress transfer from small events near the injection well does not appear to play a significant role in the reactivation of nearby faults.

2.1 Introduction

Hydraulic fracturing (Bao and Eaton, 2016; Clarke et al., 2014), waste water injection (Keranen et al., 2013), carbon capture and storage (CCS) (Verdon et al., 2013b), and the enhancement of geothermal systems (EGS) (Schoenball et al., 2012) have all shown the ability to stimulate seismicity. Numerous felt earthquakes have been linked to injection across North America and Europe, with magnitudes reaching as high as M_W 5.8 (Keranen and Weingarten, 2018). Increases in pore pressure and poroelastic stresses are considered to be the dominant physical mechanism responsible in areas of anthropogenic seismicity, reducing the effective normal stresses acting on nearby faults and fractures and thus promoting failure (Raleigh et al., 1976). However, the extent to which faulting and fracturing near the well can promote more distant seismicity is not well established. The uncertainty surrounding the continued propagation of seismicity once initial faulting has occurred has significance for the mitigation strategies currently being used in certain jurisdictions. "Traffic-light" schemes function under the assumption that if a smaller event (e.g. M 0.5 in the UK) is detected during injection, halting further operations can act to mitigate a larger, possibly damaging, earthquake (Clarke et al., 2014; Green et al., 2012). This assumption hinges on a transient change to the stress state produced from the fluid permeating the rock mass, as well as stress being relieved from the small faulting and fracturing that immediately accompanies fluid injection. However, if nearby faults and fractures receive enough elastic Coulomb stress change from the preceding events, bringing them closer to failure, by the time injection is halted due to the traffic light being exceeded, it may already be too late. In tectonic settings the transfer

of static stress is widely used in the estimation of seismic hazard, where it is applied to the distribution of aftershock sequences (Steacy et al., 2004; Stein, 1999). These Coulomb models have also been applied to fluid related triggering processes such as the seismicity associated with magmatism (Toda et al., 2002). Recent studies (e.g Catalli et al., 2013; Pennington and Chen, 2017; Sumy et al., 2014) have concluded that elastic stress transfer between induced events can also play a significant role during a sequence of induced seismicity.

Displacement on a fault changes the surrounding stress field. This stress change will act on nearby faults and fractures, and can promote or inhibit further slip. The Coulomb failure stress change, ΔCFS, acting on a fault is an effective tool for examining the stress accumulated during a sequence of events:

$$\Delta CFS = \Delta\tau + \mu'\Delta\sigma_n \quad , \tag{2.1}$$

with change in shear stress $\Delta\tau$ and change in normal stress $\Delta\sigma_n$ (positive extensive) resolved onto the fault plane, and effective coefficient of friction μ' (Harris, 1998). A positive ΔCFS means the stress conditions have changed in such a way as to promote slip, whereas negative acts to inhibit slip. Here:

$$\mu' = \mu(1-\beta) \quad , \tag{2.2}$$

where μ' is used to summarise the complex assumptions relating pore pressure change, the frictional properties of the fault, and the effective normal stress. Skempton's ratio β (Skempton, 1954) is used to relate the change in pore pressure change to the change in the applied stress: $\Delta P = -\beta\Delta\sigma_{kk}/3$. Assuming the fault zone is homogeneous and isotropic, one can relate the diagonal components of the stress tensor σ_{kk} to the normal stress σ_n (Rice, 1992; Simpson and Reasenberg, 1994). This gives $\Delta\sigma_{kk}/3 = \Delta\sigma_n$, and equations 2.1 and 2.2 are satisfied (Harris, 1998). This β parameter can be thought of as simulating the frictional stability of a fault in a porous medium. With $\beta > 0$, applied stress increase pore pressure, reducing the effective friction on the fault.

The elastic Coulomb stress changes acting on a plane due to any previous slip on surrounding faults can then be calculated using the Okada equations (Okada, 1992), identifying if slip was encouraged or discouraged by the preceding fault movements. The overall effect of stress changes acting on an earthquake population is measured using the Coulomb index (CI) – the percentage of events with positive ΔCFS (Hardebeck et al., 1998). A CI significantly above 50% is consistent with a population where elastic stress changes actively promoted slip.

This appears to be a relatively simple procedure, but determining the significance of a positive ΔCFS signal for a large number of events is non-trivial. One should appropriately consider the uncertainties in fault orientation, material properties, and slip behaviour. A study by Meier et al. (2014) highlighted the importance of a rigorous statistical treatment of static stress modelling by conducting a thorough analysis of the stress changes associated with the 1992

Landers earthquake sequence, assessing the significance of positive stress changes with regards to the modelling assumptions and the uncertainties in the input parameters They explored techniques to determine significance and the sensitivity of elastic stress models, especially to focal mechanism uncertainty. Further studies have highlighted the effect of elastic stress transfer in some injection-induced earthquake sequences, with relatively high magnitude events correlated with positive Coulomb stress changes. Catalli et al. (2013) calculated CI in excess of 75% for induced events associated with the Basel EGS, as well as giving a treatment of FM, location, and frictional uncertainties. During the 2011 Prague, OK sequence, Sumy et al. (2014) found that the M_W 5.0 foreshock, which is considered to have been induced by the nearby waste water injection, promoted the M_W 5.7 mainshock by elastic Coulomb stress transfer. Pennington and Chen (2017) also studied the events associated with waste water injection in Oklahoma, during the 2016 Pawnee sequence. They found that the three foreshocks promoted failure of the M_W 5.8 mainshock, which went on to promote failure on 67% of the events that occurred after it. Coulomb stress changes resulting from microseismic events recorded during hydraulic fracturing were calculated by Vasudevan and Eaton (2011), showing that non-double-couple source mechanisms have a significant effect on the resulting stress maps. Schoenball et al. (2012) investigated the static Coulomb stress changes for the seismicity associated with an EGS, neglecting any pore pressure change. They found that elastic Coulomb stresses may have only played a small role in promoting failure for the majority of the seismicity associated with the injection, but were more significant in the triggering of specific event clusters after shut-in occurred. Maghsoudi et al. (2018) used statistical techniques to show that spatiotemporal clusters of events, associated with a hydraulic fracturing stimulation in the Horn River Basin, exhibited evidence for inter-event triggering. They showed that the occurrence of events deviated from a purely Poisson process, and temporal clustering was present. In their study, whilst the microseismic event clusters exhibit this aftershock sequence-like pattern, the events deviate from the typical mainshock-aftershock behaviour observed in tectonic sequences. Large numbers of events also exhibit swarm-like behaviour, where the triggered events have very similar magnitudes to those that triggered them and, within a given cluster, the largest event is not typically the first.

In our study we use a microseismic dataset acquired during a hydraulic fracturing operation in the Horn River Basin (HRB). The HRB is one of the largest natural gas plays in British Columbia, Canada, and is part of the Western Canadian Sedimentary Basin (WCSB). Most of the wells in the HRB are horizontal, multi-well operations deployed from single pads, employing multi-stage hydraulic fracturing (HF) to stimulate production from three Devonian shale layers: the Muskwa, Otter Park and Evie formations (Barker, 2014). In recent years, multiple felt earthquakes associated with HF have been recorded in the WCSB (Bao and Eaton, 2016; Schultz et al., 2015), with magnitudes reaching as high as M_W 4.6 (Kao et al., 2018). Microseismic monitoring during operations has also repeatedly indicated the presence of smaller scale injection-induced fault activation (BC Oil and Gas Commision, 2012).

We use the *PSCMP* code of Wang et al. (2006) to model the cumulative elastic stress changes during a period of HF-induced fault reactivation. We use the full moment tensor solutions, including the non-double couple fault motion. Sensitivity analyses are then conducted to constrain the effects of focal mechanism uncertainty on ΔCFS through Monte Carlo methods, as developed in Catalli et al. (2013) and Meier et al. (2014). We examine the effect of the fluids on the resulting ΔCFS by varying Skempton's ratio β. Due to the observed tight clustering of events, we also compare the elastic stress changes within clusters to the total cumulative ΔCFS to investigate the significance of intra-cluster triggering.

The variability of induced seismicity between different sites and regions (e.g. Verdon et al., 2016) has been linked to differences in the background stress field (Göbel, 2015; King et al., 2014). Fault orientation has been shown to be connected to the occurrence of induced seismicity, with the $M_W > 5$ events associated with waste-water injection in Oklahoma occurring on planes well oriented to the background stresses (Alt and Zoback, 2017; Keranen et al., 2013). Thus, the calculated elastic stress changes need to be considered in the context of the in situ stress field acting on the individual fracture or fault planes. The conditional probability of failure given the in situ stress field can be determined through a quantitative risk assessment (QRA) methodology developed in Chiaramonte et al. (2007) and Walsh and Zoback (2016). QRA methods have been applied to various geomechanical issues, such as wellbore stability (Moos et al., 2003) and CCS caprock integrity (Chae and Lee, 2015). Following the approach of Walsh and Zoback (2016), the uncertainties are included in the calculation of the required pore pressure change to initiate failure (given the Mohr-Coulomb slip criterion). A "probability" of failure for a given ΔP can be determined by a Monte Carlo method of randomly sampling from distributions of the input parameters. This fault slip potential (FSP) can then be used as a proxy for the likelihood of failure for a given fluid pressure increase.

We conclude our study by interpreting the estimated elastic stress changes in the context of the estimated FSP for the activated faults.

2.2 Data

We use a microseismic dataset that was acquired during a multi-well, multi-stage hydraulic fracture treatment conducted in the HRB (described in Baird et al., 2017; Verdon and Budge, 2018). 237 stages were completed in the 10 wells drilled, using a toe-heel, zipper-frac injection pattern. Continuous monitoring was provided by three downhole microseismic arrays. For the 119 stages for which we have data, around 92,700 events were recorded, processed and catalogued. These stages of injection constitute the 10 to 12 most proximate stages to the monitoring arrays for each well, and thus are expected to give the best quality data (shown in Figure 2.1). Magnitudes (ranging from $-2.4 < M_W < 0.5$), fault radii, stress drops, slips and locations were determined for all events in the catalogue, and around 35% have full moment tensor solutions (MTs). The

processing was conducted by a service provider, ESG Solutions. This data is proprietary and is not available for public release.

Event hypocentres were initially calculated by inverting P- and S-wave travel times through a layered anisotropic velocity model. This model was determined from sonic logs, and further calibrated using the perforation shots. Once preliminary locations were found, the velocity model was then linearly tapered at the transitions between the shale layers to more accurately reflect the smooth transitions observed in the sonic logs. Events were then relocated using this refined velocity model. Double difference corrections were then applied, refining the relative locations of the events. Seismic moment, source radius and slip was found for each event by fitting a source model to the event displacement spectra (see Stork et al., 2014). The source radii for the microseismic events used in this study are distributed around 15 m, with the majority (96%) under 20 m. A small number (36 of the 923) of higher magnitude events have source radii up to 110 m.

Moment tensors were determined by inversion of polarity data and P-to-S wave amplitudes for a estimated radiation pattern (as in Vavryčuk, 2014, 2015). The fault plane and auxiliary planes were discriminated using the in situ stresses, finding the preferentially aligned nodal plane (NP) in the local stress field. This can be used as an estimate of the fault plane, over the auxiliary plane. However, the choice of nodal plane may not be significant for this elastic modelling, as discussed in section 2.3.1. Throughout this work, we refer to a nominal "primary", preferred NP chosen during the inversion, and a "secondary" nodal plane.

Some of the determined MTs include a volumetric component. The vast majority (90%) of events are effectively double-couple (DC) sources (with tensile angles less than 3°), though some events, especially smaller events closer to the well, have larger non-DC components. Events with significant tensile angles ($\alpha > 10°$), most likely associated with the opening of fractures through hydraulic stimulation, are generally far smaller in magnitude than those associated with the fault reactivation, with 84% having magnitudes less than M_W −0.5. Thus, whilst the non-DC component of slip is included in the analysis, it will have less of an effect on the overall pattern of stress change than the larger, DC sources.

No uncertainties were provided by the operating contractor. Thus, we estimate uncertainties throughout, informed by the methods through which the parameters were determined. As the location determination went through multiple stages of refinement, the absolute location uncertainty would be approximately ±50 m, whilst the relative error may be as low as ±10 m. We go on to estimate the location uncertainty further, by quantifying how diffuse each of the clusters are that map out the presumed fault planes (Figure 2.4b). The combined effect of a low relative location error and the modelling method is discussed in section 2.3.1, and more in section 2.4. The uncertainty in the fault geometries, as inferred from the MTs, is the subject of the sensitivity analysis conducted later in this work (section 2.3.3). Magnitudes, and thus source radii and slip, are considered to be well constrained, given the standard method by which they were calculated,

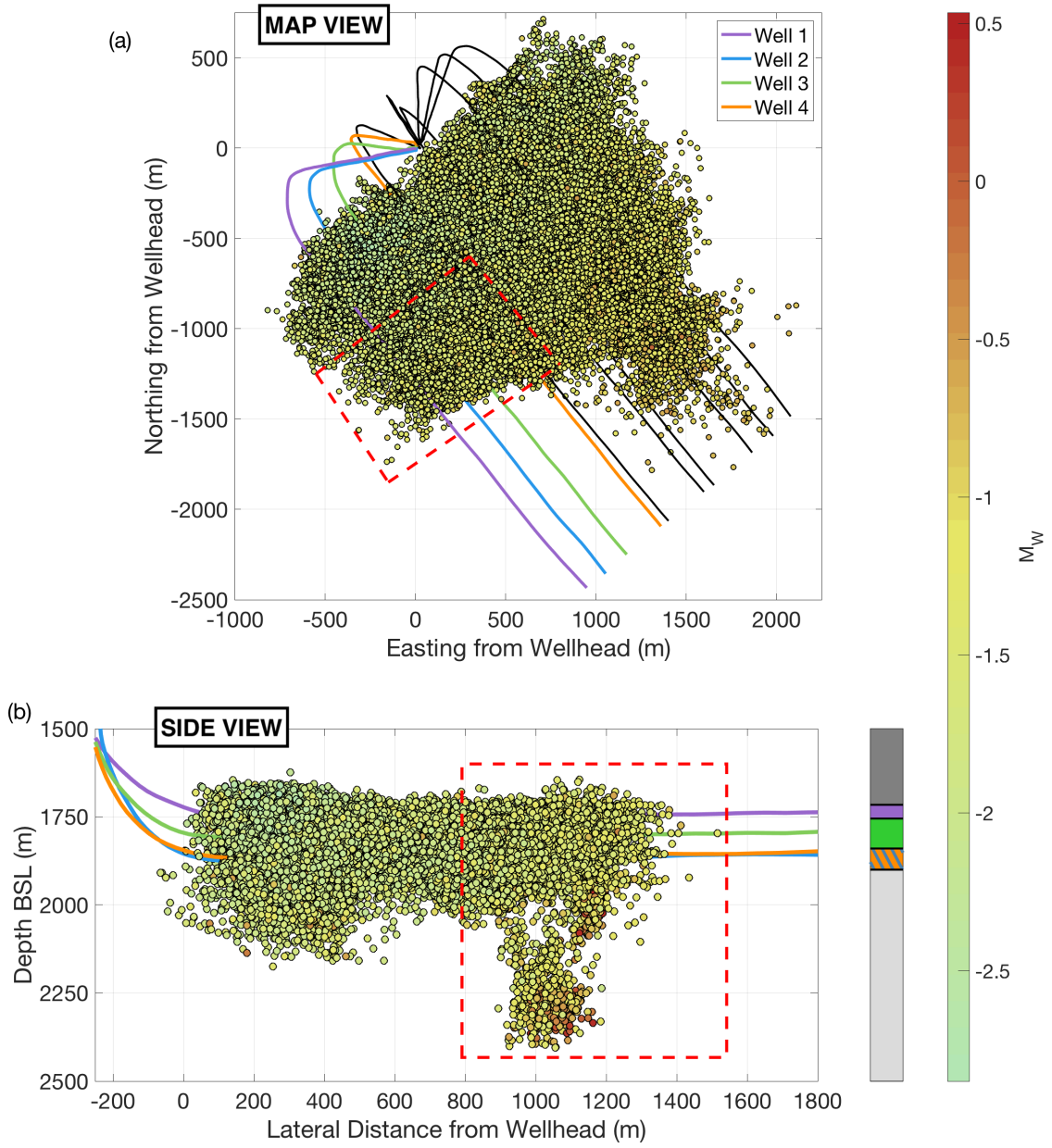

Figure 2.1: Hypocentres in plan view (a) and cross section (b) of all events detected and located during hydraulic stimulation of the 10 wells at the study site. Events are coloured by moment magnitude M_W. Wells 1 to 4 are shown as coloured lines, with the other wells being shown in black. The events associated with these wells show the clearest evidence for fault reactivation, and are the subject of this study. The red dashed boxes delineate the approximate positions of these hypothesised fault-related events. Also shown in (b) is the 1D geologic model, showing the depth of the overlying Fort Simpson formation, the three targeted shale layers (Muskwa, Otter Park and Evie), and the underlying Keg River limestone. The wells and corresponding targeted shale layers have matching colours.

and the low noise for these events detected on approximately 80 stations in deep borehole arrays.

2.2.1 Identifying Fault Reactivation

Initial examination of the microseismic event hypocentres indicated the reactivation of pre-existing faults, with clusters of events mapping out planar features that extend approximately 400 m below the wells, into the underlying Keg River limestone. The largest events were found in these clusters, with 27 events having magnitudes greater than $M_W = 0.0$, whereas the overwhelming majority of events, those associated with hydraulic fracture propagation, have magnitudes around $-2 < M_W < -1$. The largest events, and the most obvious downward growth of microseismicity, were seen in proximity to Wells 1 to 4, associated with the stimulation stages in the central portions of these wells (see Figure 2.1). Because these events represent the clearest example of fault reactivation within this dataset, we focus our analysis on the events associated with these wells and stages.

To further discriminate fault reactivation from the operationally-induced microseismicity associated with fracturing, we examined variations in the b-value of the event magnitude-frequency distribution (Gutenberg and Richter, 1944). For each stage, we clustered events based on their spatial positions using a density-based clustering algorithm DBSCAN (Ester et al., 1996). For each cluster we computed the b-value using the maximum likelihood approach (Aki, 1965). To determine the minimum magnitude of completeness (M_{MIN}) for each cluster, we use a Kolmogorov-Smirnov test, with M_{MIN} being the smallest magnitude at which the observed population can be fit with an exponential distribution with a confidence level of 95%.

The resulting magnitude-frequency distributions are shown in Figure 2.2. It is immediately apparent that the distribution of b-values is bimodal. The majority of event clusters have high b-values ($b > 1.5$), implying that they are associated with normal hydraulic fracture propagation, while a smaller number of clusters have $b \approx 1.0$, a value similar to tectonic earthquake sequences, indicating that they are associated with fault reactivation (Eaton and Maghsoudi, 2015; Eaton et al., 2014; Verdon, 2013; Verdon et al., 2013a). We therefore use $b < 1.5$ as our criteria for identifying microseismic event clusters that represent fault reactivation.

These clusters occurred mostly during two periods of injection, as can be seen in Figure 2.3. These are denoted by "reactivation periods" 1 and 2 (or, RP1 and RP2) and are separated by around 42 hours. Little seismicity occurred in the vicinity of these clusters except during these two periods. The events are shown in Figure 2.3 with the same colour as the well with which they are associated. Each reactivation period is associated with an injection stage in Well 2, with fault reactivation clusters located beneath these injection stages. Seismicity continued in these clusters after the Well 2 stages had stopped, at which point injection switched to Well 4. However, the injection stages from Well 4 are over 500 m NE from Well 2, and there is clear lateral separation between the Well 4 events and the Well 2 fault reactivation, with the Well 4 events all appearing to show operationally-induced hydraulic fracturing events. We conclude that

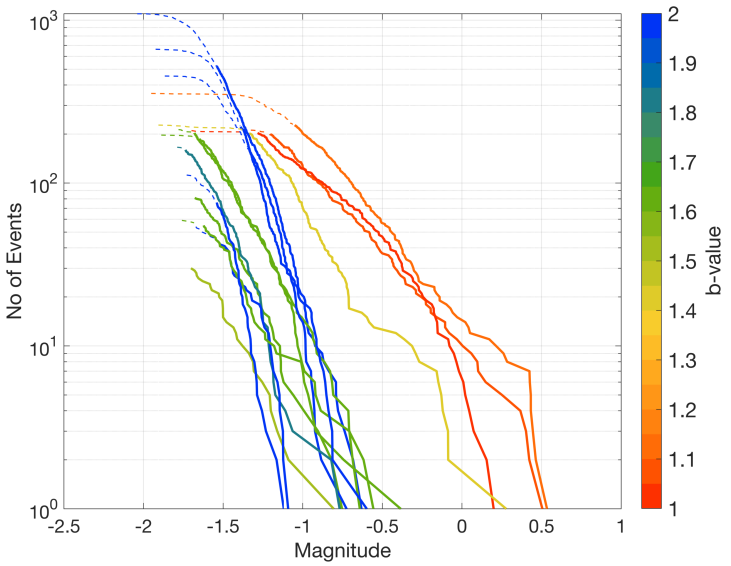

Figure 2.2: Frequency-magnitude distributions for event clusters associated with fracturing stages in Wells 1 to 4. Each line corresponds to one cluster. The resulting b-values are clearly bimodal, with most clusters having $b > 1.5$ (coloured blue/green), and a smaller number of clusters having $b < 1.5$ (coloured yellow/red). The 4 low b-value clusters are those shown in Figure 2.3, which make up the activity in reactivation periods 1 and 2.

the fault reactivation events are associated solely with the Well 2 stages, and not those of Well 4. Their apparent contemporaneity with Well 4 injection simply represents the fact that seismicity continued after injection had ceased in Well 2, as is commonly observed during injection-induced fault reactivation (Deichmann and Giardini, 2009).

An additional cluster of low b-value seismicity occurred during a later injection stage in Well 2, to the NW of the clusters shown in Figure 2.3, forming another cluster extending downwards from the well. This appears to connect to the diffuse cluster visible at around 2200 m depth in Figure 2.3. Considering all of the events that were located in this area, two main structures become apparent: a planar feature, and a more diffuse cluster, both extending between 1900-2400 m depth. Figure 2.4 shows the locations of the low b-value, fault related events, showing that these events map out two pre-existing fault structures both of which strike NE-SW, and dip towards each other.

The occurrence of events appears to be correlated tightly with the injection. We do not observe any clear aftershock-type sequences in either RP, where one large event triggers subsequent smaller ones in a spatiotemporal cluster. This type of behaviour would be indicative of a sequence with significant event-event triggering. Event clusters appear more swarm-like, where similar sized events are happening throughout the periods of activity. This swarm-like behaviour is contrasted with the results found by previous studies (Langenbruch et al., 2011; Maghsoudi et al., 2018), where there were clear patterns of triggered temporal clusters during injection-induced

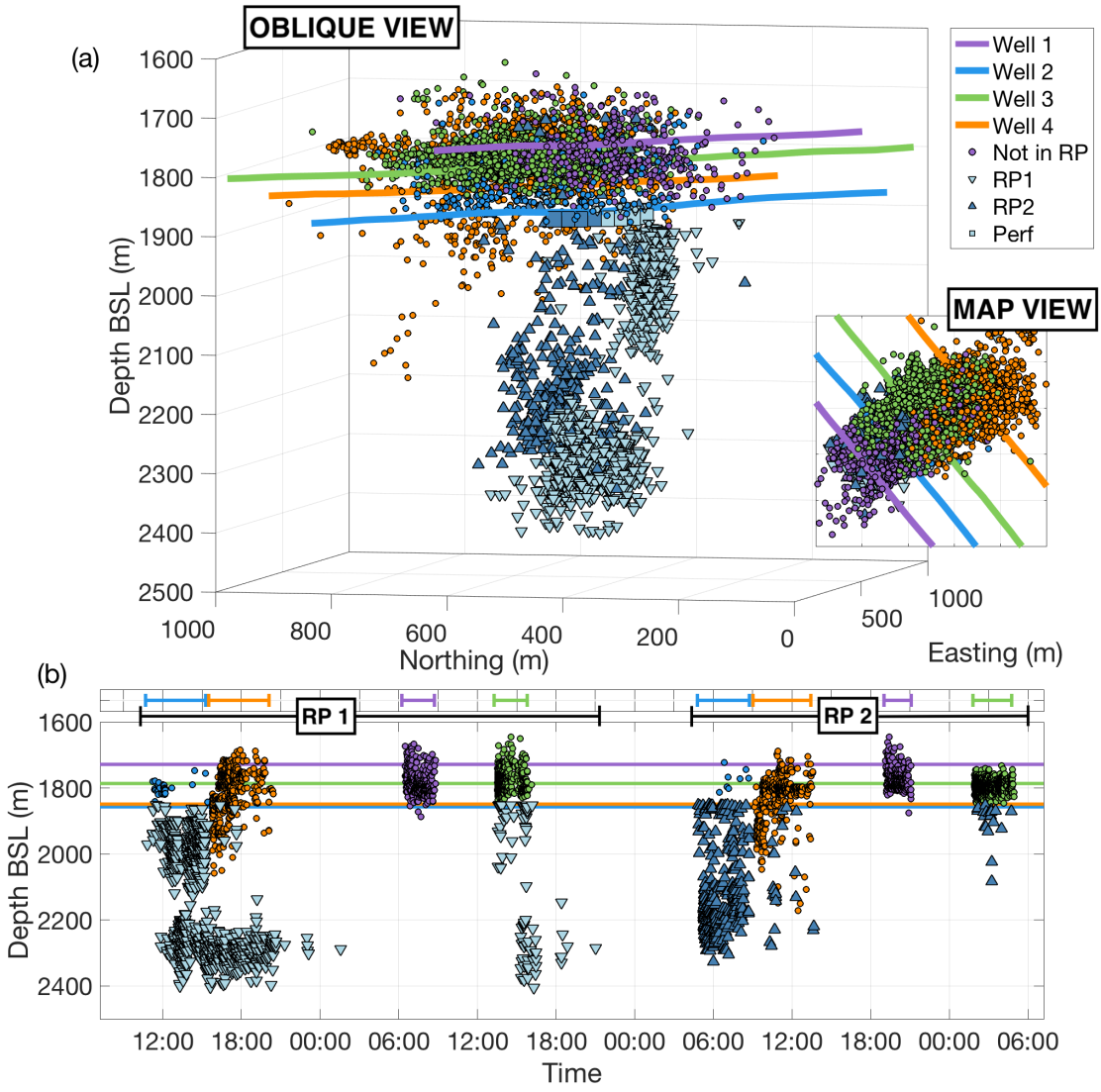

Figure 2.3: **(a)** Hypocentre locations of the studied seismicity, grouped into "reactivation periods" 1 and 2 (RP1 & RP2). Perforation shots are shown as squares, coloured in the same manner as their associated RP. Circles show nearby events considered not to be associated with the fault activation, and are coloured by their associated injection well. The map view of the seismicity is inset. **(b)** Temporal distribution of the seismicity. Injection durations are shown above, with colours denoting the well from which injection was occurring.

seismicity.

There is also no clear sign of the characteristic $r \propto \sqrt{t}$ triggering wavefront emanating from the point of injection, as exploited in many previous studies to estimate the diffusivity of the medium (Goertz-Allmann et al., 2011; Shapiro et al., 1997). This would be indicative of events triggered by the expanding wavefront of pore pressure that results during injection. The elastic Coulomb modelling that follows will attempt to probe the ambiguous mechanism behind this sequence of events.

We use a least squares minimisation algorithm to find the planes that best fit the seismicity. The RP1 plane has a strike ϕ of $250 \pm 10°$ and a dip δ of $80 \pm 5°$. The RP2 plane has a ϕ of $60 \pm 15°$ and a δ of $75 \pm 10°$. Uncertainties for these geometries are estimated given the spread of the events. These two suspected fault structures are denoted fault 1 and 2 (F1 and F2) respectively, named for the period of seismicity in which they were activated: events on F1 were seen mostly during RP1, whereas events of F2 occurred primarily during RP2, although some RP1 events also took place on F2. These planes can be seen projected onto their associated events in Figure 2.4.

If events are thought to have occurred purely on these conjugate planes, the spread of events around the faults may provide an estimate for location uncertainty. This estimate would be ±25 m for F1, and ±46 m for F2, as shown by Figure 2.4b. However, given the estimated rupture dimensions (~ 20 m), it is uncertain as to whether the events observed are actually slip on pre-existing faults, or rather smaller fractures failing in a zone around these structures. Despite their size, all of the largest events ($M_W > 0$) in the catalogue took place along these underlying planar features, we conclude that this region must be fundamentally different from that of a diffuse cloud of fractures, such as those near the wells. To compare these two interpretations, the following analysis will consider both the individual microseismic event geometries (section 2.3.1), as well as the fault planes themselves (section 2.3.2). This will also help to constrain the effect of the uncertainty in the geometries determined from the event moment tensors. The effect of Coulomb stress on the fault planes and the microseismic events should be similar if the event geometries reflect that of the larger structures.

2.2.2 Stress Model for Horn River Basin

Assuming that the vertical stress is a principal stress, which is usually the case in sedimentary basins unless significant deformation or stress rotation is present, an in situ stress model is defined by the orientation and magnitudes of the principal stresses – the vertical stress S_V, the maximum horizontal stress S_{Hmax}, and the minimum horizontal stress S_{hmin} – as well as the pore pressure P, and the S_{Hmax} orientation ϕ_H. Borehole breakouts, density log measurements, leak-off tests, shut-in pressures, mud-weights, and the modelling of breakout rotations can be used to constrain estimates in these parameters (Haimson and Cornet, 2003; Zoback, 2010).

Previous studies have estimated the stress regime in the Horn River Basin for particular operations (Sayers et al., 2016; Snelling et al., 2013), as well as the frictional properties of the

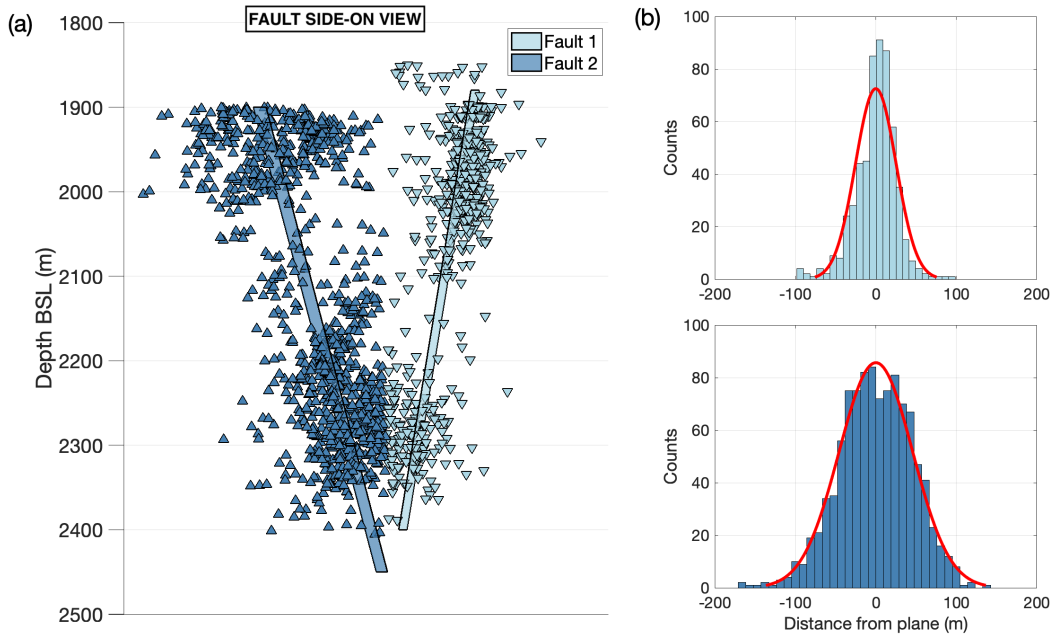

Figure 2.4: **(a)** Edge on view of events hypocentres used to define the visible fault planes. Light blue downward triangles show fault 1 events, whilst dark blue upward triangles show fault 2 events. **(b)** Histograms of lateral distance away from plane for events associated with each fault. Colours are the same as those used in (a). Red lines show fitted normal distributions, where for F1 $\mu = 0 \pm 2$ m and $\sigma = 25 \pm 2$ m, and for F2 $\mu = 0 \pm 3$ and $\sigma = 46 \pm 2$ m. These uncertainties represent the 95% confidence intervals.

shale and underlying limestone (Chou et al., 2011; Hurd and Zoback, 2012). There are a number of at-depth stress measurements in the region, which arise from the large number of shale gas operations in the Horn River Basin, as well as the adjacent Laird Basin and Montney shale play.

The stress model used in this study is calculated using data from the World Stress Map (Heidbach et al., 2016). At-depth stress measurements are taken from operator reports catalogued by Bell (2015), with each well located less than 30 km laterally from the site considered here. These measurements are shown in Figure 2.5. These data provide a ϕ_H of $55 \pm 10°$. The pore pressures given appear hydrostatic. This may be the case only for the formations from which the measurements were taken, or could be a the product of a modelling assumption on behalf of the operator. Eaton and Schultz (2018) found that, for two other reservoirs in the WCSB, regions of overpressure were common, and correlated with an increased occurrence rate of earthquakes. We were not provided with drilling data for the field, and thus do not have a measure of the in situ pore pressure for the shales. We thus use hydrostatic pore pressure as a mean value, and give it an appropriate uncertainty to account for the possibility for overpressure. Uncertainties are also estimated for the other principal stresses (see Walsh and Zoback, 2016). These will then be used in the Monte Carlo FSP analysis.

One factor not directly accounted for is the increase in pore pressure that accompanies hydraulic fracturing. The magnitude of the ΔP change, and its spatial extent, is highly dependant on the permeability structure of the reservoir (Brown and Ge, 2018a). More importantly, it is very sensitive the fracture permeability and extent. If matrix permeability is very low (~ 10 nd (Chalmers et al., 2012; Dong et al., 2017)), and fracture permeability is ignored, the ΔP perturbation will be far more than 10 MPa over a scale of tens of metres (Brown and Ge, 2018b). Fractures act to increase bulk permeability, increasing the distance over which the fluid pressure is applied, and reducing the magnitude of the resulting ΔP. Constraining these exact parameters requires complex hydromechanical modelling, and is beyond the scope of this work.

A least squares fit is applied to find the stress gradients of S_{Hmax}, S_{hmin}, S_V, and P, and their respective uncertainties (York et al., 2004). The stresses acting at the depth of the reservoir are then found by extrapolation. This gave a S_{Hmax} of 77 ± 12 MPa, S_{hmin} of 51 ± 6 MPa, S_V of 66 ± 5 MPa, and P of 27 ± 7 MPa. The mean S_{Hmax} from the well data in the region is $55/pm10^{\circ}$ (Bell, 2015). These values broadly agree with those found by Chou et al. (2011), who constructed a stress model for the HRB shales using borehole observations provided by industry, and Sayers et al. (2016), who used anisotropic seismic attributes to estimate stress conditions. In the Anderson classification scheme this is a strike-slip regime, with $S_{Hmax} > S_V > S_{hmin}$. Within the uncertainties, the regime could be considered normal faulting, however that is taken into account in the Monte-Carlo FSP analysis.

2.3 Methods & Results

2.3.1 Elastic Stress Modelling

Using the estimated slips, rupture lengths, and fault plane orientations, the deformation resulting from each event can be modelled. The code *PSCMP* by Wang et al. (2006) is used to calculate the displacement field u due to slip on a square patch. This uses the analytical Okada solution of the Green's functions for a homogeneous elastic half-space (Okada, 1992). The model then derives the stain tensor ϵ_{ij} from u, which is then related to the stress sensor σ_{ij} using Hooke's law for a linear elastic medium. This stress tensor is then resolved onto a receiver plane and rake, and the resulting Coulomb stress change ΔCFS is calculated (equation 2.1). All events during RP1 and RP2 are defined as "receivers", and each event that occurred prior to each receiver are treated as "sources" of deformation. This gave a total of 1119 receivers (of which 923 have MTs), and potentially 6602 sources (of which 1876 have MTs). Proceeding iteratively through each receiver with a MT, the cumulative elastic stress change is calculated at that receiver's hypocentre.

The elastic parameters ($\mu = 0.7$ and $\beta = 0.4$) used are based on measurements made by (Chou et al., 2011) in the HRB, as well as values obtained for formations of similar type, depth, pressures and porosities (Kohli and Zoback, 2013). Sources are modelled as square patches, with dimensions calculated to match the rupture area given by the source spectra. The average

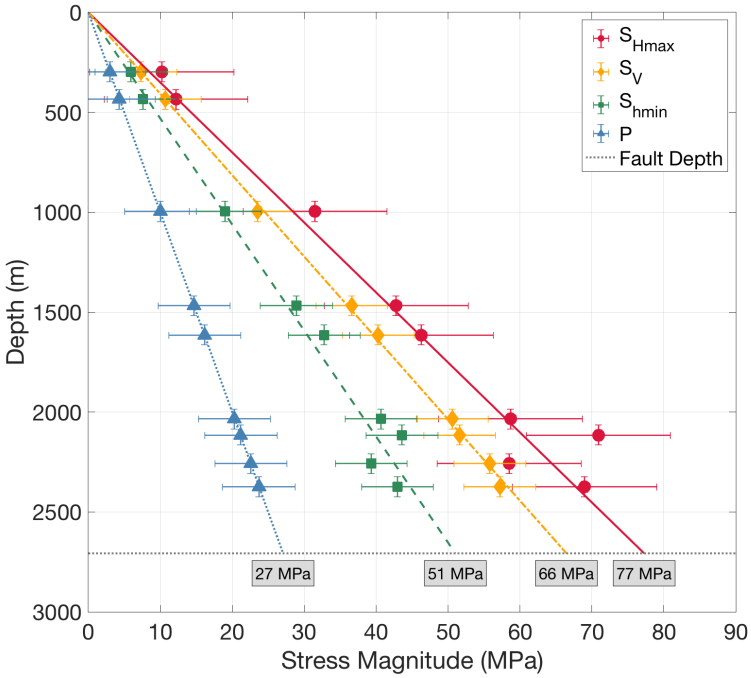

Figure 2.5: Stress gradients produced from Bell (2015) data for the Laird and Horn River Basin. The error bars show the uncertainties used for each of the stress parameters (see Walsh and Zoback, 2016). Estimates for the stresses acting at the depth of the reservoir are shown in grey boxes.

patch length is approximately 25 m, with the largest around 190 m. Slip is resolved into the strike and dip components of the plane using the rake and tensile angles (see Vavryčuk, 2011). Sources are excluded with source-receiver distances less than one source length because ΔCFS values computed using a uniform slip model become unreliable in the very near-field (see Meier et al., 2014). This step will have a significant effect on the resulting ΔCFS magnitudes and polarities, but will also aid in removing artefacts which result from uncertainties in the slip behaviour and source mechanism (Steacy et al., 2004), and stress drop (Schoenball et al., 2012). The ramifications of this are discussed in detail in section 2.4.1.

Figure 2.6 shows resulting ΔCFS values found for RP1 and RP2 when the preferred nodal plane, as identified during the MT inversion, is used. The Coulomb index for all of the events in RP1 is just below 60%, and around 12:30 and 14:30 (on the first day visible in Figure 2.3b) the windowed CI exceeds 70%. This is in contrast to RP2, where the CI for the entire population is 38% and the windowed values do not exceed 45%. The majority of the larger magnitude events ($M_W > 0$) received positive ΔCFS. However, there is no correlation between the event magnitude and ΔCFS magnitude. For both reactivation periods, no ΔCFS received from the microseismicity exceeds ±1 MPa. There are a number of events (36%) however that received positive ΔCFS

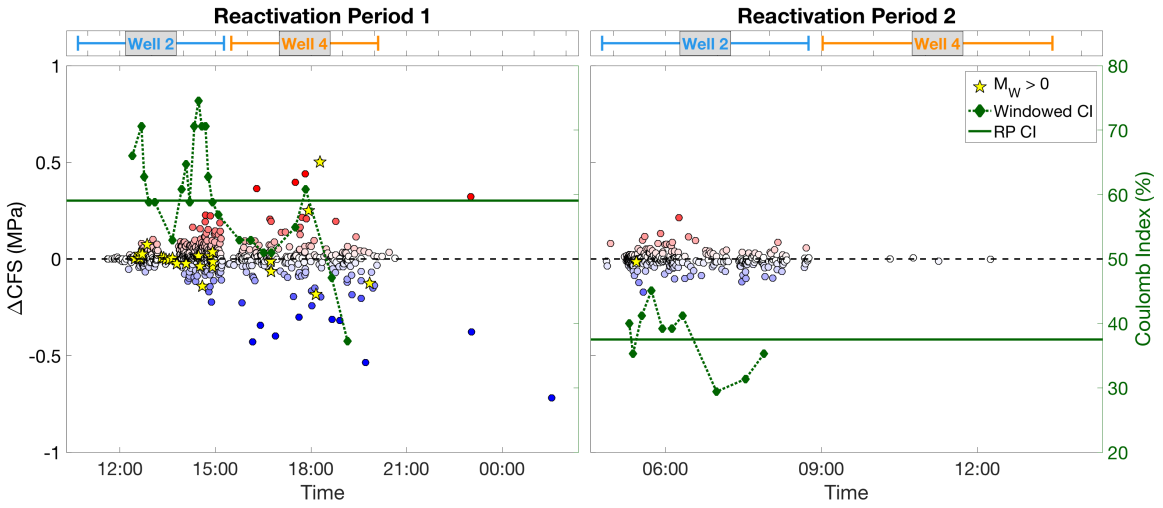

Figure 2.6: The values of the ΔCFS for the two reactivation periods, using the preferred NP. Events receiving positive Coulomb stress change are shown in red, and negative in blue. Events with $M_W > 0$ are shown as yellow stars. Note that a number of the larger magnitude events have higher magnitude, positive ΔCFS. The CI is estimated across moving windows each containing 50 events, and shown by green diamonds connected with a dotted line. The green lines show the CI for the entire period. Above, bars indicate the duration of injection plotted over the same time periods.

greater than the commonly used triggering threshold of 10 kPa (see King et al., 1994; Stein, 1999).

Previous work in this field (e.g. Catalli et al., 2013; Pennington and Chen, 2017), observe CIs generally in excess of 70%. Given the above results, elastic deformation may have only modestly promoted slip in this case, during the initial period of activity. However, during the latter period, the events were generally inhibited by the preceding elastic deformation. This implies that fluid processes such as aseismic tensile slip, pore pressure changes and poroelastic effects were most likely the dominant cause of fault reactivation.

These results are only slightly altered when the secondary nodal plane is chosen, with a CI of 61% positive for the first period and 36% for the second. The windowed CI values also show very similar temporal behaviour as for the preferred NP, with peaks around 75% early in RP1, and CI not exceeding 45% in RP2. The similarity should not be surprising however due to the inherent symmetry in the stress change pattern when using a uniform slip model (Meier et al., 2014). This results in generally similar stress change values. The NP ambiguity is further explored in section 2.3.3.

2.3.2 Resolving Stresses onto Fault Structures

In addition to computing the Coulomb stress changes for each event, we also evaluate the stress interactions between the microseismic events and the two fault planes (see section 2.2.1

for description), as in the latter section of Schoenball et al. (2012). The same geomechanical parameters as in section 2.3.1 are used, along with the preferred NP geometries. As events on F1 only occurred during the first reactivation period, only stress changes up to the end of RP1 are calculated for this plane. Events on F2 occurred during both reactivation periods, so stress changes are calculated for this plane for the entire duration of both reactivation periods. In the model, the receiver geometries were those of the individual fault planes, and receiver rake was given by the average rake of events used to define the two fault planes (see section 2.2.1). Cumulative ΔCFS was calculated in half-hour increments, accumulating sources through successive time windows. The resulting stress changes acting at a given time on the plane are then calculated at sample points gridded at 20 m intervals along the surface. This grid was defined by examining the extent of the cloud of seismicity. F1 extended for 180 m along its strike and 500 m in the dip direction. F2 extended 270 m along its strike, and 550 m in the dip. The fault dimensions can be seen in Figure 2.4. These gridded stresses can then be analysed in a similar manner to that of an event population, by examining the proportion of positive ΔCFS received (Coulomb index), or the sum, or average of the stress changes at the sample points.

The results of this analysis show a similar pattern to the elastic stress changes as calculated in section 2.3.1. In RP1, both the sum and the average stresses resolved across the plane are positive, and the effective CI (the proportion of sample points on the plane with $\Delta CFS > 0$) reaches as high as 78% around the middle of RP1 (Figure 2.7). This suggests that the elastic stress changes modestly promoted failure on F1. Similar temporal variations in CI are observed as for section 2.3.1 for the individual events. However, there is a short period during RP1 where the opposite signal is seen. At around 13 : 00, when stresses are resolved across F1, the effective CI acting is at its lowest value: ~ 35%. But when the individual events are considered, this early part of RP1 however had the relatively high CI of ~ 70%.

The similarities between the two methods of stress change determinations continues for F2 through RP1 and RP2. The CI across the second plane never exceeded 50% and rarely went above 30%, indicating that across the surface of this plane, the majority of the elastic stress changes were inhibiting failure throughout both reactivation periods. The average and total stress change magnitudes acting on the two fault planes mirror these trends, with consistently positive ΔCFS for F1 and negative for F2.

Thus, we reach the same conclusion – microseismic event slip may have modestly contributed to the failure on F1, but fluid and/or pore pressure effects must have dominated for F2, counteracting the effect of inhibiting elastic ΔCFS. This also highlights that, even when the uncertainty of resolving stresses onto the individual receiver geometries is removed, roughly the same behaviour holds. However, geometry uncertainty is obviously not removed entirely here, as the sources of deformation are still the catalogued events.

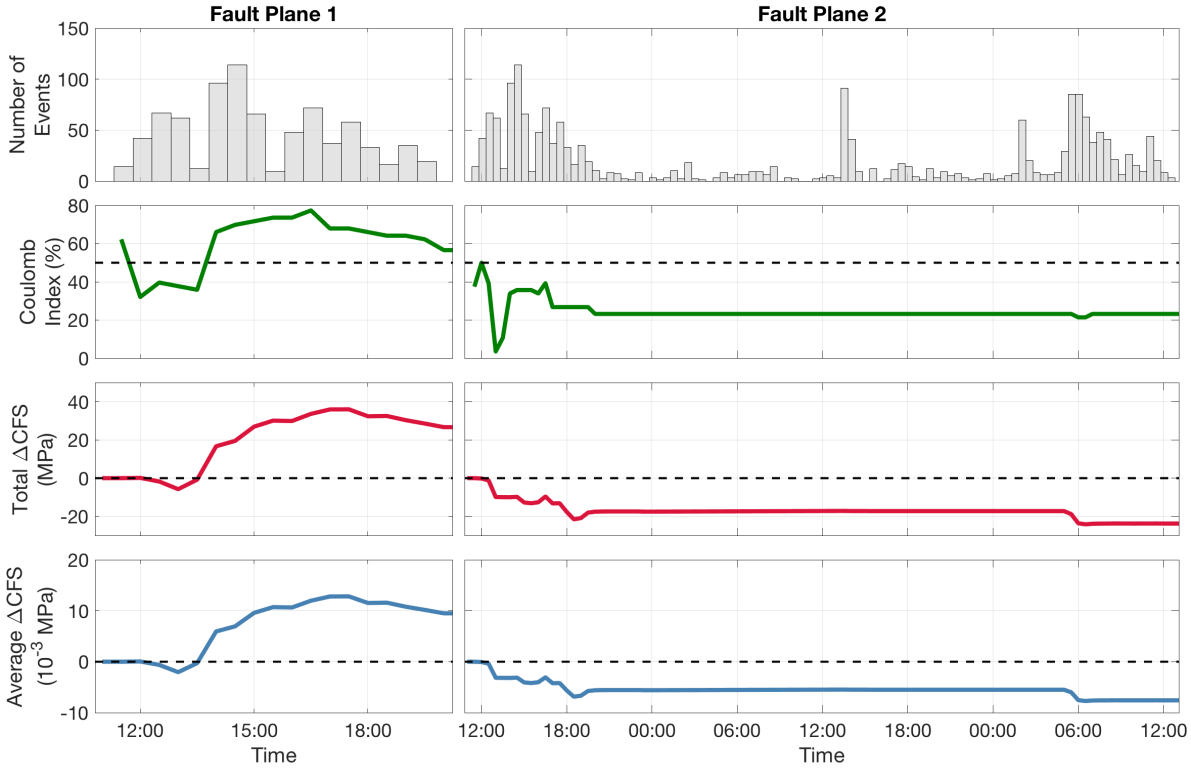

Figure 2.7: The results of mapping elastic Coulomb stress changes onto the fault planes shown in Figure 2.4. Grey bars show in the number of sources that occurred in each of the 30 minute time-bins. Green lines show the effective CI - the proportion of points across the planes which are experiencing positive ΔCFS at the time bin shown. Red show the sum of ΔCFS across every sample point on the planes. Blue show the average ΔCFS at the sample points.

2.3.3 Sensitivity Analysis

We use a Monte Carlo approach to estimate the sensitivity of ΔCFS to focal mechanism uncertainties, as in Catalli et al. (2013) and Meier et al. (2014). Using the first 500 events with MTs that occurred during the first reactivation period, 3000 test catalogues were produced. Each catalogue contains the same 500 events, but with the geometries permuted in three different fashions, giving 1000 catalogues for each type. In the first set of catalogues, the NP is randomly selected from the original FM in the catalogue. In the second case, Von Mises distributed rotations are applied to the preferred NP, representing uncertainties in the focal mechanism inversion. As no uncertainties were provided from the processing, a single FM uncertainty of $\sigma = 30°$ is given, representing a reasonable, perhaps pessimistic, value for this form of MT inversion using borehole-acquired microseismic data (Vavryčuk, 2014). A final set of test catalogues are generated with entirely random strikes, dips and rakes (Kagan, 2005). This allows us to compare the perturbed FMs stress changes to an extreme uncertainty scenario, as well as a potential null

hypothesis case, where there is no preferential alignment of failure planes. The ΔCFS modelling is then conducted in the same manner as in section 2.3.1 for each catalogue. The CI of each of the catalogues is then calculated, and the distributions in CI can be compared for each of the three FM perturbation methods.

The results of the sensitivity analysis are shown in Figure 2.8. For this subset of events, the CI when using the preferred nodal plane is 64%, and when using the secondary NP, are 63%. When the nodal plane are randomly selected for each event, the CI values are approximately normally distributed around a mean of $63 \pm 1\%$. This indicates that the choice of NP does not have a significant impact on the resulting Coulomb index when a uniform slip model is used. When the FMs are rotated by Von Mises distributed angles, the mean CI is decreased to $59 \pm 3°$. Simulating entirely random event geometries gave CI values distributed around $50 \pm 3°$, as expected for entirely randomly aligned fracture sets.

As this perturbation in fault geometry is applied, the CI distribution shifts toward that of the random focal mechanism scenario. A FM uncertainty of $\sigma = 30°$ would appear to correspond to an approximately $\pm 4\%$ uncertainty in the observed CI values. However, even when the focal mechanisms are rotated by around 30°, the positive signal observed during RP1 is still present. As shown in Catalli et al. (2013), any perturbation to the FMs appears to systematically decrease the resulting average CI. Meier et al. (2014) interpreted this result as the outcome of applying further randomness to an already uncertain, noisy FM catalogue. We see the same result here. This challenge of quantifying the effect of focal mechanism uncertainty, and the significance of the signals observed, is further discussed in section 2.4.

With injection fluids interacting with the proposed faults in this system, the effect of changing pore pressure cannot be neglected. Thus, further sensitivity analysis is conducted to examine the effect of varying Skempton's ratio β. Using the same subset of events as in the above FM analysis, stress changes are repeatedly modelled with a varying β. Values of μ' from 0 and 0.7 are used, in 0.1 increments, which corresponds to Skempton's ratio varying from $0 \leq \beta \leq 1$.

Varying Skempton's ratio appears to have a similar scale of effect on the CI as applying rotations to the event geometries (Figure 2.9). CI changes from 64% to 56%, as β varies from 0 to 1, simulating an entirely unsaturated to saturated medium. Note that when $\beta > 0.4$, CI decreases at a more rapid rate than when $0 < \beta < 0.4$. When looking at the values of the individual event ΔCFS, changing β generally acted to change the magnitude, but infrequently changed the sign – only 14% of receivers changed sign across the whole range of β. This minority are responsible for the change in CI as measured for the population. The sign of all receivers in this sample with $|\Delta\text{CFS}| > 0.05$ MPa remained constant from one extreme β to the other. This indicates that if injection fluids are interacting with the faults near the injection points (increasing β from 0.4) the value of the CI may decrease up to $\sim 4\%$. This would weaken the positive signal observed during the first reactivation period.

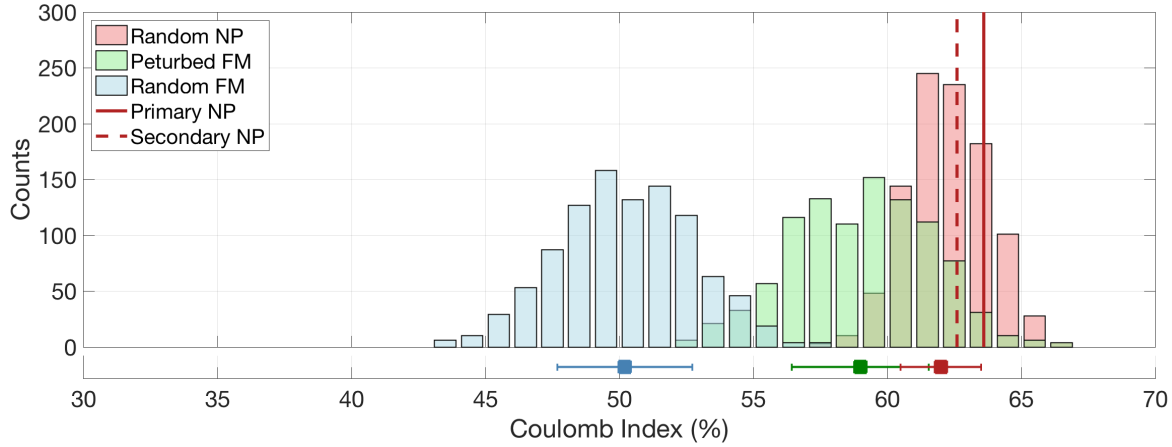

Figure 2.8: Coulomb index distributions for the subset of events used to investigate the effect of FM uncertainty. The vertical lines indicate the CIs when the preferred and secondary NPs are chosen from the original FM. The red bars shows the distribution for catalogues when the NP is chosen randomly from the original FM. The green bars show the catalogues where FMs are permuted by Von Mises distributed rotation angles. The blue bars show the catalogues with randomly oriented FMs. The horizontal lines show the standard deviations of the distributions, with squares indicating the mean CI.

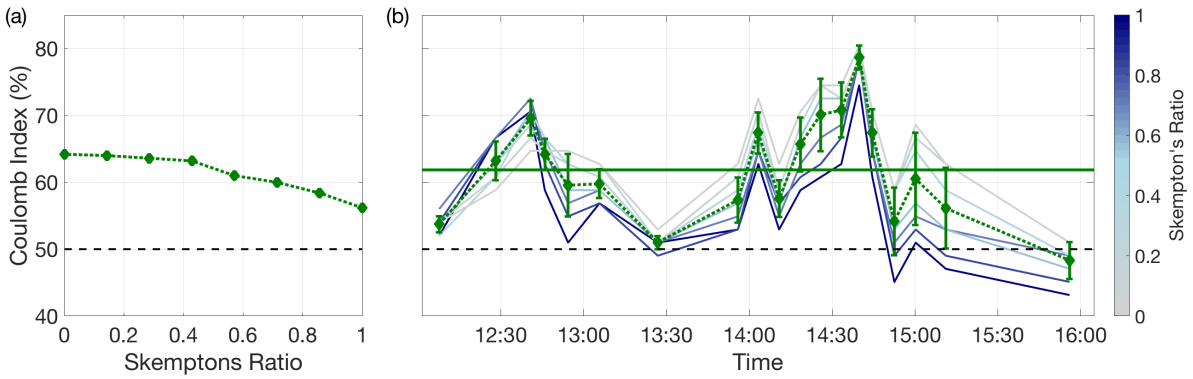

Figure 2.9: The CI change for the first 500 events in the first activation period, with a varying value of Skempton's ratio β. **(a)** The CI-β relationship for all the of events in the sample. **(b)** The temporal change in CI, calculated using moving windows, each containing 50 events. The grey-scale lines show the values of CI for the varying β values, whilst the green triangles show the mean CI for that time. The error bars give the standard deviation. The green dashed line shows the mean CI for the entire sample of events.

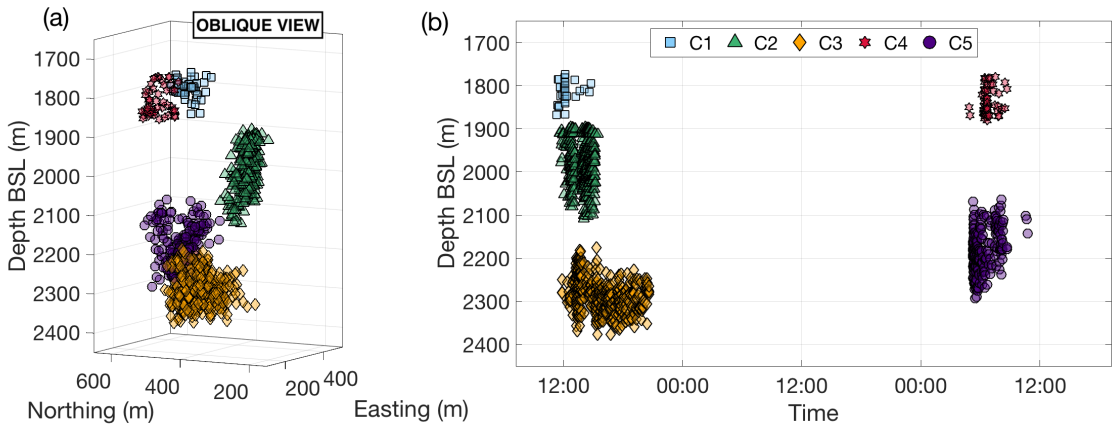

Figure 2.10: **(a)** Locations of the five clusters determined by the DBSCAN algorithm. **(b)** Temporal distribution of the clusters.

2.3.4 Cluster Stress Budget

To investigate the effect of tight clustering on the elastic stress change budget, the DBSCAN algorithm (Ester et al., 1996) is used again to identify clusters within the event population. Whereas in section 2.3.1 we used only spatial dimensions to initially identify fault reactivation, we now incorporate time as an additional dimension for the clustering analysis. A scaling factor of $c = 250$ ms^{-1} is applied to the time dimension. This value is found to best separate the clusters in the time domain. Following the method of Daszykowski et al. (2001), an optimal neighbourhood distance is calculated using the sorted k-distance approach, giving a value of 35 m. The resulting clusters are shown in Figure 2.10.

We calculate the stress changes in the same manner as section 2.3.1, however, for each receiver, only sources from within the same cluster are used. This will allow for the full cumulative stress change to be compared to the change when only the deformation from within each cluster is considered. These resulting stress change value is termed the "intra-cluster" stress change.

Figure 2.11 shows that, for the majority of events (89%), the intra-cluster ΔCFS makes up effectively all of the stress change received. This indicates the importance of tight clustering for microseismic stress transfer, as even when sources are excluded within one source length, the stress change from within the cluster contributes the majority of the ΔCFS . The relationship in Figure 2.11 also shows that when ΔCFS is significant (i.e., greater than ± 0.1 MPa), effectively all of the stress change results from within the cluster. One would expect this to be true for clusters 1 and 2, where few events outside of the cluster preceded the seismicity, but this linear relationship is also present for cluster 5 (Figure 2.12). This cluster will have received all of the ΔCFS from all of those proceeding it, but still, the majority of the stress changes comes from within that cluster. This agrees with Vasudevan and Eaton (2011), in that for microseismic events, where the spacial propagation of stress is not laterally extensive, the majority of the stress change comes

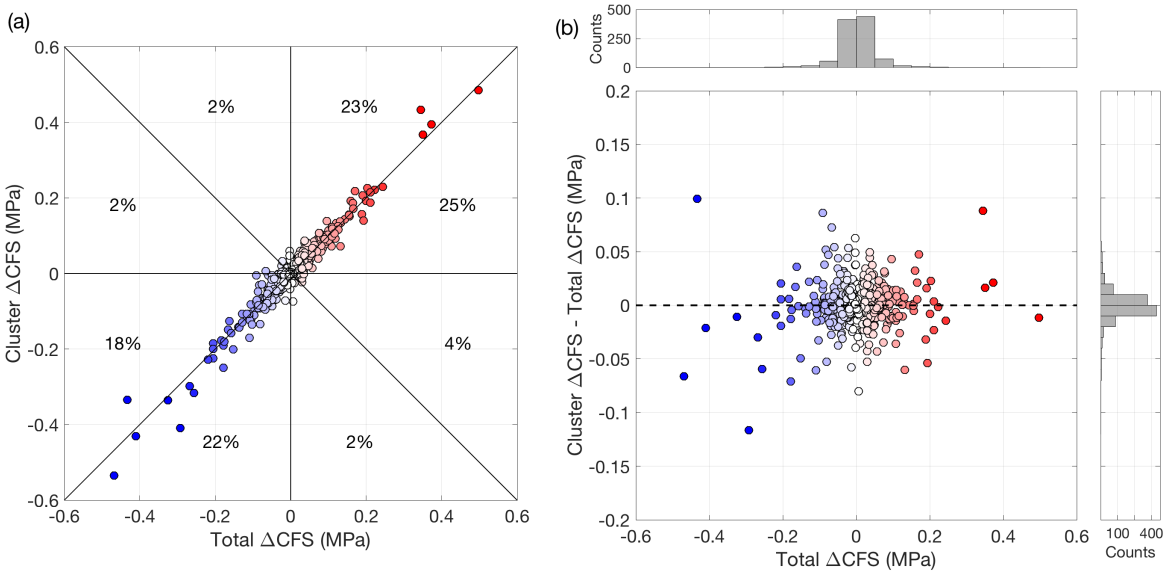

Figure 2.11: **(a)** The relationship between the total ΔCFS from all possible sources, and the stress change due to sources from only within the same cluster. Percentages break down the proportions of events (865 within clusters of a possible 1064) in each octant. For example, the NNE octant indicates 22% of events have a positive cluster ΔCFS equal to or greater than the total ΔCFS experienced from all possible sources. **(b)** The difference in intra-cluster stress change and total ΔCFS. It is clear that for the vast majority of events (97%), intra-cluster ΔCFS makes up the majority of the stress change received. The absolute difference exceeds ± 0.05 MPa for only 27 of 865 events.

from nearby sources.

2.3.5 Fault Slip Potential

The code *FaultSlipPotential* (Walsh et al., 2017) is used to conduct a probabilistic geomechanical analysis, using the methodology described in Walsh and Zoback (2016). The stress gradients, S_{Hmax} azimuth, fault geometries, and the friction coefficient are used as inputs, as well as their associated uncertainties. The principal stress magnitudes and uncertainties used are those given in section 2.2.2, along with a μ of 0.7 ± 0.1, and a $\pm 10^{\circ}$ uncertainty assumed for both the strike and dip of the two fault planes. These parameters are randomly sampled 1000 times within their uncertainties, and a resulting critical pore pressure required to initiate failure, P_C, is then calculated using Coulomb's law:

$$P_C = \sigma_n - |\tau|/\mu \quad . \tag{2.3}$$

For the range of P_C perturbations, a cumulative probability of exceeding the Mohr-Coulomb failure criterion is then found. This probability is known as the fault slip potential. *FaultSlip-Potential* uses uniform distributions from which to sample the input parameters. This will give

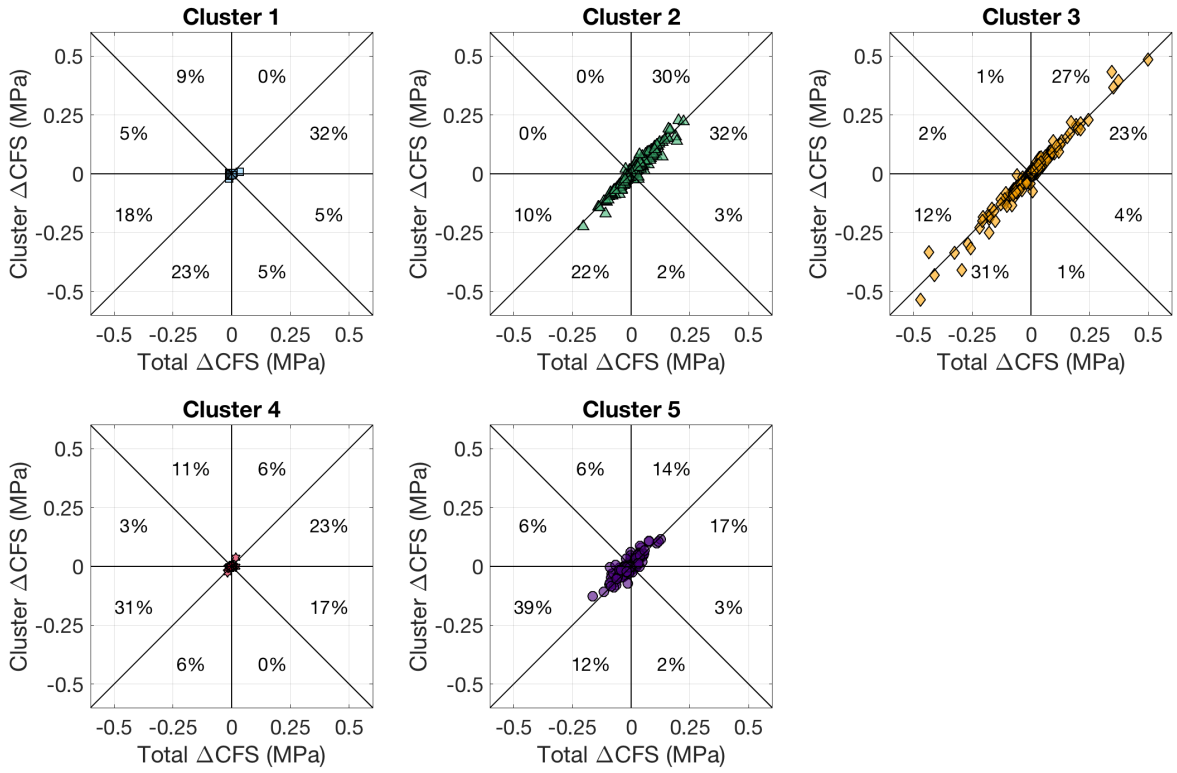

Figure 2.12: Cluster stress change against total stress change for each of the five clusters. Percentages break down the proportions of events in each octant, as in Figure 2.11a. Clusters 1 and 4 receive very little stress change, as they are low magnitude, broadly clustered events associated with the fracturing.

a narrower distribution in the resulting P_C values, than would be found when using standard errors.

We use equation 2.3 to examine the in situ stress field with respect to the fault orientations (shown in Figure 2.4), as delineated by the microseismicity. Figure 2.13 shows the computed σ_n, τ, and P_C as a function of fault strike and dip. Optimally oriented faults, where P_C is at its minimum value of 14.5 MPa, have strikes of 28°, 81°, 208°, and 261°. These are relatively close to the strikes of the planar structures: 250° and 60°.

Figure 2.14, shows the result of the probabilistic analysis using *FaultSlipPotential*, showing the cumulative density function for the probability of slip given some pore pressure perturbation ΔP for F1 and F2. The probability of failure does not exceed 50% until the pore pressure change is in excess of 15 MPa for both of the fault planes. F1 is marginally more optimally aligned for failure, with F2 requiring an additional ~ 1 MPa of pore pressure change to give the same probability of failure. This scale of pore pressure change (~ 10 MPa) is similar to that found by Chiaramonte et al. (2007), for a trap bounding fault in north-central North America. Across the range of input values, the S_{Hmin} and in situ pore pressure uncertainties had the largest effect on

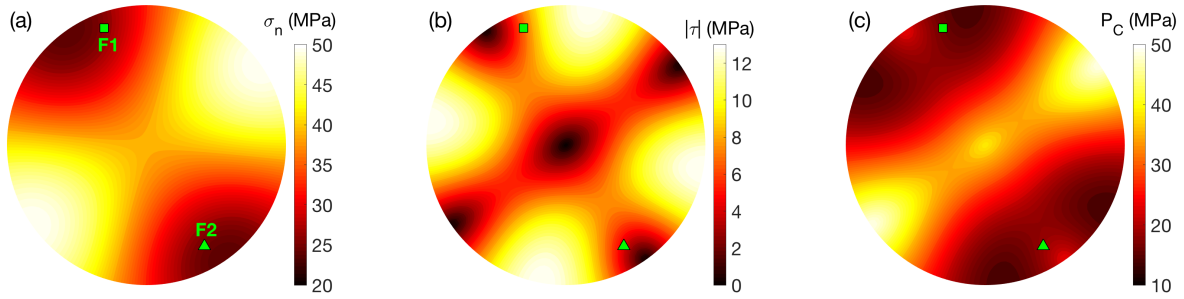

Figure 2.13: Modelled HRB in situ stresses resolved onto fault planes, assuming a coefficient of friction of 0.7. **(a)** Effective normal stress. **(b)** Shear stress. **(c)** Critical pore pressure required to reach the Mohr failure criterion. The resolved stresses are contoured at the polar projection of the normal to the fault plane, with polar angle representing the fault-normal trend, and radial angle representing the fault-normal plunge. The orientations of the two faults F1 and F2 are shown respectively by the square and the triangle, both close to the minimum P_C values.

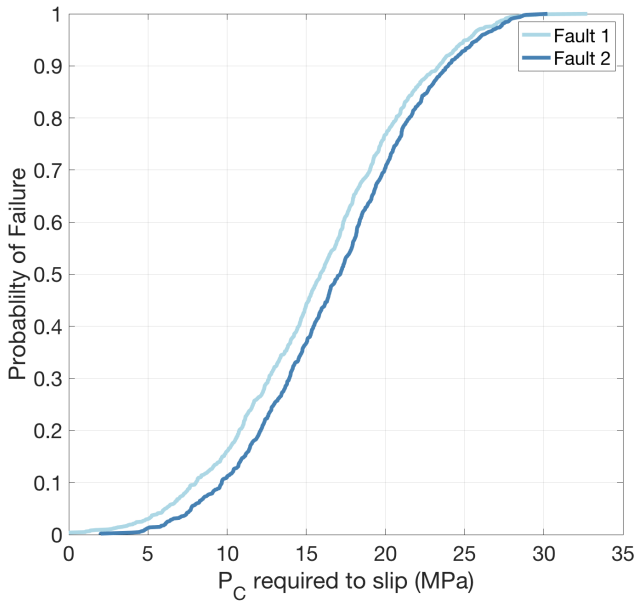

Figure 2.14: Fault slip potential probability curves for the two modelled faults.

the ΔP to slip for both faults. Significantly reducing S_{Hmin} will have the effect of shifting the Mohr circle towards the failure criterion. Increasing the in situ pore pressure will act to decrease the effective stresses acting to clamp the fault.

A ΔP required to fail of approximately 15 MPa would indicate that the two hypothesised faults here are not critically stressed within their stress field. A large pore pressure increase would be required for the Mohr-Coulomb failure criterion to be reached. With the average observed elastic stress increase on the fault planes being approximately 0.1 MPa, these planes would require two orders of magnitude larger pore pressure changes to initiate failure. Even at the extremes of

the stress model and fault parameter uncertainty, the required stress change for failure is an order of magnitude above the average elastic ΔCFS. This suggests that the interaction with high pressure injection fluids was likely to have been responsible for the activity in both reactivation periods, and elastic stress transfer did not play a major role in the fault activation. As discussed in section 2.2.2, this analysis does not take into account the potential for overpressure in the formation, other than in the uncertainty applied to the in situ P ($\pm$7 MPa). During injection downhole pressures were measured to be consistently greater than 50 MPa, giving a differential pressure between that and the in situ pore pressure of over 20 MPa. Given the top of F1 is $\sim$ 50 m from the nearest perforation, and the fact that fractures are likely to extend at least that distance, it is plausible that the pressurised fluid interacted with the pre-existing structure and exceeded this failure criterion.

This analysis however uses a simple model of fault stability, and does not take into account the possibility of frictional asperities on the fault surface. These areas of weakness would allow the failure threshold to be reached on a small fraction of the fault surface and enable failure to propagate outwards. This type of simple modelling also does not explain the spatiotemporal clustering observed here – small events near the well start the sequence, but immediately after and 400 m below, larger magnitude events occur at the base of the faults, with very little intermediate seismicity. This would also suggest a rapid transport of fluid along the faults, and then subsequent failure back up along the plane of weakness. This type of behaviour has been observed in EGS-induced microseismic sequences (Majer et al., 2007), and is described as a potential factor in the maximum observed magnitude of the injection induced seismicity (Shapiro et al., 2011). More complex fluid and fracture modelling is required to fully examine the pressure changes occurring within the fault system, however this slip potential model does indicate that these faults are not optimally oriented for failure in the regional stress state.

2.4 Discussion

2.4.1 Elastic Stress Modelling

The positive signal we observe in the first period of activity is a CI of around 60%, as well as small periods wherein CI reached around 70%. Ascribing significance to this signal, a slightly higher proportion of events receiving positive ΔCFS, is difficult, especially given the uncertainties in the FMs and the assumptions inherent in modelling elastic stress change. We see similar magnitudes of stress changes as previous studies (e.g. Schoenball et al., 2012), however our results diverge from studies which find CIs in excess of 75%, implying that elastic stress transfer played a more significant role during injection induced seismicity (e.g. Catalli et al., 2013; Pennington and Chen, 2017). We have also tested the reliability of this signal by conducting a separate analysis, wherein individual receiver geometry is bypassed, and stress changes are instead mapped onto the visible fault planes. Whilst the measured quantities are different, the same pattern emerges

– a positive signal in the first reactivation period, and a generally negative signal in the second. Testing the sensitivity to particular uncertainties conventionally, using the method employed in Catalli et al. (2013), we observe a decrease in CI by both the focal mechanism (~ 4%) and frictional uncertainty (~ 4%), which weaken the positive signal observed. However, this approach may not be a reflection of the effect of FM uncertainty on the resulting CI. As described in Meier et al. (2014), adding random noise to the FMs by applying a perturbation just adds a smearing effect, always resulting in a CI closer to 50%, no matter how significant the original signal. This method however, does show that even when FMs are rotated by, on average, a very significant amount (30°), the signal is still present. This indicates that despite FM uncertainty, the events in the first reactivation period are spatially distributed in such a way that elastic stress changes still modestly promote failure.

The inherent assumptions used and lack of data must also be considered, and their effect on the accuracy of our results. Both observational precision, and lack of data, constrain the accuracy of our modelling. Uncertainties in both the FMs and locations were not provided by the processing company, and MTs were not computed for a number of events in the original catalogues in this study due to low signal-to-noise ratios. That said, these "missing" events generally have considerably lower magnitudes ($M_W < -1.5$) than the majority of events used here (those with MTs), so the effect on the stress change from these sources is expected to be small. Their contribution to the stress changes will therefore be minimal and is assumed to not have a significant affect on the results.

The uniform slip model used, which gives rise to a number of the limitations described above (NP ambiguity, source exclusion within 1 source length), has a dramatic effect on the accuracy of our results, as it does for all Coulomb stress modelling. A fuller treatment of modelling slip distributions, however, would have been impractical in this case, with up to ~ 1400 sources being modelled for later receivers. Also, the nature of slip distribution on the fault plane is highly uncertain in itself. Ascribing some assumed rupture behaviour in the hope of more accurately reflecting the near-field stress change could in fact produce significantly more uncertain ΔCFS values within one source length.

Thus, we followed the methodology of previous works (such as Meier et al., 2014), where slip is treated as uniform, and near-field sources are ignored. This method obviously results in an lower estimate for the resulting ΔCFS magnitude, but also removes the significant effect of the uncertainty in the stress drop, slip model, and to a certain extent source location (Schoenball et al., 2012; Steacy et al., 2004). These parameters, each of which have significant uncertainties, mostly effect the near-field stress change, due to the r^{-3} power law describing the decay of ΔCFS. The resulting values can thus be considered a more accurate reflection of the triggering effect of elastic stress change. One could imagine that this exclusion step is amplified in this study in particular, where events are relatively tightly clustered. However, as shown in Figure 2.12, the ΔCFS from within clusters still makes up a significant proportion of the stress change received,

and thus effect from sources within a cluster is not negated using this method.

2.4.2 Focal Mechanism Sensitivity Analysis

Comparing our permuted focal mechanism catalogues to those with entirely random FMs (Figure 2.8) also may not provide an accurate measure of significance when considering a possible null hypothesis, as described by Meier et al. (2014). A more suitable method could involve comparing to the ΔCFS computed for events not thought to be triggered by elastic stress changes, and thus not associated with the fault activation. This could include populations near to the wells, assumed to be caused by tensile fracturing. For these events, fluid effects are expected to dominate and no considerable elastic triggering, i.e. the CI for this population would be around 50%. However, the accuracy of the focal mechanisms for these events would be even more questionable, with event size generally around 1 to 2 magnitudes smaller than the fault reactivation events. We already have considered a relatively pessimistic uncertainty for the FMs (30°), however this would most likely increase dramatically for those events where the signal-to-noise ratio is even smaller. Another consideration is the alignment of failure planes for tensile fracturing events. These events will be generally well aligned parallel to the maximum stress direction, and so their relative alignments will deviate from that a zone of random oriented fractures. Thus, due to the spatial pattern of the stress change, they will predominantly receive positive stress change, and static stress transfer will appear to play a significant role.

2.4.3 Fault Orientations

The geometry of the mapped faults and an estimate of the in situ stress regime indicate that the activity seen here was initiated by the high-pressure injection near the failure plane, as faults require in excess of 10 MPa of pore pressure change to reach the Mohr failure criterion. This is in contrast to the stress environment and fault system found in central the US, where waste-water injection has stimulated high magnitude (> 3 M_W) events regularly in recent years (Alt and Zoback, 2017). Both Walsh and Zoback (2016) and Schoenball et al. (2018) found, using the QRA methods employed here, that multiple fault systems mapped in north-central Oklahoma are preferentially aligned for failure, with some faults requiring only ~ 2 MPa of ΔP to reach a failure potential of 0.5. In our case, the required pore pressure changes are approximately six times greater.

This could provide a possible explanation as to the difference in significance of elastic ΔCFS seen in this study compared to other sites (e.g. Catalli et al., 2013; Pennington and Chen, 2017; Sumy et al., 2014). If the faults are already close to being critically stressed, then the small amounts of stress change associated with static elastic stress transfer can play a significant role. If the faults are not close to failure, then larger stress changes are required. In such cases the stress changes associated with static elastic stress transfer are not large enough, and instead the

very high pressures associated with fluids dominate the activation of faults, meaning that static stress transfer does not play a significant role.

2.5 Conclusions

For this case of injection induced fault activation, elastic stress transfer modelling suggests that during the first period of seismicity, deformation on faults and fractures may have weakly promoted further failure. However during the second period, these stress changes inhibited failure. This result is insensitive to the choice of event geometry (from the two nodal plane solutions of the MT), due to the symmetrical nature of the stress change pattern that results from a uniform slip model. Applying Von Mises distributed uncertainties to the focal mechanisms of the events appears to diminish, but does not completely eliminate, the observed CI signals. However, this is due to the nature of measuring the FM sensitivity on a population of events with already uncertain FMs, which acts to consistently shift the CI towards 50%. Variability in the Skempton's ratio is also found to diminish, but not completely eliminate, the positive CI signal. The scale to which the resulting CI distributions shift whilst varying the model parameters highlights the importance of properly incorporating the various uncertainties that affect ΔCFS calculations.

Intra-cluster stress transfer is found to be significant in this case, meaning that the elastic stress change budget is chiefly derived from events in the same cluster. This is expected for tightly clustered microseismic events, because of the small area and (size of) slip on the fault plane, resulting in spatially contained elastic stresses. Thus, events only receive significant ΔCFS when they within ~ 100 m from the source.

The weak contribution of elastic stress transfer to the failure can be interpreted with respect to the in situ stresses acting on the hypothesised fault structures. Using at-depth measurements of the regional principal stresses, the probability of slip for a given pore pressure change on the two planar structures is examined using a quantitative risk assessment technique. We find that for both faults, the pore pressure changes required to reach the failure criterion is around 15 MPa, far in excess of the reliable values of elastic stress change. This supports that, in this case, the failure was stimulated by the presence of highly pressurised fluids in the system. These faults are not critically stressed, unlike those found in the central US, which have been found to require only a few MPa of pore pressure to reach the slip criterion (Schoenball et al., 2018; Walsh and Zoback, 2016). This could provide an explanation for the difference between the ΔCFS behaviour found here and studies which concluded that this mechanism played a more significant role (Catalli et al., 2013; Pennington and Chen, 2017).

CHAPTER 3

FRACTURE OPENING STRESS TRANSFER CONTROLLING THE SPATIAL DISTRIBUTION OF FAULT ACTIVATION

The contents of the following chapter has been published as *Stress transfer from opening hydraulic fractures controls the distribution of induced seismicity* by Tom Kettlety, James P. Verdon, Maximilian J. Werner, and J. Michael Kendall in the Journal of Geophysical Research: Solid Earth, issue 125, in 2020 (Kettlety et al., 2020). I conducted all modelling and analysis in this work, and produced all figures presented here. The manuscript was written by me, and edited by James Verdon. Maximilian Werner provided further editing, and Michael Kendall contributed to the overall direction of the work that lead to this publication. Small annotations have been added to the figures, and thus they differ slightly than the published versions.

In chapter 2, we showed that interevent stress transfer could only be weakly contributing to the continuation of seismicity in that case of HF-IS. The next chapter uses a newly acquired microseismic dataset and similar elastostatic modelling methods to examine the contribution of opening hydraulic fractures in controlling the spatial distribution of fault activation.

Understanding the dominant physical processes that cause fault reactivation due to fluid injection is vital to develop strategies to avoid and mitigate injection-induced seismicity (IIS). IIS is a risk for several industries, including hydraulic fracturing, geothermal stimulation, oilfield waste disposal and carbon capture and storage, with hydraulic fracturing having been associated with some of the highest magnitude induced earthquakes ($M > 5$). As such, strict regulatory schemes have been implemented globally to limit the felt seismicity associated with operations. In the UK, a very strict "traffic light" system is currently in place. These procedures were employed several times during injection at the PNR-1z well at Preston New Road, Lancashire, UK from October to December 2018. As injection proceeded, it became apparent to the operator that stages were interacting with a seismogenic planar structure, interpreted as a fault zone, with several $M_L > 0.5$ events occurring. Microseismicity was clustered along this planar structure in a fashion that could not readily be explained through pore pressure diffusion or hydraulic fracture growth. Instead, we investigate the role of static elastic stress transfer created by the tensile opening of hydraulic fractures. We find that the spatial distributions of microseismicity are strongly correlated with areas that receive positive Mohr-Coulomb stress changes from the tensile fracture opening, while areas that receive negative Mohr-Coulomb stress change are quiescent. We conclude that the stressing due to tensile hydraulic fracture opening plays a significant role in controlling the spatiotemporal distribution of induced seismicity.

3.1 Introduction

Felt or damaging earthquakes have been induced or triggered by subsurface fluid injection related to a number of industrial activities. These include enhanced geothermal systems (EGS) at Basel (Deichmann and Giardini, 2009) and Pohang (Grigoli et al., 2018; Kim et al., 2018), waste-water injection in the central United States (Keranen et al., 2013; Walsh and Zoback, 2015), carbon capture and storage at In Sala, Algeria (Stork et al., 2015), and hydraulic fracturing in central and western Canada (Atkinson et al., 2016; Bao and Eaton, 2016; Kao et al., 2018), the central United States (Holland, 2013; Skoumal et al., 2018), and the Sichuan Basin, China (Lei et al., 2017, 2019; Meng et al., 2019). However, while the links between fluid injection and seismicity are clear, the underlying physical processes by which injection causes fault reactivation are not yet well established. This matters because developing this understanding is crucial if we are to develop methods to prevent or mitigate injection-induced seismicity (IIS). In a broad sense, the mechanism of most IIS is well established: fluid injection leads to an increase in pore-pressure, decreasing the normal stress acting on critically stressed faults, and bringing them closer to failure (Raleigh et al., 1976). On large spatial scales in relatively permeable formations (as in the case of waste-water injection), pore pressure increases transmitted over large distances by diffusion would appear to be the dominant activation mechanism (Goebel et al., 2017a; Goebel and Brodsky, 2018). In low permeability reservoirs and on smaller scales (on the order of hundreds of

metres, within hours of injection), other mechanisms can dominate: the poroelastic expansion of the rock frame; direct pressure from the injected fluids; elastic stress changes from seismic events or fracture opening; and aseismic creep (Bhattacharya and Viesca, 2019; Eyre et al., 2019; Kettlety et al., 2019).

Elastic stress change models have been used for decades to determine the triggering mechanism of tectonic earthquakes (Harris, 1998; Meier et al., 2014; Steacy et al., 2005; Stein, 1999; Wedmore et al., 2017), illuminating the sometimes unexpected spatiotemporal patterns which occur during seismic sequences. These models are regularly applied in physics-based earthquake hazard forecasts, using the observed slip on faults to model the spatial distribution of subsequent, potentially damaging, earthquakes (Cattania et al., 2018; Mancini et al., 2019). Elastostatic modelling has also been applied with tensile sources, such as the analysis by Green et al. (2015) of a seismic sequence associated with dyke intrusion in Iceland. The areas receiving positive elastic Coulomb stress changes that resulted from the opening of the dyke were well correlated with the locations of seismic events throughout the sequence. As the sequence progressed and the dyke's orientation changed, earthquake rates were suppressed in areas experiencing negative Coulomb stress changes. In hydraulic fracturing, the tensile opening of hydraulic fractures produces perturbations to the stress state in a similar manner. Spatiotemporal observations in microseismicity that would be difficult to explain through any other mechanism could also be explained through the elastic stress changes that result from the tensile opening of fractures.

Such observations were made during hydraulic fracturing at the Preston New Road PNR-1z shale gas well in Lancashire, UK in 2018 (described in Clarke et al., 2019a). This was the first onshore well in the UK to be stimulated since a government review of this technique (Mair et al., 2012). It was therefore the subject of extensive scrutiny by the public and by national media, and was extensively monitored both by the operator and by independently-funded organisations (Clarke et al., 2019a).

Hydraulic fracturing at PNR-1z was subject to a Traffic Light Scheme (TLS). This is a procedure developed to avoid felt seismicity ($M_L > 1.5$) by taking mitigating actions (e.g., reducing injection rates, pausing injection, or skipping injection stages) when induced events of particular threshold magnitudes are observed. The "red-light" threshold in the UK is set at $M_L = 0.5$, exceedance of which requires an 18-hour pause in operations. Microseismicity during injection at PNR-1z exceeded this limit on several occasions. During operations, the operator used a statistical model to forecast and manage induced seismicity (Clarke et al., 2019a). One felt event did occur, with $M_L = 1.5$ on December 11 2018. Interestingly, the observed spatiotemporal distribution of microseismicity is not easily explained by the growth of hydraulic fractures or a diffusive pore pressure increase. Thus, in this study we examine the elastic stress changes in the vicinity of the well that occurred during the opening of hydraulic fractures and the potential impact these stress changes could have on the observed microseismicity. This is distinct from a poroelastic model, which would calculate the change to the stress state that results from increasing pore

pressure deforming the rock mass itself, a continuously distributed inflation of the matrix due to increased pore fluid pressure. Here, we look at the propagation of elastic stress from discrete opening of finite model fractures.

Slip on faults, and tensile opening of fractures, will generate elastic stress changes in the surrounding rock. These changes can be resolved into changes in the normal stress σ_n (defined here as positive extensive) and shear stress τ acting on nearby structures, and combined to compute the Coulomb failure stress change ΔCFS:

$$\Delta CFS = \Delta\tau + \mu' \Delta\sigma_n \quad , \tag{3.1}$$

where μ' is the effective coefficient of friction.

Modelling of ΔCFS is a simple and effective tool for examining the effects of stress on surrounding faults or fractures – a positive value indicates that stress has changed in such a way as to promote failure, whilst a negative value means the stress change acts to inhibit failure. However, it is difficult to robustly model and interpret elastic stress changes. Defining a significance threshold for the effect on a population of events (Meier et al., 2014), quantifying model uncertainties (Catalli et al., 2013; Kettlety et al., 2019), and untangling the effects of other failure mechanisms, such as dynamic triggering or poroelasticity, all provide a significant challenge. Nonetheless, elastostatic stress modelling has repeatedly provided a robust explanation for the spatial distribution of earthquake sequences (Cattania et al., 2018; Meier et al., 2014; Steacy et al., 2005; Wedmore et al., 2017), and when applied carefully, can be an effective method of studying the triggering of induced seismicity (Catalli et al., 2013; Kettlety et al., 2019; Pennington and Chen, 2017; Schoenball et al., 2012; Sumy et al., 2014).

In this study, we examine the stress changes that result from the tensile opening of hydraulic fractures, modelled as displacement on finite patches within an elastic medium, and their effect on the distribution of microseismicity observed during the Preston New Road PNR-1z hydraulic fracturing operation in 2018 in the UK. We develop a stochastic, Monte-Carlo procedure for generating model fractures as a set of pure tensile opening discrete patches, and calculate the resulting cumulative elastic stress changes from each fracturing stage. We compare the spatial patterns in ΔCFS with respect to the spatiotemporal evolution of the microseismicity. We show the areas of positive ΔCFS from prior and current stages correlate well with the hypocentres of the observed microseismicity, and that areas where seismicity was unexpectedly quiescent received predominantly negative ΔCFS, suggesting areas are being clamped by the opening of fractures.

3.2 Hydraulic fracturing at Preston New Road, UK

In October 2018, Cuadrilla Resources Ltd. began hydraulic fracturing operations at the Preston New Road PNR-1z well in Lancashire, United Kingdom. The operation targeted the upper section of the Bowland shale, a 1.2 km thick Carboniferous natural gas-bearing formation (Andrews,

2013; Clarke et al., 2018). Hydraulic fracturing was monitored by a microseismic array of 24 3-component geophones housed in the adjacent well (PNR-2) (Clarke et al., 2019a), shown in Figure 3.2. This was combined with a surface array, composed of the local UKArray (Baptie, 2018) broadband stations operated by the British Geological Survey (BGS), supplemented by a mix of 8 broadband and 3-component short period instruments deployed by the operator as part of the monitoring program. The monitoring array, both surface and downhole, is detailed in Clarke et al. (2019a).

Over the course of 3 months, 17 stages were stimulated, with a planned injection programme of 400 m^3 of slickwater fluid and 50 tons of proppant per stage. Strict seismicity constraints – the TLS that is currently in place in the UK (Green et al., 2012) – restricted operations during many of the worked stages, with any event detected during pumping above M_L 0.5 requiring a pause in injection for a minimum of 18 hours. More than 38,000 microseismic events were detected, with magnitudes ranging from -3.1 to 1.6 (Figure 3.1). Data were processed in real-time by Schlumberger Ltd (SLB), providing event locations, M_W magnitudes and estimated source parameters. Estimates of location errors are around 10 to 50 m, typical of downhole microseismic monitoring (e.g. Jones et al., 2010; Verdon et al., 2017; Viegas et al., 2012). Focal mechanisms were independently calculated by both SLB and the BGS for 41 of the highest magnitude events using the surface station polarity data. These are also shown in Figure 3.1.

As successive stages were injected, it became apparent that the operations were interacting with pre-existing seismogenic structures (Clarke et al., 2019a). Seismicity was repeatedly occurring with magnitudes approaching or exceeding the red-light threshold. This resulted in the operator skipping stages, moving further toward the heel of the well to avoid repeatedly activating these features. In late October 2018, roughly 2 weeks after the start of operations, six events occurred that exceeded the TLS thresholds. After this, operations were paused for approximately one month, during which low levels of microseismicity continued to occur. The highest magnitude events, as well as the events during this hiatus, were predominantly located around a particular structure, a sub-vertical planar feature, striking to the NE of the injection well (Figure 3.1). As detailed in Clarke et al. (2019a), we take a sample of events to calculate the orientation of this feature: the largest ($M_W > 0$) events that took place after it was first encountered (from Stage 18); and all events that continued to occur in this zone during the month hiatus in operations. It was during this time that it became very clear that a more seismogenic planar feature was present, as the areas around each of the worked stages became quiescent except in vicinity of this feature. A least-squares planar fit to the hypocentres of these events gives its orientation: a strike ϕ of 230° and a dip δ of 70°.

The majority of the focal mechanisms also have a similar orientation as this feature, showing left-lateral strike-slip motion (see Figure 3.1 and Figure 6a of Clarke et al. (2019a)). This feature appears to be relatively well oriented within the in situ stress state in the region. Given the S_{Hmax} orientation ϕ_H of approximately 170°, and a strike-slip stress regime (Clarke et al., 2014;

Fellgett et al., 2017), faults striking to the north-east will also produce left-lateral strike slip motion (rake λ of 0°).

The location of this feature does not correlate with any discontinuities observed in the 3D reflection seismic that was acquired at this site (Clarke et al., 2019b). This may be because of its strike-slip nature, meaning there is little vertical offset to be imaged in the reflection seismic. This seismogenic feature could be described as a "fault", or potentially as a zone of pre-existing fractures. Despite the feature being around 500 m in strike, and 200 m in dip, the largest event during the monitoring had a magnitude of $M_L = 1.5$. The basic formulation of seismic moment release for a circular fault of radius r_f, shear modulus G, and slip d is given by Equation 3.2 (Aki and Richard, 2002).

$$M_0 = G d \pi r^2 \tag{3.2}$$

A $M = 1.5$ event roughly corresponds to a displacement of ~ 1 mm over a rupture length of less than 100 m. Thus, seismic failure on this feature only ever occurred on a small section of the suspected fault's area. Despite many small events occurring along its length, there is no clear evidence distinguishing if this is a single continuous fault or a dense zone of fractures. Clarke et al. (2019a) term this feature "north-east fault 1" (NEF-1). Thorough out this paper, we will refer to it as the "fault zone" adjacent to the wells.

Location uncertainties are naturally a concern when interpreting structure from microseismic data. In this case, with a single, mostly vertical, downhole array (as shown in Figure 3.2), there is the potential for systematic bias or offsets, due to its limited azimuthal coverage. However, the 3D hodogram analysis, as well as the beam-forming inversion used in the location calculation should provide more accurate back-azimuths and polarity data than simpler methods (Jones et al., 2010; Verdon et al., 2017). The locations found were also relatively similar to those independently calculated by the BGS using the surface stations. These locations are shown in Figure 3.2. Broad scale structure is generally the same, though naturally the precision of the surface-derived locations is significantly lower than that from the downhole. The velocity model was calibrated from the extensive 3D seismic data, and was refined several times during the stimulation of the well – when operations on the sliding sleeves occurred, the known times and locations were used to check its calibration. As these more involved methods of location inversion and velocity model refinement were used, we conclude the locations provided are adequate enough to interpret the spatial distribution of seismicity around the well.

The structures interpreted in the microseismic, e.g. the northward propagation of events, would also be difficult to systematically shift given some velocity model or station orientation error. Rotating the event clusters around the axis of the monitoring well, in order to shift the events in the centre of the well, would shift events at the toe of the well to be propagating only south of the well. The offset between the injection well and the heel stage events (Figure 3.3f), could be attributed to the velocity model being incorrect. However, any kind of systematic shift in the velocity model, which could counteract the separation of heel stage events far from the

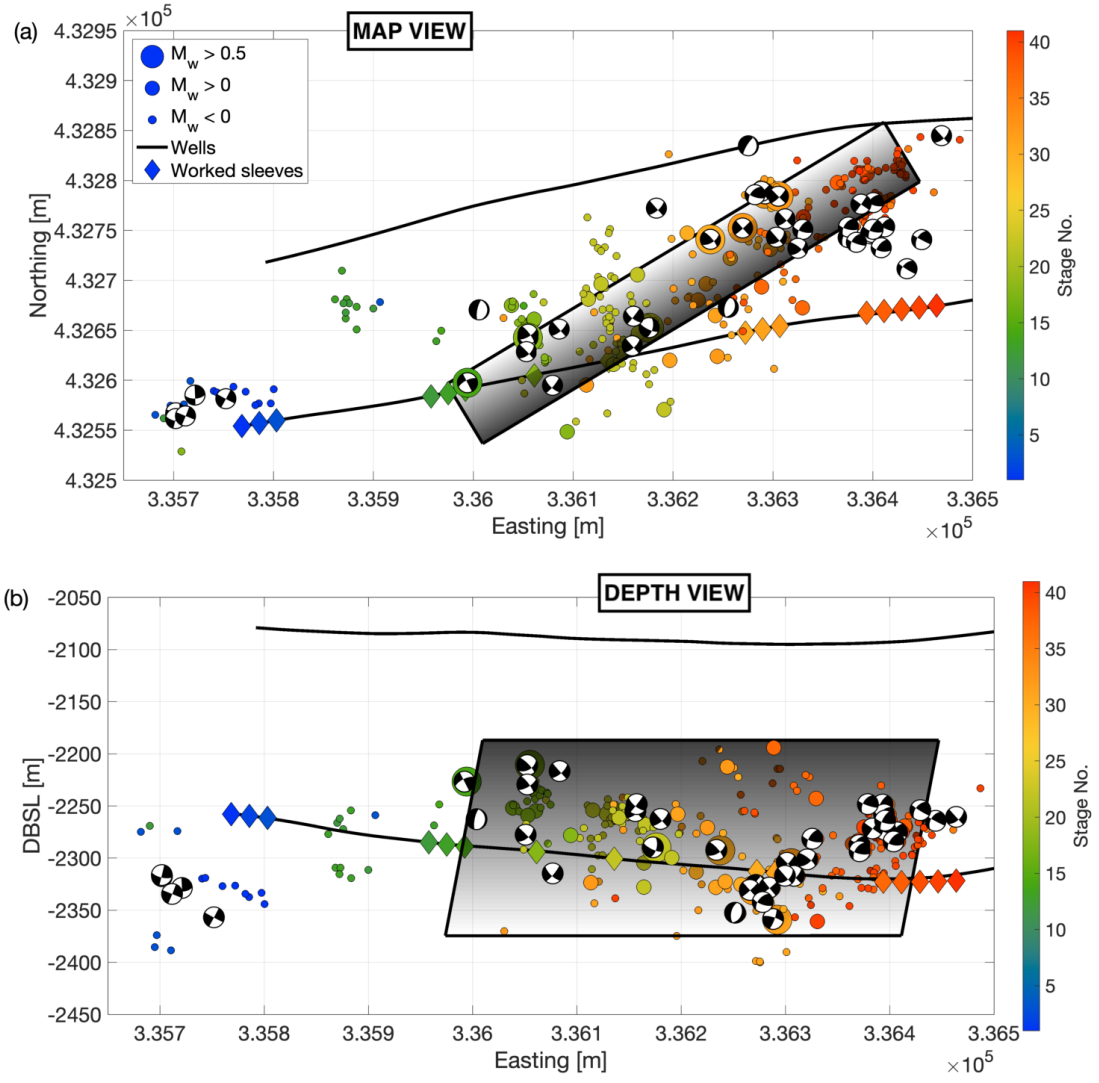

Figure 3.1: Hypocentres of events recorded by the downhole monitoring array during hydraulic fracturing operations at the Preston New Road PNR-1z well with magnitudes greater than −0.5 and a signal-to-noise ratio greater than 5. Events are shown as circles, with marker sizes indicating the magnitude range, whilst colour shows the injection stage with which the event time overlapped. Diamonds denote the centre of the sleeve position on the well, and are also coloured by stage. The grey plane denotes the inferred seismogenic "fault zone", with a strike of 230° and a dip of 70°. This was found from the least squares fit to events with M_W above 0 and the events which continued to occur during the month hiatus in operations (see Clarke et al., 2019a, for a detailed discussion). Lower hemisphere focal mechanisms are shown as black and white beach-balls, derived from the surface station polarity data (Clarke et al., 2019a).

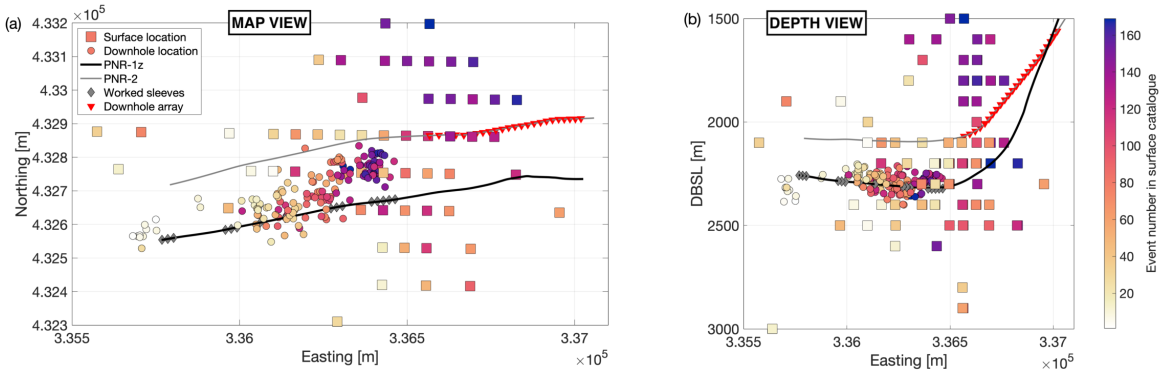

Figure 3.2: Hypocentres for 172 events located using data from both the surface and downhole arrays, and the same velocity model, allowing for comparison of the two locations. These surface-derived locations were calculated by the British Geological Survey (Baptie, 2019). Naturally, the lateral and depth resolution is far lower than that of the downhole locations. However, these surface locations generally mirror the spatial and temporal trends seen in the downhole locations, with a bias (74%) of events north of the PNR-1z well, and events trending further NE as the heel stages are injected.

injection well, would shift the events at the middle and toe of the well even further from the injection well. Thus, it is difficult to envisage purely processing errors resulting in the structure interpreted above.

Some locations for stages greater than 38 are subject to a processing artefact produced by the fundamental 180° ambiguity when locating events with a single downhole array (e.g., Jones et al., 2010). The P-wave particle motion is used to determine the back-azimuth of the event from the monitoring array. Events could therefore be placed at mirrored positions either side of the monitoring array. Evidently, the processing contractor has placed all of the events to the south of the PNR-2 well, when in reality events will have occurred both to the north and the south. This artefact does not affect the observations presented above, as a gap between the injection well and the events will be present whether or not events are placed to the north of the monitoring well.

3.2.1 Microseismic observations in detail

In this section, we focus on some noteworthy aspects of the microseismic event locations. Event hypocentres from stages illustrating behaviour of particular interest are shown in Figure 3.3. We will describe these observations sequentially, in the order the stages were injected. Full injection stages were effectively completed in ascending order, however small scale “minifracs” were conducted on Sleeves 35 through 40 just before the start of the month-long hiatus, prior to Stages 37 through 41. Only small numbers of events were generated during these minifracs, with no particularly note-worthy behaviour.

For all stages conducted at PNR-1z, the microseismicity occurred asymmetrically, propagating

to the north of the injection well. This is unlikely to be a detection effect, as the sensitivity of the array is such that it is capable of detecting events at least 1 km from the well. However, it does not detect events south of the well even for the heel-most stages, which are within 300 m of the array This suggests that hydraulic fractures grew primarily asymmetrically in a northward direction. This could also be related to more seismically-productive, shearing type events occurring in the inferred fault zone in the area approximately 250 m north of the well. Asymmetric fracture growth has been ascribed in previous work to a gradient in the geomechanical parameters, such as a laterally heterogeneous stress field, a change in the elastic properties of the rock, or the result of using sliding sleeve as opposed to plug-and-perf completions (e.g., Chorney et al., 2016; Maxwell, 2011).

As can be seen in Figure 3.3a, during Stages 2 and 3, an isolated cluster of microseismicity occurred around 200 m north-east of the injection, north of the location of sleeve 12. There is a clear gap between the events adjacent to the toe stages (1-3) and this anomalous cluster, with only a small number of low magnitude events sparsely connecting the two.

Figure 3.3b shows the microseismicity that occurred when the operator skipped forwards to stimulate Stage 12, which was roughly adjacent to the anomalous microseismicity observed during Stages 1 through 3. Here we observe microseismicity to the north of the well, connecting into the same cluster of events that occurred to the north-east of Stages 1 to 3. However, we observe little microseismicity to the west back near these toe stages: what little microseismicity that is observed here is primarily the post-injection tailing of events from the earlier stimulation, not a re-activation of events. It is interesting, therefore, to consider why activity around Stages 1-3 was able to create a cluster of microseismicity adjacent to Stage 12, but activity near Stage 12 was not able to have the obverse effect on microseismicity near the toe stages.

During Stage 18, very little fluid was injected (around 8 m^3). However, this stage produced a significant microseismic response, with over 1200 events occurring in a cluster extending over 150 m to the north of the injection point. This stage generated relatively high magnitude microseismicity, with 8 events above M_w 0, and a M_L 0.5 trailing event around one hour after injection ceased. It is very unusual for an injection volume of around 8 m^3 to create a hydraulic fracture over 150 m in length, and to produce such significant amounts of microseismicity. Events that took place in the 6 hours after injection had a combined moment release of 3.10×10^{10} Nm. This constituted a notably large increase in the ratio of seismic moment release to injection volume compared to the previous stages. This is also relatively close to the upper bound of moment release proposed by the McGarr et al. (2002) relation, which for this small injected volume and a shear modulus of 25 GPa, would be around 2×10^{11} Nm. Previous stages had a far lower "seismic efficiency" (Hallo et al., 2014; Shapiro et al., 2010), with moment release less than 0.1% of this theoretical upper bound for each of their injected volumes.

During Stage 22 (Figure 3.3d), the full planned volume of just over 400 m^3 was injected, however with only around a third of the planned proppant (~ 17 t) . This was conducted in

two separate injection periods on October 25th 2018. This stage generated a large number of events, around 5700, with 12 events with $M_w > 0$. During the first period, events propagated perpendicular to the injection well, appearing to trace the hydraulic fracture growth northwards from the well. However, in the second period, events began to extend laterally, both east and west of the initial line of fracture growth, clustering along the seismogenic "fault zone" described above (Clarke et al., 2019a). Events extended along ~ 70% of the feature's length, tracing back toward Stages 12-14, and extending north of Stages 30-32.

Stages 30 through 41 continued to interact with this seismogenic zone, with large numbers of events clustering further north of the well. However, events rarely propagated westward, back along this structure, i.e. towards the stages which had been previously stimulated. This is shown in Figure 3.3e, for Stage 32. If it is assumed that this planar feature is a pre-existing fault or a zone of pre-existing fractures, one would anticipate that when stages reconnect to this seismogenic area, events would again be stimulated along its length, especially as the pore pressure around these faults or fractures has been increased by the previous injection, so we might expect successive injection would continue to stimulate seismicity back westward along its length. Stress relaxation may contribute somewhat to the limited reactivation as subsequent stages reconnect along the fault's length. However, previous cases of fault reaction have observed repeated reactivation into the same fault as injection reconnects (Kettlety et al., 2019).

The clear clustering of events at a notable distance from the injection well is apparent in Figures 3.3e and f, for Stages 32 and 38 respectively: clusters of microseismicity are not centred at the point of injection. If microseismicity were being driven directly by elevated fluid pressures, then we might expect more microseismicity to occur near to the well. These gaps between the well and the focus of the microseismicity are seen for stages all along the well, although they are particularly prominent for the latter stages at the heel of the well (Stages 37-41). This absence of microseismicity immediately adjacent to the well could be due to the tensile opening of fractures being a more aseismic process than shear slip on small faults or fractures that is occurring within the fault zone.

3.2.2 Spatiotemporal evolution of microseismicity

Shapiro et al. (1997) show that, where microseismicity is driven by diffusion of pore pressure, it should develop along a characteristic triggering front that extends a distance r from the injection point as a function of time t:

$$r = \sqrt{4\pi D t} \quad , \tag{3.3}$$

where D is the hydraulic diffusivity. It has also recently been shown that the hydraulic fracture growth can produce similar r-t behaviour (Barthwal and van der Baan, 2019). In contrast, a simple model of hydraulic fracture growth can provide the upper bound for the seismicity distribution. Under constant flow conditions and assuming minimal leak-off of fracturing fluid,

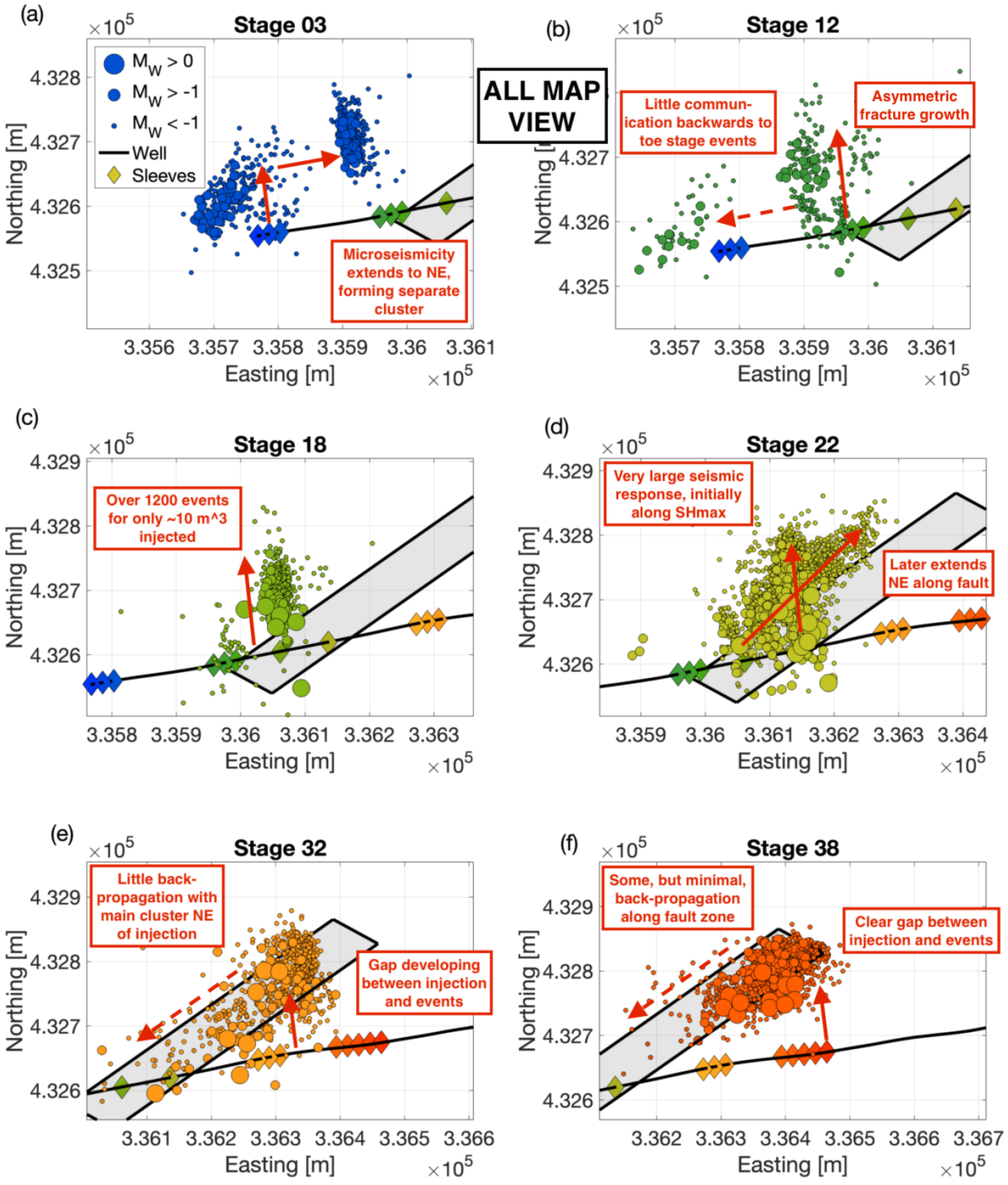

Figure 3.3: Event locations for several stages during which unexpected or anomalous seismicity occurred. Events shown here are those with a signal-to-noise ratio of greater than 5. Events and stations are shown in the same manner as Figure 3.1. Pertinent observations are annotated on the figures with red arrows and text boxes.

microseismicity driven directly by hydraulic fracture propagation might be expected to show a linear distance-time relationship, since the length of the hydraulic fracture L scales with the injection rate Q, the height of the fracture h_f, and its width w_f (Economides and Nolte, 2003; Shapiro et al., 2006a):

$$L = \frac{Qt}{2h_f w_f} \quad . \tag{3.4}$$

Figure 3.4 shows examples of the r vs. t behaviour for several stages: these plots are typical for the PNR-1z microseismicity. In Figure 3.4 we also show the expected r vs. t produced by the diffusivity approach (Equation 3.3) using various values of D, and for the hydraulic fracture propagation approach with minimal leak off (Equation 3.4), using approximate values of $h_f = 25$ m and $w_f = 2.5$ mm.

We do not observe the $r \propto t^{1/2}$ behaviour, characteristic of diffusion-controlled microseismicity. Realistic values of diffusivity for hydraulically fractured rock are considered to be 1.0 m^2 s^{-1} (~ 1 D) or less, which Figure 3.4 shows is clearly not adequate to describe the observed spatiotemporal distribution (Gehne and Benson, 2017, 2019; Tan et al., 2018). Instead, we observe microseismicity occurring near-instantaneously across a range of distances from the injection point. This behaviour is weakly consistent with the linear relationship between r and t posited by Equation 3.4 for hydraulic fracture propagation with minimal leak-off, because in such circumstances, given a typical flow rate at PNR-1z of 0.07 m^3 s^{-1}, we might expect a hydraulic fracture to propagate a distance of 300 m in less than 10 minutes. Note, however, that this is an upper bound, because in reality we expect multiple hydraulic fractures to form, sharing the overall injection volume between the fractures, and because Equation 3.4 assumes that no fluid is lost to the surrounding formation.

The near-instantaneous onset of microseismicity, regardless of hypocentral distance from the well, implies that pore pressure diffusion is not driving the microseismic activity, as this would produce microseismicity growing outward from the well with time. In contrast, stress transfer effects occur instantaneously, and so might provide a mechanism for fault reactivation that is more consistent with these observations.

3.3 Elastostatic stress modelling

3.3.1 Stochastic hydraulic fracture model

To produce the loading, or sources, for our stress transfer simulations, we require estimates of the number of hydraulic fractures, their orientation, length and height, and the amount of tensile fracture opening that takes place. This can be done using coupled hydro-mechanical fracture stimulation codes (e.g., Profit et al., 2016; Warpinski et al., 1994), as commonly used by industry. However, such models are highly dependent on poorly-constrained geomechanical input parameters, which may be tuned based on observations made during operations (Profit et al.,

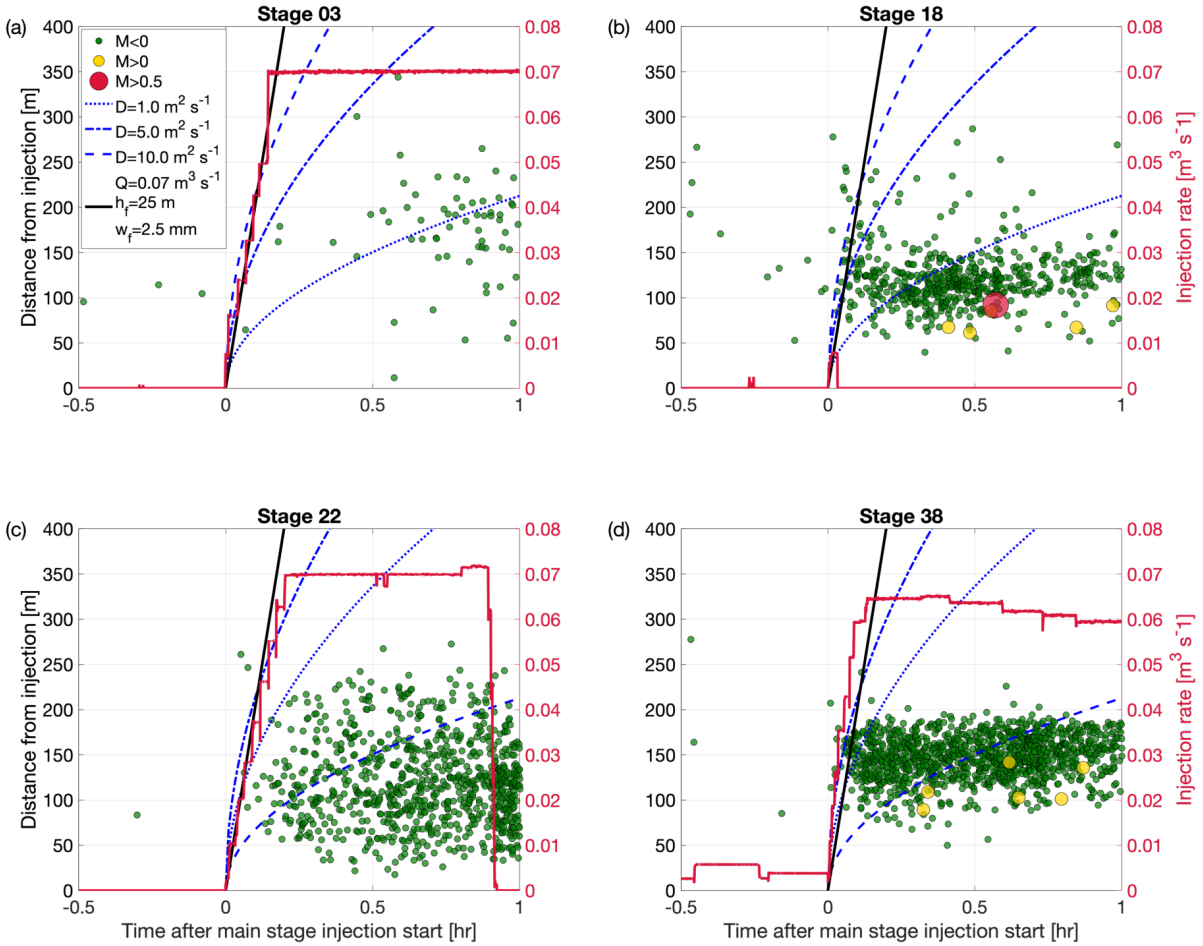

Figure 3.4: Spatiotemporal evolution of microseismicity for selected stages. We show the distance of events from the mid-point of the active injection sleeve as a function of time from the start of the main injection phase for each stage. Points are coloured by the event magnitude, showing the magnitude of the TLS, with $M_w < 0$ coloured green, $M_w > 0$ yellow, and $M_w > 0.5$ coloured red. The injection rate for each stage is shown as a red line. Blue lines denote the expected distance of diffusion-controlled microseismicity (Equation 3.3) for three different diffusivities. The black line shows the distance expected for events showing the growth of hydraulic fractures (Equation 3.4).

2016). Detailed modelling of this kind is beyond the scope of this study, which aims primarily to evaluate not the hydraulic fractures themselves, but their impact on the stress conditions in the surrounding rock. Instead, we adopt a stochastic approach, generating hydraulic fracture populations by drawing their properties (positions, orientations, dimensions, etc.) from statistical distributions representing typical, expected hydraulic fracturing cases. The use of a stochastic approach allows us to create thousands of model realisations, such that we can identify features in the resulting deformation that are consistent across a range of input hydraulic fracture models, and so may be considered robust and not dependent on a single choice of model parameterisation.

We assume that both the lateral (i.e., along-well) and vertical locations of the fractures are normally distributed around the sleeve location, producing an ellipsoid which extends to match the extent of the observed microseismic clouds, as well as those observed from other hydraulic fracturing sites (Chorney et al., 2016; Kettlety et al., 2019; Urbancic et al., 2003). This truncated normal distribution has a mean of 0 m, a standard deviation of 25 m, and a limit of ±100 m. For the stages with an obvious gap in microseismicity between the well and the cluster (e.g. Stage 38 and onwards), this assumes that the initial propagation and opening of fractures is mostly aseismic, and then the seismicity observed is the result of changes in stress that occur during injection, promoting slip in a more seismogenic area. Fractures are modelled as uniformly opening rectangular patches, oriented in the direction of S_{Hmax} (strike of 170° and dip of 90°) with an on average 10° von Mises random perturbation to the geometry. Fractures are randomly set to propagate either north or south from the well, with a bias of 80% extending north, to match the observations from the microseismic data.

We use the analytical solutions for the opening of a Griffith crack, commonly employed in fracture modelling, to approximate the fracture width (Perkins and Kern, 1961). For the injection rates at PNR (0.07 m^3 s^{-1}), a shear modulus of 25 GPa, a Poisson's ratio of 0.25 (believed to be appropriate for this setting, as described in section 3.3.2), and a fracture aspect ratio of 0.2, the fracture width is around 2.1 mm. The total number of fractures is then calculated by dividing the total volume of fluid injected in the stage by the total volume within the average 75 m long fracture. We set fractures to have a fixed aspect ratio AR of $L_{dip}/L_{str} = 0.2$. Fracture lengths L_{str} are sampled from a truncated normal distribution, with a minimum value of 25 m, a maximum of 250 m, a mean of 50 m and a deviation of 50 m, with at least 1 fracture above 100 m in length. L_{dip} is then calculated from the L_{str} and AR. These values were again chosen to approximate the expected stimulated zone for each stage, as well as being comparable to hydraulic fracture dimensions estimated at other sites (accounting for the smaller injection volumes used at PNR-1z (~ 400 m^3 per stage), compared to many wells in North America (> 1000 m^3 per stage)). Fracture width for each of the model fractures is then defined as the total volume of fluid injected divided by the total area of all generated fractures ($d_f = V_{tot}/\sum_i^{n_f} L_{str,i} L_{dip,i}$). This gives a width very similar to that found using the solutions of Perkins and Kern (1961) or Nordgren (1972), with normally distributed values of 2.6 ± 0.3 mm for each set of fractures.

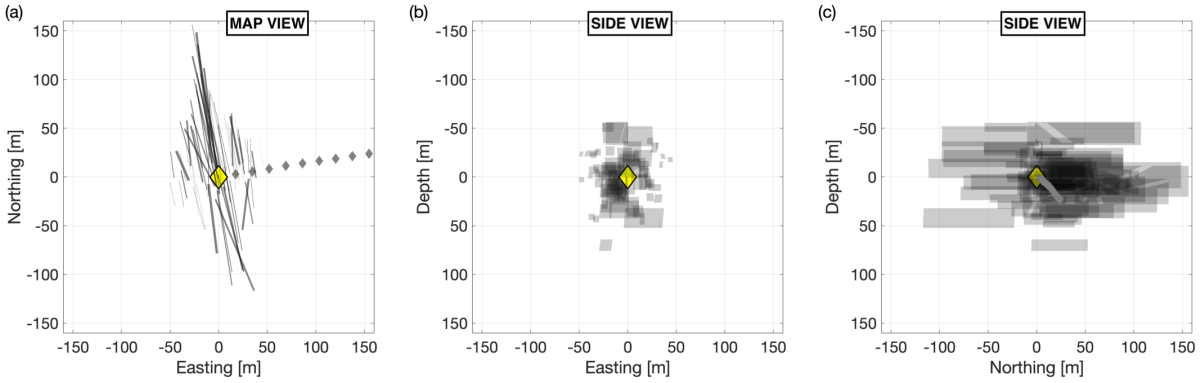

Figure 3.5: An example fracture set randomly generated for opening fractures around stage 1 (shown as a yellow diamond), given in three perspectives: **(a)** map view; **(b)** z-x cross-section view; and **(c)** an z-y cross-section. The patches of tensile opening as shown as black squares. The distributions that govern their location, length, and orientation are described in section 3.3. The Monte-Carlo model takes 1000 of these sets for each stage, and calculates the resulting median elastic ΔCFS for a volume around the well and fault zone.

The modelled fractures are then ordered, with the longest fractures located closer to the centre of the sleeve, producing an ellipsoidal stimulated volume of tensile opening fractures around each stage. An example of a fracture set produced in this manner is shown in Figure 3.5.

3.3.2 Modelling Stress Change

The opening patches are treated as the sources in the elastic stress change model. We use PSCMP developed by Wang et al. (2006) to compute the resulting changes in stress. This approach uses the analytical Okada solution (Okada, 1992) for the Green's function for a homogeneous elastic half-space to calculate the strain field, and Hooke's law to find the resulting change in the stress field.

The resulting elastostatic stress changes within the volume around the well are resolved onto the receiver geometry of the fault plane identified in Figure 3.1 – a ϕ of 230°, δ of 70°, and λ of 0° – in order to compute the ΔCFS using Equation 3.1.

The effective coefficient of friction μ' in equation 3.1 is derived from μ by $\mu' = \mu(1-\beta)$, and is an attempt to account for the way in which a change in pore pressure p effects the change in the normal stress $\Delta\sigma_n$ (Rice, 1992; Simpson and Reasenberg, 1994). This is achieved through the Skempton's coefficient β (Skempton, 1954) where, through a series of assumptions concerning the material properties of faults, it can be found that $\beta = -p/\sigma_n$. The value of μ' can range from 0 to 0.8, and varies between tectonic settings and lithologies. Typical values of μ' are generally around $\mu' = 0.4$ ($\mu = 0.7$ and $\beta = 0.4$), which we adopt here (Harris, 1998; King et al., 1994; Stein, 1999). We assume a shear modulus of 25 GPa, and a Poisson's ratio of 0.25. These values have been used in previous studies on induced seismicity (e.g., Catalli et al., 2013; Pennington and Chen, 2017; Schoenball et al., 2012), and are consistent with laboratory measurements of the

frictional and mechanical properties of shales (Islam and Skalle, 2013; Kohli and Zoback, 2013). These values are also similar to those found from studies of the Bowland shale, the formation targeted by PNR-1z (Herrmann et al., 2018).

Using the stochastic process described above, we model 1,000 fracture set realisations for each stage. We compute the ΔCFS for each case, and compute the median ΔCFS value for each point in the subsurface for each stage. We also examine the variability of the ΔCFS change across the 1,000 model instances: ΔCFS values that do not change significantly across a wide population of models can be considered robust.

Figure 3.6 shows an example of the median modelled ΔCFS changes for Stage 22, and the variability introduced by our stochastic modelling approach. Lobes of negative Coulomb stress change dominate to the east and west of the hydraulic fractures, whilst positive lobes extend north and south of the fracture tips, as well as above and below. The variability within the zone of hydraulic fracture propagation is high. This is because the ΔCFS values in close proximity to opening fractures can be very high, and so modelled stress changes within this zone will be strongly dependent on the particular stochastically-generated fracture model used as the input. However, further from the fracture zone, the median absolute difference in ΔCFS values is low. In these areas, the stress change is not sensitive to the particular stochastic fracture model used, and so can be considered to be more robust. In other words, the general distribution and shape of the lobes of positive and negative ΔCFS seen in Figure 5 exist for all fracture models that have tensile fractures extending roughly 100 m from the well. Therefore, the use of the median value allows us to examine the typical effect of the fracture sets, without the perturbations produced by the generation of random fractures.

To assess the significance of stress transfer effects, we interpolate the median modelled ΔCFS changes onto the location of each microseismic event, assuming the left-lateral faulting mechanism on the inferred plane. From this we compute the Coulomb Index, CI, which gives the proportion of events within a population that received positive ΔCFS changes. If stress transfer effects are playing a significant role, then we would expect most microseismicity to occur within lobes of positive ΔCFS, and therefore the CI would be high – typically > 70% (e.g., Catalli et al., 2013; Harris, 1998; Steacy et al., 2005).

3.3.3 Model Scenarios

For a given stage, we compute the median ΔCFS values for 3 points in time. We compute the stress change created by all of the preceding stages - this represents the stress conditions at the start of the selected stage. We refer to this as the "prior" ΔCFS. We compute the stress change created by hydraulic fracturing of the stage in question. This shows the ΔCFS produced by that stage. We refer to this as the "current" ΔCFS. Finally, we combine the stress change from all preceding stages and the stage in question. This represents the overall ΔCFS conditions that will be present at the end of a stage. We refer to this as the "total" ΔCFS. Obviously, the "total"

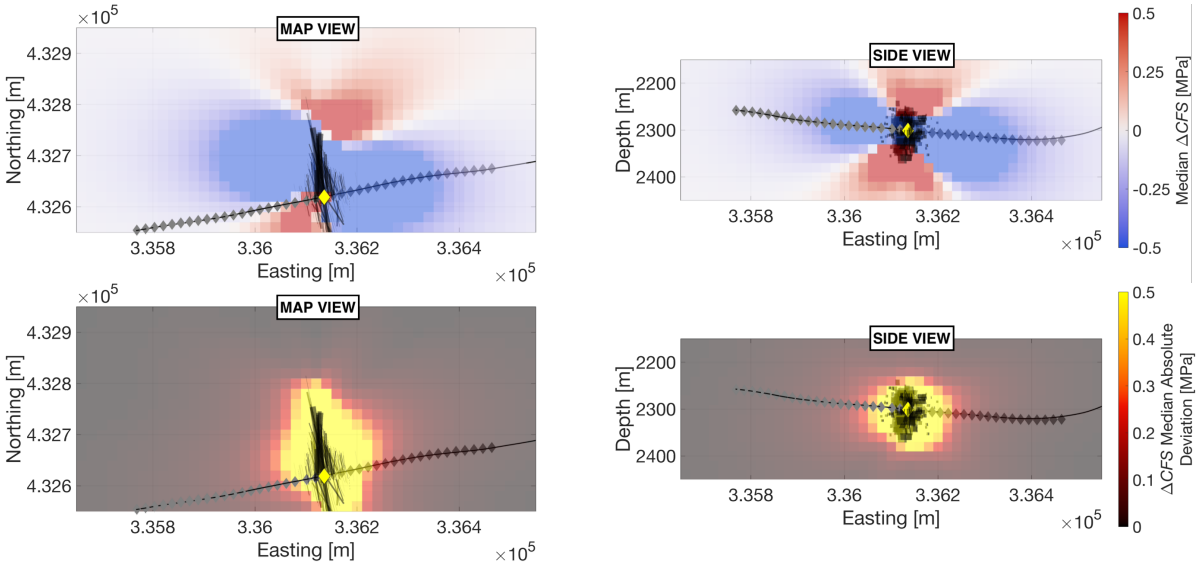

Figure 3.6: Elastic stress change maps showing the ΔCFS resolved onto the fault zone orientation received during Stage 22. An example of a single fracture set is shown as black patches within the volume. (a) and (b) show the value of the median stress change at two slices within the 3d volume (though the position of the stage location), whilst (c) and (d) show the median absolute deviation in that average value.

stress conditions and the end of one stage will be the "prior" stress change for the following one.

3.4 Results

Figure 3.7 shows maps of ΔCFS changes for our 3 scenarios, in this case for Stage 32. This figure also shows the ΔCFS change at the hypocentral location of each microseismic event that occurred during the stage. A visual inspection of these plots shows that microseismic event densities are significantly higher within the lobes of positive ΔCFS. The magnitudes of positive stress change received by most events are around 0.1 MPa, going up to around 1 MPa. These observations suggest that stress transfer effects are indeed playing a role in controlling where microseismicity occurs; this role can be further demonstrated by considering the CI values, shown on a stage-by-stage basis in Figure 3.8. We find that the majority of the stages have high values of CI, consistent with microseismicity that is triggered by stress transfer, especially when the cumulative impact of multiple stages is taken into account. This effect appears to be particularly strong for the latter stages where reactivation of the fault zone was taking place.

In Figures 3.9 – 3.11 we examine some of these stress transfer effects in more detail, with particular focus on some of the observations presented in Section 3.2.1. Figure 3.9a shows a map of ΔCFS produced by Stages 1 to 3 at the toe of the well. In Figure 3.3a we observed a cluster of events occurring roughly 100 m to the north-east of the main event cluster. We see that this region is at the centre of a large positive ΔCFS lobe created by the tensile fracture opening from

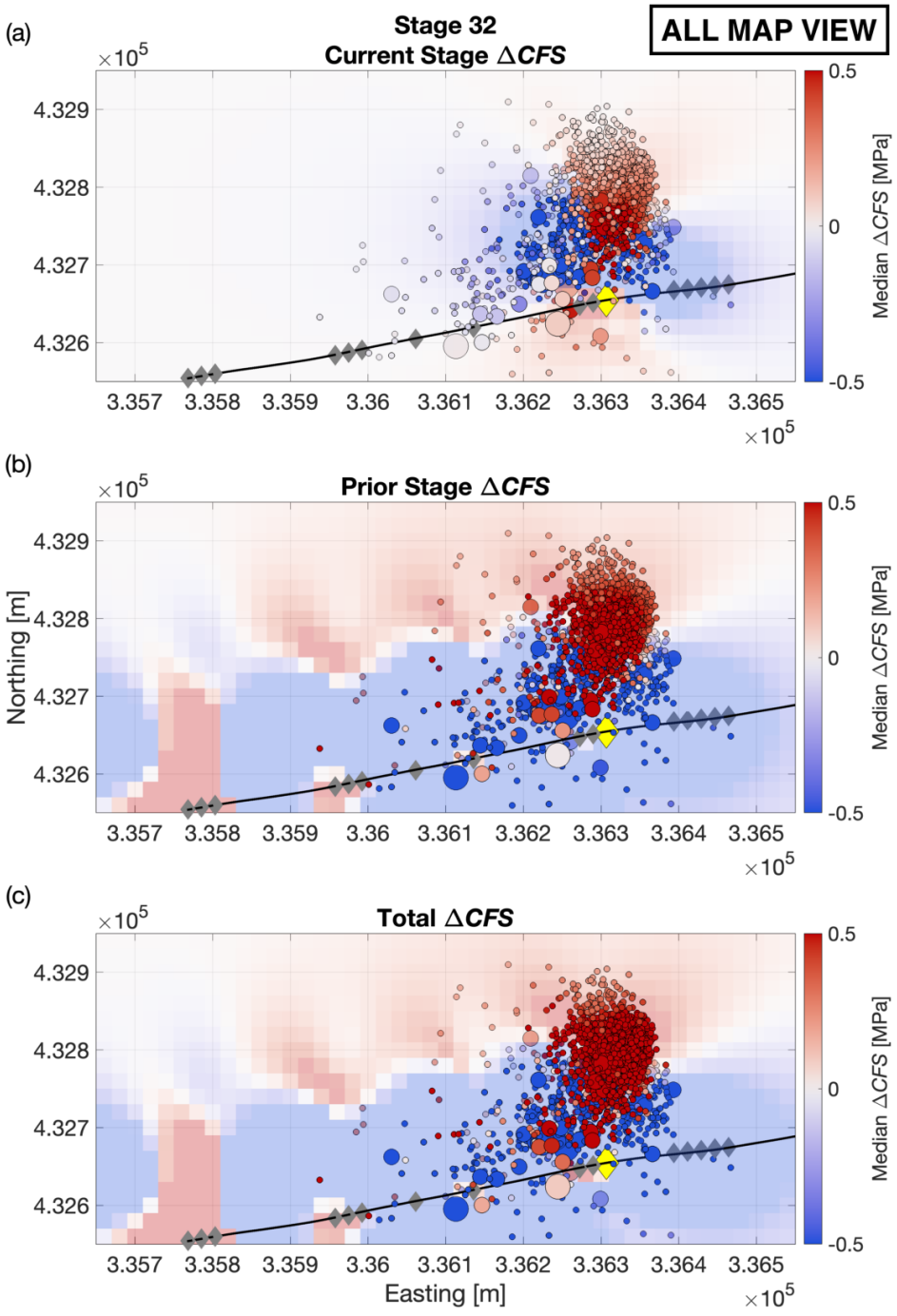

Figure 3.7: An example of the median stress changes calculated for stage 32. Each shows the stage 32 events, with the median elastic ΔCFS resolved onto the inferred orientation of slip on the fault plane and their hypocentre location. The map of ΔCFS is a slice through the 3D volume taken at the depth of the stage, which is shown as a yellow diamond. **(a)** The "current stage" ΔCFS is the stress change from the opening of fractures during stage 30. **(b)** The "prior stage" ΔCFS is the linear sum of the stress changes from all the previous stages resolved onto the stage 30 events. **(c)** The total ΔCFS is the combined prior and current stage stress changes.

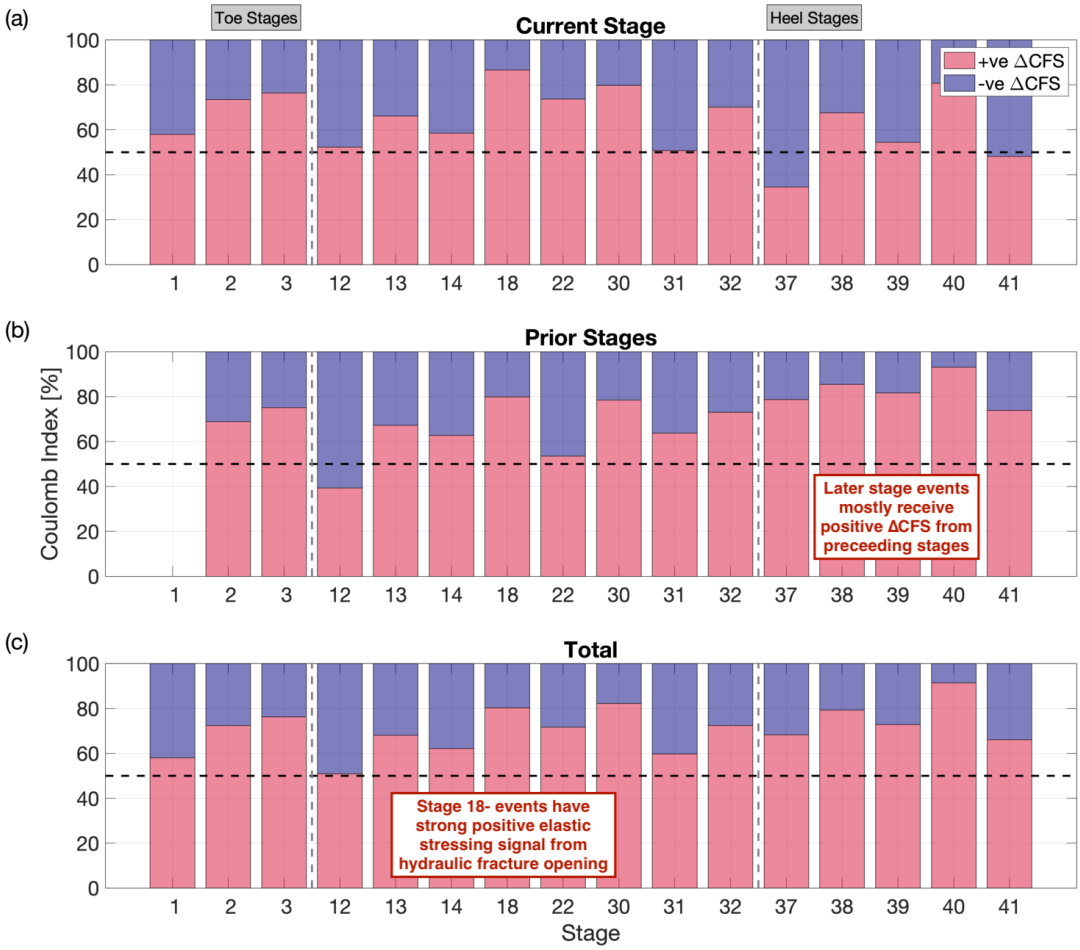

Figure 3.8: The Coulomb Index – the proportion of events in a population receiving positive median ΔCFS – for each of the events separated by stage for the **(a)** current stage, **(b)** prior stage, and **(c)** combined prior and current stage ΔCFS calculations. It can be seen that for stages from 18 (those that encountered the seismogenic fault zone), CI is largely well above 50%, and frequently in excess of 70%. The heel stage (37-41), whilst not appearing to be significantly effected by stress triggering during each of the stages, show strong signals for the prior stages. Stages 3 and 18, both of which showed anomalous seismicity, show significant correlation between positive stress change and event hypocentre location, with CI in excess of 70%.

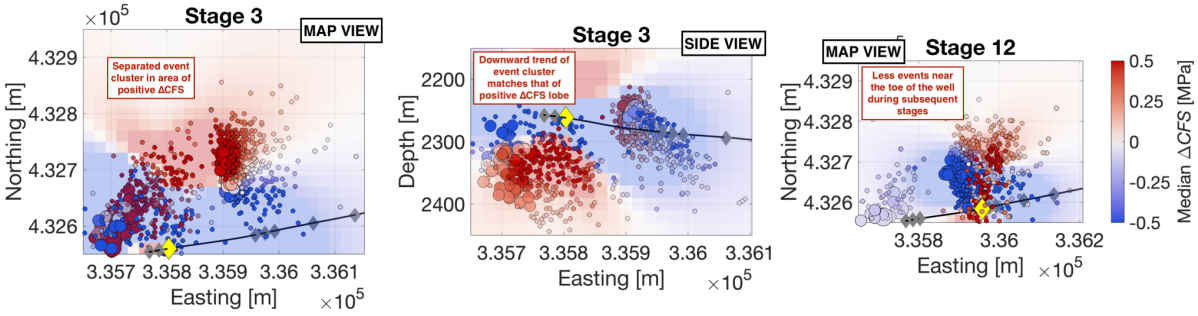

Figure 3.9: Changes in Coulomb stress during stages at the toe of the well. In (a) we show a map of ΔCFS produced by Stages 1 to 3 combined, with the microseismic events from Stage 3 overlain. The cluster of events to the NE, further from the injection point, occurs in a region of positive ΔCFS. In (b) we show a cross-section of ΔCFS produced by Stage 3: the lobe of positive ΔCFS below the well extends with a dip of approximately 45°, matching the observed microseismicity. In (c) we show a map of ΔCFS produced by Stage 12, with the microseismicity produced this stage. The region to the west of this stage is now in a lobe of negative ΔCFS, and microseismicity is suppressed here.

the toe injeciton stages. In contrast, during Stages 12 and 13, we did not observe microseismicity back-propagating in the reciprocal direction. Figure 3.9c shows the ΔCFS produced by Stage 12. We note that this region is within a lobe of negative ΔCFS. This stress-shadowing effect (Green et al., 2015) as the ΔCFS shifts from positive to negative as the hydraulic fracturing moves from west to east might explain why microseismicity appears able to propagate to the north-east ahead of the fracturing, but is suppressed in the region behind the active stage. What seismicity persists in that stress shadow may be continuing due to the large increase in pore pressures from the injection into Stages 1 to 3 at the toe of the well.

Figure 3.9b shows a cross-section of the median ΔCFS produced by Stage 3. Positive lobes extend above and below the well, with a plane of null ΔCFS dipping at about 45°. The events around the well fall within this lobe, which results in a structure that appears to dip at the same angle. Our interpretation is that this angle does not represent dipping hydraulic fractures, since in this strike-slip environment the intermediate principal stress is oriented vertically, but instead is caused by microseismic events being limited to this lobe of positive ΔCFS.

Figure 3.10 shows the ΔCFS produced by all of the previous stages prior to Stage 18, and the microseismicity that occurred during Stage 18. This stage produced a surprisingly large microseismic response from an injection volume of less than 10 m^3, with 8 events above $M_w > 0$ and events extending over 150 m from the injection point. In Figure 3.10 we observe that the locations of these events are strongly portioned into the lobe of positive ΔCFS produced by these prior stages, with a CI = 80%. Our interpretation is that the earlier stages caused pre-stressing of fractures in this region, such that a small perturbation in the stress state caused by the small injection volume was able to produce such a large number and extent of events.

Figure 3.11a shows the ΔCFS produced by Stage 22. As for Stages 1 through 3, we observe

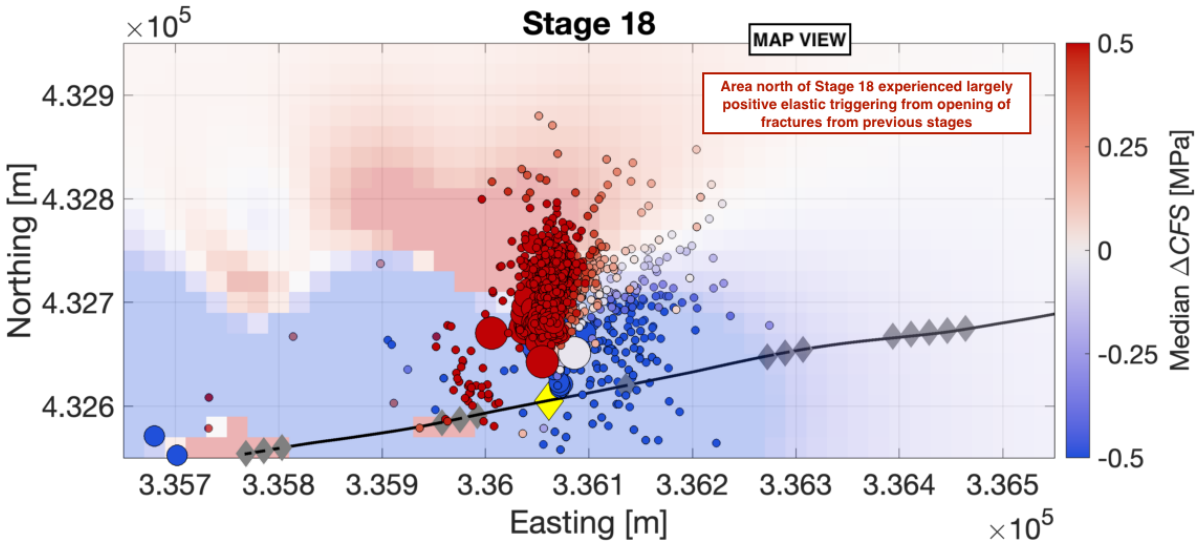

Figure 3.10: Map of ΔCFS changes produced by all stages prior to Stage 18, with the Stage 18 microseismicity overlain. Stage 18 saw minimal injection, yet produced significant amounts of microseismicity. In this figure we see that the effect of the prior stages was to create positive ΔCFS in this region.

a lobe of positive ΔCFS extending both above and to the north-east of the modelled tensile fractures, within which most of the microseismicity falls, with CI = 74% for this stage. Figure 3.11b shows the cumulative ΔCFS from all previous stages and Stage 38, with microseismic events from Stage 38 overlain. Again, we observe a very high CI = 80% for this scenario. Whereas during Stage 22 we observed north-eastward propagation of events along the fault zone, in these latter stages we do not observe significant numbers of events propagating back to the south west. Figure 3.11 shows that the cumulative impact of the latter stages is to place this portion of the fault zone within a lobe of negative ΔCFS, and therefore seismicity is less prevalent. This significance of this effect can be seen in Figure 3.8b: for Stages 30 to 41, when considering the cumulative impact of prior stages, the CI values are consistently at approximately 80% indicating event location is consistent with elastic stress transfer. As hydraulic fractures are created during each stage, a lobe of positive ΔCFS is pushed towards the north-east, while a lobe of negative ΔCFS is created behind (i.e., to the west) of the active stage. This geometry of positive and negative ΔCFS lobes appears to have a strong control on whether the fault zone is, and is not, reactivated.

For a number of stages, including the example of Stage 32 shown in Figure 3.7, a number of the largest events ($M_W > 0$) occur in areas of consistently negative median elastic ΔCFS, mostly near the injection point and the injection well. Obviously, this stress transfer effect is occurring contemporaneously as injection of hundreds of cubic metres of fluid at over 50 MPa. Clearly, stress transfer from fracture opening will not be the sole driver for seismicity during this case of fault reactivation. The increase of pore pressure, and the associated poroelastic stress

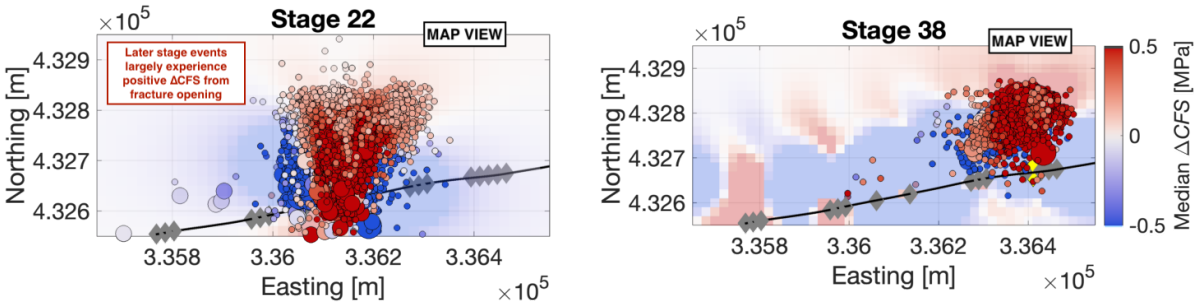

Figure 3.11: Maps of ΔCFS in stages towards the heel of the well. In (a) we show the ΔCFS produced by Stage 22, overlain with the microseismicity from this stage: a lobe of positive ΔCFS extends to the north-east, in which microseismicity is observed. In (b) we show the ΔCFS produced by all stages up to 38 (inclusive), and the microseismicity produced by Stage 38: the area to the west, behind the active stage is now in a region of negative ΔCFS, and microseismicity in this region is suppressed.

change, immediately adjacent to the well will naturally give rise to seismicity in areas that receive negative elastic stress change on the order of 1 MPa.

Using the derivations of Rudnicki (1986) for pore pressure and poroelastic stress change in a 3D homogeneous poroelastic medium, we can estimate the approximate magnitude and extent of pore pressure change ΔP for a $Q = 0.07$ m^3 s^{-1}, 90 minute injection (the rate and pump time of the largest stages during PNR-1z operations). For this estimate we use an average matrix permeability around the injection point of 5 mD, a Biot-Willis coefficient of 0.7, a shear modulus of 20 GPa, a drained Lame parameter of 20 GPa, an undrained Lame parameter of 25 GPa, and a dynamic viscosity of the fluid of 1 mPa s. At the end of pumping the stage, this simple model gives a ΔP of at least 0.5 MPa out to a radius of ~ 50 m from the point of injection, and within 10 m, ΔP exceeds 10 MPa. The change to the stress tensor from increased pore pressure provides a Coulomb stress change on the receiver fault geometry of at least 0.5 MPa around 70 m NNW-SSW from the injection point. 12 hours after injection, a ΔP of at least 0.5 MPa will extend out ~ 100 m from the point of injection. The poroelastic stress decays rapidly as elevated pore pressures diffuse into the surrounding medium and decrease in magnitude, so by 12 hours after injection, poroelastic ΔCFS is less than 0.1 MPa 50 m from of the injection. Thus, both during the stage and after, the magnitude of stress changes from both the diffusion of elevated pore pressures and poroelastic ΔCFS are comparable to the fracture opening elastic stress transfer. Without a complex model of the permeability structure around the well, providing conduits for increased ΔP, the spatiotemporal distribution of events does not clearly correlate with the areas of increased poroelastic stress or pore pressure.

Interevent static Coulomb stress increase is most likely another mechanism contributing to the failure of events within the fault zone that receive negative stress change from opening fractures. As the several $M_w > 0$ events occur, failing in a left-lateral strike-slip fashion in the fault zone, positive stress changes will extend around 100 m from the tips of the fault, encouraging

continued failure along its length. This effect will naturally be combined with the static stress change from opening fractures, however the magnitude of the interevent stress changes will be smaller in comparison due to the relatively small size of the events. There is also no clear aftershock-type sequences in the spatiotemporal distribution of events that occur after the $M_w > 0$ events, which would be a clear indicator of interevent triggering.

The spatial distribution of seismicity will naturally reflect the multiple mechanisms at play, and thus only the elastic model of fracture opening will not account for every event's location. What is notable, however, is that during most injection stages, the majority of events are located in areas that do receive positive stress from fracture opening, and that this mechanism provides a possible explanation for the unexpected observations in the microseismic.

3.5 Discussion

Using a simplified model of distributed fracture opening around a hydraulic fracturing well, we have seen that microseismic event locations were predominantly distributed in regions of positive stress change when resolved onto the geometry of an inferred adjacent fault zone. Specifically, unexpected microseismic event locations during several stages, that would otherwise be difficult to explain, are located in regions of positive stress as generated by a simple model of tensile opening of hydraulic fractures.

3.5.1 Model Uncertainties

The input parameters used in this model, such as fracture dimensions and distribution, or elastic moduli, are not overly tuned to this specific location or site – they are broadly applicable to most hydraulic fracturing cases. Model fractures are centred on the injection point and their locations follow fairly generic distributions for stimulated ellipsoids around an injection point. Thus, it is noteworthy that, despite this generality, many of the observations are consistent with static stress transfer promoting failure on the inferred failure mechanism of the larger fault zone. Naturally, the extent of the ΔCFS lobes are dependent on the fracture modelling parameters, such as the average length of the fractures, and could thus be varied in order to increase or decrease the significance of the results. For example, model fracture growth could be offset by small distances (tens of metres), within the uncertainty, to shift most events into the areas of positive stress change. However, we found that generic values gave a clear indication of stress triggering, through good agreement between areas of positive stress change and event location, and consistently high CI.

The magnitude of the ΔCFS change will be sensitive to model assumptions, such as the shear modulus, and the modelled fracture opening. We do not take into account the effects of leak off or proppant during injection, as in our model the total amount of fracture opening is sufficient to contain all of the injected fluid. In reality, some of this fluid will be lost to the formation, reducing

the total volume of fluid available to cause fracture opening. Since our model fracture lengths are chosen from a fixed distribution, and the fracture widths are constrained by analytical solutions (Perkins and Kern, 1961), the net effect of a reduced injection volume would be to reduce the number of fractures in the stochastic model. The overall deformation is computed by adding the deformation produced by each hydraulic fracture, so a reduction in the number of fractures would reduce the magnitudes of the modelled stress change, but would not change the polarity of the ΔCFS change. This magnitude is already sensitive to the elastic parameters used, as well as the simplistic uniform-slip source model, which can lead to unreliable stress changes within the near-field of the source (Kettlety et al., 2019; Meier et al., 2014; Steacy et al., 2004). Thus, we deliberately choose not to interpret this magnitude. Instead, we focus on the sign of the modelled ΔCFS (i.e., if microseismic events occur in regions experiencing positive ΔCFS), since this is far more consistent and robust than the magnitude. Most events within the positive lobes do receive stress changes in excess of the triggering thresholds for critically stressed faults, which range from 0.001 to 0.5 MPa (Freed, 2005; Kilb et al., 2002; Shapiro et al., 2006b).

Accounting for the effects of leak-off and proppant in the fracturing fluid can also affect the calculation of fracture width. Reducing net flow into the fracture by accounting for leak-off would decrease the calculated width, whilst proppant increases the slurry viscosity and would act to increase the width (Nordgren, 1972). However, accounting for these effects would not significantly modify the overall stress change shape as we estimate that the width of each individual fracture would only change on the order of 0.1 mm. This would only have a small effect on the distance to which the lobes propagate, which is more sensitive to factors such as the spatial distribution of fractures and the shear modulus. Thus, the width parameter affects the magnitude of the stress, rather than the sign of ΔCFS.

When modelling the deformation produced by cumulative stages, we assume that the hydraulic fractures from each stage remain open, and we linearly sum maps for the previous stages. This situation is unlikely to be the case in reality, because as pressures reduce after each injection stage, fractures will begin to close. However, the flowback volumes between stages were small, typically less than $20-25$ percent of the injected volume (over the course of weeks during the hiatus period specifically), and some (though not all, see Clarke et al., 2019a) of the stages had proppant injected, which would serve to keep hydraulic fractures open after injection stops. Therefore, the extent to which fractures closed after injection, reducing the magnitude of stresses that are transferred to subsequent stages, is not well constrained. Naturally, adding the stress change from some earlier stages by a different factor would have the effect of altering the prior and total ΔCFS, shifting the positions of some of the positive and negative lobes somewhat. However, more complex fracture modelling would have to be conducted to determine the relative amount of fracture closing during each stage, and thus the scaling of the effect of each individual stage, with time.

Therefore the magnitudes of the ΔCFS values could be higher or lower than those we describe

here, depending on the assumptions concerning the factors described above. However, our study is primarily concerned with the polarity of the ΔCFS signal: whether events occur in regions that are experiencing positive or negative ΔCFS change, as described by the CI value. The shapes of the positive and negative ΔCFS lobes are primarily controlled by three factors: the orientations of the hydraulic fractures, the assumed length of the hydraulic fractures, and the orientations of the receiving fractures on which microseismicity occurs.

The orientation of the hydraulic fractures is determined from the in situ stress state, which has been well constrained from borehole measurements within the PNR-1z well (Clarke et al., 2014, 2019b; Fellgett et al., 2017). The orientations of the receiving fractures have been determined by consistent, well-constrained source mechanism observations (Clarke et al., 2019a), as shown in Figure 3.1. The lengths of the hydraulic fractures that we have used in our model are based on generic assumptions about hydraulic fracture lengths given the injection volumes used. However, they are similar to the fracture lengths, between 100 to 300 m, that have been calculated by the operator based on their observed pumping parameters (Cuadrilla Resources Ltd., 2019). Therefore, while the magnitudes of the ΔCFS values may not be well constrained, the spatial distributions of positive and negative values, and therefore our results expressed in terms of the CI, can be considered to be robust.

3.5.2 Possible Impact on Fault Rupture Dimensions

Assuming the basic formulation of seismic moment given in Equation 3.2 holds, maximum earthquake magnitude would be controlled purely by the dimensions of the fault on which induced seismicity is being triggered. For the feature identified in Figure 3.1, assuming a typical stress drop value of a rupture (~ 1 MPa) along a 500 m by 200 m area, this corresponds roughly to a M 3 event. The largest event size during the operations had M_L = 1.5, approximately 30 times smaller than this potential maximum magnitude, corresponding to a rupture radius of less than 100 m as discussed earlier. Our modelling shows that the ΔCFS values on the fault were positive in some places, but negative in others. This clamping at certain points along the fault, in particular the regions behind (i.e., to the west of) the active stage, could be seen as a mechanism for the limited rupture extent on this inferred fault plane. However, previous studies have shown that rupture extent is not limited to the portion of a fault zone receiving positive stress during failure along its length (Ampuero and Rubin, 2008; Ripperger et al., 2007). Dynamic stress changes during rupture can quickly overcome regional stress and local, smaller scale stress changes (Meng et al., 2012; Preuss et al., 2019). Also, it is certainly not clear this zone is a well connected fault surface or just a region of pre-existing fractures that are oriented favourably in the present regional stress state. Thus, the likelihood of a M 3 event is not well constrained.

Many of the proposed mechanisms for constraining the maximum magnitude during an induced sequence (e.g. Shapiro et al., 2011) function under the assumption of a limited rock volume stimulated by injection. Shapiro et al. (2011) assume that seismicity is driven by pore

pressure diffusion, however an analogous argument could be made with respect to the dimensions of the portion of the fault that receives positive ΔCFS. Fracture opening does introduce significant changes to the stress state in hydraulic fracturing settings, and for well-oriented faults adjacent to the operations (i.e where the magnitudes of stress transfer are significantly positive) this could modify the extent and shape of the "stimulated" rock volume greatly. While this clamping effect is a possibility for general cases of fracture opening stress transfer, the model proposed by Shapiro et al. (2011) produces a truncated Gutenberg and Richter (1944) distribution, which is not observed at the PNR-1z site (Clarke et al., 2019a). Thus it is by no means clear that this is occurring in this case of injection-induced fault activation.

3.6 Conclusions

During hydraulic fracturing at PNR-1z, we observed the reactivation of a pre-existing fault that produced tens of thousands of microseismic events, the largest of which was felt by nearby populations, and several of which required the operator to pause their activities under the conditions of the UK's traffic light scheme. Here, we have investigated the role of elastostatic stress transfer in triggering these events, as well as producing other microseismic observations that are not obviously driven solely by injection-induced pore-pressure increases or the growth of hydraulic fractures.

To do this, we develop a stochastic approach to modelling hydraulic fractures as a loading source for the elastic stress transfer model. This allows us to assess the impact of expected, generic fracture sets, without being overly influenced by the results of a particular representation of the hydraulic fractures. We then look at the median ΔCFS of the 1000 realisations that were conducted.

We find that the observed microseismicity occurs predominantly within volumes of rock that receive positive median ΔCFS. This indicates that stress-transfer effects produced by the tensile opening of hydraulic fractures are in part driving the spatiotemporal distribution of induced seismicity at PNR-1z. These elastic effects, whilst often considered to be less significant than the increase in pore-pressure, appear to play a role in pre-stressing nearby fractures or faults, as well as promoting failure near instantaneously at anomalously larger distances from the point of injection.

For the particular orientations of the hydraulic fractures and the pre-existing fault at PNR-1z, the tensile fracture opening creates positive ΔCFS to the north-east of the active stage, with multiple stages adding cumulatively to this effect. Because stimulation progressed eastward along the well, each new stage was therefore injecting into a volume of rock that had been pre-stressed by the previous stage. This may have contributed to the repeated exceedance of the TLS threshold over multiple stages. In contrast, the regions to the west of the active stage were clamped by the tensile fracture opening, suppressing microseismic activity in these areas.

This implies that if the wells were drilled in the opposite E-W direction, proceeding injection stages would have actively clamped the fault, rather than stimulating it further. The fault was not identified on any of the 3D reflection seismic data that was acquired for the site however, and thus it was not possible to know its orientation prior to the fault being reactivated.

These effects will be highly dependent on the specific orientations of both the hydraulic fractures and the receiving faults, and so cannot easily be generalised to other sites. However, the stochastic modelling approach, combined with the PSCMP modelling code, is able to provide results at a speed that could plausibly be applied in near real time during injection operations. Doing so could enable operators to identify whether their planned stimulation program is likely to stress or to clamp any faults identified during injection, and potentially to make appropriate adjustments to their program to minimise induced seismicity.

CHAPTER 4

REAL-TIME MAXIMUM MAGNITUDE FORECASTING DURING HYDRAULIC FRACTURING

This chapter is in part based on the published work *Real-Time Imaging, Forecasting, and Management of Human Induced Seismicity at Preston New Road, Lancashire, England* by Huw Clarke, James P. Verdon, Tom Kettlety, Alan F. Baird, and J. Michael Kendall in Seismological Research Letters, issue 90, pages 1902-1915, in 2019 (Clarke et al., 2019a). Presented here is an adapted version of part of this paper, comprising my contribution to the work: the application of the real-time maximum magnitude forecasting. This chapter does not contain any of the specific wording of the above publication, but is naturally related in its structure and style. All results were recalculated accounting for more recent findings, and I produced all figures presented below.

Chapters 2 and 3 showed how elastostatic modelling can be used to examine the spatial distribution of induced seismicity. Chapter 3 specifically showed how elastic stresses due to opening fractures can encourage and discourage failure on parts of a fault system. As the size of the rupture relates directly the magnitude of earthquakes, any effect which could potentially limit the rupture on a fault near injection may effect the size of the largest induced events. Whilst the previous modelling of these physical processes was used to explain the behaviour of seismicity retrospectively, in this chapter we use statistical models to forecast the magnitudes of induced events during injection.

Recent studies have developed statistical methods for quantifying the expected maximum magnitude of induced events during injection. A forecast of the magnitude of induced events during injection could be key to strategies aimed at mitigating induced seismicity, and assist in operational decision-making, making operators aware of the onset of fault activation and the need to implement proactive measures during injection. In this chapter, we describe the application of these methods to the Preston New Road PNR-1z operations. We implemented two statistical models to forecast the expected maximum magnitude of the events, M_{max}, in real-time. We found that maximum event magnitude could be forecasted accurately, though event and injection data must be combined across injection stages in order to not underestimate M_{max}. This demonstrates that each injection stage cannot be taken in isolation, and the fluid volumes of stages that had reactivated the fault previously must be taken into account when this type of modelling is conducted. This means real-time interpretation and analysis of the microseismic event locations is an important element in the application of these statistical models.

4.1 Introduction

Understanding the underlying physical mechanisms behind injection-induced seismicity (IIS), as discussed in the previous chapter, naturally aids in the development of mitigation strategies. However, the effectiveness and exact application of these strategies in real-time is still debated (Baisch et al., 2019; Bosman et al., 2016). Traffic light schemes (TLSs) have now been imposed by regulators of hydraulic fracturing (HF) in several countries, each requiring operators to change the injection programme in response to recorded seismicity (Kendall et al., 2019). If the magnitudes of events exceed particular thresholds mitigating action must be taken, including reducing injection rates, halting injection, or flowing back the well in order to limit the assumed changes in stress occurring around the point of injection, regardless of the underlying triggering mechanism. The thresholds themselves vary widely, as do the imposed consequences of exceedance. In Alberta, Canada, the "red light" is set at $M = 4$, and requires all operations at that site to cease and a full inquiry to be conducted by the regulator. In contrast, the UK has a red light of $M_L = 0.5$, and requires an 18 hour pause of injection, during which time seismicity is monitored (Oil and Gas Authority, 2018).

TLSs applied simply will only ever been reactive in nature, as they rely on mitigating action to be taken after a large event has occurred. "Trailing events" have also been observed during IIS, where induced events increase in magnitude after injection. An example of this is the Preese Hall well in Lancashire, England, which was stimulated in 2011. Events during injection were imperceptible, and did not exceed M_L 1.3, however a M_L 2.3 event took place approximately 10 hours after injection ceased (Clarke et al., 2014). The risk of these trailing events can lead to TLS thresholds being reduced, in an effort to avoid the potential of large events the scheme is actually designed to avoid. This can result in imposed thresholds that may be considered too low

to operate, as injection may be halted frequently due to seismicity that, whilst elevated from the smallest events, is far from hazardous.

Managing seismicity during injection is naturally the goal of a IIS mitigation strategy, but requires analysis of seismicity in real-time to assess the potential for future larger events. This analysis varies depending on the monitoring being conducted. Microseismic monitoring, processing and locating many small precursor events in real-time can enable faults to be identified and avoided directly, for example, by the alignment of events on faults (e.g., Eyre et al., 2019; Kettlety et al., 2019) or a decrease in Gutenberg-Richter (GR) b-value (e.g., Kettlety et al., 2019). High b (around 2.0) denotes there are more small events to large events, whilst $b \sim 1.0$, typical of tectonic sequences (Frohlich and Davis, 1993), implies there are more larger events relative to the number of small events. This can be seen from equation 4.1 (Gutenberg and Richter, 1944):

$$\log(N) = a + bM \quad , \tag{4.1}$$

with N equal to the number of events greater than magnitude M, b equal to the gradient of the line when plotted semi-logarithmically, and a is the activity rate describing the number of events at $M = 0$. High b-values have been associated with operationally-induced events (e.g., Eaton and Maghsoudi, 2015; Verdon et al., 2013a), and thus a drop towards $b = 1.0$ is indicative of seismicity that is associated with fault activation, as opposed to the growth of hydraulic fractures.

Statistical forecasting can use this microseismic data collected during operations to forecast the expected maximum magnitude in real-time. As IIS follows the GR distribution (van der Elst et al., 2016), and the number (Shapiro et al., 2010) or cumulative moment release (Hallo et al., 2014; McGarr, 2014; McGarr et al., 2002) of events can be scaled to the injected volume, the observed seismicity and injection rates can be used to model the population of events and extrapolated to the total planned volume to be injected. This was applied in a retrospective manner to a large HF dataset in Verdon and Budge (2018), who showed that this could have been used to potentially mitigate the larger events that occurred during operations.

In this chapter, I show the results of the application of these statistics-based maximum magnitude forecasting to the Preston New Road PNR-1z operations. This was done in real-time during operations, the results of which are presented in Clarke et al. (2019a). Those presented here are slightly adapted to include more recent analysis, specifically the discrepancy between the local and moment magnitude scales.

4.2 Preston New Road microseismicity

As the site, the development of microseismicity, and the fault activation itself has been described in the previous chapter (i.e., Kettlety et al., 2020), I will forgo repeating a full description here. However, the following will highlight some observations in the PNR-1z data that are particularly relevant to the application and results of the statistical forecasting.

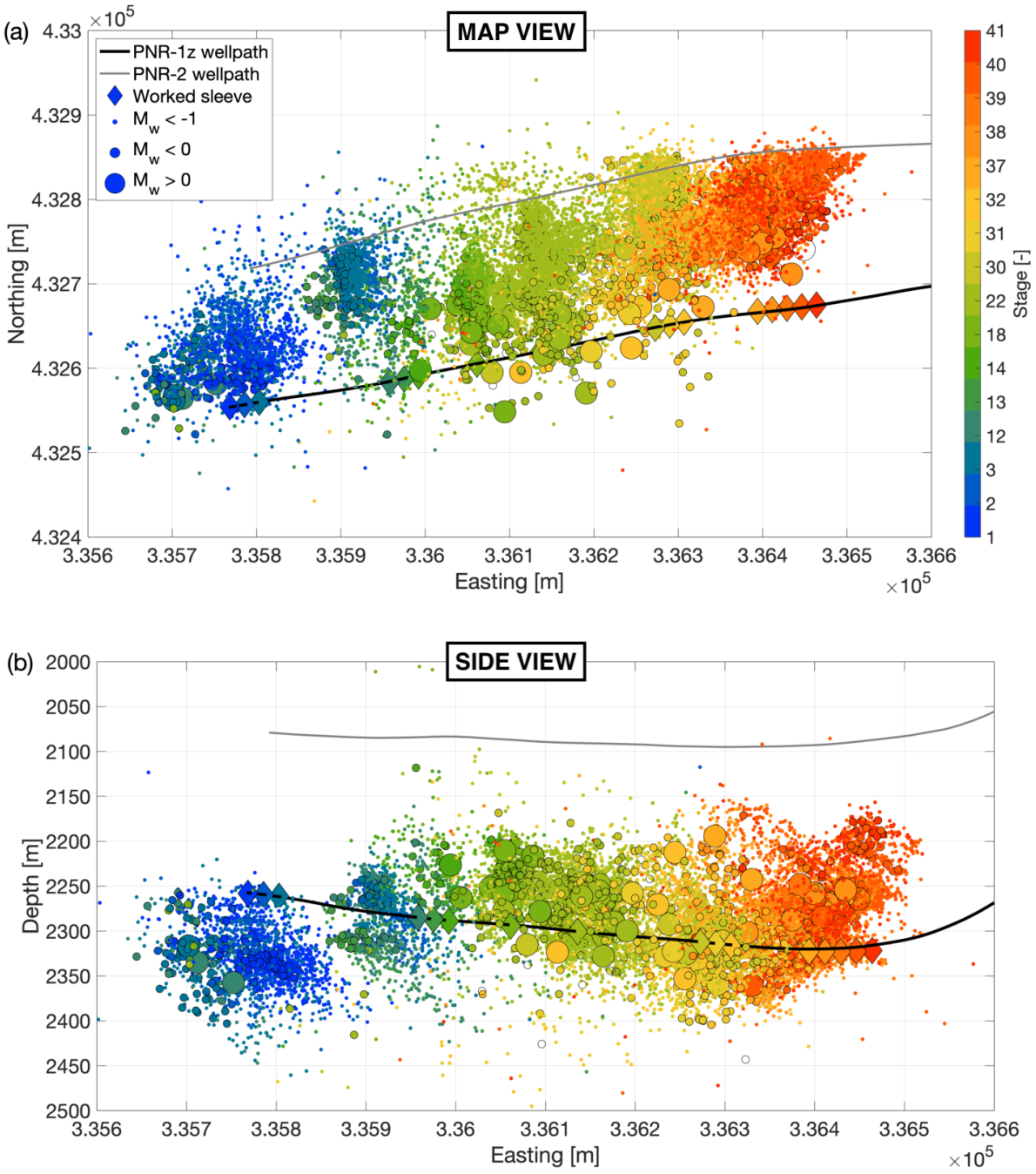

Figure 4.1: Hypocentral locations of events recorded by the downhole array during PNR-1z operations. The lines show the well paths, with the black showing PNR-1z, and the grey showing PNR-2. Diamonds show the locations of the sliding sleeves along the well, through which injection takes place. Events are shown are dots, coloured by stage with size indicating the magnitude.

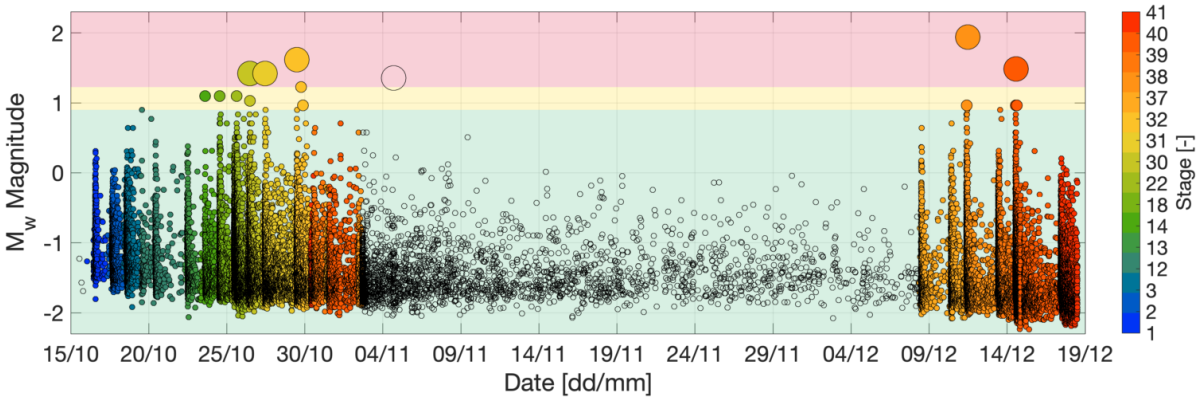

Figure 4.2: The magnitude evolution of events that occurred during PNR-1z. Events are shown as dots, coloured by stage with sizes indicating the magnitude of events. The coloured background shows the magnitude thresholds imposed by the UK TLS, converted from local magnitude M_L to moment magnitude M_w using Equation 4.2. Events with no colour occurred at least one day after injection of the last stage. These predominantly took place during the hiatus period, during which many small events continued along the NE fault structure.

Figure 4.1 shows that during the majority of stages of injection, events were repeatedly clustering on previously activated features. The toe stages (1 through 3) stimulated a cluster of eastward dipping seismicity, the orientation and location of which roughly matched a small discontinuity observed in the reflection seismic surveys of the site. This prompted the operator to skip to Stages 12 through 14 to avoid these seismogenic structures, where seismicity again repeatedly occurred on lineaments which appeared to be indicative of the activation of pre-existing structures, rather than the growth of hydraulic fractures. Skipping sleeves further west along the injection well to Stage 18 again proved unsuccessful, as a small volume of injected fluid stimulated a very strong seismic response. Stage 22 seemingly encountered the same structure stimulated during Stage 18, with events illuminating a NE-striking steeply dipping zone of enhanced microseismicity. Stages 30 through 40 continued to induce thousands of microseismic events per stage along this same feature, either a fault or zone of natural fractures. It was only the injection of Stage 41 where event magnitudes subsided, implying that the injection was interacting with the feature to a lesser extent.

A noticeable increase in the magnitude of induced events began from Stage 14, with each stage producing events above the amber-light threshold, and Stage 30 was the first to have a red-light trailing event. Prior to the November 2018 operational hiatus, the largest event occurred during Stage 32, a M_L 1.1, for which there was a single felt report. After this event, several minifracs on the heel-most stages (35 to 41) were conducted. Two days after the final minifrac was conducted, another red light trailing event occurred, with a magnitude of M_L 0.7. Over the rest of the hiatus, magnitudes and seismicity rates subsided, though the region around the NE fault zone remained active, further indicating the presence of a seismogenic feature. Operations

resumed over a month after the last stage, with the injection of Stage 37 on December 8th 2018. Stimulation did not induce any large events during this stage, with magnitudes remaining below $M_L = 0$. Around 1 hour after the injection of Stage 38, during which only a single amber event was recorded, the December 11th M_L 1.6 event occurred in the NE fault zone, with a FM indicative of the left-lateral NE-SW strike slip motion, consistent with the orientation of the microseismic cluster. After a two day pause in injection, Stage 39 proceeded with no events above $M_L > 0$, and was followed 24 hours later by Stage 40. This stage stimulated the last red-light event recorded during PNR-1z, a M_L 0.9 which took place around ten minutes before the end of injection. Stage 41 proceeded two days later without a single event above M_L -1.

From Stage 18, events clustered along the NE feature repeatedly, with an orientation consistent with many of focal mechanisms of the largest events, as described in the previous chapter. If this zone of greater seismicity is a fault, its damage zone may act as a permeable pathway along which increased fluid pressure would travel with repeated injection (Faulkner et al., 2010). Multiple stages increasing the density of fractures through this zone would enhance its permeability further. It could be expected that microseismic activity would continue along the faults length as injection repeatedly fed into it, further decreasing normal stress, and triggering small pre-existing slip surfaces to fail. This is not clearly observed, with activity mostly clustered to the north east of each stage. However, to a lesser extent, events do continue along the fault's length, especially in regions that have been injected into by prior stages. Thus, the compartmentalisation of the event clusters during each stage does not rule out that the fault zone is somewhat hydraulically connected, especially after stages repeatedly stimulate it.

The occurrence of large magnitude trailing events is naturally a concern operationally, as if there is no sign of increased seismicity during injection, it is more difficult for the operator to enact mitigating strategies. This gives statistical real-time M_{max} forecasting the opportunity to assess the nature of seismicity, indicating the activation of a fault during injection, as opposed to hours or days later.

4.2.1 Local and moment magnitudes

Accurate determination of magnitudes for small events is vital to assess the magnitude-frequency distribution and moment release during injection. These quantities are used directly by statistical forecasting methods, as described in the following section. They are also a key part of the implementation of the UK TLS, which is based on local magnitudes. These are calculated from the surface displacement, detected by the local monitoring network. This network of broadband instruments and 3-component geophones has a wide azimuthal range around the site, and is able to detect events down to a M_L of less than -1.0. The local magnitude scale in the UK (Luckett et al., 2019) corrects for near-surface attenuation effects, and thus would be thought to be inappropriate for use downhole. However, the service provider did still calculate M_L using the amplitude of the downhole waveforms for each event, as shown as the light blue dots in

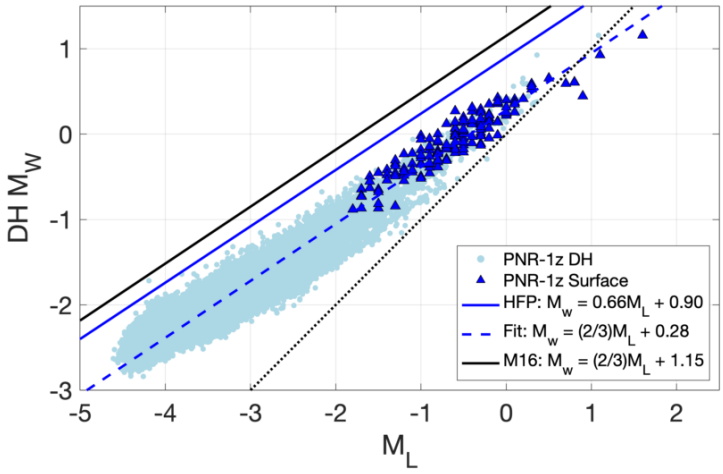

Figure 4.3: Moment M_w to local M_L magnitude relation for PNR-1z events. Events with M_L recorded by the surface array are shown as blue triangles, whilst those recorded by the downhole (DH) are shown as light blue dots. The solid lines give two M_w-M_L relationships for comparison, the black showing the Munafò et al. (2016) relation for small tectonic earthquakes ($M < 4$), and the blue showing the relation derived using the surface waveforms recorded during PNR-1z. These surface calculations were performed by another contractor, Q-con. The blue dashed line shows the least squares fit of a line with a gradient of 2/3, the expected gradient from the theoretical derivations of M_w-M_L for small events (Deichmann, 2006, 2017). It is clear that the downhole calculations are systematically underestimating M_w by around 0.6 magnitude units, when compared calculations from surface measurements.

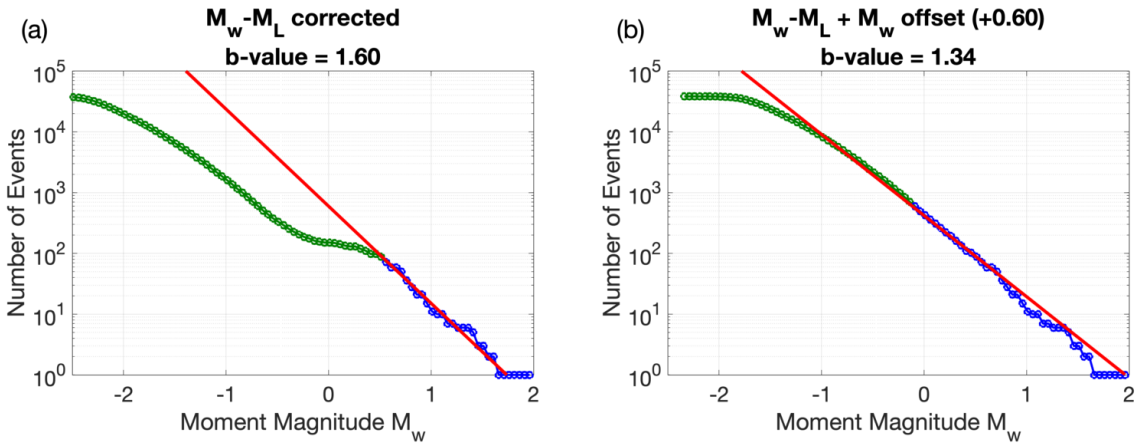

Figure 4.4: The magnitude-frequency distribution for PNR-1z events, with two corrections applied. (a) shows the distribution when the magnitudes of the larger events have been corrected using their surface M_L and the M_w-M_L relationship (Equation 4.2). There is clearly a discontinuity between the surface-derived M_w and the M_w given in the downhole catalogue. (b) shows the distribution when a correction of +0.6 has been applied to all events that weren't detected on the surface, and thus don't have a reliable M_L. This now gives a consistent b-value from $-1 < M_w < 2$.

Figure 4.3. The downhole array primarily measured event size through the moment magnitude M_w, which is based on the spectral content of the recorded waveforms. The amplitude of the low frequency plateau is used to calculate seismic moment, and thus moment magnitude (see Stork et al., 2014). In practise, however, there were several issues with the execution of the downhole measurement of M_w.

Once events with $M_L > 0$ began to occur, it became clear that M_w magnitudes were diverging from what was expected both theoretically and by preceding studies (Deichmann, 2006, 2017; Munafò et al., 2016), that being a linear relationship between local and moment magnitude with $M_w \propto 2/3 M_L$. M_w magnitudes were saturating at around a magnitude of around 1.0 (as shown by the blue triangles in Figure 4.3), and once the waveforms were inspected the reason became clear. Above a reported downhole M_w of 0, the displacement began to exceed the amplitude range of the instruments, and the waveforms began to clip. Any measurement based on the spectra of these clipped waveforms naturally gives an inaccurate value of the energy in the low frequency range, and thus an inaccurate M_w. This is combined with the lack of sensitivity of the downhole instruments, 15 Hz geophones, to low frequencies (< 10 Hz). At larger magnitudes, a higher proportion of energy of the waves is located in this low frequency band, and thus magnitudes will be underestimated further for the larger events (see Kendall et al., 2019).

Fortunately, the events for which these effects are most severe were recorded by the surface array, which was composed of mostly broadband instruments, which can give a more accurate measure of event magnitude. In the following work, I correct the M_w of events recorded on the surface using the surface-derived M_w-M_L relationship. This was calculated by a service company for CRL, and was given in the hydraulic fracture plan for PNR-2 (Cuadrilla Resources Ltd, 2019):

$$M_w = 0.66 M_L + 0.90 \quad . \tag{4.2}$$

This is consistent with theoretical derivations of M_w-M_L relationships (Deichmann, 2006, 2017) and relationships derived for small tectonic earthquakes (Munafò et al., 2016).

Further comparison of the downhole and surface-derived moment magnitudes reveals another issue with the downhole recorded M_w. Once the large magnitude events are corrected, there appears to be a clear break in the magnitude-frequency relationship, as shown in Figure 4.4a, at around M_w 0. The slope b is consistent between the two populations, however there is an apparent offset in the magnitudes either side of this break. With the larger event magnitudes being more reliable, this offset is indicative of the downhole-derived M_w systematically underestimating event moment magnitudes, even for the small $M < 0$ events, where clipping was not occurring. This could be due to several factors including the velocity or density at the source used in the calculation of M_w, the limited sensitivity in low frequencies of the downhole geophones, the unknown efficacy of coupling of the geophones in the wellbore, and the small azimuthal range that the downhole array covers. This last point arises from the radiation pattern correction term in the calculation of seismic moment, which assumes that an average value for the whole focal sphere can be used. For PNR, only a small section of the focal sphere is covered by the

downhole array. If events have a broadly similar mechanism (by broadly aligning on a fault or fracture zone for example) this may result in a systematic offset. This difference could also result from a processing artefact, as inappropriate methods of spectral transform can lead to similar inaccuracies in the spectral content of the waveforms (Stork et al., 2014).

The service provider who processed this data set (SLB) have not disclosed the exact method used in calculating M_w, and thus exactly which of these factors is responsible for the underestimation is difficult to determine. In short of recalculating magnitudes for over 30,000 events, the magnitude-frequency distribution can be made consistent across the population using a simple correction, which assumes that small events are all equally affected by the systematic underestimation. We apply a correction of 0.6 to the remaining smaller events for which there are were measurements of M_L from the surface. The resulting magnitude-frequency distribution with this correction applied is shown in Figure 4.4b, giving a consistent b-value of 1.3.

4.3 Maximum magnitude forecasting

In order to statistically forecast the maximum magnitude M_{max} for an earthquake population, it must be characterised by a statistical model. An example of an empirical model that can be used in this manner is the GR relation, given in Equation 4.1. If the magnitude-frequency distribution for a population of events is determined, it can then be extrapolated to larger numbers of events in order to estimate the likelihood of a large event occurring. To within a given level of confidence, the M_{max} can be found simply from the GR distribution, as the point at which $N = 1$ is naturally the largest magnitude event in the population. Multiple models have been developed which in part utilise this approach for seismicity induced by injection (e.g., Hallo et al., 2014; McGarr, 2014; Shapiro et al., 2010; van der Elst et al., 2016). They each relate the rate and size of earthquakes to the injected volume, though each take a slightly different approach. Combining the magnitude-frequency distribution and these quantities, the population can be forecasted for when the future total volume V_T is injected.

In this work, I examine two statistical frameworks, both of which have been previously applied to hydraulic fracturing datasets (Verdon and Budge, 2018): Hallo et al. (2014) seismic efficiency S_{eff}; and the Shapiro et al. (2010) seismogenic index SI.

4.3.1 Seismic efficiency

McGarr (1976) introduced a relationship between total injected volume and the size of the largest induced event, which was developed further in McGarr (2014). Cumulative seismic moment release ΣM_0 is related to total injected volume V_T by the shear modulus μ:

$$\Sigma M_0 = 2\mu V_T \quad . \tag{4.3}$$

This is based on the assumption that all deformation induced by the injected volume is released seismically, and so should be taken as an upper-bound. However, it is known that much of the

deformation induced by injection is aseismic (e.g., Bhattacharya and Viesca, 2019; Eyre et al., 2019). Hallo et al. (2014) define the "seismic efficiency" S_{eff} as the ratio of the observed moment, that which is released seismically, to the theoretical maximum described in Equation 4.3:

$$\Sigma M_0 = S_{eff} \mu V_T \quad . \tag{4.4}$$

S_{eff} can vary in time and space depending on the properties of the rock or the injection parameters, for example (e.g. Kwiatek et al., 2019). By rearranging Equation 4.4, we can calculate S_{eff} in real-time using the observed seismicity and the volume of fluid that has already been injected. The cumulative moment release, the GR b-value of the events, and the prospective total volume V_T can be used to estimate the magnitude of the largest event in an earthquake population M_{max} at time t (Hallo et al., 2014):

$$M_{max}(t) = \frac{2}{3}\left(\log_{10}\left(\frac{S_{eff}(t)\mu V_T\left(\frac{3}{2} - b(t)\right)}{b(t)10^{9.1}}\right) + \log_{10}\left(10^{b(t)\delta} - 10^{-b(t)\delta}\right)\right) \quad , \tag{4.5}$$

where δ is the probabilistic bin-size around M_{max}, which is included to ensure that mathematically, for a range of cumulative seismic moments and magnitudes of completeness M_{min}, there is only a single event with the largest magnitude. Verdon and Budge (2018) found that an extra factor of 0.5 must be added to the M_{max} value found from Equation 4.5 in order to account for the inherent uncertainty in drawing a single $N = 1$ point from the GR distribution, and ensure a 95% confidence in the forecasted M_{max}. Using the observed $b(t)$, $S_{eff}(t)$ and a planned V_T, the maximum magnitude can be forecasted during injection of a hydraulic fracture stage.

4.3.2 Seismogenic index

Shapiro et al. (2010) define the seismogenic index SI using the number of events $N_t(M)$ (occurring at time t that are larger than a magnitude M), the volume injected at this time V_t, and the GR b-value:

$$SI = \log_{10}\left(\frac{N_t(M)}{V_t}\right) + bM \quad . \tag{4.6}$$

If it is assumed that earthquake occurrence is an independent Poisson process, the probability P that an event larger than M does not occur for a total injected volume V_T is given by:

$$P = \exp(-V_T 10^{SI - bM}) \quad . \tag{4.7}$$

From this, the M_{max} at time t can be forecasted within a given confidence level χ:

$$M_{max}(t) = \frac{1}{b(t)}\left(SI(t) - \log_{10}\left(-\frac{\ln(\chi)}{V_T}\right)\right) \quad . \tag{4.8}$$

We use a χ of 0.95 (i.e., 95% confidence) in order to conservatively forecast the M_{max}.

These two frameworks were compared and contrasted in Verdon and Budge (2018) using a large hydraulic fracturing microseismic dataset. It was found that the S_{eff} method produced

more accurate forecasts in the range $1 < M_{max} < 2$, with SI generally overestimating M_{max}. For both methods, forecasted M_{max} was always above but generally less than 0.5 larger than the observed largest event magnitude when $M < 1$. However, when the largest observed event exceeded $M > 1$, the SI-derived forecasted M_{max} diverged quickly above 0.5 of the observed largest event magnitude, with the overestimation of M_{max} becoming more severe with increasing magnitude. This indicates that SI forecasts are generally more conservative when $M_{max} > 1$, whilst S_{eff} forecasts are more reflective of the observed population. We still compute SI-based forecasts, as that parameter has been more calculated than S_{eff} for previous cases of HF-IS (e.g., Dinske and Shapiro, 2013; Schultz et al., 2018), and thus there is value in providing a comparison between the two methods.

4.4 Methods and results

When running these models during operations, a choice must be made over the time window over which to calculate M_{max}. Including or excluding prior stages of injection will naturally change the S_{eff}, SI, or b, and thus change the resulting forecast. In effect, this choice brings with it an assumption of the hydraulic connectivity between populations of events. Each stage could be considered to be a separate event population, stimulated just by the injected volume of that stage (as in Verdon and Budge, 2018). However, if events are clearly connected, for example, occurring on the same structure, each stage cannot be treated in isolation, and event and injection data must be combined to get an accurate forecast.

Both "stage-by-stage" forecasts as well as combined models were computed during operations. For the case of PNR-1z, it is clear from the microseismicity that certain stages are reactivating the same features. Stages 1 through 3 are generally stimulating the same cluster at the toe of the injection well, whilst from Stage 18, injection is interacting with the NE fault zone. The fault zone could be assumed to be hydraulically connected, meaning successive injection would result in more moment release and larger events, increasing the forecasted maximum magnitude. If this assumption is reasonable, stage-by-stage M_{max} forecasts would not accurately reflect the observed seismicity, and would under-predict M_{max}. Combining data from multiple stages should then give more accurate forecasts.

4.4.1 Stage-by-stage forecasts

Figures 4.5, 4.6, and 4.7 show the results of the stage-by-stage forecasts. Here, time steps of 10 minutes are used to calculate S_{eff} and b, and evaluate the forecasted M_{max}. We use a shear modulus of 25 GPa, which is based on measured values for shales, including samples from the Bowland (Clarke et al., 2019b; Herrmann et al., 2018; Kohli and Zoback, 2013). b is computed here using the maximum-likelihood approach of Aki (1965). To find the magnitude of completeness M_{min}, a Kolmogorov-Smirnov test at a 10% acceptance level is used. This assesses the quality of

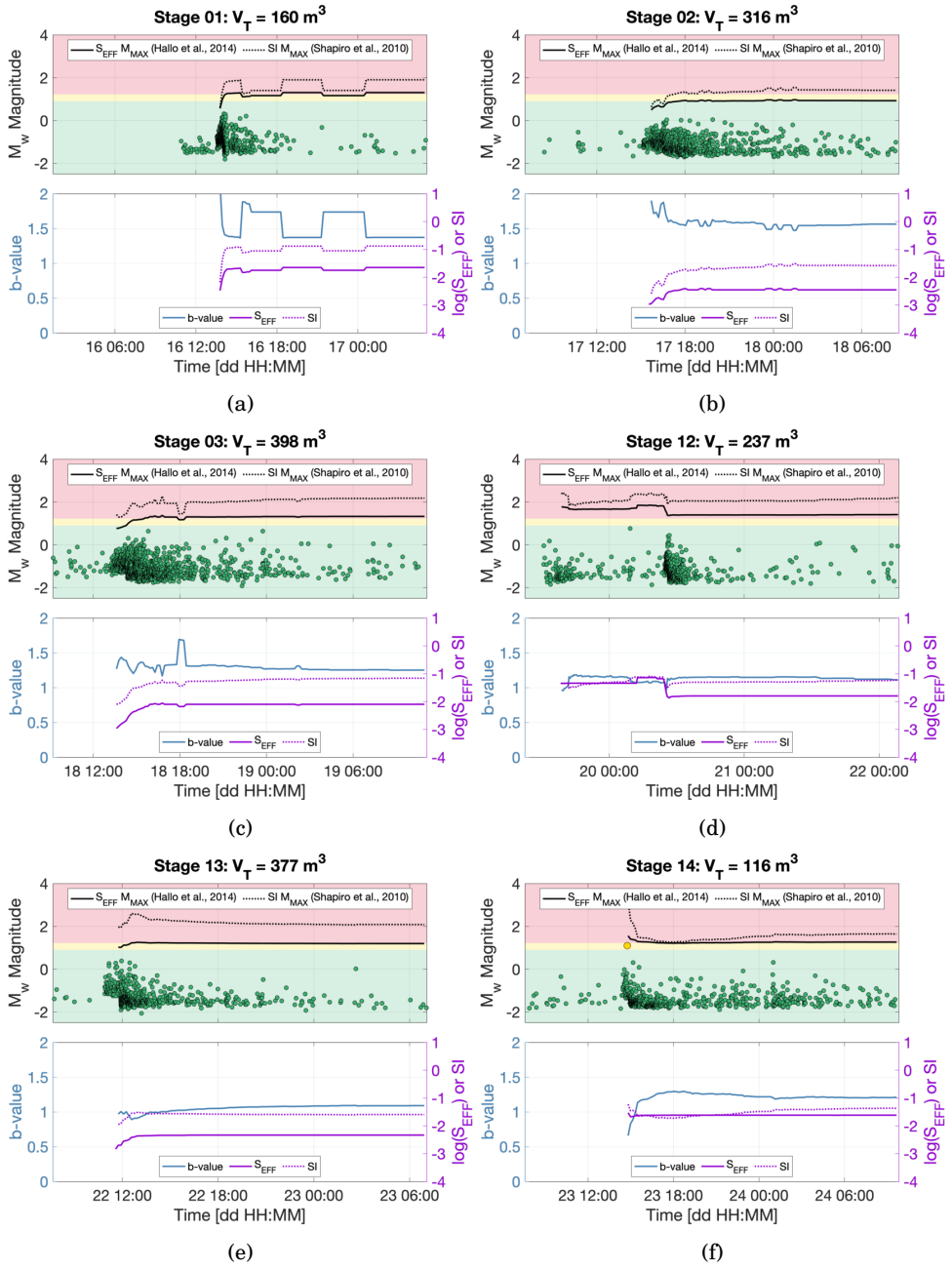

Figure 4.5: Maximum magnitude stage-by-stage forecasts, calculated in 5 minute increments, for Stages 1 through 14 of PNR-1z operations. Each figure shows the forecasts in the upper panel, as black solid or dotted lines, with events shown as circles coloured by magnitude. Background colours show how each event is classified with respect to the TLS thresholds, converted from M_L to M_w using Equation 4.2. The tile shows the total volume V_T used in the calculation of M_max, which corresponds to the fluid injected during that stage. The bottom panel of each figure shows the running GR b-value, S_{eff}, and SI.

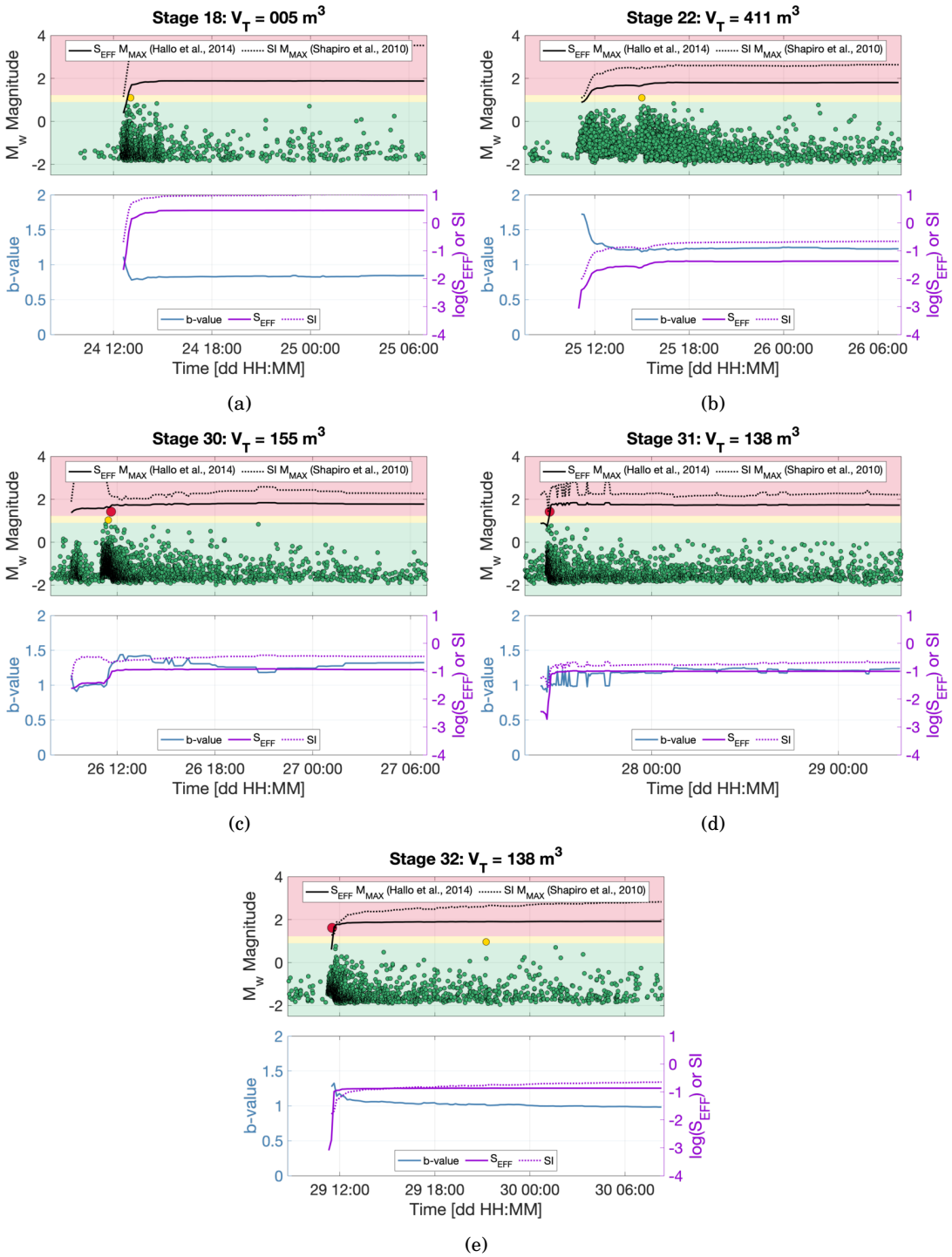

Figure 4.6: Maximum magnitude stage-by-stage forecasts, calculated in 5 minute increments, for Stages 18 through 32 of PNR-1z operations. They are formatted as in Figure 4.5.

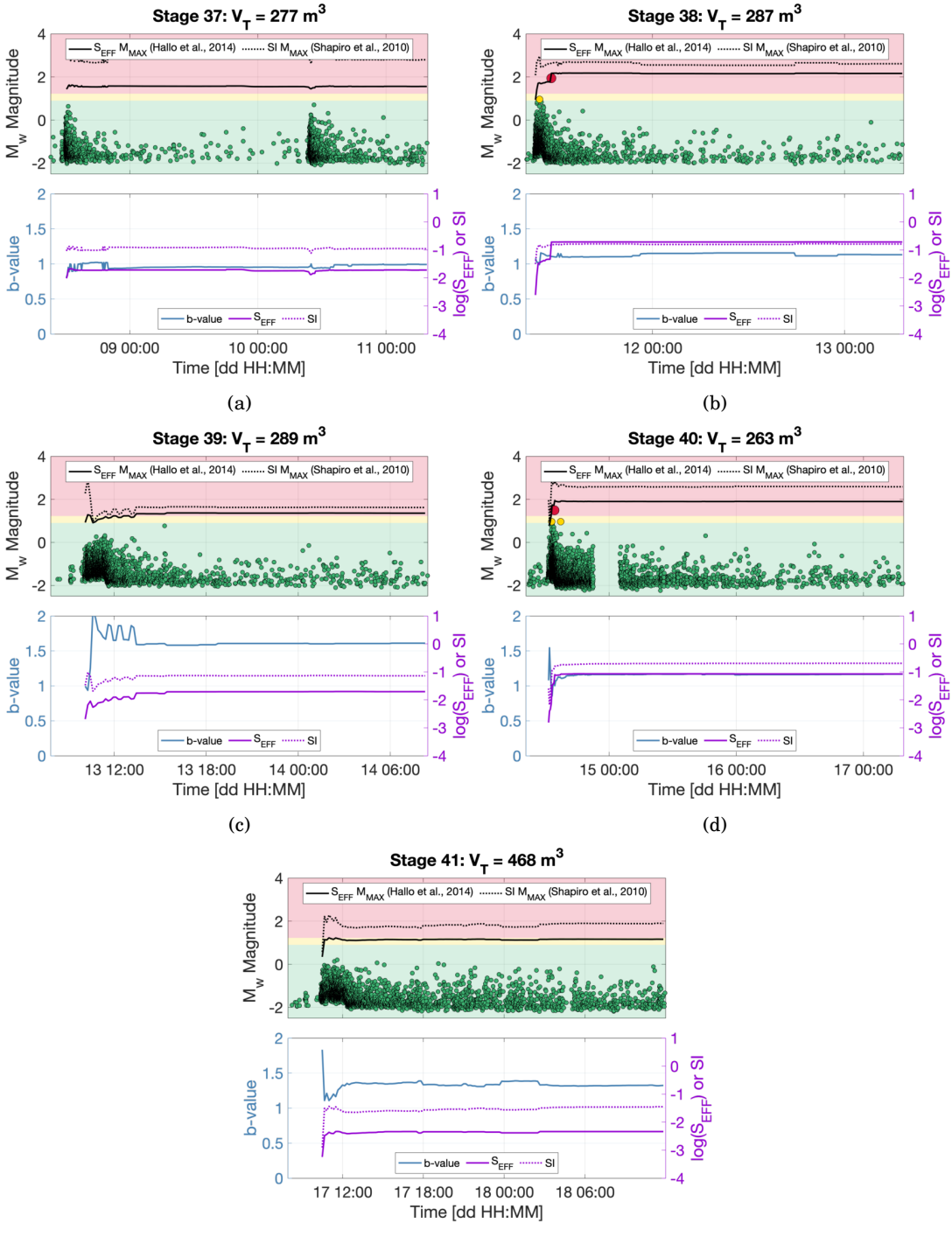

Figure 4.7: Maximum magnitude stage-by-stage forecasts, calculated in 5 minute increments, for Stages 37 through 41 of PNR-1z operations. They are formatted as in Figure 4.5.

the fit between the observed magnitude distribution and the GR relation (as in Williams and Le Calvez, 2013). For the whole population of events observed at PNR-1z, with magnitudes corrected as described above, this gives a b-value of 1.3, as shown in Figure 4.4b. Magnitudes are binned in 0.05 increments, and a minimum number of events to begin calculating a b-value is set at 50.

Stage-by-stage forecasts for Stages 1 to 3 and 12 to 14 (Figure 4.5) show that forecasts were appropriately conservative for these early stages, with the S_{eff}-derived M_{max} just above the amber light threshold (M_L = 0.5). Forecasts are within M_w 0.1 of the recorded TLS event during Stage 14. SI-derived M_{max} is consistently larger than the S_{eff}, with forecasts repeatedly exceeding M_w 2.0 even during these relatively quiet stages.

During Stage 18, both S_{eff} and SI are far higher than any other stage, due to the large number of events for the small volume of fluid injected. This results in a forecasted M_{max} that does forecast the amber light event that took place during that stage (Figure 4.6). Events that took place after Stages 22 and 31 are both successfully forecasted using the S_{eff} method, with the M_{max} within 0.5 of the resulting largest event. In contrast, stage-by-stage forecasts for Stages 30 and 32 do not forecast the largest event accurately, with M_{max} during injection being over 0.5 less than the eventual largest event (Figure 4.6).

The Stage 38 M_L 1.6 event was also not forecasted by the S_{eff} forecast during injection, though only by 0.2 (Figure 4.7). The red-light event during Stage 40 was forecasted using the stage-by-stage method, with a S_{eff}-derived M_{max} of M_w 1.7 from early in the injection and a event magnitude of M_w 1.5. Stages 37, 39 and 41 produced no events above the amber-light threshold, and S_{eff} forecasts remained around a M_{max} of M_L 0.5. SI-derived forecasts generally do encompass the large events which are missed by the S_{eff}, however they frequently overestimate the magnitude of the observed seismicity by a significant amount.

4.4.2 Combined forecasts

Combining event and injection data of the heel stages (37 through 41), as shown in Figure 4.8, results in the S_{eff}-derived M_{max} accurately forecasting the M_L 1.6 event to within 0.1. SI forecasts remain high, overestimating the observed seismicity by 1.0 magnitude units. When data from all stages is combined (Figure 4.9), the forecasted M_{max} remain near constant at M_w 2.4 after the first period of operations, with the S_{eff} M_{max} being around 0.4 above the eventual largest magnitude event (M_w 2.0).

4.5 Discussion

4.5.1 Effect on operations

This forecasting approach was conducted live during operations and results were presented to the operator in real-time. Whilst still experimental, they became a part of the evidence contributing to operational decision-making and restart decisions when TLS events paused injection. It was

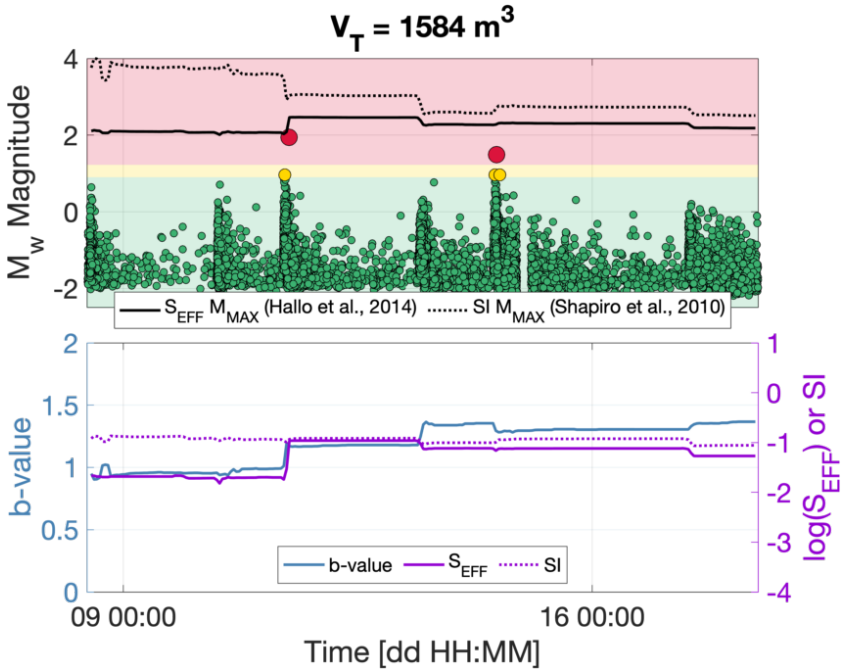

Figure 4.8: Maximum magnitude combined forecasts, calculated in 2 hour increments. These forecasts use data for Stages 37 through 41 of PNR-1z operations, those which occurred prior to the largest event during operations. They are formatted as in Figure 4.5.

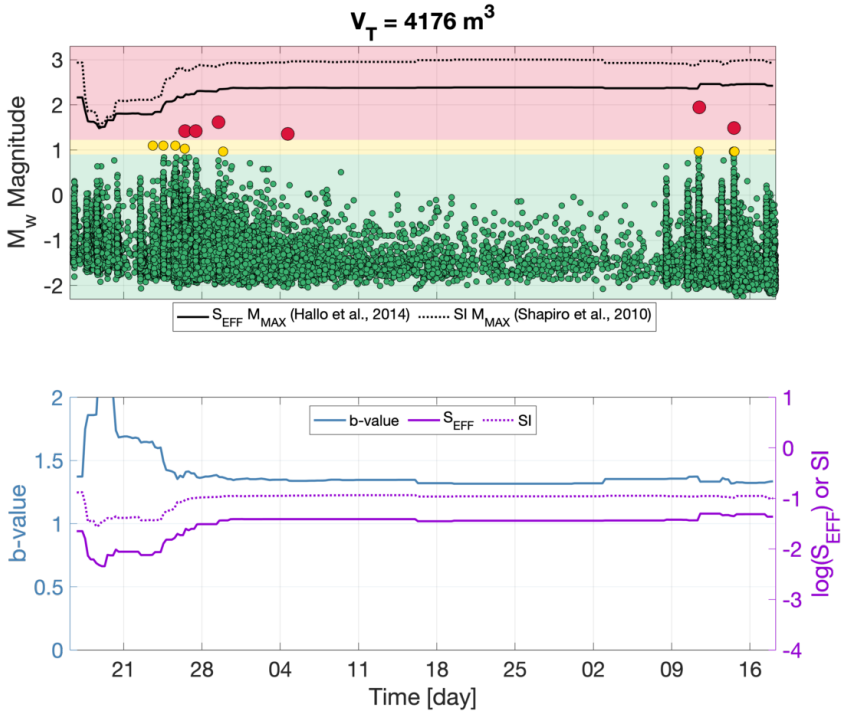

Figure 4.9: Maximum magnitude combined forecasts, calculated in 2 hour increments, for all injection stages of PNR-1z operations. They are formatted as in Figure 4.5.

particularly relevant to the decision to restart injection at the heel most stages in December 2018, after the month hiatus.

The placement of proppant is paramount to a successful injection stage, as after injection pressure is reduced in situ stress acts to close the newly created fractures, and thus reduce the newly enhanced permeability next to the well. However, before any sand can be added to the injection fluid, around 100 m^3 of fluid must be pumped in order to initiate fracture growth. The majority of proppant is injected near the end of the stage as proppant concentrations are gradually increased throughout pumping. Stages halted due to the occurrence of TLS events have effectively been wasted, as the majority of proppant has not been placed. Seismic risk, through the injection of fluid, has in effect been increased unnecessarily.

Forecasts produced during the hiatus period, which did not fully account for the disparities in the downhole moment magnitudes (section 4.2.1), showed that events much larger than $M \sim 2$ were not expected on the NE fault given the observed S_{eff} and b-values (as shown in Clarke et al., 2019a). Events above the TLS thresholds were expected, however, which would limit the placement of proppant of stages that may interact with the fault. These findings were reported to the OGA in November 2019, and the operator restarted injection in early December 2019 at the heel most stages of the well (37-41), in the hope that these sleeves were beyond the eastern extent of the fault, an assumption that was supported by the microseismic event locations. These forecasts supported the operator's conclusion that even if the stages did interact with the fault, the resulting seismicity would still fall within the objectives of the regulator – minimising any shaking felt on the surface (events with $M_L > 2$). As described above, these stages did in fact still connected to the NE fault, resulting in two more TLS red light events, including the M_L 1.6 that was felt by a few members of the public near to the site. Magnitudes did remain within forecasted levels (Clarke et al., 2019a), even though this real-time forecasting did not benefit from the corrections to the downhole M_w measurements.

With the updated results shown here, combined M_{max} forecasts give M_w 2.4 (M_L 2.3), within 0.4 of the observed largest event, the M_L 1.6 (M_w 2.0). As the S_{eff}-based forecasts are the upper 95% confidence value of M_{max} given in Equation 4.5, applied through the addition of 0.5, the output of Equation 4.5 is consistent with the observed seismicity. This further supports this method for use in real-time, though these updated results may naturally have affected decision-making during PNR-1z operations.

4.5.2 Stage-by-stage vs. combined forecasts

Whilst stage-by-stage forecasts were relatively successful for early stages during PNR-1z (Figure 4.5), this manner of forecasting each stage of injection was not appropriate for later stages (Figure 4.7), where larger events occurred soon after or during injection. This observation, when combined with the clustering of events along a single seismogenic feature from Stage 18, supports that each stage cannot be treated in isolation to guarantee successful M_{max} forecasts. With

the NE fault running obliquely to the well, it is reasonable to assume that adjacent stages of injection are stimulating parts of the same feature. Repeated injection into the same zone will have a compounding effect, and thus the forecasted largest event magnitude will increase with successive stages.

Combining data for the multiple stages which intersected the fault (Figures 4.8 and 4.9) gives more accurate forecasts, as the S_{eff} and b are better characterised for the seismogenic feature, and V_T is larger, giving larger M_{max}. In the case studied by Verdon and Budge (2018), the small fault structures present were oriented almost perpendicular to the well direction, and thus only one to two stages stimulated activity on each feature (as described in Kettlety et al. (2019)). This provides an explanation as to why the stage-by-stage treatment was successful in the Verdon and Budge (2018) case study and not for PNR-1z operations. This result emphasises the necessity of conducting these forecasts alongside analysis of the microseismic events locations and an understanding of the geomechanics at each injection site. How well connected seismogenic structures are to each stage of injection must be considered in order to account for multiple stages feeding into the same faults.

4.5.3 Seismic efficiency and seismogenic index

The results shown here provide a good case study to compare the effectiveness of both frameworks used to compute M_{max}. The SI-based forecasts are consistently higher, and thus more conservative, than the S_eff-based forecasts across all scenarios shown above, consistent with Verdon and Budge (2018). The evolution of SI mirrors that of $\log(S_{eff})$ as expected, with the number of events naturally related to the total seismic moment release. When forecasts are compared to the observed seismicity, however, SI gives forecasts which generally over-estimate M_{max}, sometimes by multiple magnitude units. This further supports S_{eff}-based forecasts as more realistic estimates of largest event magnitude after injection, and thus their utility as a tool to mitigate HF-IS. SI tended to produce forecasts with events close to or exceeding the objectives of regulator in enforcing a TLS with such low magnitude thresholds. Thus, many more stages would not have been completed at PNR-1z had injection been curtailed when SI forecasts exceeded this threshold.

The maximum SI for any stage during PNR-1z was -0.4, for Stage 30 (Figure 4.6c), but was around -1 for the majority of stage-by-stage and combined forecasts. An $SI \sim -1$ is on the high end of the range of values for several hydraulic fracturing sites in Canada (Schultz et al., 2018; Verdon and Budge, 2018), and similar to many geothermal sites (Dinske and Shapiro, 2013). It is also greater than several hydraulic fracturing sites studied in Dinske and Shapiro (2013), at Cotton Valley and the Barnett shale, which had $-9 < SI < -3$. These sites in Texas show relatively very little seismicity for the fluid volumes injected, and indicates clearly the contrast in the likelihood for HF to stimulate fault activation in different geological settings. The SI differences are representative of the causative factors of HF-IS, including differences in the

prevalence and proximity of critically stressed faults, stress anisotropy, and geomechanical or frictional properties of the host rock.

4.6 Conclusion

Microseismic monitoring of Preston New Road hydraulic fracturing operations provided a unique opportunity to apply real-time statistical maximum magnitude forecasting, in an effort to aid in operational decision-making and avoid induced seismicity. The strict TLS in place in the UK leads operators to proactively avoid any seismogenic structures, and identify areas that may produce events which exceed the low thresholds before large events occur.

The Gutenberg-Richter b-values were combined with microseismic event and injection data to populate a predicative model of future seismicity, given some volume of fluid to be injected. Two models were tested, each with its own method of characterising the amount of seismicity per unit volume of fluid injected. These models were largely successful in forecasting the magnitude of the largest events that occurred during operations. The Hallo et al. (2014) seismic efficiency model provided more accurate forecasts than those based the Shapiro et al. (2010) seismogenic index, with the latter generally overestimating the largest event magnitude.

Forecasts were also better able to forecast M_{max} when data from multiple stages were combined, accounting for the interconnected nature of the stimulated seismicity. The short time between large events occurring and the start of injection implies that adjacent stages feed into the same features, and compound the effect of injection on the largest event magnitude. This is consistent with the microseismic observations, in which multiple stages repeatedly interacted with a seismogenic feature. Single stages cannot be treated in isolation in this case.

The results of these models were taken into account by the operator of PNR-1z and the UK regulator, and had an impact on operational decisions. Whilst seismicity did continue after mitigating actions were taken by the operator, the seismicity observed fell within the forecasted values. Analysis conducted after operations into the discrepancy between the downhole and surface measures of moment magnitude, a key quantity in the calculation of M_{max} using the Hallo et al. (2014) method, affected the forecasts such that the M_{max} values were almost exactly that of the observed largest events. The issues surrounding the robust calculation of M_w are further highlighted in this study, and have proven key to accurate M_{max} forecasts.

Though more advanced mitigating techniques are being developed (Kwiatek et al., 2019; Mignan et al., 2017), simple TLSs are currently the most ubiquitous form of regulation of HF-IS. Though the response to the exceedance of the magnitude thresholds is in effect entirely retroactive, real-time microseismic monitoring and analysis, combined with the forecasting approaches detailed above, can give far more information to the operator to proactively respond to and mitigate induced seismicity.

CHAPTER 5

INTERPRETATION AND ANALYSIS OF PRESTON NEW ROAD PNR-2 FAULT ACTIVATION

The contents of the following chapter has been submitted for review as *The M_L 2.9 August 2019 earthquake in Lancashire, UK, induced by hydraulic fracturing during Preston New Road PNR-2 operations* by Tom Kettlety, James P. Verdon, Matthew Hampson, and Lucy Craddock to Seismological Research Letters in 2020. What is presented below represents a version of the paper prior to its submission, and thus may differ in its content from the final published work. The manuscript was written by myself, and edited by James Verdon. I produced all figures and conducted all of the modelling that is shown below. Matthew Hampson and Lucy Craddock provided details of operations and information regarding the acquisition and analysis of the dataset used here.

This paper uses the methods applied in chapters 2 and 4 on a recent, and highly consequential, case of hydraulic fracturing-induced fault activation. We analyse and interpret the earthquakes that occurred at Preston New Road, Lancashire, in 2019, those which in part motivated the UK government to impose a moratorium on fracking. This very well monitored sequence provides an opportunity to test some of the models used in the previous chapters, and see if they are able to still function after a notable increase in the size of induced events.

Hydraulic fracturing at Preston New Road, Lancashire, UK, in August 2019 induced several felt earthquakes, including two events above local magnitude M_L 2.0. After the largest event occurred, with a magnitude of M_L 2.9, hydraulic fracturing at the site was halted. Subsequently, the UK government has imposed a de facto moratorium on fracking pending further scientific investigation. In this study, we provide the first analysis of the microseismic observations made during this case of hydraulic fracturing-induced fault activation. More than 57,000 microseismic events were detected during operations using a downhole geophone array, with a minimum magnitude of M_w −2.6. Locations and magnitudes revealed the growth of hydraulic fractures and their interaction with several preexisting structures. The spatiotemporal distribution of events suggests that a hydraulic pathway was created between the stimulated zone and a nearby NW-SE striking fault, on which the largest events occurred. The aftershocks of the M_L 2.9 event clearly delineate the rupture plane, with their spatial distribution forming a halo of activity around the rupture area of the mainshock. As the fault was activated, the magnitude distribution became distinctly bimodal, with a much lower Gutenberg-Richter b-value for events above M_w 0 than below, suggesting a break in scaling between a hydraulic fracturing regime and a tectonic regime of seismicity. This poses a challenge for real-time monitoring systems and mitigation strategies which rely on the assumption that the nature of microseismicity observed during injection can be extrapolated to forecast the behaviour of the system hours or days later. The activated fault was also very well oriented for failure in the regional stress field, significantly more so than the fault that was activated during previous operations at the adjacent PNR-1z well in 2018. The differing orientations within the stress field likely explain why this PNR-2 fault produced larger events, despite receiving a smaller pressure perturbation, when compared to the 2018 sequence. This indicates that in situ stress conditions play a key role in controlling the magnitudes of events induced by hydraulic fracturing.

5.1 Introduction

Earthquakes caused by subsurface fluid injection have been widely reported globally, being associated with various industries including geothermal energy (Deichmann and Giardini, 2009; Grigoli et al., 2018; Kim et al., 2018)], underground waste water storage (Keranen et al., 2013), and CO2 sequestration (Stork et al., 2015). For many years, hydraulic fracturing (HF) of low-permeability reservoirs was assumed to pose a relatively low risk of induced seismicity, with the National Research Councils (2012) suggesting that "the process of hydraulic fracturing ... does not pose a high risk for induced felt seismic events ($M > 2$)". Since then, however, induced seismicity has been observed in the United States (Holland, 2013; Skoumal et al., 2018), the Western Canadian Sedimentary Basin (WCSB; Bao and Eaton, 2016; Kao et al., 2018; Schultz et al., 2015), and the Sichuan basin, China (Lei et al., 2017; Meng et al., 2019). Overall, cases of hydraulic fracturing-induced seismicity (HF-IS) are rare when compared to the total number

of stimulated wells drilled, for example Atkinson et al. (2016) showed that less than 1% of stimulated wells in the WCSB are associated with $M > 3$ events. The occurrence of HF-IS is extremely variable between different basins (van der Baan and Calixto, 2017; Verdon et al., 2016), and even between different formations within the same basin (Skoumal et al., 2018).

In the UK, only 3 wells have been hydraulically fractured within the Carboniferous Bowland Shale formation, and all have resulted in events of sufficient size to be felt by nearby populations. The Bowland is one of the many basins which stretch across northern England, UK created during the extensional environment that existed in the Early Carboniferous. Later Varsican compression in the region created the fold-and-thrust belt, characterised by NE-SW trending en echelon faults and a thickening of the basinal strata.

The wells lie within a few km of each other on the Fylde Peninsula in Lancashire, NW England, and were operated by Cuadrilla Resources Ltd. (CRL). The first of these was the Preese Hall well, which was stimulated in 2011, producing an M_L 2.3 event (Clarke et al., 2014). This led to the imposition of a moratorium for over a year by the government, after which a Traffic Light Scheme (TLS) was introduced to mitigate induced seismicity at future sites (Oil and Gas Authority, 2018). This scheme has an amber threshold at M_L 0, and a red threshold at M_L 0.5, making it the strictest threshold to be used in the regulation of hydraulic fracturing anywhere in the world (Kendall et al., 2019).

In 2018 CRL drilled two horizontal wells into the Bowland Shale at the Preston New Road (PNR) well site, approximately 4 km to the south of Preese Hall. The first of these wells, PNR-1z, was stimulated in late 2018. Several events with magnitudes larger than M_L 0.5 occurred, entailing pauses in operations under the TLS, and the largest event to occur had a magnitude of M_L 1.5 (Clarke et al., 2019a; Kettlety et al., 2020).

In August 2019, CRL commenced the stimulation of the PNR-2 well, which lies approximately 200 m shallower, and 200 m to the north of the PNR-1z well (Figure 5.1). However, operations were halted after the occurrence of a M_L 2.9 event at 0830 local time on August 26, after only 7 of the planned 40 stages of injection had been completed. The UK government has subsequently imposed a further moratorium on hydraulic fracturing, pending further scientific analysis (BEIS, 2019). As the first onshore hydraulic fracturing site in the UK since 2011, the PNR wells were closely monitored by both CRL and the British Geological Survey (BGS). This included surface and downhole microseismic arrays, monitoring of surface and groundwater chemistry, air quality control, and local traffic monitoring. Whilst the relatively large NE-SW trending reverse faults are present in the basin, and were identified from reflection seismic surveys of the PNR site (Cuadrilla Resources Ltd, 2019), none of the seismicity that occurred during the hydraulic fracturing at PNR is clearly associated with these pre-existing structures.

The effectiveness of TLSs as a method to mitigate HF-IS is the subject of on-going debate and research (Baisch et al., 2019; Bosman et al., 2016; Clarke et al., 2019a), though they are still the most common method by which HF-IS is regulated. However, they are relatively simplistic

in their operation, with decisions taken solely on the magnitude of the largest event. Dedicated high-resolution microseismic monitoring can facilitate the direct observation of fault activation through, for example, the spatial alignment of events along fault planes (e.g., Eyre et al., 2019; Kettlety et al., 2019), a drop in the Gutenberg-Richter (GR) (Gutenberg and Richter, 1944) b-value (e.g., Kettlety et al., 2019; Verdon and Budge, 2018), or an increased seismicity rate (Clarke et al., 2019a; Maxwell et al., 2008, 2009; Verdon and Budge, 2018). This could give operators the opportunity to change the injection program to mitigate further interaction with a suspected fault by, for example, skipping stages along the well, reducing injection rates or volumes, or varying the viscosity of the fluid. More complex injection schemes to mitigate IS have been developed and are the subject of ongoing research (e.g., Hofmann et al., 2019). When combined with these methods of observation and real-time analysis, simple TLSs can be adapted into more appropriate mitigation schemes, such as the adaptive TLSs proposed by Mignan et al. (2017). The use of such an approach has been demonstrated by Kwiatek et al. (2019), and was applied at the PNR-1z well, as described by Clarke et al. (2019a).

One such method of real-time analysis and operational decision-making is statistics-based maximum magnitude forecasting. Like tectonic earthquakes, HF-IS is typically observed to follow the empirical GR distribution (van der Elst et al., 2016) with number of events as a function of magnitude following a power law distribution. This can be combined with the observation that the total number of events (Shapiro et al., 2010) or cumulative seismic moment (Hallo et al., 2014) scales with the total injected volume. Therefore, the current rate of seismicity as a function of injection volume can be extrapolated to the planned total volume to be injected, from which the maximum expected magnitude of an event in the population can be estimated using the GR distribution. The real-time application of these methods relies on the assumption that the seismicity during injection is statistically representative of events that occur after injection has ceased. In effect, for these methods to be functional, they assume that seismicity that is symptomatic of fault activation (as opposed to hydraulic fracture growth) can be detected prior to large events occurring, and quickly enough to enable some proactive measure to be taken. Kwiatek et al. (2019) demonstrated the use of this approach to guide operational decision-making at a geothermal project in Helsinki, Finland, and Clarke et al. (2019a) used this approach to guide decision-making during the stimulation of the PNR-1z well in 2018, accurately forecasting the M_L 1.5 event that occurred.

In this study, we describe in detail the HF-IS that occurred during stimulation of the Preston New Road PNR-2 well in August 2019. We show how the spatiotemporal evolution of the microseismicity images the activation of the fault system on which the largest events occurred, and how this system relates to the fault zone encountered by previous operations at the site (Clarke et al., 2019a). We then examine the changes in magnitude distributions and seismicity rates between injection stages and show how the maximum magnitude forecasting methods were again used to guide operational decisions.

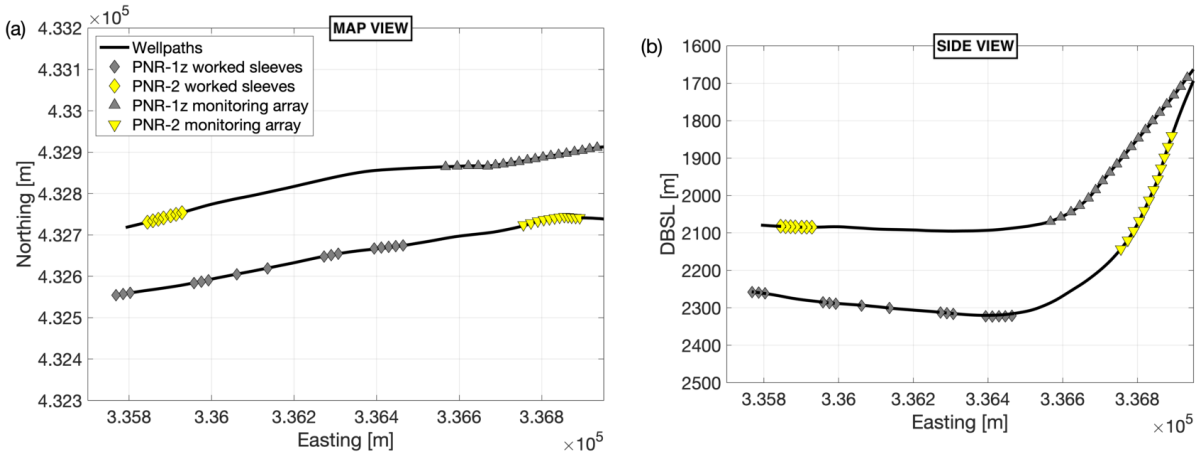

Figure 5.1: Map (a) and depth (b) view of the well paths and sliding sleeve locations worked during hydraulic fracturing at Preston New Road in 2018 (PNR-1z) and 2019 (PNR-2). Sleeves (shown as diamonds) are numbered from the toe (the furthest extent of the well) to the heel of the well. Microseismic monitoring stations are shown as triangles. During PNR-2 operations in 2019, only the first 7 sleeves were worked.

Variability in the behaviour of induced seismicity has been linked to the relative orientations of faults and stress (e.g., Göbel, 2015), with high magnitude seismicity more likely to occur on faults better oriented for failure in the regional stress field (Alt and Zoback, 2017; Keranen et al., 2013; Schoenball et al., 2018; Skoumal et al., 2019). We conclude this paper by comparing the orientations of the two faults that reactivated during stimulation of PNR-1z and PNR-2 operations within the regional tectonic stresses, showing that difference in fault stability are likely to have contributed to the differences in fault activation behaviour between the two operations.

5.2 Hydraulic fracturing at Preston New Road

The Preston New Road site consists of two horizontal wells, drilled to a depth of between 2 and 3 km into the uppermost 500 m of the Carboniferous Bowland Shale, a thick (1.2 km at PNR) natural gas bearing formation which extends across the north of England (Andrews, 2013; Clarke et al., 2018). The wells are located in the south of the Fylde peninsula, in the north west of England, near the town of Blackpool, Lancashire. The first and deeper horizontal well is denoted PNR-1z, and the second well, drilled approximately 200 m above and to the north of PNR-1z, is denoted PNR-2. PNR-1z was hydraulically fractured between October and December 2018, monitored by a surface array of 11 broadband seismometers and short period instruments, and 24 downhole geophones placed in the PNR-2 well (Clarke et al., 2019a).

Hydraulic fracturing of PNR-2 began in August 2019. Monitoring was provided by the same surface array as used for PNR-1z (Figure 1 of Clarke et al. (2019a)), and the downhole monitoring was provided by 12 geophones installed in the build section (i.e. where the well deviates from

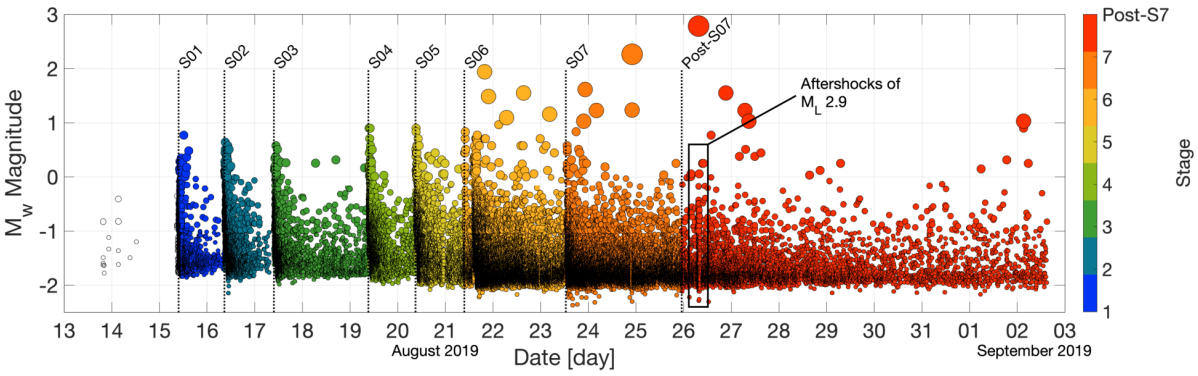

Figure 5.2: Evolution of seismicity for operations at PNR-2. The start of pumping each stage is highlighted by dotted lines and is accompanied by an increased rate of seismicity. After Stage 6 (S06) the magnitude of events markedly increases, indicating the interaction between injection and the fault zone. Events are denoted to be "Post-Stage 7" two days after the stage was injected. The M_L 2.9 occurred more than 48 hours after the injection of Stage 7. The small number of events which took place before Stage 1 were the result of injection tests through Sleeve 1.

vertical to horizontal) of PNR-1z (Figure 5.1).

The first 6 stages were pumped without incident from August 15th to 21st 2019. However, several hours after the end of the 6th stage, an event with M_L 1.6 occurred, followed by an M_L 1.0 event the next day. The 7th stage was pumped on the August 23rd, with a reduced volume and increased fluid viscosity, with the intention of limiting the spatial extent of fracture growth and thereby reducing the likelihood of interacting with faults. No $M_L > 0$ events were recorded during the injection this stage. However, several hours after the stage, an M_L 1.1 event was recorded, and this was followed by an M_L 2.1 event on August 24th, and a M_L 2.9 event on August 26th. The full temporal evolution of the seismicity is shown in Figure 5.2. In total over 58,000 microseismic events were detected and located by a processing contractor (Schlumberger Ltd).

5.2.1 Local and moment magnitudes

Accurate measurement of earthquake magnitudes in real time is a significant challenge when monitoring induced seismicity (Kendall et al., 2019). At the PNR site, different magnitude scales were used for the surface and downhole arrays. The primary purpose of the surface array was to administer the TLS, which is defined using the UK local magnitude M_L scale (Luckett et al., 2019). However, this scale incorporates near-surface attenuation and free-surface effects, and so is not calibrated for downhole instruments. Therefore, the downhole array provided moment magnitudes, M_w. Because these scales diverge at low magnitudes (Kendall et al., 2019), a relation was developed by the operator using data from PNR-1z (Cuadrilla Resources Ltd, 2019):

$$M_w = 0.66 M_L + 0.90 \quad . \tag{5.1}$$

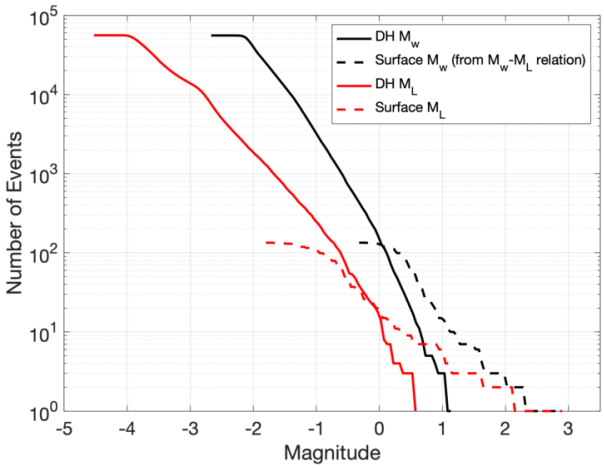

Figure 5.3: Magnitude-frequency distributions for events recorded during PNR-2. Magnitudes shown here are computed in two different ways. Solid lines show the moment (black) and local (red) magnitude calculated by the service company using the downhole array. The red dashed line shows the local magnitude of events as reported by the BGS using the surface array, and black dashed line shows the corresponding moment magnitude derived from the M_w-M_L relationship for PNR (Equation 5.1). A step can be seen between the downhole and surface derived moment magnitudes at around $M = 0.3$, indicative of a processing or instrumental artefact.

This was derived using simple linear regression, comparing the M_L and M_w values measured from the surface array during operations.h This is consistent with the theoretical derivations of M_w-M_L for small earthquakes (Deichmann, 2006, 2017), and is similar in form to that found by Munafò et al. (2016).

The larger events that occurred during stimulation of both wells produced subsurface motions that were beyond the dynamic range of the downhole geophones, on which instrumental settings were at their most sensitive to enable detection of the smallest magnitudes possible, and at frequencies that were below the range of the 15 Hz geophones. Therefore, the downhole M_w estimates for the largest events were systematically underestimated (e.g., Viegas et al., 2012). Thus, the relation given in Equation 5.1 was calculated using M_w and M_L magnitudes that were found using only surface station data. Due to the unreliable nature of the downhole-derived M_w for events with $M_w > 0$, we use more accurate M_L values from the surface array and Equation 5.1 to calculate M_w for events which were detected at the surface.

When the downhole and surface-derived moment magnitudes are compared, however, another issue with the downhole-recorded M_w is revealed, as shown in Figure 5.3. Once we apply the M_w-M_L relationship using the surface M_L measurements, a break in the magnitude frequency relationship becomes evident for the M_w values, at around $M = 0.3$. This indicates that there is a systematic offset between the moment magnitudes measured using the downhole instruments and the surface. Several factors could be leading to this, including the velocity or density at the source used in the calculation of M_w, the use of an inappropriate spectral transform method,

the limited sensitivity from low frequencies of the downhole geophones, the unknown efficiency of coupling of the geophones in the wellbore, and the small azimuthal range that the downhole array covers.

We are reporting on the magnitudes as they were delivered to the operator and regulator during operations. Thus, it is beyond the scope of this analysis to recalculate moment magnitudes for over 55,000 events. The population can be made consistent however in assuming the downhole magnitudes all suffer from a consistent offset, and a simple linear correction can be applied to all events were not detected on the surface. This would act to remove the step visible in Figure 5.3, and make M_w magnitudes consistent across the whole population. We apply an correction of 0.2 magnitude units to all events not recorded by the surface array, which gives the consistent magnitude-frequency distribution across the magnitude range. This appears effective, though is simplistic, with a preferable solution being a full recalculation of downhole moment magnitudes. However, as that was not possible during operations, we apply a simple correction that would have been possible. Further investigation into this issue is ongoing and will be the subject of future work.

5.3 Evolution of seismicity during PNR-2 operations

Figure 5.4 shows a map and cross section of all of the events with $M_w > -1.5$ coloured by stage, with the main features discussed hereafter annotated. Figure 5.5 shows the temporal evolution of the microseismicity, from the first 5 stages that did not produce $M_L > 0$ events, through to the latter stages where larger events occurred. Hypocentral locations of events on a stage-by-stage basis are shown in the supplementary materials.

Stage 1 was completed with no events exceeding M_L 0, and the majority of events spatially distributed symmetrically in a 300 m long linear feature centred on the injection point, typical of "normal" HF. These are the first events to occur in the centre of the "NS cluster" shown in Figure 5.4. Events extended NNW-SSE, along the maximum horizontal stress direction, $\theta_H = 170°$ (Clarke et al., 2019b), consistent with the orientation of HF growth during PNR-1z. These events are therefore indicative of the growth of hydraulic fractures from the well. A smaller population of events did begin to extend on a second lineament around 50 m west and 100 m deeper than Sleeve 1, extending primarily south of the well. These events are located the same lateral position as a small planar feature that was identified by the operator during PNR-1z operations.

Microseismicity during Stages 2 and 3 mostly occurred in the same NS cluster, extending the hydraulic fractures by around 100 m to the north. A large cluster of events did form to the west of the well, around 50 m further west than the smaller lineament observed during Stage 1. This "W cluster" is at a similar depth to PNR-2, but is offset laterally from the toe of the well by around 100 m. This cluster could be the result of further hydraulic fracture development; however, it is not clear why there is a gap in hydraulic fracture growth between the point of injection and

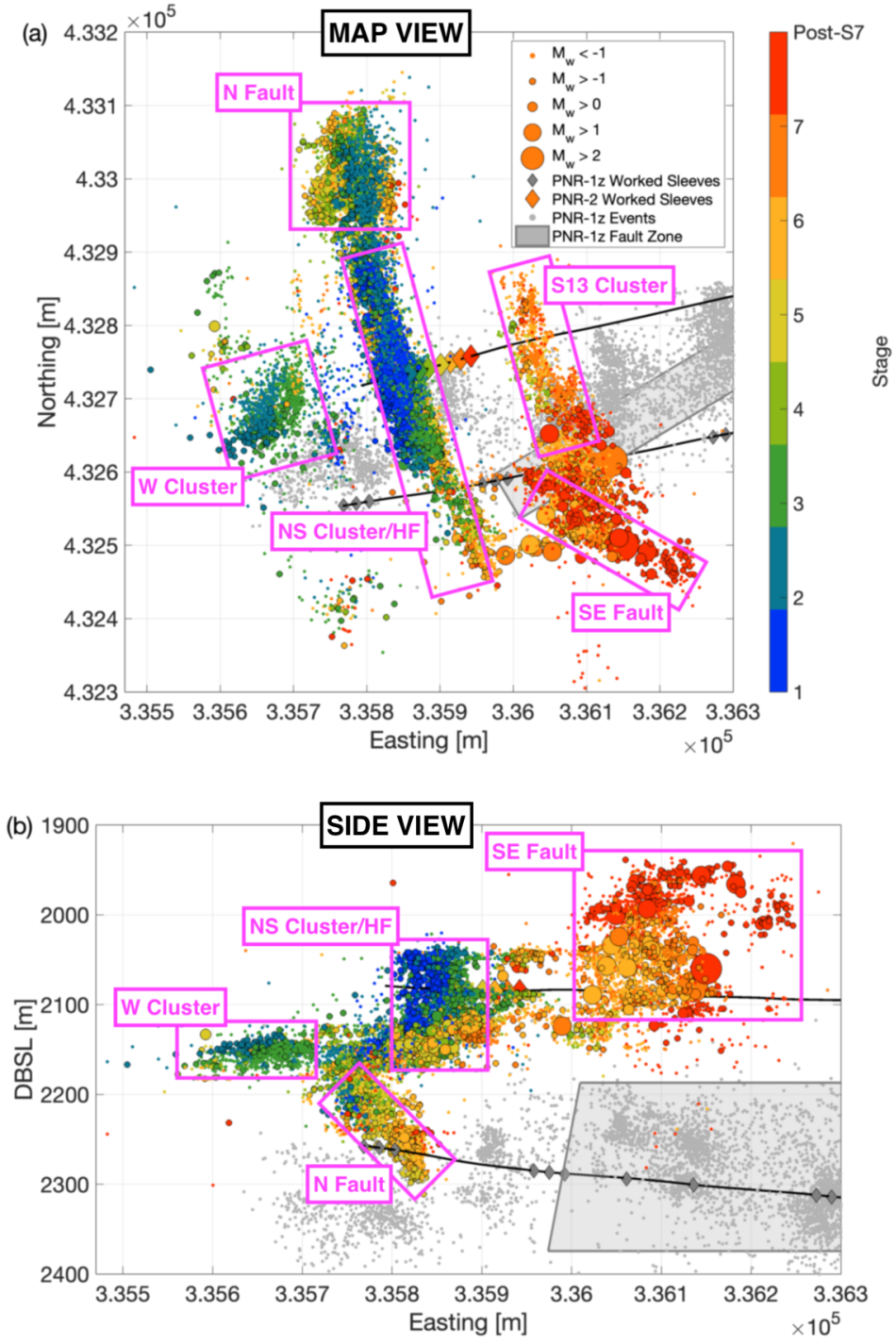

Figure 5.4: Map view of all events recorded up to September 13th 2019 with M_w greater than −1.5. Event hypocentres are shown as circles, coloured by the stage with which they were associated, and sized by magnitude. The well paths of PNR-1z and PNR-2 are shown as black lines, with PNR-1z to the south of and below PNR-2.

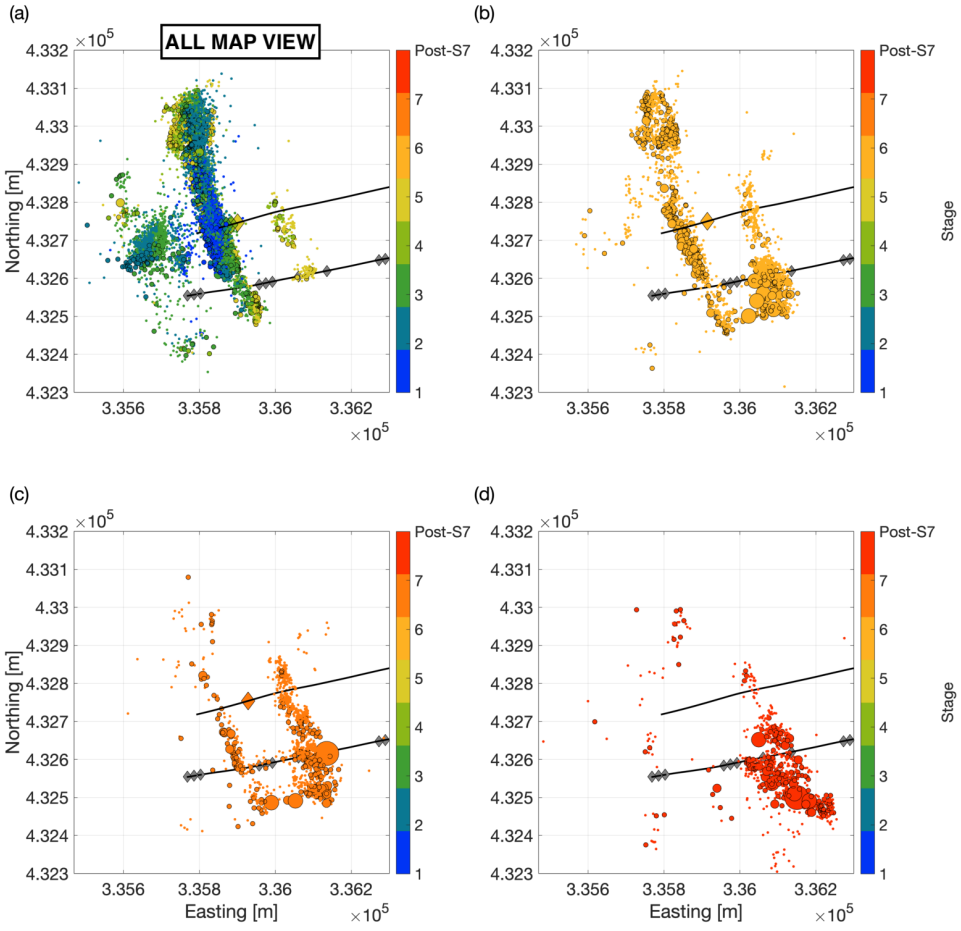

Figure 5.5: Temporal evolution of microseismicity at PNR-2. In (a) we show a map of Stages 1-5, in (b) we show Stage 6, in (c) we show Stage 7 (up to midnight on August 26), and in (d) we show the seismicity that occurred from midnight on August 26th until the end of the monitoring period.

this westward cluster. This could be the result of a stress shadow forming from the opening of fractures in the central NS cluster (eg., Kettlety et al., 2020; Nagel et al., 2013). The magnitude of the largest events increased slightly from Stage 1, though all were below M_L 0 and thus did not exceed the TLS thresholds. These largest events all took place during or immediately after injection, within the central NS cluster.

During Stages 2 and 3, another structure also starts to become visible. At the northern tip of the NS cluster, around 250 m from the injection point, events begin to illuminate a planar feature that has a northward strike and a dip of approximately 60°. This structure extends roughly 130 m below the NS cluster that maps the hydraulic fracture propagation. We interpret these events as resulting from fluid pressure reactivating a small fault. This “N fault” has a similar orientation to some of the seismic discontinuities identified in 3D reflection seismic data (Cuadrilla Resources Ltd, 2019) although it is not co-located with any of these. While these events appear to occur on a reactivated structure, none of the events exceed $M_L > 0$.

The microseismicity during Stage 4 again took place again along the same NS cluster, indicating further injection into the same hydraulic fracture network. Further activation of the N fault described above was also observed, though the magnitudes of events along this feature continued to be small. In addition, events begin to appear further to the east of the injection point, roughly at the position of Sleeve 13 (S13) of the PNR-2 well. This secondary cluster is detached from the main NS cluster, where the majority of events had occurred thus far. The "S13 cluster" is around 100 m further east along the track of the injection well, and during Stage 4 extended in a small lineament roughly 50 m to the south, with a similar orientation to the main NS cluster, parallel to θ_H. The orientation and growth of this feature from the well suggests it was a new zone of hydraulic fracture growth. It is yet unclear why new HF nucleation would take place at a section of the well through which no injection was occurring, rather than at the position of the Stage 4 sleeve. It could be a similar stress-shadow effect as suggested above, with increased fluid pressure near the well stimulating growth of fractures outside of a zone of quiescence immediately adjacent to the large hydraulic fractures already created in the NS cluster. This explanation of the Sleeve 13 cluster is by no means a definitive conclusion and its origin requires further study.

During Stage 5, microseismicity continued to occur predominantly along the main NS cluster and the eastward-dipping fault structure at its northern end. More events are also observed along the easternmost cluster at S13, with events increasing its length both north and south of PNR-2, occurring around 2 hours after injection began. The magnitude of events within this S13 cluster remained low, most with $M_w < -1$. Approximately 12 hours after injection of Stage 5 had stopped, the S13 cluster again grew further to the south, with a population of around hundred low-magnitude ($M_w < -1$) events. We interpret this delayed onset of events as being caused by continued fluid pressure diffusion from the hydraulically stimulated areas reaching a more seismogenic volume of rock of the south of S13 after injection had ceased.

Stage 6 was pumped in two separate phases on August 21st, with the majority of events taking place during and after the second, approximately 90-minute phase of injection. During pumping, events again predominantly took place on the central NS cluster, indicating much of the injected fluid was continuing to enter the previously stimulated zone, even though the Stage 6 sleeve is over 50 m to the east of this zone (Figure 5.5). After injection stopped, significant amounts of microseismicity continued to occur along the length of the S13 cluster. Approximately 5 hours after injection, a M_L 1.6 event occurred at the southern tip of the S13 cluster. This triggered the TLS red light, suspending any injection for at least 18 hours. In the two days of observation that followed, 5 more $M_L > 0$ events occurred, including a 0.9 and a 1.0, all of which were located in the same region at the southern end of the S13 cluster (Figure 5.5).

On the August 23 the operator injected Stage 7, using a reduced fluid volume and an increased fluid viscosity in an attempt to reduce the likelihood of further interaction with any seismogenic features to the south of the PNR-2 well. During injection, microseismicity was observed mostly

along the S13 cluster, with a smaller number of events still occurring on the main NS feature to the west. During injection, no M_L >0 events occurred. However, larger events began to take place on its southern tip of the S13 structure around 5 hours after injection stopped, including a M_L 1.1 event located between the southern tips of the NS cluster and the S13 cluster. Many more events continued within the southern portion of the S13 cluster over the following 2 days, including a M_L 0.5 event 14 hours after the end of Stage 7; followed 19 hours later by a M_L 2.1 earthquake, both located over 100 m south of the injection well at the tip of the S13 cluster.

5.3.1 The ML 2.9 earthquake

On the morning of August 26th, over 60 hours after the end of Stage 7, the M_L 2.9 occurred. On the morning of the event, intermittent data acquisition on the downhole array lead to a loss of acquisition, and no downhole data was recorded for a 15 second prior to and during the earthquake. The event was well recorded by the surface array. The downhole array was able to capture a burst of microseismicity immediately after the mainshock, with rates of microseismicity remaining elevated for approximately 30 minutes after the M_L 2.9 event.

The locations provided by the surface array are less precise than those from the downhole system (Kettlety et al., 2020). Therefore, we use the locations of these aftershock events to identify the position of the M_L 2.9 rupture. These are mapped in Figure 5.6: they occur along a near-vertical plane that extends away to the SE from the southern tip of the S13 cluster, where the highest levels of seismicity had previously occurred. A least-squares fit to these aftershock events give a plane with strike of 140° and a dip of 85°. Interestingly, the aftershocks appear to occur around an elliptical zone, where the centre of this ellipse is quiescent. Our interpretation is that the aftershocks are occurring in a "halo" around the rupture surface of the M_L 2.9 event, with the aftershocks occurring at the edges of the fault, where stresses will have accumulated during rupture. The plane fitted to the M_L 2.9 aftershock cluster has dimensions of approximately 300 m by 250 m, giving an area of approximately 8×10^4 m^2.

Seismic moment is related to fault area A, shear modulus μ, and slip length d, by Equation 1 (Aki and Richard, 2002):

$$M_0 = \mu d A \quad . \tag{5.2}$$

Given a shear modulus of 25 GPa, and a slip of 10 mm (an appropriate estimate given the magnitude of the event and a stress drop between 1-10 MPa), the estimated rupture area for the M_L 2.9 event from equations 1 and 2 is around 8×10^4 m^2, which is consistent with the area delineated by the aftershocks as described above. No further injection took place after Stage 7 and the magnitudes of seismicity subsided. The microseismic array was removed at the end of September 2019, when operations at PNR were officially suspended. 25 more events were detected by the surface array after the M_L 2.9, the last occurring on October 6th, 2019. After

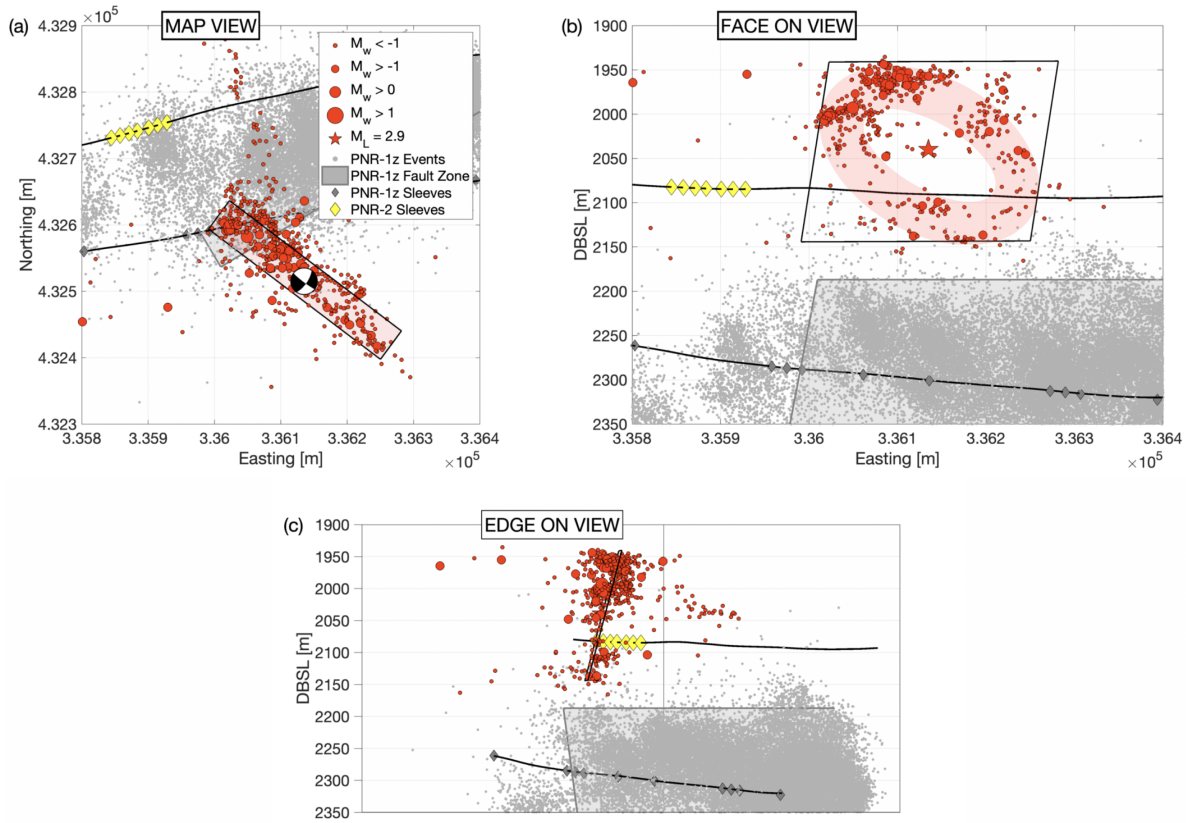

Figure 5.6: The hypocentres of aftershocks occurring within 1 hour of the M_L 2.9 event, used to delineate the activate SE fault. (a) shows a map view, whilst (b) and (c) show two oblique perspectives of the fault in three dimensions. The lower hemisphere focal mechanism shown in (a) is that of the M_L 2.9 earthquake. The plane shown in (a) and (c) is found by a least square fit to the events in the aftershock cluster. The "halo" annotated in (b) highlights the ring of the events around a region of quiescence, with the inferred location of the M_L 2.9 event at its centre.

operations were suspended from September 2019, only 3 of these 25 events had $M_L > 0$, the largest being a 0.2.

The focal mechanism for the M_L 2.9 event was determined from the surface array and is shown in Figure 5.6a. The orientation of the NW-SE nodal plane is consistent with the plane fitted to the aftershocks. This further supports that this plane is representative of the fault zone of the largest events observed during PNR-2 operations.

Overall, our interpretation of the observed microseismicity is as follows. During Stages 1 to 5, a hydraulic fracture zone extended both to the north and south of the well, along the maximum horizontal stress orientation. At the northern end of this feature, a pre-existing structure was intersected, dipping to the east below the zone of operations, but it did not produce significant levels of seismicity. From Stage 5 onwards, a second zone of hydraulic fracturing initiated further to the east, roughly at the position of Sleeve 13. The mechanism by which fluid was transferred to initiate fractures at this point remains unclear. This fracture zone propagated to the south,

where it intersected a pre-existing fault striking to the SE. As stimulation proceeded, more of the injected fluid entered the S13 fracture zone, via which it was transferred to the SE fault, with the transfer of pressure and onset of fault reactivation taking place over a time-scale of hours, such that much of the seismicity occurred after injection had ceased. After Stage 7, prolonged seismicity occurred over several days without further injection, ultimately leading to the M_L 2.9 event, after which seismicity subsided.

5.3.2 Relationship between PNR-1z and PNR-2 seismicity

Figure 5.4 also shows the microseismicity that occurred during stimulation of the PNR-1z well in 2018, and the NEF-1 fault plane that was identified by Clarke et al. (2019a). We find that there is little or no spatial overlap between the two event populations, with the PNR-2 events occurring generally 100 m above the interval stimulated by PNR-1z. The PNR-2 N fault does extend downwards to the depth of PNR-1z events, but this fault is over 400 m further to the north than the zone stimulated by PNR-1z.

The largest events to occur during PNR-2 are found above the SW end of the NEF-1 fault plane identified for PNR-1z. his led to an initial supposition that events could have been occurring on a shallower extension of the same feature. However, once the NW-SE strike of the reactivated fault was unambiguously delineated by the aftershocks of the M_L 2.9 event, it was clear that seismicity from the two wells was occurring on two different features, since the fault reactivated at PNR-1z had a NE strike, whereas the fault reactivated at PNR-2 had a SE strike. We did not observe any microseismicity along the NEF-1 feature identified by Clarke et al. (2019a) during stimulation of PNR-1z. Evidently the 200 m vertical and lateral separation between the wells was sufficient to prevent a linkage from forming between the two stimulated zones.

5.4 Microseismic event magnitude distributions

The magnitude distribution of the events for each stage, shown in Figure 5.7, further illuminates the behaviour of the hydraulic fracture and fault systems.

For the first five stages, the magnitude-frequency distributions have moderate b values ($1 < b < 1.5$). During Stages 1, 2, 3, and 5 the number of larger events appears to be somewhat under-represented, perhaps indicating a physical constraint on rupture dimensions, created for example by the limited dimensions of the pore pressure perturbation during early stages, resulting a truncated power law distribution (e.g., Shapiro et al., 2011). Only Stage 4 has a magnitude-frequency distribution that fits well to the GR power law relationship.

From Stage 7, where we begin to observe activation of the SE fault, the frequency magnitude distribution becomes bimodal, with $1 < b < 1.5$ for magnitudes below 0, but b-values below 1 for larger magnitudes (those with $M_w > 0$). This decrease in the b-value for larger events suggests a shift from “hydraulic fracturing” into a “tectonic” regime, where the fault activation is

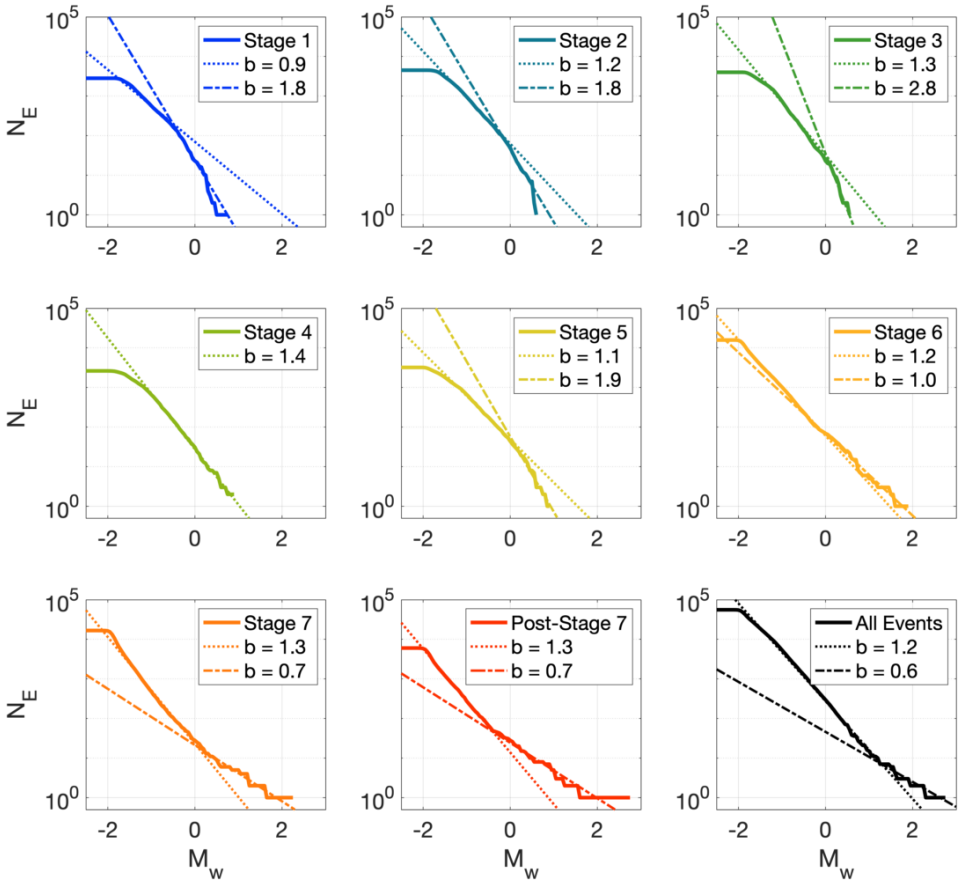

Figure 5.7: Magnitude distributions of event populations for each injection stage, with GR b-values for the populations fitted. It is clear that from Stage 6, the population becomes distinctly bimodal, with a far lower b at the tail-end of the distribution, with values indicative of tectonic earthquakes.

releasing tectonic stresses, producing a higher proportion of larger events (e.g., Kettlety et al., 2019; Verdon et al., 2013c). The distribution of "tectonic-like" events is superposed on top of the magnitude distribution of the smaller HF events, leading to a flat-tailed, bimodal distribution. This observation has been made before by Igonin et al. (2018), but attributed to the hypothesis of "characteristic earthquakes", where large events relative to a fault's surface occur more frequently than expected by the GR distribution. However, this effect is still disputed (Kagan et al., 2012).

Using the maximum likelihood approach Aki (1965), with minimum magnitude of completeness found using a Kolmogorov-Smirnov test with a 10% acceptance level, the overall b-value for all events is around 1.1. This method allows the quality of the fit to be assessed between the observed magnitude distribution and the GR relation (e.g., Williams and Le Calvez, 2013), and gives a M_C of -1.0. Using the method of van der Elst et al. (2016), the significance of the occurrence of the M_L 2.9 (M_w 2.8) above the over GR distribution can be assessed. Given the 3,224 events above a M_C of -1.0, the expected M_{MAX} should be approximately M_w 2.2. The

probability of occurrence q of an event with magnitude M_q is given by (van der Elst et al., 2016):

$$M_q = M_{MAX} - \frac{1}{b}\log(\ln(-q)) \tag{5.3}$$

From Equation 5.3, the probability of a M_w 2.8 event is just under 20%. Thus, while the M_L 2.9 event is larger than the expected M_{MAX} given the distribution of smaller events, it is perhaps not unreasonably so.

5.5 Maximum magnitude forecasting

As in Clarke et al. (2019a), and Chapter 4 of this thesis, we applied statistics-based maximum magnitude forecasting in real time during operations at PNR-2, using both the seismic efficiency (S_{eff}; Hallo et al., 2014) and seismogenic index (SI; Shapiro et al., 2010) methods. The seismic efficiency term S_{eff} modifies the McGarr (1976, 2014) relation relationship between injected volume ΔV and cumulative seismic moment release ΣM_0 to account for aseismic moment release:

$$\Sigma M_0 = S_{eff}\mu\Delta V \quad . \tag{5.4}$$

By measuring the S_{eff} and b-value during operations, the expected magnitude of the largest event M_{MAX} can be estimated (Hallo et al., 2014):

$$M_{MAX} = \frac{2}{3}\left(\log\left(\frac{S_{eff}\mu\Delta V\left[\frac{3}{2}-b\right]}{b10^{9.1}}\right)\right) + \frac{2}{3}\log\left(10^{b\delta} - 10^{-b\delta}\right) \quad , \tag{5.5}$$

where δ is the probabilistic bin-size around M_{MAX}, which is included to ensure that mathematically, for a range of cumulative seismic moments and magnitudes of completeness M_C, there is only a single event with the largest magnitude (see Hallo et al., 2014). Verdon and Budge (2018) found that an extra factor of 0.5 must be added to the M_{MAX} found from Equation 5.5 in order to account for the uncertainty inherent in sampling events from the GR distribution, and ensure a 95% confidence on the forecasted M_{MAX}.

The seismogenic index SI of Shapiro et al. (2010) proposes a linear scaling between the number N of induced events, larger than a magnitude M, and the injection volume:

$$SI = \log\left(\frac{N(M)}{\Delta V} + bM\right) \quad . \tag{5.6}$$

For both methods, once the S_{eff} or SI has been calculated from observed data, the expected population of events can be extrapolated for some prospective total volume V_T to be injected. From this, the GR b-value is used to then find the largest expected event.

b-values are computed using the method described in the previous section. We require a minimum of 50 events in order to compute a b-value, though this is quickly exceeded during each stage, with thousands of events occurring during each stage. Because the b-value is computed

using the Aki (1965) maximum likelihood approach above a M_C value, that is typically $M_w = -1$, the resulting values will be dominated by the frequency-magnitude distribution at lower magnitudes. It therefore may not incorporate the effects of the bimodal distribution described above.

For the injection and seismicity during PNR-1z, Clarke et al. (2019a) found this method of maximum magnitude estimation was effective, accurately forecasting the largest event that occurred, a M_L 1.5. In making these estimates, Clarke et al. (2019a) combined both cumulative injection volumes and cumulative seismicity across multiple stages, since it was clear that many stages injected fluid into the same seismogenic feature.

The situation is more ambiguous for PNR-2 seismicity. Clearly Stages 6 and 7 injected fluid into the SE fault zone. During Stage 5, we observed microseismic activity in the eastern S13 cluster, but it is not clear that at this time that this fracture zone had reached the fault. Stages 1 to 4 did not appear to directly intersect the fault. However, we cannot rule out the possibility that the fluid pressure could diffuse from the southern end of the NS cluster, and potentially lead to all of the toe stages being hydraulically connected to the SE fault zone.

Therefore, in our forecasting approach we consider a selection of scenarios, including treating each stage as an isolated injection event; combining stages 5 to 7 which generated the S13 cluster and intersected the fault; and considering all stages cumulatively.

Figure 5.8 shows the results of the stage-by-stage forecasting, whereby forecasts are produced using injection volumes and events from each stage separately. In this case the prospective total volume V_T of each forecast is the volume injected during the stage. These forecasts were successful for the first 5 stages, forecasting M_{MAX} in the range of $1 < M_w < 1.5$ when using the Hallo et al. (2014) S_{eff} method, and $2 < M_w < 2.5$ when using the Shapiro et al. (2010) SI method. As in Verdon and Budge (2018) and Clarke et al. (2019a), the SI method tends to produce more conservative forecasts than S_{eff}, which is driven by the different scaling exponent assumed between ΔV and ΣM_0: 1.0 for S_{eff}; and 1.5 for SI (Clarke et al., 2019a). However, for Stage 7, the forecast M_{MAX} values during injection were approximately 1.0 using S_{eff} and 1.5 using SI, whereas this stage was followed by events with magnitudes up to M_W 2.8 (M_L 2.9).

Figure 5.9 shows the forecasts when Stages 5 to 7 are combined, and when all PNR-2 events are combined. In both cases the resulting forecasts for Stage 6 onwards, when the larger events occurred, are similar. The S_{eff} approach forecasts M_{MAX} of approximately 2.0 during Stage 6, matching the seismicity that occurred after this stage. The occurrence of trailing events after Stage 6 increased the forecast slightly to approximately $M_{MAX} = 2.4$ during Stage 7. However, this represents a slight under-prediction with respect to the M_L 2.9 (M_w 2.8) largest event that occurred after this stage

The SI method values were consistently higher, with the forecast values being larger than a M_{MAX} of 2.5 during the earlier stages (before any evidence of fault reactivation had occurred), increasing to slightly more than $M_{MAX} = 3$ during and after Stage 5. Therefore, this method did

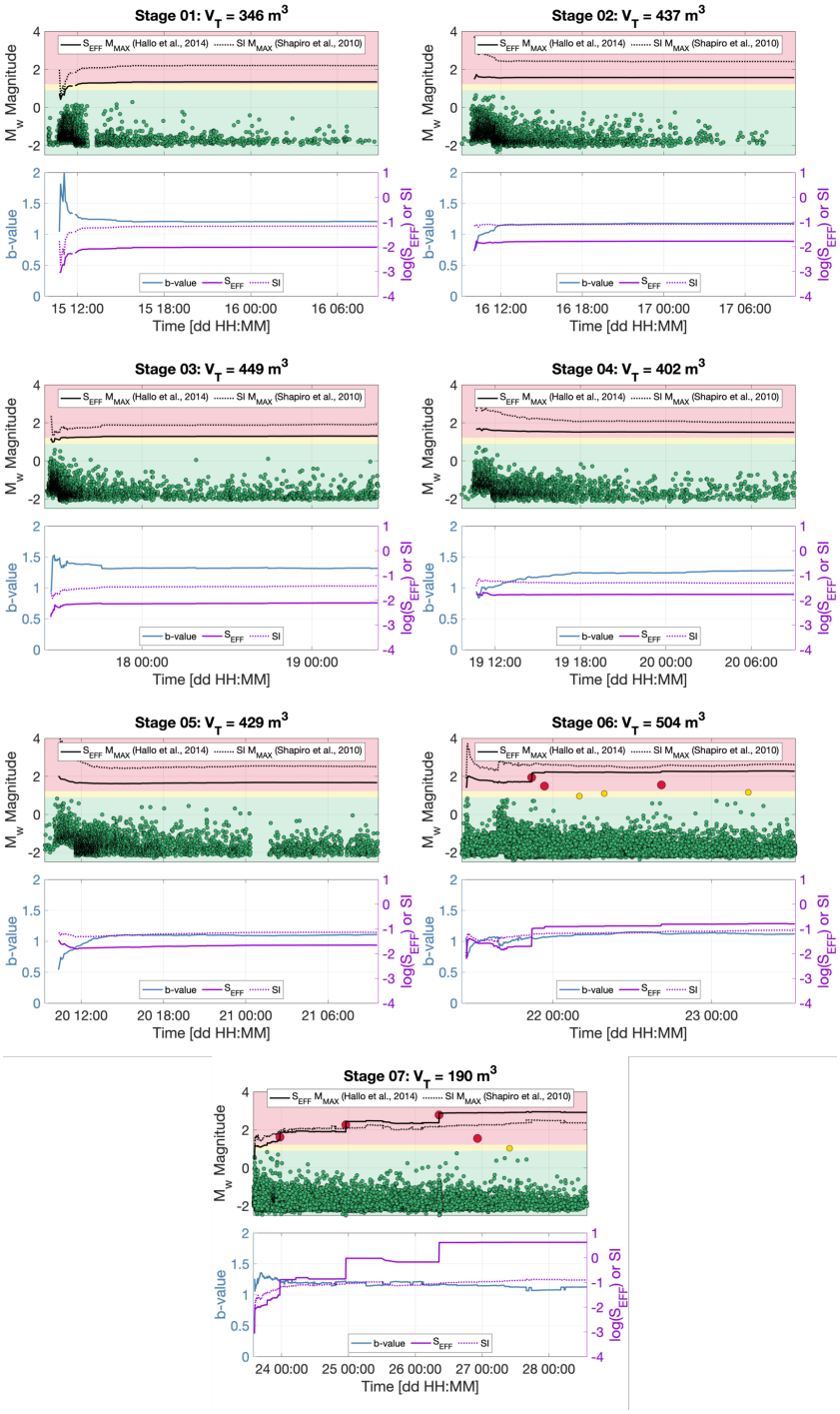

Figure 5.8: M_{MAX} forecasts on a stage-by-stage basis. Circles show the events, coloured by their magnitude with respect to the TLS thresholds in M_w. The solid black line shows the M_{MAX} produced by the Hallo et al. (2014) S_{eff} method, whilst the dotted line shows the M_{MAX} from the Shapiro et al. (2010) SI method. The lower figure for each stage shows the evolution of the b-value (solid blue line), S_{eff} (solid purple), and SI (dotted purple) during operations.

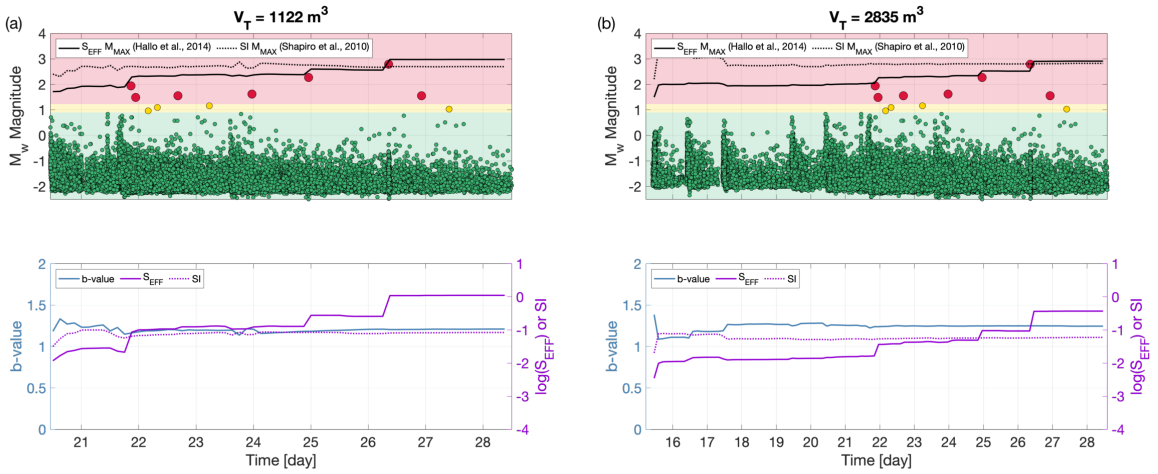

Figure 5.9: Maximum magnitude forecast when (a) data from Stages 5 through 7 are combined, and (b) all PNR-2 event and injection data are combined. Figures are formatted in the same manner as Figure 5.8.

predict the largest magnitude event that occurred. However, the SI forecast is above $M_{MAX} = 2.5$ even during the early stages, where no evidence of interaction with the fault was observed. The evolution of SI did not capture the evolution of the system from normal hydraulic fracturing to fault reactivation during the latter stages

However, while the S_{eff} method did slightly under-predict the observed M_{MAX}, after Stage 6 it was clear from both methods, and from observations of the bimodal, flat-tailed magnitude distribution (Figure 5.7), that a change in the seismic response had taken place. The rates of seismicity release were larger than those observed during stimulation of PNR-1z: whereas Clarke et al. (2019a) report a maximum SI value of -1.8, the maximum SI value during PNR-2 stages which activated the fault was $SI = -0.7$. This implies an order of magnitude more events occurring per unit volume injected. The observed SI value of -0.7 is towards the upper end of seismogenic index values observed during hydraulic fracturing in the WCSB (Schultz et al., 2018; Verdon and Budge, 2018) and in the Sichuan Basin, China (Lei et al., 2019).

This change in behaviour was not visible during pumping of Stage 6, because the interaction with the fault took several hours to develop as the pressure propagated outwards from the injection point. During pumping of Stage 6, no event had $M_L > 0$. This highlights a potential challenge for real-time control measures for mitigation of induced seismicity. This issue poses as much of an issue to Traffic Light Schemes as it does adaptive measures described above, since the fault interaction only became evident after pumping stopped.

Nevertheless, once the fault interaction had been identified, the operator took steps to mitigate further seismicity during pumping of Stage 7 and reduce the likelihood of further interaction with the fault. A stage of only 160 m^3 was pumped, reduced from the over 400 m^3 of the preceding 6 stages, and fluid viscosity was increased, such that the pressure pulse would not extend as far

from the well. Evidently, this mitigation action was not successful, as Stage 7 did create further reactivation of the fault, leading to the M_L 2.9 event. Again, during Stage 7 no $M_L > 0$ events occurred, indicating the time lag between injection and seismicity required for the pressure pulse to reach the fault.

We therefore conclude that the sequence of events at PNR-2 shows that our ability to image, understand and, to an extent, forecast seismicity during hydraulic stimulation is not lacking. It is unclear however what mitigation actions will, short of ceasing operations entirely, and will not be successful in reducing the levels of seismicity associated with injection. Therefore, further study into the efficacy of operational actions that could prevent continued interaction with identified faults is required.

5.6 In-situ stress acting on faults

The NEF-1 fault activated during PNR-1z had dimensions of approximately 500 by 200 m (Clarke et al., 2019a; Kettlety et al., 2020), whereas the rupture area of the SE fault activated during PNR-2, as delineated by the aftershocks described above, had dimensions of approximately 300 by 250 m. The PNR-1z NEF-1 fault was intersected by around 10 stages of injection, with a combined injection volume of over$1,600$ m^3, during 2018 operations, whilst the PNR-2 SE fault was intersected by at most 3 stages (Stages 5, 6 and 7), with a combined volume of approximately $1,000$ m^3. However, the largest magnitude event that occurred on NEF-1 during PNR-1z (M_L 1.5) was significantly smaller than those that occurred on the SE fault during PNR-2 (M_L 1.6, 2.1, and 2.9). This disparity in the event magnitudes produced by the two structures can be examined in the context of their orientation with respect to the regional stress field. Clarke et al. (2019b) describe the stresses at the Preston New Road site, with gradients of maximum horizontal stress of 0.032 ± 0.006 MPa/m, minimum horizontal stress of 0.017 ± 0.004 MPa/m, vertical stress of 0.026 ± 0.001 MPa/m, and pore pressure of 0.012 ± 0.001 MPa/m, with the maximum horizontal stress having a strike of $\theta_H = 170 \pm 10°$.

We resolve normal stress σ_n and shear stress τ onto both of the fault orientations and compute the critical pore pressure P_C, required to exceed the Mohr-Coulomb failure envelope (e.g., Chiaramonte et al., 2007; Kettlety et al., 2019; Walsh and Zoback, 2016):

$$P_C = \sigma_n - \frac{|\tau|}{\phi} \quad , \tag{5.7}$$

where ϕ is the coefficient of friction. We use a value of $\phi = 0.6$ here, which is consistent with previous studies of fault friction (Harris, 1998; Schoenball et al., 2012) and laboratory measurements of shales (Kohli and Zoback, 2013), including those from the Bowland basin (Herrmann et al., 2018).

Critical pore pressure can be used as a measure of fault stability (Chiaramonte et al., 2007; Schoenball et al., 2018), where faults with high P_C require a large amount of pore pressure

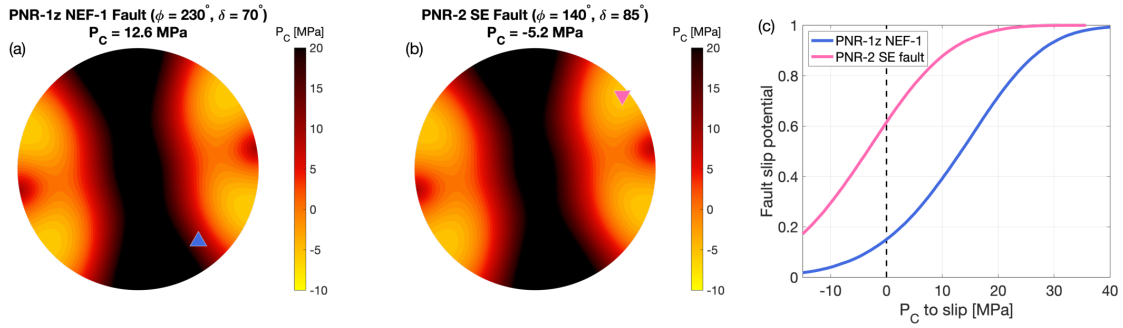

Figure 5.10: Lower-hemisphere stereographic poles-to-plane projections of critical pore pressure P_C for the two fault depths at PNR. (a) shows the P_C for the NE-striking fault of PNR-1z (at a depth of 2300 m), with the green triangle showing the orientation of the plane. (b) shows P_C for the SE fault activated during PNR-2 (at around 2100 m depth), with an inverted green triangle showing its orientation. The titles in each plot show the P_C value at the orientations of the faults. (c) shows the cumulative probability curves for failure for a given P_C.

increase in order to reach the failure envelope, and faults with low or negative P_C are already close to failure in the given stress field. These can be considered critically stressed, with small stress perturbations potentially inducing slip. Figures 5.10a and 5.10a show the values of P_C for all orientations at the approximate depths of the two wells (2100 m for PNR-2 and 2300 m for PNR-1z), with triangles showing the orientations of the PNR-1z NEF-1 and PNR-2 SE faults.

Naturally, the parameters which make up P_C are uncertain, with fault orientations, stress gradients, in situ pore pressure, fault depths, and friction coefficients each having, sometimes significant, inherent uncertainty. To account for these in the calculation of P_C, and in the characterisation of the relatively likelihood of fault slip, a quantitative risk assessment methodology is used (Chiaramonte et al., 2007; Schoenball et al., 2018; Walsh and Zoback, 2015). A Monte-Carlo method of random sampling within the uncertainties of these input parameters is used to calculate a cumulative probability distribution of pore pressure change required to reach the failure criterion (i.e. P_C). This can then be used as a measure of the relative "probability" of failure (Walsh and Zoback, 2016). This is termed the fault slip potential (FSP) of a fault, and the cumulative probability curves computed for the PNR faults (assuming uncertainties of $\pm 10°$ in fault orientations and ± 50 m in fault depth) are shown in Figure 5.10c.

Figure 5.10a shows that the PNR-1z NE fault has a P_C value of around 13 MPa, meaning it is relatively close to the minima of P_C in the stress field and could reach the failure envelope given a perturbation to the stress state. However, the PNR-2 SE fault (Figure 5.10b) has a significantly negative P_C of -5 MPa, meaning in its orientation is already beyond the Mohr-Coulomb failure threshold prior to any injection occurring. Such a situation should not be possible since it would imply that slip would be occurring prior to injection. Negative P_C values can be attributed to uncertainties in the input parameters or the inherent cohesion of the fault, which is an unknown parameter. The relative values of FSP however still show that the PNR-2 SE fault

has a significantly higher probability of failure than the NEF-1 feature at lower P_C values.

The PNR-2 SE fault is better aligned for failure, and this provides an explanation as to why the SE fault gave such a significant seismic response from a smaller perturbation relative to the PNR-1z fault. Several studies have shown the importance of fault orientation within the stress field (e.g., Alt and Zoback, 2017; Keranen et al., 2013; Schoenball et al., 2018; Skoumal et al., 2019), and the comparison between the PNR-1z NEF-1 feature and the PNR-2 SE fault demonstrates this explicitly.

5.7 Conclusion

We describe the fault activation that occurred during the hydraulic fracturing operation at the Preston New Road site, Lancashire, UK, in 2019. We use the microseismic event locations are used to interpret the development of seismicity leading up the felt events. After three relatively typical stages of injection, during which hydraulic fractures appeared to be growing along the S_{Hmax} direction as expected, events began to occur in a disconnected cluster further east along the unworked section of the well, south of Sleeve 13 of the PNR-2 well. Two further stages of injection produced more seismicity in this S13 cluster, with many events occurring hours after injection ceased, implying that diffusion of pore pressure was playing a significant role in initiating seismicity. The final two stages of injection began to stimulate felt seismicity in this zone south of the S13 cluster, with magnitudes again increasing in the hours after injection. A M_L 1.6 event occurred after Stage 6, and the operator reduced injection volumes and increased fluid viscosity for Stage 7. However, within 24 hours of Stage 7, events with magnitudes of M_L 2.1 and M_L 2.9 occurred in the same region.

The M_L 2.9 event was not directly imaged by the downhole instruments, which were undergoing maintenance at the time. However, the aftershock locations, and the microseismicity which continued over the following days, mapped a planar feature striking NW-SE. This orientation matches that of the focal mechanisms of the largest events, and the spatial dimensions of the aftershocks are consistent with the rupture area for a M_L 2.9 event. The delay in seismicity between injection and the activity in the clusters which connected to the fault zone suggests that the diffusion of increased fluid pressure, reducing normal stress and declamping the fault (Goebel et al., 2015; Raleigh et al., 1976), was the most likely mechanism for fault activation. While poroelastic stress transfer (Segall and Lu, 2015), elastic stress transfer from prior events (Kettlety et al., 2019; Schoenball et al., 2012) or fracture opening (Kettlety et al., 2020), and aseismic creep (Bhattacharya and Viesca, 2019; Eyre et al., 2019) may have also contributed, further investigation and modelling of the system is required to confirm the extent to which these mechanisms played a role.

The event frequency magnitude distribution showed an evolution as the injection proceeded. Earlier stages showed fewer larger events than expected, with the magnitude distribution

appearing to roll off above $M_w > 0$, implying that rupture may have been limited by the stimulated volume (Shapiro et al., 2011). However, as the SE fault zone began to be activated by injection, the magnitude distribution became bimodal, with more large events ($M_w > 0$) than expected from the GR distribution at lower magnitudes. We interpret this as a shift from a hydraulic fracturing-dominated regime, to a tectonic regime of seismicity. The shift into a tectonic regime has previously been observed in hydraulic fracturing datasets in which fault activation occurs (e.g., Igonin et al., 2018).

Statistical maximum magnitude forecasting is based on scaling between number and size of events with injection volume, extrapolated to a final planned volume, with the expected largest event size then computed from the GR distribution. For these models to be a useful tool to mitigate felt seismicity, they must be able to forecast accurately and react to a change in the nature of the seismicity quickly, whilst injection is occurring. Activity in the fault zone took place hours after injection ceased, and the seismicity that occurred during injection had a sufficiently high overall b-values that some forecasts under-predicted the size of the largest events. That said, the operator was able to identify the increased rate of seismicity relative to the PNR-1z well and adjusted the injection program to reduce the likelihood of further fault interaction. Evidently this adjustment was not successful, and further research into potential operational actions that could prevent further interaction with identified faults is clearly warranted.

There were clear differences in the behaviour of fault activation between the triggering of the NEF-1 fault zone during PNR-1z operations, and the SE-striking fault during PNR-2 operations. The 500 m long PNR-1z fault zone intersected the injection well around halfway along the well's length and at least 10 stages activated it, leading seismicity with a largest event size of M_L 1.6. However, the largest event it produced had a magnitude of M_L 1.5. In contrast, the approximately 300 m long PNR-2 fault was triggered at a distance of around 200 m by 3 stages of injection, producing 3 events with $M_L > 1.5$, including the M_L 2.9. While other factors such as the frictional properties of the two faults cannot be ruled out, the PNR-2 SE fault is significantly better aligned for failure when compared to the PNR-1z NEF-1 fault zone. The higher slip potential on the SE fault likely explains the relative ease with which PNR-2 operations triggered a significantly larger event on a more distant fault system.

CHAPTER 6

CONCLUSIONS

In this thesis I have used microseismic data to inform geomechanical and statistical models of injection-induced seismicity. As the previous chapters have mostly been composed of published manuscripts, they each contain their own conclusions with references to the wider issues of IIS. This chapter will emphasise the key findings, how they relate to the central questions posed in chapter 1, and how they will lead to future work. These questions can be summarised as:

- What makes some reservoirs more seismogenic than others?
- What physical processes control injection-induced fault activation?
- How best can we mitigate induced seismicity?

6.1 Summary of results

In chapter 2 I examined the role of interevent stress transfer in the continuation of seismicity during hydraulic fracturing-induced fault activation using a data set from the Horn River Basin, British Columbia, Canada. During hydraulic fracturing there, some stages of stimulation induced deeper and larger magnitude seismicity, but others did not. We investigated whether or not this could be explained by elastic stress transfer, a mechanism that is well known for its role in triggering earthquakes in tectonic sequences, and is a key component in physics-based forecasting models. However, we found that there was no clear signal of stress interaction in this case, which contrasts with findings from several other recent cases of induced seismicity (Catalli et al., 2013; Pennington and Chen, 2017; Sumy et al., 2014). For these recent cases where interevent stress transfer has been shown to be significant, the faults were well-oriented for failure in their

regional stress state, with a very low P_C value (Schoenball et al., 2018; Walsh and Zoback, 2015). This means that a minimal perturbation would be capable of producing slip. For the case studied in chapter 2, we found that despite these faults being relatively well oriented in the regional stress field, there is low stress anisotropy at the site. This results in low shear stress acting on the faults, and so relatively high perturbations to the stress are required in order to reach the failure envelope. Thus, in areas where faults are far closer to failure, the small magnitude stress changes associated with interevent stress transfer can play a much more important role. As a result, the "footprint" of the perturbation was relatively small, and only the stages that were in very close proximity to the fault were able to create induced seismicity. A lateral or vertical separation of roughly 100 m between the fault and the injection point was sufficient to prevent fault reactivation.

In chapter 3 I continued my investigation of the mechanism of elastostatic stress transfer, however this time the opening of hydraulic fractures, rather than slip from prior microseismic events, as the source of stress change. This was motivated by the observation that, during stimulation of the Preston New Road PNR-1z well in Lancashire, UK in 2018, the spatial distribution of events was inconsistent with pore pressure change being the causative mechanism. We found that microseismic events were located predominantly in areas where opening hydraulic fractures promote failure of the fault. This indicates that elastic stress changes from opening fractures were controlling the parts of the fault which are most active when they are stimulated.

In chapter 4 I examined the ability of statistical models to forecast the maximum magnitude of induced events in real-time during hydraulic fracturing operations. Statistical models have been developed relating the injected volume and the number or size of events that are induced, which when combined with the Gutenberg-Richter relation, can be used to find the maximum magnitude of the largest event in a population (Hallo et al., 2014; McGarr, 1976, 2014; Shapiro et al., 2010; Verdon and Budge, 2018). I applied the forecasting method in real time to the microseismicity recorded during hydraulic fracturing at the PNR-1z well. I found that accurate forecasts could only be found when injection volumes and microseismicity from multiple stages were combined. This can be explained naturally from the locations and focal mechanisms of the microseismic events, which showed that multiple stages of injection activated a single feature, hence the injection and microseismicity must be treated cumulatively. We also showed that by applying these methods during operations, we can provide the operator with an increased understanding of the fault activation, and can directly assist in operational decision-making.

In chapter 5 I used the methods and insights developed in the previous chapters to analyse the seismicity induced by stimulation of the Preston New Road PNR-2 well in 2019. Hydraulic fracturing stimulated two $M > 2$ events that were felt by many within kilometres of the site. The locations of microseismic events showed that the first stages produced hydraulic fracture growth without any interaction with faults. The last three stages began to activate a fault zone around 250 m from the point of injection. Whilst the largest event was not recorded by the

downhole monitoring array, its aftershocks were, and clearly map out the extent of the earthquake rupture. The fault activation could also be observed through a drop in the Gutenberg-Richter b-value, indicating a shift from a fluid-induced regime of microseismicity with high b-values, to a tectonic regime, with a larger proportion of bigger events. This notable drop in b-value at higher magnitudes was observed around two injection stages before the largest event, and thus could be used as simple a diagnostic for operations activating faults. Maximum magnitude forecasting of the sequence showed that, without accounting for the shift in the magnitude-frequency distribution that accompanies the change in seismicity regime, the forecasts slightly under-predicted the observed seismicity. In situ stress analysis at the site further highlighted that the orientation of faults and the high stress anisotropy can control the amount of seismicity they produce once they are stimulated by injection.

6.2 Overall findings

The first of the central questions of injection-induced seismicity asks which factors can exacerbate induced seismicity in a particular area. In both of the cases I studied in this thesis, I found evidence that the in situ stress acting on the activated faults appears to control both the fault activation mechanism, and the amount of seismicity produced. In areas of high stress anisotropy, well aligned faults are closer to failure, requiring a smaller pressure perturbation to slip. This manifests itself in numerous ways, including smaller, more distant, but better aligned faults generating larger magnitude events, despite receiving a smaller pressure perturbation from a smaller volume of injection. In situ stress also appeared to play a role in controlling which physical mechanism had a greater effect during the activation of a fault.

These observations reinforce the importance of thoroughly characterising the in situ stresses around an injection well prior to operations. Without it, accurately assessing the risk of failure for any detected faults will become very difficult. Naturally, in situ stress and fault alignment are two factors of many, others of which include the fictional and geomechanical properties of the rocks (e.g., Goebel et al., 2017b).

The second question asks which physical processes contribute most strongly to cases of IIS. This work has also shown that elastic stress transfer can play a role in hydraulic fracturing-induced fault activation. However, it is not interevent stress transfer of microseismic events that significantly controls seismicity, but the opening of fractures, which determines which areas receive positive and negative ΔCFS changes, and therefore which areas will be moved towards the failure threshold. The large stress changes that result from opening fractures can prestress areas and enhance seismicity, or increase normal stress and potentially suppress seismicity.

The last question asks what practical steps can be taken to best avoid and mitigate IIS. The statistical methods tested in the latter half of the thesis showed that maximum magnitude forecasting can be successfully applied during operations, and used as a tool to guide decision-making.

This enables mitigation methods to be enacted in advance of the largest events occurring. However, chapter 5 showed that whilst the forecasts were in part reflecting the change in behaviour of the seismicity, they struggle to capture the shift in the magnitude frequency distribution entirely. Most importantly, whilst mitigating action was taken during PNR-2 operations after the fault was identified, the reduction in volume and increase in fluid viscosity was still unsuccessful in mitigating the largest events.

6.3 Applications and recommendations

As this thesis has involved the application of novel scientific methods, some practical hurdles were encountered. Here, I will discuss how the techniques used in this thesis could be completed in a more effective manner, and give practical recommendations for hypothetical future operations.

6.3.1 Stress state and fault orientation

It is clear that fault orientation and stress state are vital controls on the likelihood and severity of induced seismicity. Effort is already put into identifying the orientation of faults near injection sites (within ~ 1 km) using reflection seismic imaging and analysis of the structural trends in the region. However, as was the case for the seismicity in the Bowland basin, faults that were activated in this strike-slip stress regime had little vertical throw, and thus were not visible as clear reflectors. More complex attribute analysis is required to pick out these structures before injection to better assess seismic risk, especially in stress regimes where low throw faults are likely to slip.

A related factor which has already been discussed in the previous section is clearly characterising the stress state around the injection well, to examine what structures are liable to slip throughout operations. Thorough analysis of the well logs after drilling can provide good constraints on the density, and thus the vertical stress, as well as the maximum stress direction and magntiude (from borehole breakouts and drilling induced tensile fractures, see Tingay et al. (2008); Zoback et al. (1985, 2003)). Minimum horizontal stress magnitude can be measured during pumping from leak off tests and mini-fracs, however only estimates of the magnitude of the maximum horizontal stress are possible (Bell, 2015; Ervine and Bell, 1987; Haimson and Cornet, 2003). It is vital that these measurements are taken prior to and during pumping to accurately assess the risk of faults, identified both before (by reflection seismic) and during operations (from microseismic event locations).

6.3.2 Maximum magnitude forecasting

The application of real-time maximum magnitude forecasting presented unique challenges, as is the case with any application of new software. This method, however, was made more challenging than strictly necessary by a number of factors. The smaller programming issues will be discussed

first, and will be followed by the larger, operational challenges. Figure 6.1 shows the forecasting processing workflow. As is clear, there are many steps in the analysis, and multiple points in the workflow where the reprocessing is necessary to account for the increasing amount of data which are produced over the course of a hydraulic fracturing operation.

The maximum magnitude forecasting code was written into a MATLAB Application, providing a single graphical user interface from which data files were specified, b-value and forecasting parameters could be adjusted, and all results were displayed. The choice was made to adapt the raw code into this format such that it could be used more easily by an operator. However, when it came to real-time use of the application, the source code required continuous adjustment to account for the changing file formats that were produced by the service company.

Specifically, the seismic event and injection data were stored in text files connected to a central server. These files were updated dozens of times per minute to add more injection and event data, or the quality control (QC) process updated the measurements of the event properties (location, magnitude, etc). Only a subset of these variables were exacted from these files (event time, seismic moment, injection time, and injection rate), but the location of these variable within the event and injection files changed repeatedly and without warning between stages. It took time to modify the source code for a new file format, and made combining data from multiple stages very difficult. One clear recommendation to an operator using this technique is specifying the file format of the data prior to pumping, and keeping it consistent throughout operations.

More importantly was the issue surrounding the measurement of seismic magnitude, both from the surface and downhole arrays, as was discussed in Chapter 5, section 5.2.1. Clearly, there were issues with correctly determining magnitudes, which stem from the instruments used, their lack of azimuthal coverage, and the processing methods used (see Stork et al., 2014). It is naturally recommended that instruments sensitive to a range of frequencies are used, and that magnitude estimates, especially for larger events, are not biased by the limited response of geophones. This is potentially a more expensive prospect for an operator, and economic considerations may limit the use of some instruments. Nonetheless, the gain of the instruments in any array should be set such that the smaller events are detectable on a number of receivers, but some are still able to capture the energy from the largest events without exceeding their dynamic range (i.e. clipping). This added complexity in the array set up will naturally require more careful processing of the data, to weight magnitude estimates from some stations over others. However, this will lead to more accurate magnitudes over all.

The systematic uncertainty in the magnitude estimates can clearly lead to errors in maximum magnitude forecasting produced in real time, and more careful calibration of magnitude scales could be performed prior to full scale operations. It became necessary to use the more accurate estimates of local and moment magnitude from surface data to correct for the inaccuracy of magnitudes calculated downhole. These corrections were mostly made after the operations, and thus the forecasts produced in real-time were somewhat inaccurate, underestimating M_max

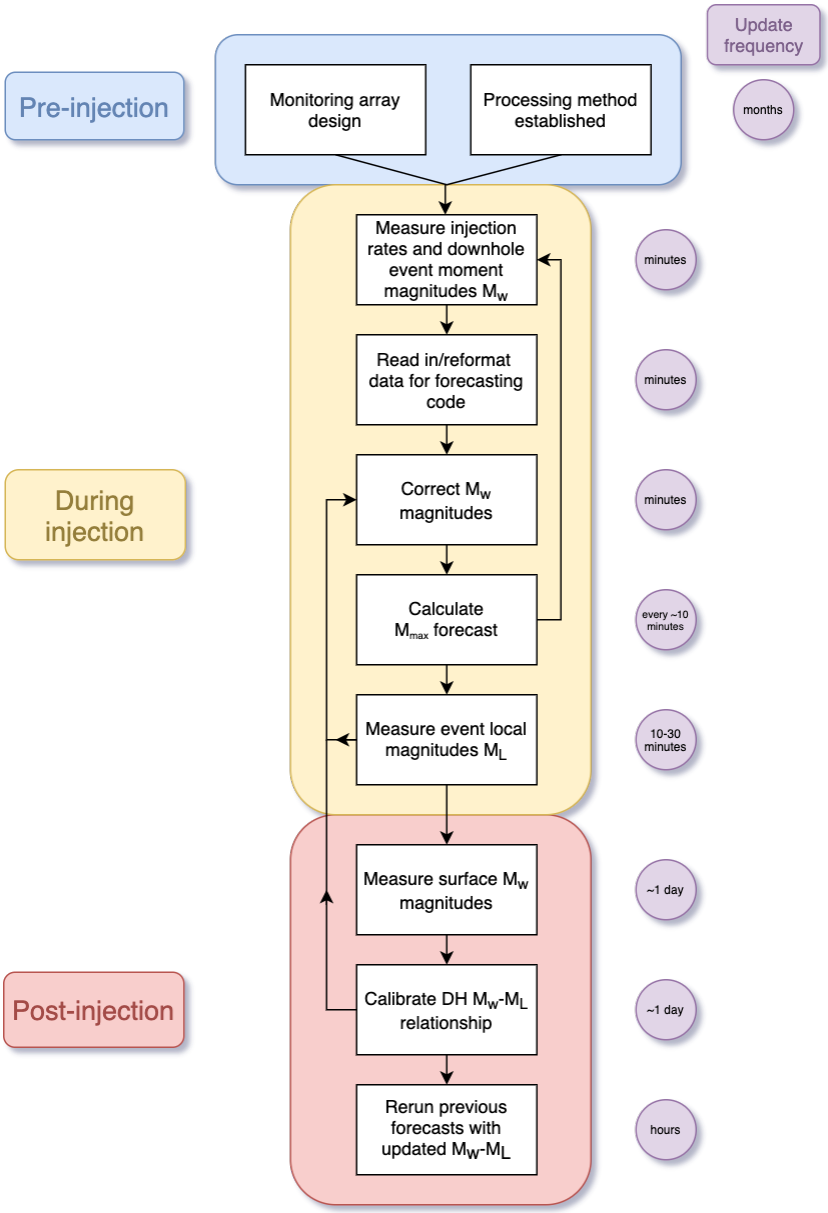

Figure 6.1: A flowchart of the processing steps necessary to conduct the maximum magnitude forecasting used in Chapters 4 and 5. This represents the steps that had to be taken during the application of forecasting, some of which (e.g. "Correct M_w magnitudes") could be excluded if monitoring and processing methods are improved. Some processes, like "Correct M_w magnitudes", are only possible after some data has already been collected, and inaccuracies in downhole (DH) measurements have been identified. Update frequencies in purple refer to how frequently calculations or measures were made, and how frequently their products can be fed back into the modelling. While much can be done during operations, many corrections required a significant amount of analysis post-pumping to compute.

by as much as ~ 0.5. Given this is on the order of the uncertainty of magnitudes (again ~ 0.5), this discrepancy is not overly large, however, when operational decisions are guided by a traffic light scheme with narrow thresholds between the green and red lights, this is a significant underestimation. Thus, if the calibration between surface local magnitude and downhole moment magnitudes is conducted early in operations, using event data from the first stages or mini-fracs, the forecasts will be more accurate throughout.

6.4 Future work

Whilst the individual case studies highlighted in this thesis can develop our understanding of IIS, the results are somewhat specific to their respective sites. Broad assessment of a large number of fields with adequate seismic monitoring needs to be conducted, comparing seismic activity with rock types, stress regimes, stress anisotropy, and friction or geomechanical properties. These data however, are difficult to obtain and are generally proprietary. This is especially true for high quality microseismic and in situ stress data.

More work needs to be done to better understanding the geomechanical behaviour of faults and their response to stress changes from injected fluid. Conducting frictional and geomechanical tests on rocks from the sites studied above will act as a basis for geomechanical models. This can enable a complete comparison between the rock properties, geomechanical models, local stress field, and microseismic response to injection. This is the aim of large scale projects such as SHAPE-UK, part of the UK Unconventional Hydrocarbon challenge grants. If this broad study is successful, combining laboratory measurements of rock properties and geomechanical models of many sites of induced seismicity, relationships could be developed that may clarify the controls of exactly what makes some reservoirs more seismogenic than others.

The microseismic data for Preston New Road PNR-2 operations are also of particularly high quality. Directly imaging the aftershocks of the large events, which were well resolved by the surface stations, may allow for more advanced study of the rupture process. If slip models of the fault activation can be developed, they can be compared to the microseismic data and modelling of fluid pressures at the site to see exactly how the transfer of fluid pressure stimulated failure. This would not only be of scientific value, but could also play a role in understanding how the adjustment of injection parameters may affect the pressure changes that nearby faults experience. Having slip models will also allow for a more accurate assessment of interevent triggering during this sequence, which could answer questions concerning the effectiveness of the mitigation efforts once larger events started to occur near to the fault.

BIBLIOGRAPHY

Ake, J., K. Mahrer, D. O'Connell, and L. Block (2005), Deep-injection and closely monitored induced seismicity at Paradox Valley, Colorado, *Bulletin of the Seismological Society of America*, *95*(2), 664–683, doi:10.1785/0120040072.

Aki, K. (1965), Maximum likelihood estimate of b in the formula $\log N = a - bm$ and its condience limits, *Bulletin of the Earthquake Research Institute*, *43*, 237–239.

Aki, K., and P. G. Richard (2002), *Quantitative Seismology*, 2nd ed., University Science Books.

Alt, R. C., and M. D. Zoback (2017), In situ stress and active faulting in Oklahoma, *Bulletin of the Seismological Society of America*, *107*(1), 216–228, doi:10.1785/0120160156.

Altmann, J. B., T. M. Müller, B. I. Müller, M. R. Tingay, and O. Heidbach (2010), Poroelastic contribution to the reservoir stress path, *International Journal of Rock Mechanics and Mining Sciences*, *47*(7), 1104–1113, doi:10.1016/j.ijrmms.2010.08.001.

Ampuero, J. P., and A. M. Rubin (2008), Earthquake nucleation on rate and state faults - Aging and slip laws, *Journal of Geophysical Research: Solid Earth*, *113*(1), 1–21, doi:10.1029/2007JB005082.

Andrews, I. J. (2013), The Carboniferous Bowland Shale gas study: geology and resource esimation, *Tech. rep.*, British Geological Survey for Department of Energy and Climate Change, London, UK.

Atkinson, G. M., D. W. Eaton, H. Ghofrani, D. Walker, B. Cheadle, R. Schultz, R. Shcherbakov, K. Tiampo, J. Gu, R. M. Harrington, Y. Liu, M. van der Baan, and H. Kao (2016), Hydraulic Fracturing and Seismicity in the Western Canada Sedimentary Basin, *Seismological Research Letters*, *87*(3), 631–647, doi:10.1785/0220150263.

Baird, A. F., J.-M. Kendall, Q. J. Fisher, and J. Budge (2017), The role of texture, cracks and fractures in highly anisotropic shales, *Journal of Geophysical Research: Solid Earth*, *122*, doi:10.1002/2017JB014710.

Baisch, S., C. Koch, and A. Muntendam-Bos (2019), Traffic light systems: To what extent can induced seismicity be controlled?, *Seismological Research Letters*, *90*(3), 1145–1154, doi:10.1785/0220180337.

Bao, X., and D. W. Eaton (2016), Fault activation by hydraulic fracturing in western Canada, *Science*, *2583*, 9, doi:10.1126/science.aag2583.

Baptie, B. (2018), Earthquake seismology 2017/2018, *Open Report OR/18/029*, British Geological Survey.

Baptie, B. (2019), Earthquake seismology 2018/2019, *Open Report OR/19/039*, British Geological Survey.

Barbour, A., J. Norbeck, and J. Rubinstein (2017), The effects of varying injection rates in Osage County, Oklahoma, on the 2016 Mw 5.8 Pawnee earthquake, *Seismological Research Letters*, *88*(4), 1–14, doi:10.1785/0220170003.

Bardwell, G. E. (1966), Some statistical features of the relationship between rocky mountain arsenal waste disposal and frequency of earthquakes, *The Mountain Geologist*, *3*(1), 37–42.

Barker, J. (2014), Horn River Basin: Unconventinoal Shale Gas Play Atlas, *Tech. Rep. June*, BC Oil and Gas Commision.

Barnhart, W. D., H. M. Benz, G. P. Hayes, J. L. Rubinstein, and E. Bergman (2014), Seismological and geodetic constraints on the 2011 Mw5.3 Trinidad, Colorado earthquake and induced deformation in the Raton Basin, *Journal of Geophysical Research: Solid Earth*, *119*, 7923–79,339, doi:10.1002/2014JB011227.

Barthwal, H., and M. van der Baan (2019), Role of fracture opening in triggering microseismicity observed during hydraulic fracturing, *Geophysics*, *84*(3), KS105–KS118, doi:10.1190/geo2018-0425.1.

BC Oil and Gas Commision (2012), Investigation of Observed Seismicity in the Horn River Basin, *Tech. Rep. August*, BC Oil and Gas Commision.

Bell, J. S. (2015), In situ stress orientations and magnitudes in the Liard Basin of Western Canada, *Tech. rep.*, Natural Resources Canada, doi:10.4095/295742.

Bhattacharya, P., and R. C. Viesca (2019), Fluid-induced aseismic fault slip outpaces pore-fluid migration, *Science*, *364*(6439), 464–468, doi:10.1126/science.aaw7354.

Bommer, J. J., S. Oates, J. M. Cepeda, C. Lindholm, J. Bird, R. Torres, G. Marroquín, and J. Rivas (2006), Control of hazard due to seismicity induced by a hot fractured rock geothermal project, *Engineering Geology*, *83*(4), 287–306, doi:10.1016/j.enggeo.2005.11.002.

Boore, D., and J. Boatwright (1984), Average body-wave correction coefficients, *Bulletin of the Seismological Society of America*, *74*, 1615–1621.

Bosman, K., A. Baig, G. Viegas, and T. Urbancic (2016), Towards an improved understanding of induced seismicity associated with hydraulic fracturing, *First Break*, *34*, 61–66.

Brown, M. R. M., and S. Ge (2018a), Small earthquakes matter in injection-induced seismicity, *Geophysical Research Letters*, *45*, 5445–5453, doi:10.1029/2018GL077472.

Brown, M. R. M., and S. Ge (2018b), Distinguishing Fluid Flow Path from Pore Pressure Diffusion for Induced Seismicity, *Bulletin of the Seismological Society of America*, *108*(6), 3684–3686, doi:10.1785/0120180149.

Butcher, A., R. Luckett, J. P. Verdon, J. M. Kendall, B. Baptie, and J. Wookey (2017), Local magnitude discrepancies for near-event receivers: Implications for the u.k. traffic-light scheme, *Bulletin of the Seismological Society of America*, *107*, 532–541.

Carder, D. S. (1945), Seismic investigations in the Boulder Dam area, 1940–1944, and the influence of reservoir loading on local earthquake activity, *Bulletin of the Seismological Society of America*, *35*(4), 175–192.

Catalli, F., M.-A. Meier, and S. Wiemer (2013), The role of Coulomb stress changes for injection-induced seismicity: The Basel enhanced geothermal system, *Geophysical Research Letters*, *40*, 72–77, doi:10.1029/2012GL054147.

Cattania, C., M. J. Werner, W. Marzocchi, S. Hainzl, D. Rhoades, M. Gerstenberger, M. Liukis, W. Savran, A. Christophersen, A. Helmstetter, A. Jimenez, S. Steacy, and T. H. Jordan (2018), The forecasting skill of physics-based seismicity models during the 2010-2012 canterbury, New Zealand, earthquake sequence, *Seismological Research Letters*, *89*(4), 1238–1250, doi: 10.1785/0220180033.

Chae, K. S., and J. W. Lee (2015), Risk analysis and simulation for geologic storage of CO_2, in *Proceedings of the World Congress on Advances in Civil, Environmental and Materials Research*, p. 20, Incheon, Korea.

Chalmers, G. R. L., D. J. K. Ross, and R. M. Bustin (2012), Geological controls on matrix permeability of Devonian Gas Shales in the Horn River and Liard basins, northeastern British Columbia, Canada, *International Journal of Coal Geology*, *103*, 120–131, doi:10.1016/j.coal.2012.05.006.

Chiaramonte, L., M. D. Zoback, J. Friedmann, and V. Stamp (2007), Seal integrity and feasibility of CO_2 sequestration in the Teapot Dome EOR pilot: Geomechanical site characterization, *Environmental Geology*, *54*(8), 1667–1675, doi:10.1007/s00254-007-0948-7.

Chorney, D., B. Lee, and S. Maxwell (2016), Microseismic geomechanical modelling of asymmetric upper Montney hydraulic fractures, in *GeoConvention 2016: Optimizing Resources*.

Chou, Q., H. J. Gao, and M. Somerwil (2011), Analysis of geomechanical data for Horn River Basin gas shales, north-east British Columbia, Canada, in *SPE Middle East Unconvential Gas Conference and Expibition*, p. 12, Society of Petroleum Engineers, Muscat, Oman, doi: 10.2118/142498-MS.

Clarke, H., L. Eisner, P. Styles, and P. Turner (2014), Felt seismicity associated with shale gas hydraulic fracturing: The first documented example in Europe, *Geophysical Research Letters*, *41*(23), 8308–8314, doi:10.1002/2014GL062047.

Clarke, H., P. Turner, R. M. Bustin, N. Riley, and B. Besly (2018), Shale gas resources of the Bowland Basin, NW England: a holistic study, *Petroleum Geoscience*, *24*(3), 287–322, doi: 10.1144/petgeo2017-066.

Clarke, H., J. P. Verdon, T. Kettlety, A. F. Baird, and J. M. Kendall (2019a), Real‚ÄêTime Imaging, Forecasting, and Management of Human‚ÄêInduced Seismicity at Preston New Road, Lancashire, England, *Seismological Research Letters*, *90*(5), 1902–1915, doi:10.1785/0220190110.

Clarke, H., H. Soroush, and T. Wood (2019b), Preston new road: The role of geomechanics in successful drilling of the uk's first horizontal shale gas well, in *EAGE Annual Meeting, London*, EAGE.

Cocco, M., S. Hainzl, F. Catalli, B. Enescu, A. M. Lombardi, and J. Woessner (2010), Sensitivity study of forecasted aftershock seismicity based on Coulomb stress calculation and rate- and state-dependent frictional response, *Journal of Geophysical Research: Solid Earth*, *115*(5), 1–15, doi:10.1029/2009JB006838.

Corfield, S. M., R. L. Gawthorpe, M. Gage, A. J. Fraser, and B. M. Besly (1996), Inversion tectonics of the variscan foreland of the british isles, *Journal of Geological Society, London*, *153*, 17–32.

Cuadrilla Resources Ltd (2019), Hydarulic Fracture Plan PNR 2, *Tech. rep.*, Cuadrilla Resources Ltd.

Cuadrilla Resources Ltd. (2019), Preston New Road-1z: LJ/07-09(z) HFP Report, *Tech. rep.*, Cuadrilla Resources Ltd.

Daszykowski, M., B. Walczak, and D. Massart (2001), Looking for natural patterns in data Part 1. Density-based approach, *Chemometrics and Intelligent Laboratory Systems*, *56*(2), 83–92, doi:10.1016/S0169-7439(01)00111-3.

Davies, R., G. Foulger, A. Bindley, and P. Styles (2013), Induced seismicity and hydraulic fracturing for the recovery of hydrocarbons, *Marine and Petroleum Geology*, *45*, 171–185, doi:10.1016/j.marpetgeo.2013.03.016.

Deichmann, N. (2006), Local Magnitude, a Moment Revisited, *Bulletin of the Seismological Society of America*, *96*(4A), 1267–1277, doi:10.1785/0120050115.

Deichmann, N. (2017), Theoretical Basis for the Observed Break in M _{L} / M _{W} Scaling between Small and Large Earthquakes, *Bulletin of the Seismological Society of America*, *107*(2), doi:10.1785/0120160318.

Deichmann, N., and D. Giardini (2009), Earthquakes Induced by the Stimulation of an Enhanced Geothermal System below Basel (Switzerland), *Seismological Research Letters*, *80*(5), 784–798, doi:10.1785/gssrl.80.5.784.

Dinske, C., and S. A. Shapiro (2013), Seismotectonic state of reservoirs inferred from magnitude distributions of fluid-induced seismicity, *Journal of Seismology*, *17*(1), 13–25, doi:10.1007/s10950-012-9292-9.

Dong, T., N. B. Harris, K. Ayranci, C. E. Twemlow, and B. R. Nassichuk (2017), The impact of composition on pore throat size and permeability in high maturity shales: Middle and Upper Devonian Horn River Group, northeastern British Columbia, Canada, *Marine and Petroleum Geology*, *81*, 220–236, doi:10.1016/j.marpetgeo.2017.01.011.

Drew, J., R. S. White, F. Tilmann, and J. Tarasewicz (2013), Coalescence microseismic mapping, *Geophysical Journal International*, *195*(3), 1773–1785, doi:10.1093/gji/ggt331.

Eaton, D. W., and S. Maghsoudi (2015), 2b... or not 2b? interpreting magnitude distributions from microseismic catalogs, *First Break*, *33*(10), 79–86.

Eaton, D. W., and R. Schultz (2018), Increased likelihood of induced seismicity in highly overpressured shale formations, *Geophysical Journal International*, *214*(1), 751–757, doi:10.1093/gji/ggy167.

Eaton, D. W., J. Davidsen, P. K. Pedersen, and N. Boroumand (2014), Breakdown of the Gutenberg-Richter relation for microearthquakes induced by hydraulic fracturing: Influence of stratabound fractures, *Geophysical Prospecting*, *62*(4), 806–818, doi:10.1111/1365-2478.12128.

Economides, M. J., and K. G. Nolte (2003), *Reservoir Stimulation*, 3rd ed., 5-1 – 5-14 pp., John Wiley, Hoboken, N.J.

Ellsworth, W. L. (2013), Injection-induced earthquakes, *Science*, *341*(6142), 1225,942, doi:10.1126/science.1225942.

Ervine, W. B., and J. S. Bell (1987), Subsurface in Situ Stress Magnitudes From Oil-Well Drilling Records: an Example From the Venture Area, Offshore Eastern Canada., *Canadian Journal of Earth Sciences*, *24*(9), 1748–1759, doi:10.1139/e87-167.

Ester, M., H.-P. Kriegel, J. Sander, and X. Xu (1996), A density-based algorithm for discovering clusters in large spatial databases with noise, in *2nd International Conference on Knowledge Discovery and Data Mining*, p. 226, Portland, OR.

Evans, D. M. (1966), The Denver Area Earthquakes and the Rocky Mountain Arsenal Disposal Well, *The Mountain Geologist*, *3*(1), 23–36, doi:10.1130/eng-case-8.25.

Eyre, T. S., D. W. Eaton, D. I. Garagash, M. Zecevic, M. Venieri, R. Weir, and D. C. Lawton (2019), The role of aseismic slip in hydraulic fracturing–induced seismicity, *Science Advances*, *5*(8), eaav7172, doi:10.1126/sciadv.aav7172.

Farahbod, A. M., H. Kao, J. F. Cassidy, and D. Walker (2015), How did hydraulic-fracturing operations in the Horn River Basin change seismicity patterns in northeastern British Columbia, Canada?, *The Leading Edge*, *34*(June), 658–633, doi:10.1190/tle34060658.1.

Faulkner, D. R., C. A. Jackson, R. J. Lunn, R. W. Schlische, Z. K. Shipton, C. A. Wibberley, and M. O. Withjack (2010), A review of recent developments concerning the structure, mechanics and fluid flow properties of fault zones, *Journal of Structural Geology*, *32*(11), 1557–1575, doi:10.1016/j.jsg.2010.06.009.

Fellgett, M., A. Kingdon, J. Williams, and C. Gent (2017), State of stress across UK Regions, *Tech. rep.*, British Geological Survey.

Freed, A. M. (2005), Earthquake Triggering By Static, Dynamic, and Postseismic Stress Transfer, *Annual Review of Earth and Planetary Sciences*, *33*(1), 335–367, doi:10.1146/annurev.earth.33.092203.122505.

Frohlich, C., and S. D. Davis (1993), Teleseismic b Values; Or, Much Ado About 1.0, *Journal of Geophysical Research*, *98*(B1), 631–644, doi:10.1029/92JB01891.

Frohlich, C., C. Hayward, B. Stump, and E. Potter (2011), The Dallas-Fort Worth earthquake sequence: October 2008 through May 2009, *Bulletin of the Seismological Society of America*, *101*(1), 327–340, doi:10.1785/0120100131.

Gehne, S., and P. M. Benson (2017), Permeability and permeability anisotropy in Crab Orchard sandstone: Experimental insights into spatio-temporal effects, *Tectonophysics*, *712-713*, 589–599, doi:10.1016/j.tecto.2017.06.014.

Gehne, S., and P. M. Benson (2019), Permeability enhancement through hydraulic fracturing: laboratory measurements combining a 3D printed jacket and pore fluid over-pressure, *Scientific Reports*, *9*(1), 1–11, doi:10.1038/s41598-019-49093-1.

Göbel, T. (2015), A comparison of seismicity rates and fluid-injection operations in Oklahoma and California: Implications for crustal stresses, *The Leading Edge*, *34*(6), 640–648, doi:10.1190/tle34060640.1.

Goebel, T. H., S. M. Hosseini, F. Cappa, E. Hauksson, J. P. Ampuero, F. Aminzadeh, and J. B. Saleeby (2016), Wastewater disposal and earthquake swarm activity at the southern end of the Central Valley, California, *Geophysical Research Letters*, *43*(3), 1092–1099, doi:10.1002/2015GL066948.

Goebel, T. H., M. Weingarten, X. Chen, J. Haffener, and E. E. Brodsky (2017a), The 2016 Mw5.1 Fairview, Oklahoma earthquakes: Evidence for long-range poroelastic triggering at >40 km from fluid disposal wells, *Earth and Planetary Science Letters*, *472*, 50–61, doi:10.1016/j.epsl.2017.05.011.

Goebel, T. H., G. Kwiatek, T. W. Becker, E. E. Brodsky, and G. Dresen (2017b), What allows seismic events to grow big?: Insights from b-value and fault roughness analysis in laboratory stick-slip experiments, *Geology*, *45*(9), 815–818, doi:10.1130/G39147.1.

Goebel, T. H. W., and E. E. Brodsky (2018), The spatial footprint of injection wells in a global compilation of induced earthquake sequences, *Science*, *361*(6405), 899–904, doi:10.1126/science.aat5449.

Goebel, T. H. W., E. Hauksson, F. Aminzadeh, and J. Ampuero (2015), An objective method for the assessment of fluid injection induced seismicity and application to tectonically active regions in central California, *Journal of Geophysical Research: Solid Earth*, *120*, 7013–7032, doi:10.1002/2015JB011895.

Goertz-Allmann, B. P., A. Goertz, and S. Wiemer (2011), Stress drop variations of induced earthquakes at the Basel geothermal site, *Geophysical Research Letters*, *38*(9), L09,308, doi:10.1029/2011GL047498.

Green, C. A., P. Styles, and B. J. Baptie (2012), Shale gas fracturing review & recommendations for induced seismic migration, *Tech. rep.*, DECC.

Green, R. G., T. Greenfield, and R. S. White (2015), Triggered earthquakes suppressed by an evolving stress shadow from a propagating dyke, *Nature Geoscience*, *8*(8), 629–632, doi:10.1038/ngeo2491.

Grigoli, F., S. Cesca, A. P. Rinaldi, A. Manconi, J. A. López-Comino, J. F. Clinton, R. Westaway, C. Cauzzi, T. Dahm, and S. Wiemer (2018), The November 2017 Mw 5.5 Pohang earthquake: A possible case of induced seismicity in South Korea, *Science*, *360*(6392), 1003–1006, doi:10.1126/science.aat2010.

Guion, P. D., P. Gutteridge, and S. J. Davies (2000), Carboniferous sedimentation and volcanism on the laurussian margin, in *Geological History of Britain and Ireland*, edited by N. H. Woodcock and R. A. Strachan, pp. 227–271, Blackwell Science.

Gupta, H. K. (1985), The present status of reservoir induced seismicity investigations with special emphasis on Koyna earthquakes, *Tectonophysics*, *118*(3-4), 257–279, doi:10.1016/0040-1951(85)90125-8.

Gutenberg, B., and C. F. Richter (1944), Frequency of earthquakes in California, *Bulletin of the Seismological Society of America*, *34*, 185–188.

Haimson, B. C., and F. H. Cornet (2003), ISRM suggested methods for rock stress estimation-part 3: Hydraulic fracturing (HF) and/or hydraulic testing of pre-existing fractures (HTPF), *International Journal of Rock Mechanics and Mining Sciences*, *40*(7-8), 1011–1020, doi:10.1016/j.ijrmms.2003.08.002.

Hallo, M., I. Oprsal, L. Eisner, and M. Y. Ali (2014), Prediction of magnitude of the largest potentially induced seismic event, *Journal of Seismology*, *18*(3), 421–431, doi:10.1007/s10950-014-9417-4.

Hamilton, D. H., and R. L. Meehan (1971), Ground rupture in the Baldwin Hills, *Science*, *172*, 333–344.

Hanks, T. C., and H. Kanamori (1979), A moment magnitude scale, *Journal of Geophysical Research*, *84*, 2348–2350.

Hardebeck, J. L., J. J. Nazareth, and E. Hauksson (1998), The static stress change triggering model: Constraints from two southern California aftershock sequences, *Journal of Geophysical Research*, *103*(B10), 24,427–24,437.

Harris, R. A. (1998), Introduction to special section: Stress triggers, stress shadows, and implications for seismic hazard, *Journal of Geophysical Research: Solid Earth*, *103*(B10), 24,347–24,358, doi:10.1029/98JB01576.

Healy, J. H., W. W. Rubey, D. T. Griggs, and C. B. Raleigh (1968), The Denver Earthquakes, *Science*, *161*(3848), 1301–1310.

Heidbach, O., M. Rajabi, K. Reiter, M. Ziegler, and WSM Team (2016), World Stress Map Database Release 2016, *GFZ Data Services*, doi:10.5880/WSM.2016.001.

Hennings, P. H., J.-E. Lund Snee, J. L. Osmond, H. R. DeShon, R. Dommisse, E. Horne, C. Lemons, and M. D. Zoback (2019), Injection-induced seismicity and fault slip potential in the Fort Worth Basin, Texas, *Bulletin of the Seismological Society of America*, *XX*(Xx), doi:10.1785/0120190017.

Herrmann, J., E. Rybacki, H. Sone, and G. Dresen (2018), Deformation Experiments on Bowland and Posidonia Shale—Part I: Strength and Young's Modulus at Ambient and In Situ p c–T Conditions, *Rock Mechanics and Rock Engineering*, *51*(12), 3645–3666, doi:10.1007/s00603-018-1572-4.

Herrmann, R. B., S.-K. Park, and C.-Y. Wang (1981), The Denver earthquakes of 1967-1968, *Bulletin of the Seismological Society of America*, *71*(3), 731–745.

Hofmann, H., G. Zimmermann, M. Farkas, E. Huenges, A. Zang, M. Leonhardt, G. Kwiatek, P. Martinez-Garzon, M. Bohnhoff, K. B. Min, P. Fokker, R. Westaway, F. Bethmann, P. Meier, K. S. Yoon, J. W. Choi, T. J. Lee, and K. Y. Kim (2019), First field application of cyclic soft stimulation at the Pohang Enhanced Geothermal System site in Korea, *Geophysical Journal International*, *217*(2), 926–949, doi:10.1093/gji/ggz058.

Holland, A. A. (2013), Earthquakes triggered by hydraulic fracturing in south-central Oklahoma, *Bulletin of the Seismological Society of America*, *103*(3), 1784–1792, doi:10.1785/0120120109.

Horton, S. (2012), Disposal of hydrofracking waste fluid by injection into subsurface aquifers triggers earthquake swarm in central arkansas with potential for damaging earthquake, *Seismological Research Letters*, *83*(2), 250–260, doi:10.1785/gssrl.83.2.250.

Hsieh, P. A., and J. D. Bredehoeft (1981), A reservoir analysis of the Denver earthquakes: A case of induced seismicity, *Journal of Geophysical Research*, *86*(B2), 903–920, doi:10.1029/jb086ib02p00903.

Hubbert, M. K., and W. W. Rubey (1959), Role of Fluid Pressure in Mechanics of Overthrust Faulting, *Bulletin of the Geological Society of America*, *70*, 115–166, doi:10.1130/0016-7606(1959)70[115:ROFPIM]2.0.CO;2.

Hurd, O., and M. D. Zoback (2012), Stimulated shale volume characterization: Multiwell case study from the Horn River Shale: I. Geomechanics and Microseismicity, in *SPE Annual Technical Conference and Exibition*, Society of Petroleum Engineers, doi:10.2118/159536-MS.

Igonin, N., M. Zecevic, and D. W. Eaton (2018), Bilinear Magnitude-Frequency Distributions and Characteristic Earthquakes During Hydraulic Fracturing, *Geophysical Research Letters*, *45*(23), 12,866–12,874, doi:10.1029/2018GL079746.

Islam, M. A., and P. Skalle (2013), An experimental investigation of shale mechanical properties through drained and undrained test mechanisms, *Rock Mechanics and Rock Engineering*, *46*(6), 1391–1413, doi:10.1007/s00603-013-0377-8.

Jones, G. A., D. Raymer, K. Chambers, and J. M. Kendall (2010), Improved microseismic event location by inclusion of a priori dip particle motion: A case study from Ekofisk, *Geophysical Prospecting*, *58*(5), 727–737, doi:10.1111/j.1365-2478.2010.00873.x.

Jost, M. L., T. Busslberg, O. Jost, and H. P. Harjes (1998), Source parameters of injection-induced microearthquakes at 9 km depth at the ktb deep drilling site, germany, *Bulletin of the Seismological Society of America*, *88*, 815–832.

Kagan, Y. Y. (2005), Double-couple earthquake focal mechanism: Random rotation and display, *Geophysical Journal International*, *163*(3), 1065–1072, doi:10.1111/j.1365-246X.2005.02781.x.

Kagan, Y. Y., D. D. Jackson, and R. J. Geller (2012), Characteristic earthquake model, 1884-2011, R.I.P., *Seismological Research Letters*, *83*(6), 951–953, doi:10.1785/0220120107.

Kao, H., R. Visser, B. Smith, and S. Venables (2018), Performance assessment of the induced seismicity traffic light protocol for northeastern British Columbia and western Alberta, *The Leading Edge*, *37*(2), 117–126, doi:10.1190/tle37020117.1.

Kendall, J.-m., A. Butcher, A. L. Stork, J. P. Verdon, and R. Luckett (2019), How big is a small earthquake ? Challenges in determining microseismic magnitudes, *First Break*, *37*(February), 51–56.

Keranen, K. M., and M. Weingarten (2018), Induced seismicity, *Annual Review of Earth and Planetary Sciences*, *46*, 149–174, doi:https://doi.org/10.1146/annurev-earth-082517-010054.

Keranen, K. M., H. M. Savage, G. A. Abers, and E. S. Cochran (2013), Potentially induced earthquakes in Oklahoma, USA: Links between wastewater injection and the 2011 Mw 5.7 earthquake sequence, *Geology*, *41*(6), 699–702, doi:10.1130/G34045.1.

Keranen, K. M., M. Weingarten, G. A. Abers, B. A. Bekins, and S. Ge (2014), Sharp increase in central Oklahoma seismicity since 2008 induced by massive wastewater injection, *Science*, *345*(6195), 448–451.

Kettlety, T., J. P. Verdon, M. J. Werner, J. M. Kendall, and J. Budge (2019), Investigating the role of elastostatic stress transfer during hydraulic fracturing-induced fault activation, *Geophysical Journal International*, *217*, 1200–1216, doi:10.1093/gji/ggz080.

Kettlety, T., J. P. Verdon, M. J. Werner, and J. M. Kendall (2020), Stress transfer from opening hydraulic fractures controls the distribution of induced seismicity, *Journal of Geophysical Research: Solid Earth*, *125*, doi:10.1029/2019JB018794.

Kilb, D., J. Gomberg, and P. Bodin (2002), Aftershock triggering by complete Coulomb stress changes, *Journal of Geophysical Research: Solid Earth*, *107*(B4), ESE 2–1–ESE 2–14, doi:10.1029/2001jb000202.

Kim, K.-H., J.-H. Ree, Y.-H. Kim, S. Kim, S. Y. Kang, and W. Seo (2018), Assessing whether the 2017 Mw 5.4 Pohang earthquake in South Korea was an induced event, *Science*, *360*(6392), 1007–1009, doi:10.1126/science.aat6081.

Kim, W. Y. (2013), Induced seismicity associated with fluid injection into a deep well in Youngstown, Ohio, *Journal of Geophysical Research: Solid Earth*, *118*(7), 3506–3518, doi:10.1002/jgrb.50247.

King, G. C. P., R. S. Stein, and J. Lin (1994), Static stress changes and the triggering of earthquakes, *Bulletin of the Seismological Society of America*, *84*(3), 935–953.

King, V. M., L. V. Block, W. L. Yeck, C. K. Wood, and S. A. Derouin (2014), Geological structure of the Paradox Valley Region, Colorado, and relationship to seismicity induced by deep well injection, *Journal of Geophysical Research : Solid Earth*, *119*, 4955–4978, doi:10.1002/2013JB010651.Received.

Kirby, G. A., H. E. Baily, R. A. Chadwick, D. J. Evans, D. W. Holliday, S. Holloway, A. G. Hulbert, T. C. Pharaoh, N. J. P. Smith, N. Aitkenhead, and B. Birch (2000), The structure and evolution of the craven basin and adjacent areas, *Subsurface geology memoirs*, British Geological Survey.

Kohli, A. H., and M. D. Zoback (2013), Frictional properties of shale reservoir rocks, *Journal of Geophysical Research: Solid Earth*, *118*(9), 5109–5125, doi:10.1002/jgrb.50346.

Kwiatek, G., T. Saarno, T. Ader, F. Bluemle, M. Bohnhoff, M. Chendorain, G. Dresen, P. Heikkinen, I. Kukkonen, P. Leary, M. Leonhardt, P. Malin, P. Martínez-Garzón, K. Passmore, P. Passmore, S. Valenzuela, and C. Wollin (2019), Controlling fluid-induced seismicity during a 6.1-km-deep geothermal stimulation in Finland, *Science Advances*, *5*(5), eaav7224, doi:10.1126/sciadv.aav7224.

Langenbruch, C., C. Dinske, and S. A. Shapiro (2011), Inter event times of fluid induced earthquakes suggest their Poisson nature, *Geophysical Research Letters*, *38*(21), L21,302, doi:10.1029/2011GL049474.

Latimer, A., M. Hill, and J. Hendrick (2017), Pore Pressure Anomalies in the Horn River Basin, Northeastern BC, in *Geoconvention 2017*, p. 1.

Lei, X., D. Huang, J. Su, G. Jiang, X. Wang, H. Wang, X. Guo, and H. Fu (2017), Fault reactivation and earthquakes with magnitudes of up to M_{W} 4.7 induced by shale-gas hydraulic fracturing in Sichuan Basin, China, *Scientific Reports*, *7*(1), 7971, doi:10.1038/s41598-017-08557-y.

Lei, X., Z. Wang, and J. Su (2019), The December 2018 ML 5.7 and January 2019 ML 5.3 Earthquakes in South Sichuan Basin Induced by Shale Gas Hydraulic Fracturing, *Seismological Research Letters*, *90*(3), 1099–1110, doi:10.1785/0220190029.

Luckett, R., L. Ottemöller, A. Butcher, and B. Baptie (2019), Extending local magnitude ML to short distances, *Geophysical Journal International*, *216*(2), 1145–1156, doi:10.1093/gji/ggy484.

MacLean, B. C., and D. W. Morrow (2004), Bovie structure: Its evolution and regional context, *Bulletin of Canadian Petroleum Geology*, *52*(4), 302–324, doi:10.2113/52.4.302.

Maghsoudi, S., J. Baró, A. Kent, D. Eaton, and J. Davidsen (2018), Interevent Triggering in Microseismicity Induced by Hydraulic Fracturing, *Bulletin of the Seismological Society of America*, *108*(3A), 1133–1146, doi:10.1785/0120170368.

Mair, R., M. Bickle, D. Goodman, B. Koppelman, J. Roberts, R. Selley, Z. Shipton, H. Thomas, A. Walker, E. Woods, and P. Younger (2012), Shale gas extraction in the UK: a review of hydraulic fracturing, *Tech. Rep. June*, The Royal Society.

Majer, E. L., R. Baria, M. Stark, S. Oates, J. Bommer, B. Smith, and H. Asanuma (2007), Induced seismicity associated with Enhanced Geothermal Systems, *Geothermics*, *36*(3), 185–222, doi: 10.1016/j.geothermics.2007.03.003.

Mancini, S., M. Segou, M. Werner, and C. Cattania (2019), Improving Physics‚Äêbased Aftershock Forecasts during the 2016‚Äê2017 Central Italy Earthquake Cascade, *Journal of Geophysical Research: Solid Earth*, *124*, doi:10.1029/2019jb017874.

Manga, M., C. Y. Wang, and M. Shirzaei (2016), Increased stream discharge after the 3 September 2016 Mw 5.8 Pawnee, Oklahoma earthquake, *Geophysical Research Letters*, *43*(22), 11,588–11,594, doi:10.1002/2016GL071268.

Maxwell, S. (2011), Microseismic hydraulic fracture imaging: The path toward optimizing shale gas production, *The Leading Edge*, *March*, 340–346, doi:10.1190/1.3567266.

Maxwell, S. C., J. Shemeta, E. Campbell, and D. Quirk (2008), Microseismic deformation rate monitoring, in *SPE Annual Technical Conference*, p. SPE116596, Denver, Colorado.

Maxwell, S. C., M. Jones, R. Parker, S. Miong, S. Leaney, D. Dorval, D. D'Amico, J. Logel, E. Anderson, and K. Hammermaster (2009), Fault activation during hydraulic fracturing, in *SEG Annual Meeting Expanded Abstracts*, pp. 1552–1556.

McGarr, A. (1976), Seismic moments and volume changes, *Journal of Geophysical Research*, *81*(8), 1487–1494, doi:10.1029/jb081i008p01487.

McGarr, A. (2014), Maximum magnitude earthquakes induced by fluid injection, *Journal of Geophysical Research: Solid Earth*, *119*, 1008–1019, doi:10.1002/2013JB010597.

McGarr, A., and A. J. Barbour (2017), Wastewater Disposal and the Earthquake Sequences During 2016 Near Fairview, Pawnee, and Cushing, Oklahoma, *Geophysical Research Letters*, *44*, 9330–9336, doi:10.1002/2017GL075258.

McGarr, A., D. Simpson, and L. Seeber (2002), *Case histories of induced and triggered seismicity*, vol. 81A, 647–661 pp., International Association of Seismology.

Meier, M., M. J. Werner, J. Woessner, and S. Wiemer (2014), A search for evidence of secondary static stress triggering during the 1992 Mw 7.3 Landers, California, earthquake sequence, *Journal of Geophysical Research: Solid Earth*, *119*, 3354–3370, doi:10.1002/2013JB010385.

Meng, L., J. P. Ampuero, J. Stock, Z. Duputel, Y. Luo, and V. C. Tsai (2012), Earthquake in a maze: Compressional rupture branching during the 2012 Mw 8.6 Sumatra earthquake, *Science*, *337*(6095), 724–726, doi:10.1126/science.1224030.

Meng, L., A. Mcgarr, L. Zhou, and Y. Zang (2019), An Investigation of Seismicity Induced by Hydraulic Fracturing in the Sichuan Basin of China Based on Data from a Temporary Seismic Network, *Bulletin of the Seismological Society of America*, *109*(1), 348–357, doi:10.1785/0120180310.

Mignan, A., M. Broccardo, S. Wiemer, and D. Giardini (2017), Induced seismicity closed-form traffic light system for actuarial decision-making during deep fluid injections, *Scientific Reports*, *7*(13607), doi:10.1038/s41598-017-13585-9.

Moos, D., P. Peska, T. Finkbeiner, and M. Zoback (2003), Comprehensive wellbore stability analysis utilizing quantitative risk assesment, *Journal of Petroleum Science and Engineering*, *38*, 97–110, doi:10.1016/S0920-4105(03)00024-X.

Munafò, I., L. Malagnini, and L. Chiaraluce (2016), On the relationship between M_{w} and M_{L} for small earthquakes, *Bulletin of the Seismological Society of America*, *106*(5), 2402–2408, doi:10.1785/0120160130.

Nagel, N., F. Zhang, M. Sanchez-Nagel, B. Lee, and A. Agharazi (2013), Stress shadow evaluations for completion design in unconventional plays, in *SPE Unconventional Resources Conference*, p. SPE167128, Calgary, Canada.

Nordgren, R. (1972), Propagation of a vertical hydraulic fracture, *Society of Petroleum Engineers Journal*, *12*(04), 306–314, doi:10.2118/3009-PA.

Oil and Gas Authority (2018), Consolidated Onshore Guidance, Version 2.2, *Tech. rep.*, BEIS.

Okada, Y. (1992), Internal deformation due to shear and tensile faults in a half-space, *Bulletin of the Seismological Society of America*, *82*(2), 1018–1040.

Parsons, T., Y. Ogata, J. Zhuang, and E. L. Geist (2012), Evaluation of static stress change forecasting with prospective and blind tests, *Geophysical Journal International*, *188*(3), 1425–1440, doi:10.1111/j.1365-246X.2011.05343.x.

Pearson, C. (1982), Parameter and a magnitude moment relation- ship from small earthquakes observed during hydraulic fracturing experiments in crystalline rocks, *Geophysical Research Letters*, *9*, 404–407.

Pennington, C., and X. Chen (2017), Coulomb stress interactions during the M_W 5.8 Pawnee sequence, *Seismological Research Letters*, *88*(4), 1024–1031, doi:10.1785/0220170011.

Perkins, T. K., and L. R. Kern (1961), Widths of Hydraulic Fractures, *Journal of Petroleum Technology*, *13*(9), 937–949, doi:10.2118/89-PA.

Pratt, W. E., and D. W. Johnson (1926), Local subsidence of the Goose Creek oil field, *Journal of Geology*, *34*(7-1), 577–590, doi:10.1086/623352.

Preuss, S., R. Herrendörfer, T. Gerya, J. P. Ampuero, and Y. Dinther (2019), Seismic and aseismic fault growth lead to different fault orientations, *Journal of Geophysical Research: Solid Earth*, *2*(1), 2019JB017,324, doi:10.1029/2019JB017324.

Price, R. A. (1994), *Geological Atlas of the Western Canadian Sedimentary Basin*, chap. 2, pp. 13–24, Canadian Society of Petroleum Geologists, Calgary, Alberta and Alberta Research Council.

Profit, M., M. Dutko, J. Yu, S. Cole, D. Angus, and A. Baird (2016), Complementary hydro-mechanical coupled finite/discrete element and microseismic modelling to predict hydraulic fracture propagation in tight shale reservoirs, *Computational Particle Mechanics*, *3*(2), 229–248, doi:10.1007/s40571-015-0081-4.

Raleigh, C. B., J. H. Healy, and J. D. Bredehoeft (1976), An experiment in earthquake control at Rangely, Colorado, *Science*, *191*, 1230–1237.

Rice, J. R. (1992), Fault stress states, pore pressure distributions, and the weakness of the San Andres fault, in *Fault Mechanics and Transport Properties of Rocks*, vol. 51, edited by B. Evans and T.-f. Wong, chap. 20, pp. 475–503, International Geophysics, San Diego, California.

Ripperger, J., J. P. Ampuero, P. M. Mai, and D. Giardini (2007), Earthquake source characteristics from dynamic rupture with constrained stochastic fault stress, *Journal of Geophysical Research: Solid Earth*, *112*(4), 1–17, doi:10.1029/2006JB004515.

Rudnicki, J. W. (1986), Fluid mass sources and point forces in linear elastic diffusive solids, *Mechanics of Materials*, *5*(4), 383–393, doi:10.1016/0167-6636(86)90042-6.

Sayers, C., M. Lascano, E. Gofer, L. den Boer, M. Walz, A. Hannan, S. Dasgupta, B. Goodway, M. Perez, and G. Purdue (2016), Geomechanical model for the Horn River formation based on seismic AVA inversion, in *SEG Technical Program Expanded Abstracts 2016*, vol. 35, doi:10.1190/segam2016-13711507.1.

Schoenball, M., and W. L. Ellsworth (2017), A Systematic Assessment of the Spatiotemporal Evolution of Fault Activation Through Induced Seismicity in Oklahoma and Southern Kansas, *Journal of Geophysical Research: Solid Earth*, *122*(12), 10,189–10,206, doi:10.1002/2017JB014850.

Schoenball, M., C. Baujard, T. Kohl, and L. Dorbath (2012), The role of triggering by static stress transfer during geothermal reservoir stimulation, *Journal of Geophysical Research: Solid Earth*, *117*(9), 2–13.

Schoenball, M., F. R. Walsh, M. Weingarten, and W. L. Ellsworth (2018), How faults wake up: the Guthrie-Langston, Oklahoma earthquakes, *The Leading Edge*, *37*(2), 100–106, doi: 10.1190/tle37020100.1.

Schultz, R., V. Stern, M. Novakovic, G. Atkinson, and Y. J. Gu (2015), Hydraulic fracturing and the Crooked Lake Sequences: Insights gleaned from regional seismic netowrks, *Geophysical Research Letters*, *42*, 2750–2758, doi:10.1002/2015GL063455.

Schultz, R., G. Atkinson, D. W. Eaton, Y. J. Gu, and H. Kao (2018), Hydraulic fracturing volume is associated with induced earthquake productivity in the duvernay play, *Science*, *359*(6373), 304–308, doi:10.1126/science.aao0159.

Seeber, L., and J. G. Armbruster (1993), Natural and Induced Seismicity in the Lake-Erie Lake-Ontario Region - Reactivation of Ancient Faults with Little Neotectonic Displacement, *Geographie Physique Et Quaternaire*, *47*(3), 363–378.

Segall, P. (1989), Earthquakes triggered by fluid extraction, *Geology*, *17*(10), 942–946, doi:10. 1130/0091-7613(1989)017<0942:ETBFE>2.3.CO.

Segall, P., and S. Lu (2015), Injection-induced seismicity: Poroelastic and earthquake nucleation effects, *Journal of Geophysical Research: Solid Earth*, *120*, 5082–5103.

Shapiro, S., E. Huenges, and G. Borm (1997), Estimating the crust permeability from fluid-injection-induced seismic emission at the KTB site, *Geophysical Journal International*, *131*(2), F15–F18, doi:10.1111/j.1365-246X.1997.tb01215.x.

Shapiro, S. A., C. Dinske, and E. Rothert (2006a), Hydraulic-fracturing controlled dynamics of microseismic clouds, *Geophysical Research Letters*, *33*(14), 1–5, doi:10.1029/2006GL026365.

Shapiro, S. A., J. Kummerow, C. Dinske, G. Asch, E. Rothert, J. Erzinger, H. J. Kümpel, and R. Kind (2006b), Fluid induced seismicity guided by a continental fault: Injection experiment of 2004/2005 at the German Deep Drilling Site (KTB), *Geophysical Research Letters*, *33*(1), 2–5, doi:10.1029/2005GL024659.

Shapiro, S. A., C. Dinske, C. Langenbruch, and F. Wenzel (2010), Seismogenic index and magnitude probability of earthquakes induced during reservoir fluid stimulations, *Leading Edge*, *29*(3), 304–309.

Shapiro, S. A., O. S. Krüger, C. Dinske, and C. Langenbruch (2011), Magnitudes of induced earthquakes and geometric scales of fluid-stimulated rock volumes, *Geophysics*, *76*(6), WC55–WC63, doi:10.1190/geo2010-0349.1.

Simpson, R. W., and P. A. Reasenberg (1994), Earthquake-induced static stress changes on central california faults, *U. S. Geological Survey Prof. Paper 1550-F*.

Skempton, A. W. (1954), The pore-pressure coefficients a and b, *Géotechnique*, *4*, 143–147.

Skoumal, R. J., M. R. Brudzinski, and B. S. Currie (2015), Earthquakes induced by hydraulic fracturing in Poland township, Ohio, *Bulletin of the Seismological Society of America*, *105*(1), 189–197, doi:10.1785/0120140168.

Skoumal, R. J., R. Ries, M. R. Brudzinski, A. J. Barbour, and B. S. Currie (2018), Earthquakes Induced by Hydraulic Fracturing Are Pervasive in Oklahoma, *Journal of Geophysical Research: Solid Earth*, *123*(12), 10,918–10,935, doi:10.1029/2018JB016790.

Skoumal, R. J., J. O. Kaven, and J. I. Walter (2019), Characterizing Seismogenic Fault Structures in Oklahoma Using a Relocated Template‚ÄêMatched Catalog, *Seismological Research Letters*, *90*(4), 1535–1543, doi:10.1785/0220190045.

Skoumal, R. J., A. J. Barbour, M. R. Brudzinski, T. Langenkamp, and J. O. Kaven (2020), Induced Seismicity in the Delaware Basin, Texas, *Journal of Geophysical Research: Solid Earth*, *125*(1), doi:10.1029/2019JB018558.

Snelling, P., M. de Groot, C. Craig, and K. Hwang (2013), Structural controls on stress and microseismic response - a Horn River Basin case study, in *SPE Unconventional Resources Conference Canada, Calgary,*, Society of Petroleum Engineers, doi:10.2118/167132-MS.

Steacy, S., D. Marsan, S. S. Nalbant, and J. McCloskey (2004), Sensitivity of static stress calculations to the earthquake slip distribution, *Journal of Geophysical Research*, *109*, 16, doi:10.1029/2002JB002365.

Steacy, S., J. Gomberg, and M. Cocco (2005), Introduction to special section: Stress transfer, earthquake triggering, and time-dependent seismic hazard, *Journal of Geophysical Research*, *110*(B05S01), doi:10.1029/2005JB003692.

Stein, R. S. (1999), The role of stress transfer in earthquake occurrence, *Nature*, *402*, 605–609, doi:10.1038/45144.

Stork, A. L., J. P. Verdon, and J. M. Kendall (2014), The robustness of seismic moment and magnitudes estimated using spectral analysis, *Geophysical Prospecting*, *62*(4), 862–878, doi:10.1111/1365-2478.12134.

Stork, A. L., J. P. Verdon, and J. M. Kendall (2015), The microseismic response at the In Salah Carbon Capture and Storage (CCS) site, *International Journal of Greenhouse Gas Control*, *32*, 159–171, doi:10.1016/j.ijggc.2014.11.014.

Sumy, D. F., E. S. Cochran, K. M. Keranen, M. Wei, and G. A. Abers (2014), Observations of static Coulomb stress triggering of the November 2011 M_W 5.7 Oklahoma earthquake sequence, *Journal of Geophysical Research: Solid Earth*, *119*(3), 1904–1923, doi:10.1002/2013JB010612.

Tan, Y., Z. Pan, J. Liu, X. T. Feng, and L. D. Connell (2018), Laboratory study of proppant on shale fracture permeability and compressibility, *Fuel*, *222*(February), 83–97, doi:10.1016/j.fuel.2018.02.141.

Tingay, M. R. P., J. Reinecker, and B. Müller (2008), Borehole breakout and drilling-induced fracture analysis from image logs, *Tech. Rep. Guidelines: Image Logs*, World Stress Map Project.

Toda, S., R. S. Stein, and T. Sagiya (2002), Evidence from the AD 2000 Izu islands earthquake swarm that stressing rate governs seismicity, *Nature*, *419*(6902), 58–61, doi:10.1038/nature00997.

Toda, S., R. S. Stein, K. Richards-Dinger, and S. B. Bozkurt (2005), Forecasting the evolution of seismicity in southern California: Animations built on earthquake stress transfer, *Journal of Geophysical Research: Solid Earth*, *110*(5), 1–17, doi:10.1029/2004JB003415.

Urbancic, T., S. Maxwell, and R. Zinno (2003), Assessing the effectiveness of hydraulic fractures with microseismicity, in *SEG Technical Program Expanded Abstracts 2003*, doi:10.1190/1.1817923.

van der Baan, M., and F. J. Calixto (2017), Human-induced seismicity and large-scale hydrocarbon production, *Geochemistry Geophysics Geosystems*, *18*, 2467–2485, doi:doi:10.1002/2017GC006915.

van der Elst, N. J., H. M. Savage, K. M. Keranen, and G. A. Abers (2013), Enhanced Remote Earthquake Triggering at Fluid-Injection Sites in the Midwestern United States, *Science*, *341*(July), 164–167, doi:10.4159/harvard.9780674430501.c21.

van der Elst, N. J., M. T. Page, D. A. Weiser, T. H. Goebel, and S. M. Hosseini (2016), Induced earthquake magnitudes are as large as (statistically) expected, *Journal of Geophysical Research: Solid Earth*, *121*, 4575–4590, doi:10.1002/2016JB012818.

van Thienen-Visser, K., and J. N. Breunese (2015), Induced seismicity of the groningen gas field: History and recent developments, *The Leading Edge*, *June*.

Vasudevan, K., and D. W. Eaton (2011), Hydraulic fracturing: Coulomb failure stress in fracture networks, *CSEG Recorder*, *36*(9), 24–31.

Vavryčuk, V. (2011), Tensile earthquakes: Theory, modeling, and inversion, *Journal of Geophysical Research: Solid Earth*, *116*(12), 1–14, doi:10.1029/2011JB008770.

Vavryčuk, V. (2014), Iterative joint inversion for stress and fault orientations from focal mechanisms, *Geophysical Journal International*, *199*(1), 69–77, doi:10.1093/gji/ggu224.

Vavryčuk, V. (2015), Inversion for the composite moment tensor, *Bulletin of the Seismological Society of America*, *105*(6), 3024–3035, doi:10.1785/0120150163.

Verdon, J. P. (2013), Fractal dimension of microseismic events via the two-point correlation dimesion, and its correlation with b values, in *4th EAGE Passive Seismic Workshop, Amsterdam*.

Verdon, J. P., and J. Budge (2018), Examining the Capability of Statistical Models to Mitigate Induced Seismicity during Hydraulic Fracturing of Shale Gas Reservoirs, *Bulletin of the Seismological Society of America*, doi:10.1785/0120170207.

Verdon, J. P., A. Wuestefeld, J. T. Rutledge, I. G. Main, and J.-M. Kendall (2013a), Correlation between spatial and magnitude distributions of microearthquakes during hydraulic fracture stimulation, in *EAGE Annual Meeting, London*, EAGE.

Verdon, J. P., J. M. Kendall, A. L. Stork, R. A. Chadwick, D. J. White, and R. C. Bissell (2013b), A comparison of geomechanical deformation induced by 'megatonne' scale co_2 storage at sleipner, weyburn and in salah, *International Journal of Greenhouse Gas Control*, *110*, E2762–W2771.

Verdon, J. P., J.-M. Kendall, A. L. Stork, R. A. Chadwick, D. J. White, and R. C. Bissell (2013c), Comparison of geomechanical deformation induced by megatonne-scale CO$_2$ storage at Sleipner, Weyburn, and In Salah., *Proceedings of the National Academy of Sciences of the United States of America*, *110*(30), E2762–71, doi:10.1073/pnas.1302156110.

Verdon, J. P., J. M. Kendall, A. C. Horleston, and A. L. Stork (2016), Subsurface fluid injection and induced seismicity in southeast saskatchewan, *International Journal of Greenhouse Gas Control*, *54*, 429–440.

Verdon, J. P., J.-M. Kendall, S. Hicks, and P. Hill (2017), Using beamforming to maximise the detection capability of small, sparse seismometer arrays deployed to monitor oil field activities, *Geophysical Prospecting*, *65*, 1582–1596.

Viegas, G., A. Baig, W. Coulter, and T. Urbancic (2012), Effective monitoring of reservoir-induced seismicity utilizing integrated surface and downhole seismic networks, *First Break*, *30*(7), 77–81.

Walsh, F. R., and M. D. Zoback (2015), Oklahoma's recent earthquakes and saltwater disposal, *Science Advances*, *1*(e1500195), 1–9, doi:10.1126/sciadv.1500195.

Walsh, F. R., and M. D. Zoback (2016), Probabilistic assessment of potential fault slip related to injectioninduced earthquakes: Application to north-central Oklahoma, USA, *Geology*, *44*(12), 991–994, doi:10.1130/G38275.1.

Walsh, F. R., M. D. Zoback, D. Pais, M. Weingarten, and T. Tyrrell (2017), FSP 1.0: A Program for Probabilistic Estimation of Fault Slip Potential Resulting From Fluid Injection, User Guide from the Stanford Center for Induced and Triggered Seismicity, *Tech. rep.*, Stanford Center for Induced and Triggered Seismicity.

Wang, R., F. Lorenzo-Martín, and F. Roth (2006), PSGRN/PSCMP - A new code for calculating co- and post-seismic deformation, geoid and gravity changes based on the viscoelastic-gravitational dislocation theory, *Computers and Geosciences*, *32*(4), 527–541.

Warpinski, N., Z. Moschovidis, and I. Abou-Sayed (1994), Comparison Study of Hydraulic Fracturing Models - Test Case: GRI Staged Field Experiment No. 3, *Proceedings of the SPE Production and Facilities, February 1994*, *9*(SPE 28158), 17–18, doi:10.2118/25890-PA.

Wedmore, L. N., J. P. Faure Walker, G. P. Roberts, P. R. Sammonds, K. J. McCaffrey, and P. A. Cowie (2017), A 667 year record of coseismic and interseismic Coulomb stress changes in central Italy reveals the role of fault interaction in controlling irregular earthquake recurrence intervals, *Journal of Geophysical Research: Solid Earth*, *122*(7), 5691–5711, doi:10.1002/2017JB014054.

Weingarten, M., S. Ge, J. W. Godt, B. a. Bekins, and J. L. Rubinstein (2015), High-rate injection is associated with the increase in U.S. mid-continent seismicity, *Science*, *348*(6241), 1336–1340, doi:10.1126/science.aab1345.

Williams, M. J., and J. Le Calvez (2013), Reconstructing frequency-magnitude statistics from detection limited microseismic data, *Geophysical Prospecting*, *61*(SUPPL.1), 20–38, doi:10.1111/j.1365-2478.2012.01097.x.

Wilson, T. K., and R. M. Bustin (2019), Basin modelling and thermal history of the horn river and liard basins, cordova embayment, and adjacent parts of the western canada sedimentary basin, *Geoscience bc summary of activities 2018*, Energy and Water, Geoscience BC.

Wright, G., M. McMechan, and D. Potter (1994), *Geological Atlas of the Western Canadian Sedimentary Basin*, chap. 3, pp. 13–24, Canadian Society of Petroleum Geologists, Calgary, Alberta and Alberta Research Council.

Yeck, W. L., M. Weingarten, H. M. Benz, D. E. McNamara, E. A. Bergman, R. B. Herrmann, J. L. Rubinstein, and P. S. Earle (2016), Far-field pressurization likely caused one of the largest injection induced earthquakes by reactivating a large preexisting basement fault structure, *Geophysical Research Letters*, *43*(19), 10,198–10,207, doi:10.1002/2016GL070861.

Yoon, S. H., Y. J. Joe, C. S. Koh, J. H. Woo, and H. S. Lee (2018), Sedimentary processes and depositional environments of the gas-bearing Horn River shale in British Columbia, Canada, *Geosciences Journal*, *22*(1), 33–46, doi:10.1007/s12303-017-0053-1.

York, D., N. M. Evensen, M. L. Martínez, and J. De Basabe Delgado (2004), Unified equations for the slope, intercept, and standard errors of the best straight line, *American Journal of Physics*, *72*(3), 367–375, doi:10.1119/1.1632486.

Zoback, M. D. (2010), *Reservoir Geomechanics*, Cambridge University Press.

Zoback, M. D., D. Moos, L. Mastin, and R. N. Anderson (1985), Well bore breakouts and in situ stress, *Journal of Geophysical Research*, *90*(B7), 5523, doi:10.1029/JB090iB07p05523.

Zoback, M. D., C. A. Barton, M. Brudy, D. A. Castillo, T. Finkbeiner, B. R. Grollimund, D. B. Moos, P. Peska, C. D. Ward, and D. J. Wiprut (2003), Determination of stress orientation and magnitude in deep wells, *International Journal of Rock Mechanics and Mining Sciences*, *40*(7-8), 1049–1076, doi:10.1016/j.ijrmms.2003.07.001.